The University Of Calgary

A Predictive Model For A Circulating Fluidized Bed Riser Reactor

by

David Michael John Puchyr

A Dissertation
Submitted To The Faculty Of Graduate Studies
In Partial Fulfillment Of The Requirements For The
Degree Of Doctor Of Philosophy

Department Of Chemical And Petroleum Engineering

Calgary, Alberta
September, 1998

© David Michael John Puchyr 1998

National Library
of Canada

Acquisitions and
Bibliographic Services

395 Wellington Street
Ottawa ON K1A 0N4
Canada

Bibliothèque nationale
du Canada

Acquisitions et
services bibliographiques

395, rue Wellington
Ottawa ON K1A 0N4
Canada

Your file Votre référence

Our file Notre référence

The author has granted a non-exclusive licence allowing the National Library of Canada to reproduce, loan, distribute or sell copies of this thesis in microform, paper or electronic formats.

The author retains ownership of the copyright in this thesis. Neither the thesis nor substantial extracts from it may be printed or otherwise reproduced without the author's permission.

L'auteur a accordé une licence non exclusive permettant à la Bibliothèque nationale du Canada de reproduire, prêter, distribuer ou vendre des copies de cette thèse sous la forme de microfiche/film, de reproduction sur papier ou sur format électronique.

L'auteur conserve la propriété du droit d'auteur qui protège cette thèse. Ni la thèse ni des extraits substantiels de celle-ci ne doivent être imprimés ou autrement reproduits sans son autorisation.

0-612-38498-5

Canada

Abstract

This dissertation presents a predictive, two-dimensional, time-averaged hydrodynamic model for a circulating fluidized bed (CFB) riser operating in the fast fluidization regime with downward flow of gas and solids near the wall. The basis for the model is a substantially augmented core-annulus approach with both gas and solids ascending in the core and descending in the annulus. Rigorous development of the mass and momentum conservation equations results in a novel material interchange scheme between the core and annulus, for both phases, and unprecedented sophistication in the pressure drop calculation. In addition to predicting the axially varying core radius and pressure, the model predicts the axially and radially varying solids mass flux and velocity, gas mass flux and velocity, and voidage given the riser geometry, inlet temperature, pressure and solids mass flux, and physical properties of the gas and solids. With the use of a neoteric simulator, extensive comparisons between the model predictions and published experimental data demonstrate that the model is successful in representing the hydrodynamics in a CFB riser.

A coupled hydrodynamic and kinetic reaction model for a CFB riser reactor stems from a slightly simplified version of the elaborate two-dimensional hydrodynamic model. The reactor model also manifests itself in the simulator and generates residence time distribution functions for both gas and solids phases that deviate markedly from plug flow conditions, which emulates experimental observation. Derivation of the energy conservation equation and its incorporation into the coupled hydrodynamic-kinetic reaction model demonstrates that near isothermal operation of a CFB riser reactor is possible, even for highly exothermic reactions. Simulations also confirm that, for a reversible reaction, the conversion in a CFB riser reactor with downward flow of gas and solids near the wall is much less than the conversion in a comparable dense phase pneumatic transport reactor that behaves as a plug flow reactor.

Acknowledgments

First of all, I must thank Professor Leo Behie for the countless times I was taken aback by his overwhelming generosity; he financed my attendance at CSChE '96, in Kingston, CSChE '97, in Edmonton, and Fluidization IX, in Durango, to mention but a few examples. I am most thankful that he initiated contact for me with Hyprotech Ltd., where I met his former graduate student Dr. Rudi Stocker.

Rudi, the "POLYSIM Mastermind", is my friend and mentor. He granted me the freedom I needed to pursue graduate studies while working at Hyprotech and keeps me humble by perpetually expanding my vocabulary. I am glad to have met him and my acquaintance with him will be long-lived.

I am truly grateful to my many friends and the hundreds of people that I have met at The Den, who, whether they know it or not, indirectly contributed to the completion of this dissertation by providing me with much needed escapes from the glare of my computer monitor. My ever present need for socialization was fulfilled by my always understanding friends, particularly Jason Koch and Sonia "Excellent you are, Baby!" Poon.

Finally, I appreciate the financial support that was granted in the form of The John S. Poyen Scholarship and DB Robinson And Associates Travel Grant.

Contents

List of Tables

List of Figures

Nomenclature

Symbols

A	=	Area
a, b, c	=	Radial Profile Parameters In The Core
C_d	=	Drag Coefficient
D	=	Diameter
d, e, f	=	Radial Profile Parameters In The Annulus
E	=	Energy
F	=	Force
F_i	=	Mole Flow Rate Of Component i
G	=	Mass Flux
g	=	Gravity
H	=	Height
$\mathcal{H}$	=	Enthalpy
k	=	Mass Transfer Coefficient
K, ω, h, k	=	Axial Profile Parameters For Second Order Responses
K, τ, k	=	Axial Profile Parameters For First Order Responses
L	=	Length
MW	=	Average Molecular Weight
P	=	Pressure
R	=	Radius
r	=	Radial Co-ordinate
R_g	=	Universal Gas Constant
r_j	=	jth Reaction Rate
t	=	Time
T	=	Temperature
u	=	Velocity

x_i	=	Material Interchange Delimiting Co-ordinate
y	=	Mole Fraction
z	=	Axial Co-ordinate
z_i	=	Lower Zone-Upper Zone Interface Axial Co-ordinate
$\alpha, \beta, \gamma, \delta$	=	Re-Circulation Ratio Parameters
$\mathcal{F}$	=	Mass Fraction
Δ	=	Change
$\dot{m}$	=	Mass Flow Rate
ϵ	=	Voidage
Λ	=	Momentum Rate
ν	=	Stoichiometric Coefficient
Ω	=	Normalized Mass Balance Function At The LZUZI
ϕ	=	Core Fraction
ψ	=	Slip Factor
ψ_i	=	Radial Mass Flux Profile Coefficients
ρ	=	Density
Ar	=	Archimedes Number
Fr	=	Froude Number
Re_c	=	Modified Reynolds Number $= \rho u_{g\mathrm{in}} D / \mu \sqrt{\phi_g}$
Sc	=	Schmidt Number $= \mu / D_v \rho$
Sh_c	=	Modified Sherwood Number $= k D \sqrt{\phi_g} / D_v \rho$

Subscripts

a	=	Annulus
ac	=	Annulus To Core
c	=	Core
ca	=	Core To Annulus
g	=	Gas
in	=	Inlet
p	=	Particle
s	=	Solids
t	=	Terminal
0	=	Center-Line
1	=	Wall

Superscripts

i	=	ith Axial Discretized Grid Block
$\bar{}$	=	Average Value
$\star$	=	Indicates integration from $z = 1$ to $z = 0$

Acronyms

CFB	=	Circulating Fluidized Bed
CFD	=	Computational Fluid Dynamics
CSTR	=	Continuous Stirred Tank Reactor
DPM	=	Discrete Particle Modeling
FCC	=	Fluid Catalytic Cracking
HDCFB	=	High Density Circulating Fluidized Bed
KTGF	=	Kinetic Theory Of Granular Flow
LDCFB	=	Low Density Circulating Fluidized Bed
LZUZI	=	Lower Zone-Upper Zone Interface
PFR	=	Plug Flow Reactor
RTD	=	Residence Time Distribution

1 Introduction

The economic driving force present in most human endeavors provides the motivation for mathematical modeling. In chemical engineering applications, the abstract concept of modeling manifests itself in various forms such as process conception, design, and optimization, to name but a few. All of the manifestations can be amalgamated under the genus of using mathematics to predict the future, the profound implications of which are obvious.

A concrete example of the power of modeling was realized by engineers at Monsanto Company when they used Hyprotech Ltd.'s process simulator, "HYSYS", to optimize the production of the herbicide "Round-Up". The process was plagued by reactor liquid level shrink and swell that resulted in blow over of the product and a loss of yield (McMillan et al., 1996). Using the 50 kUS$ simulator, the engineers built a model of the process in cyberspace, examined several scenarios, and optimized the most promising scheme—all without disrupting the real process. The savings that resulted from the implementation of the optimized process amounted to a staggering 30 to 90 MUS$ per year!

Modeling entire chemical engineering processes is an absolutely enormous task. Fortunately, since chemical processes proceed in a series of unit operations, engineers can devise stand-alone models for each unit operation, which renders the task of modeling the entire process less daunting. Of particular interest in chemical engineering are chemical reactors.

Most chemical reactors operate with either a fixed or fluidized bed of solid catalyst. In a gas-solid fixed bed catalytic reactor, the solids remain stationary as a gas passes through the voids between the solids. In a gas-solid fluidized bed reactor, the drag of the upward flowing gas on the solid particles counteracts the weight of the solids thereby mobilizing the particles, which then flow freely with the characteristics of a fluid. Various flow structures within a fluidized bed reactor can exist depending upon physical and operational characteristics of the bed.

1.1 Fluidization Regimes

Six distinct hydrodynamic regimes, conceptually represented in Figure 1, exist when a gas passes upward through a bed of Group B particles (Grace, 1986). When the

Figure 1: Group B Particle Fluidization Regimes

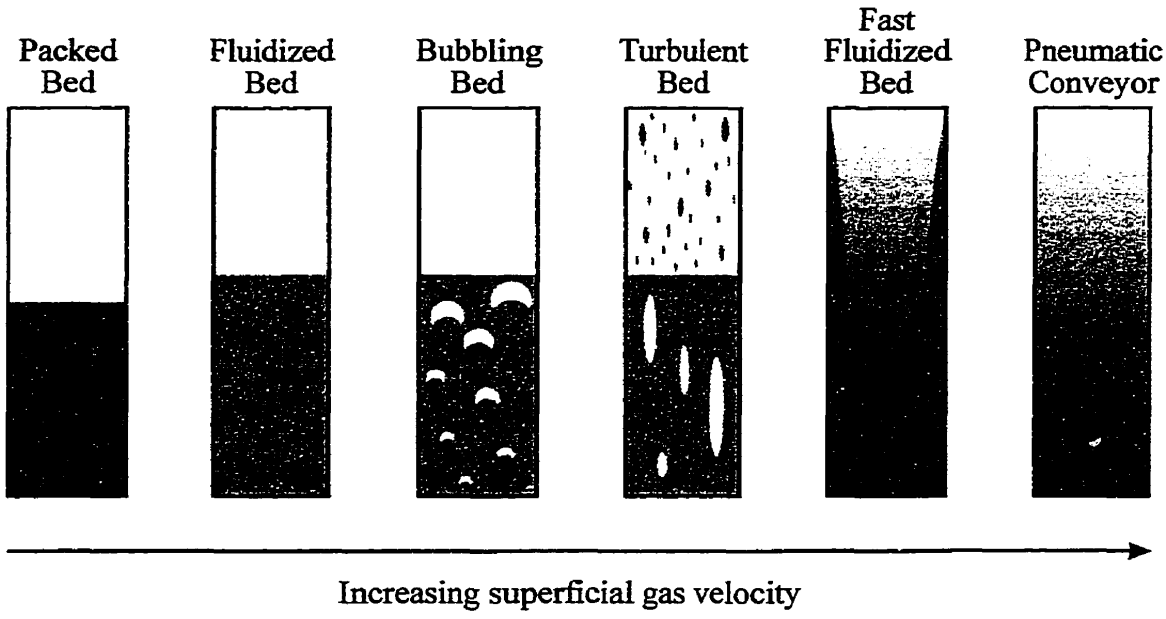

superficial velocity of the gas is low, the particles do not move and the pressure drop through the "packed" bed is given by the Ergun (1952) equation. If the superficial velocity of the gas increases, there is a velocity at which the force of drag on the particles exactly equals the weight of the bed. The particles become suspended by the gas and the bed unlocks. At incipient or minimum fluidization, the particles are fully suspended and the bed has moved from the packed to "fluidized" bed regime. The suspension behaves as a fluid.

If the superficial gas velocity increases above the minimum fluidization velocity, the Two Phase Theory Of Fluidization (Toomey and Johnstone, 1952) becomes applicable: Gas in excess of that required to incipiently fluidize the bed passes through the bed as bubbles. The "bubbling" bed regime is the third of the hydrodynamic regimes. When a bubble reaches the top surface of the suspension, it bursts, which ejects some

of the finer particles into the freeboard region above the suspension. Cyclones capture and return entrained particles to the base of the bed.

A further marked increase in the superficial gas velocity results in a different hydrodynamic regime. The relatively high gas velocity causes significant entrainment of particles in the freeboard region, which designates the onset of the "turbulent" bed regime (Chehbouni et al., 1994). If, in addition to the re-circulation of the entrained particles, more solids are fed, the height of the suspension increases but its density remains constant. The superficial gas velocity in the turbulent regime is typically an order of magnitude greater than that of the bubbling bed regime.

The superficial gas velocity in the "fast fluidization" regime is greater than that of the turbulent regime but is of the same order of magnitude. A fast fluidized bed is characterized by a region of relatively high solids concentration at the base of the bed and a relatively low solids concentration in the upper portion of the bed. In the upper portion of the bed, gas and solids ascend in the center of the riser and descend at the wall (i.e. exhibit core–annular flow). Typically, a system of externally mounted cyclones capture and return the entrained solids to the base of the bed. Without a substantial solids re-capturing system, the bed is quickly emptied of solids.

When the superficial gas velocity is increased so as to induce a change from the fast fluidization regime, the final hydrodynamic regime is encountered: The "pneumatic transport" regime. The velocity of the gas in this regime is sufficient to convey all of the particles upward and out of the riser. As with a fast fluidized bed, a system of cyclones, or ballistic separator, recycle the solids back to the base of the riser for re-injection. Further increases in the superficial gas velocity do not cause a change in the hydrodynamics of the riser.

Varying degrees of solids entrainment occur when the superficial gas velocity is greater than the incipient fluidization velocity. If the entrained solids are re-circulated back to the bottom of the bed, it can be classified as a "circulating fluidized bed" (CFB) (Berruti et al., 1995); however, the connotation of a CFB is a bed operating

in the fast fluidization regime. Throughout this dissertation, any reference to a CFB is restricted to the connotational definition of a fast fluidized bed.

1.2 CFB Apparatus

A gas and solids injection system, riser, gas and solids separation system, and solids reservoir are the key features or components of a CFB system. Figure 2, a schematic representation of a CFB, illustrates these features. Naturally, many configurations of each component exist.

The gas and solids injection system may intimately couple the two phases outside of the riser, as in the case of a non-mechanical solids injection system (Pugsley, 1995), or inside the riser, as in the case of an L-valve or J-valve injection system. A mechanical solids feeder, such as a screw feeder or slide valve, may also introduce the solids into the riser. In many cases, a gas distributor is present at the base of the riser to ensure a uniform distribution of the gas phase before it enters the riser.

The riser cross-section is circular or rectangular and is constant throughout the entire riser length, unlike many conventional fluidized beds where the freeboard region may exhibit a large increase in the cross-sectional area to disengage the solids. The exit configuration of the riser is generally categorized as smooth or abrupt and, depending on operating conditions and particle characteristics, can greatly influence the hydrodynamics in the riser (Pugsley et al., 1997).

The massive carry-over of solids, a design feature of a CFB, necessitates the use of a substantial gas and solids separation system. Typically, a system of primary and secondary cyclones and a bag filter are adequate for solids re-capture. In a catalytic riser reactor, the use of an attrition resistant catalyst is necessary (Contractor et al., 1994) due to the excessive and violent contact between the solids and walls.

The CFB shown in Figure 2 is a variable inventory system because of the solids reservoir (Kunii and Levenspiel, 1991), which allows for control over the inlet solids mass flux. Catalyst regeneration, a common requirement of chemical reactors, can

Figure 2: Schematic Representation Of A CFB System

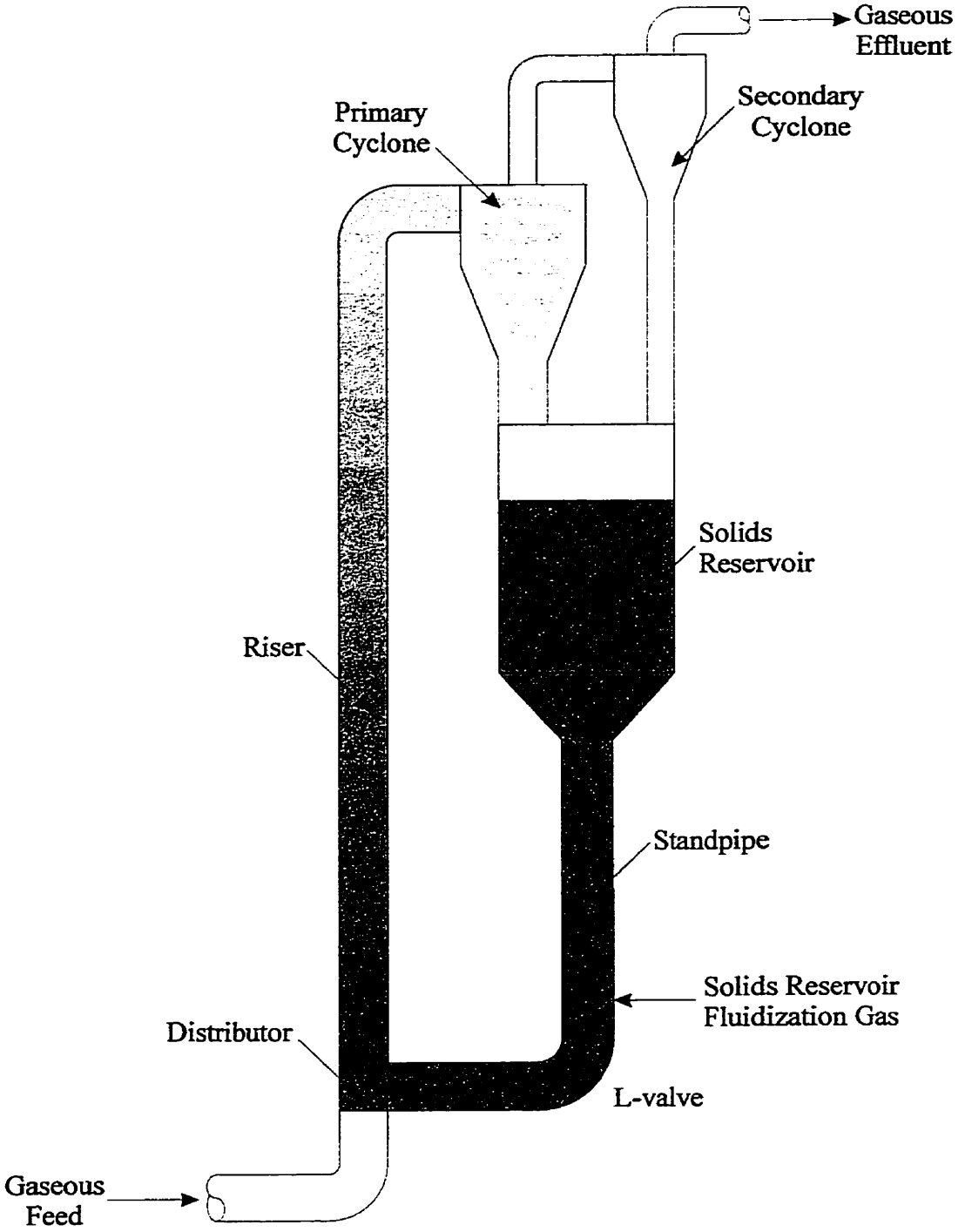

also take place in the solids reservoir. One of the distinct advantages fluidized bed reactors have over fixed bed reactors is that catalyst regeneration can be continuous in a fluidized bed.

Researchers use various techniques to model fluidized bed reactors. Obviously, the accuracy of model predictions is a function of the model itself. Due to the complex nature of the system, conceptual misunderstanding and/or computational restraints introduce shortcomings into fluidized bed reactor models. Shortcomings due to the latter beckon for rectification as computational power increases, thus making model development an iterative, evolutionary process. Additionally, and more importantly, improved understanding and radical new representations of observed phenomena allow for quantum leaps in model development and accuracy.

1.3 Scope

The thrust of the research presented in this dissertation is on modeling a CFB riser reactor operating in the fast fluidization regime. Countless variations in the configuration of a fast fluidized riser exist, such as the location and number of gas feeds, entrance and exit configurations, solids injection mechanisms, and more. Therefore, further refinement of the scope of the model is required to make it tractable. To that end, the model presented in this dissertation applies to riser reactors adhering to the following restrictions: The riser

- operates in the fast fluidization regime with downward flow of gas and solids near the wall,
- has a single gas feed at the base of the riser,
- uses a solids injection mechanism that introduces the particles at the base of the riser with a positive velocity,
- contains mono-disperse, spherical particles of Geldart Group A or B classification (Geldart, 1973), and

- has a smooth exit.

Even with these imposed restrictions, CFB modeling is a formidable task that requires unbridled creativity, in-depth knowledge of scientific computing, and fundamental understanding of physical phenomena.

An incredible number of recent experimental observations exist in open literature that give a clear picture of the characteristics of CFBs operating within the confines mentioned above. Consequently, simulation and comparison with published data, rather than direct experimentation, validate the model presented in this dissertation.

1.4 Objectives

In general, shortcomings inherently exist in fluidized bed reactor models. The primary objective of the research presented in this dissertation is to take the next step on the evolutionary path of CFB model development, thereby improving on the accuracy of previously published models. The approach exploited to realize the ultimate objective uses a time-averaged, steady-state, axi-symmetric representation of a CFB. Specific objectives that must be met in order to achieve improved realism in the riser reactor model are:

1. **Incorporate the downward flow of gas and solids at the wall.**

    - The downward flow of gas and solids in a CFB riser reactor is back-mixing, which can have catastrophic effects on conversion, selectivity, and yield. Therefore, it is imperative to include this phenomenon in a reactor model, even though it generates tremendous numerical overhead and complexity in both the model itself and the solution algorithms.

2. **Develop a novel core-annulus material interchange scheme.**

- Most material interchange computational algorithms, which are elaborated upon in Section 2, rely on a mass transfer coefficient. The existing algorithms can be divided into two types of schemes: Some schemes require experimental measurements while others are based on obscure analogies to other unrelated transport phenomena. The former type of scheme is not applicable for design purposes and the latter is not very well founded.

3. **Include the contribution of the acceleration of solids in the pressure drop calculation.**

   - Neglecting the contribution of the acceleration of solids in the pressure drop calculation can result in the over-prediction of the solids concentration in the riser in addition to affecting reaction rates in a riser reactor.

4. **Account for reactions that incur a change in moles.**

   - In heterogeneous gas-solid reactions there is often a significant change in moles that should most definitely be accounted for since it affects the hydrodynamics in the riser. Models developed prior to the one presented in this dissertation do not account for a change in moles and, consequently, have restricted application.

5. **Devise a general, numerical algorithm for solving coupled hydrodynamic and kinetic reaction equations.**

   - By itself, a hydrodynamic model can be very complicated. The level of complexity dramatically increases when the hydrodynamic model is coupled with a kinetic reaction model. Moreover, the kinetic reaction model may contain several reactions occurring concurrently, each with non-linear rate equations. An analytical solution to the resulting system of coupled,

non-linear differential equations is not likely to be determined. The alternative is to use a numerical algorithm.

Additionally, the model should be predictive—the only inputs to it should be particle characteristics and riser operating conditions and geometry (design variables).

2 Literature Review

Interest in CFBs has sparked a massive proliferation of publications by academic and industrial researchers alike. No less than 40% of the papers presented at Fluidization IX (Durango, CO, 98.05.17–98.05.22), a conference encompassing all types of fluidization, dealt with CFBs. A logical starting point for delving into the many facets of CFBs is outlining the operating conditions that demarcate conventional fluidized beds from circulating fluidized beds.

Empirical correlations can estimate the transition velocities designating the onset of the CFB regimes. Bi et al. (1995) deem the transition velocity of a turbulent bed to a fast fluidized bed as the "critical velocity" (u_{se}) and found that

$$u_{se} = 1.53\sqrt{\frac{gD_p(\rho_p - \rho_g)}{\rho_g}} \tag{1}$$

correlates data from many independent sources using risers greater than 5.5 m tall and 75 mm in diameter quite well. Similarly, the "choking velocity" (u_{ch}), above which the bed is operating in the pneumatic transport regime, can be calculated using the correlation of Bi and Fan (1991):

$$\frac{u_{ch}}{\sqrt{gD_p}} = 21.6\left(\frac{G_s}{\rho_g u_{ch}}\right)^{0.542} \mathrm{Ar}^{0.105}. \tag{2}$$

Inherent advantages of Equation 2 over other correlations for the choking velocity (Yang, 1975, 1983; Punwani et al., 1976) are that it is state-of-the-art and explicitly includes the inlet solids mass flux. The inclusion of the solids mass flux makes Equation 2 predictive (i.e. no experimental measurements are required) and highly useful for simulation studies.

Equations 1 and 2 give distinct, discrete boundaries between hydrodynamic regimes. However, over the past few years, the definition of the fast fluidization regime has undergone further refinement and segregation.

2.1 Circulating Fluidized Bed Subclasses

Zhu and Bi (1995) give qualitative subclassifications of the fast fluidization regime based on the operation and application of the CFB. Non-catalytic processes, such as coal combustion and iron ore reduction, proceed at a low reaction rate and do not require a high solids mass flux or gas superficial velocity since the solids constitute the desired reaction component. Gas back-mixing is generally not a concern. Conversely, in gas-solids catalytic processes, such as fluid catalytic cracking and the oxidation of *n*-butane to maleic anhydride, the desired product is in the gas phase and gas back-mixing is not desirable. Additionally, catalyst deactivation may occur as a reaction proceeds, which makes solids back-mixing undesirable. Zhu and Bi (1995) classify a bed used in a non-catalytic CFB process operating with a relatively low solids mass flux ($\sim$<200 kg m^{-2}s^{-1}) and superficial gas velocity ($\sim$<10 m s^{-1}) as a low density circulating fluidized bed (LDCFB). They classify a bed used in a catalytic CFB process operating with a relatively high solids mass flux and superficial gas velocity as a high density circulating fluidized bed (HDCFB). Throughout this dissertation, regardless of the operation and/or application, an LDCFB is considered to be a bed operating in the fast fluidization regime with downward flow of gas and solids at the wall; an HDCFB is considered to be a bed operating in the fast fluidization regime with no net downward flow of gas or solids at any point in the riser.

2.1.1 Characteristics Of An LDCFB

From a macroscopic perspective of observed axial solids behavior, an LDCFB with a smooth exit is comprised of two zones. The "lower dense zone" is characterized by a relatively high solids concentration and the "upper dilute zone" is characterized by a relatively low solids concentration. A plot of average voidage versus riser height exhibits an inflection point, which is a quantifiable boundary between the two zones. Kruse et al. (1995) further subdivide the lower dense zone into a "bottom zone" and "splash zone". They cite the works of Svensson et al. (1993) and Werther and Wein

(1994) for describing the bottom zone solids behavior as similar to a bubbling fluidized bed. The disappearance of bubbles and rapid decrease in the solids concentration characterizes the splash zone.

Many researchers (Puchyr et al., 1997; Berruti et al., 1995; Pugsley, 1995; Patience and Chaouki, 1995) dub the lower dense zone as the "acceleration zone" and the upper dilute zone as the "fully developed zone". In fact, in a non-reactive riser with a constant cross-sectional area, these descriptions are misnomers because the solids accelerate throughout the length of the riser due to the expansion of the (compressible) gas phase. "Lower dense zone" and "upper dilute zone" are more appropriate designations.

In the upper dilute zone there are radial non-uniformities in the solids mass flux and velocity profiles. Both the profiles have a maximum at the center-line of the riser (Nieuwland et al., 1996; Motte et al., 1996; Miller and Gidaspow, 1992; Rhodes et al., 1992) and are zero near the riser wall. The radius of the core (r_c) in an LDCFB is defined as the radial location at which the solids profiles are zero. In the core, $0 \leq r \leq r_c$, the solids flow in the positive, upward direction. In the annulus, the region concentrically surrounding the core and bound by the riser wall ($r_c \leq r \leq R$), the solids flow in the negative, downward direction. The core radius varies throughout the height of the riser and is a function of riser operating conditions and geometry. Several empirical correlations that predict the location of the core radius are available (Yang, 1998; Bi et al., 1996; Werther, 1994).

The core radius increases with height in the riser and, since the solids mass flux profile directly relates to the core radius, it too varies with height. Consequently, the radial solids mass flux profile is close to parabolic in the lower portion of the riser and tends to flatten out in the upper portion. By conservation of mass at steady-state, the net solids mass flux at any axial location in the riser is equal to the inlet solids mass flux. So, as the solids mass flux profile goes from near parabolic to nearly flat, there is a decrease in the center-line value and a net migration of solids from the center of

the riser to the wall. Figure 3, extracted from Brereton et al. (1993), illustrates this phenomenon.

Figure 3: Net Solids Flow Patterns In An LDCFB (from Brereton et al., 1993)

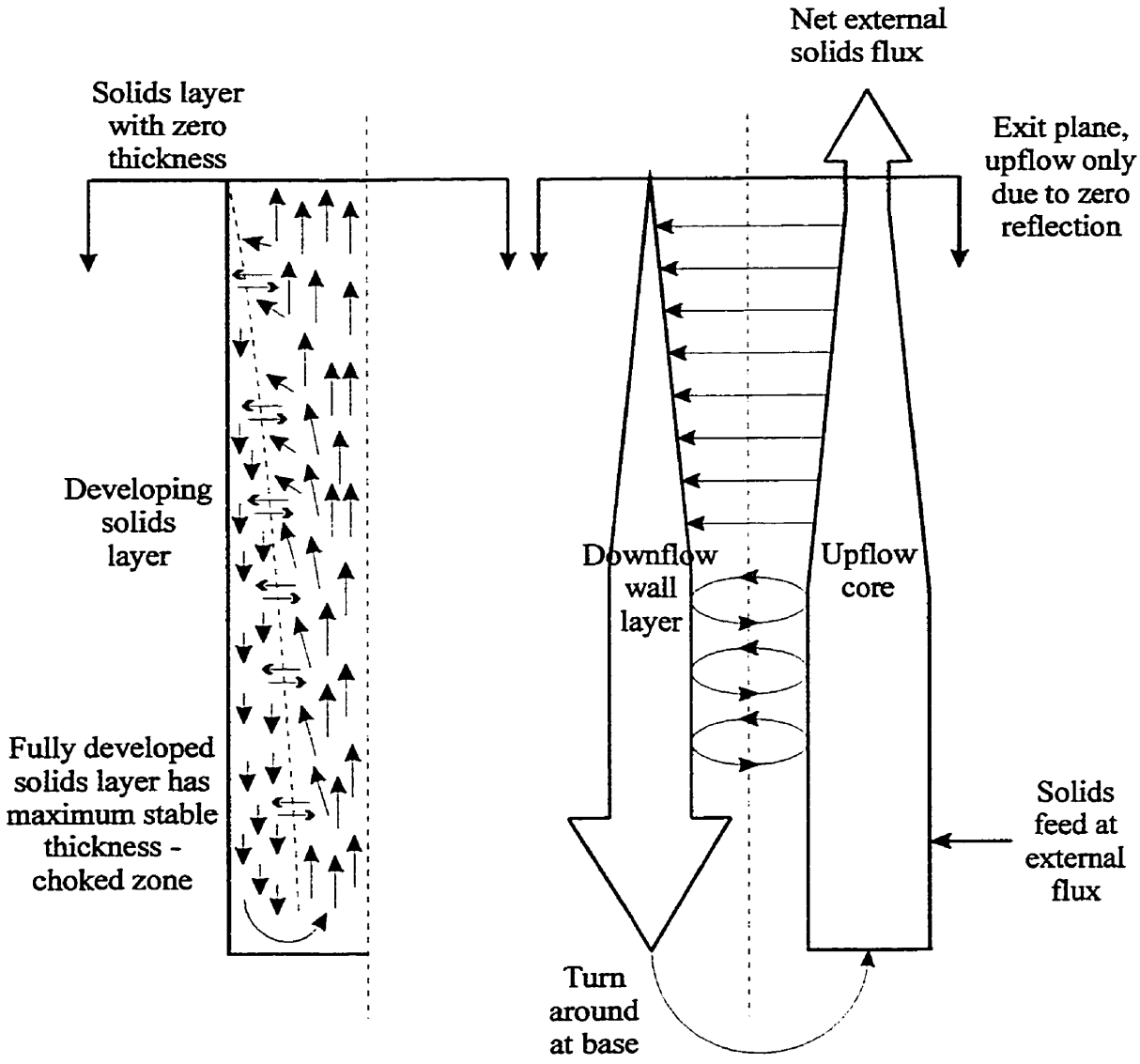

Up to this point, the discussion of the upper dilute zone has been restricted to the solids phase. Experimentation to gain insight into gas phase characteristics is relatively sparse, primarily due to the expense of the necessary equipment.

Using a radioactive tracer and detection equipment, Patience and Chaouki (1993)

generated gas phase residence time distributions that show very little axial dispersion but do indicate significant back-mixing. Data acquired by Kruse et al. (1995) and Namkung and Kim (1996) clearly demonstrates that the gas phase flows upward in the interior of the riser and incontrovertibly proves that it flows downward near the wall, a characteristic that many models neglect. Thus, the core-annulus flow structure undoubtedly also exists for the gas phase but the location of the gas phase core radius may not necessarily coincide with the solids phase core radius.

The flow structure in the lower dense zone is far less well defined for both phases largely due to the re-injection and internal re-circulation of solids. However, two certainties are that the solids concentration is greatest at the base of the riser as is the rate of change of the pressure drop.

2.1.2 Characteristics Of An HDCFB

Bi (1997) describes an HDCFB not as a new hydrodynamic regime, but as an LDCFB in which the lower dense zone extends through the entire length of the riser. Consequently, the apparent solids concentration throughout the riser is in the 80% range as evidenced by several researchers (Issangya et al., 1996; Contractor et al., 1994). The solids concentration greatly influences the reaction rate of a gas-solid catalytic reaction, which makes HDCFBs attractive for catalytic reaction processes. Additionally, unlike an LDCFB, there is no net downward flow of solids at the riser wall; non-linear radial solids mass flux profiles exist but the net flow of solids is never in the negative direction. Moreover, data acquired by Contractor et al. (1994) on a pilot scale rig used to oxidize *n*-butane to maleic anhydride clearly demonstrates that there is very little axial dispersion and virtually no back-mixing in the gas phase. Therefore, HDCFBs exhibit concurrent, upward flow of both the gas and solids phases throughout the entire riser length.

Bi and Zhu (1995) outline four conditions that are required to achieve HDCFB operation:

1. Sufficient blower capacity and pressure to avoid operational fluctuations,
2. High pressure in the solids return leg, which can be achieved with a large hydrostatic head of solids,
3. Proper equipment design to facilitate the re-circulation of solids, and
4. Small particles to avoid traversing into the turbulent regime.

Various modeling techniques, outlined in the next Section, allow engineers to simulate the operation of both low and high density circulating fluidized beds.

2.2 Modeling Techniques

Harris and Davidson (1994) classify LDCFB models into three categories:

1. Models that describe axial solids hold-up but do not explicitly predict the radial distribution.
2. Models that describe radial distribution of the solids hold-up and velocity profiles by dividing the riser into two or more regions.
3. Models that use fundamental equations of fluid dynamics.

Researchers now recognize that the first type of model is an inadequate representation of the complex LDCFB system. The second category of models encapsulates both core-annulus and cluster models. These types of models are the most popular in literature and many, many models exist. Section 2.2.3 elaborates on significant core-annulus type models and Section 2.2.2 expounds upon significant cluster type models. Computational fluid dynamics (CFD) models, Section 2.2.1, are notoriously complex when compared with their time-averaged counterparts. At times, practical application is more important than theoretical validity, which explains the proliferation of cluster and core-annulus type models relative to CFD models.

2.2.1 Computational Fluid Dynamics

The future of modeling fluidized beds is computational fluid dynamics. It offers the potential to fundamentally represent the gas and solids phases in any bed configuration and in any hydrodynamic regime. However, hardware limitations, such as processor speed and memory, hamper the all-encompassing power of CFD at this time. Consequently, a trade-off between adhering to constitutive equations and invoking assumptions to simplify calculations occurs.

2.2.1.1 *Sinclair And Co-Workers*

Sinclair and Jackson (1989) cite the "injection of a good deal of empiricism" of several time-averaged models to account for various phenomena as the motivation for embarking upon the development of a fundamentally sound model. They assert that incorporation of both the mean and fluctuating velocity components of the gas and solids phases is necessary to account for four mechanical interactions:

1. The interaction between mean gas and mean solids velocities that results in drag,

2. The interaction between the mean and fluctuating velocities in the gas phase that results in Reynolds stresses.

3. The interaction between the mean and fluctuating velocities in the solids phase that results in stresses in particle agglomerations, and

4. The interaction between particles and gas phase turbulent fluctuations that either dampen or amplify particle fluctuations, or vice versa.

In order to avoid invoking arbitrary assumptions in their model, Sinclair and Jackson (1989) restrict the application of their model to laminar flow of gas-solids suspensions of what they consider to be relatively large particles ($\sim< 150\,\mu$m), thereby negating the contributions of the second and fourth interactions mentioned above.

In the Sinclair-Jackson Model, transfer of momentum in the solids phase occurs via shearing and particle-particle collisions. Additionally, a "particle temperature", which is proportional to the mean square of the random component of the particle velocity, characterizes the random kinetic energy of the particles. The basis for this approach is the Kinetic Theory Of Granular Flow (KTGF).

Although Sinclair and Jackson (1989) do not present a direct comparison with experimental data, their model does qualitatively predict the axial and radial segregation of solids in a CFB. (Pita and Sundaresan (1991) compare the model with experimental data.) The most notable, unexpected result of the Sinclair-Jackson Model is that multiple steady-states exist for a riser with a fixed inlet mass flux.

Bolio et al. (1995) extend the work of Louge et al. (1991), whose work is based on the work of Sinclair and Jackson (1989). The model Bolio et al. (1995) present accounts for turbulence in the gas phase using a two-equation closure model. The two-equation model is superior to one-equation models because an independent transport equation, rather than a specified turbulent mixing length relation, determines the turbulent energy dissipation rate. Bolio et al. (1995) acknowledge that one disadvantage of turbulent kinetic energy-turbulent energy dissipation ($k-\epsilon$) models is that they neglect the anisotropy of velocity fluctuations. However, a major advantage is that the two-equation closure model is integrable over the entire radial domain, which negates the requirement of an empirical boundary condition function at the wall.

Empiricism appears in the model in the form of necessary inputs that include the pressure gradient, center-line voidage, and specularity factor, thus rendering it non-predictive. Notwithstanding the inapplicability to design applications, the model is successful because it matches experimental data very well and even predicts solids velocity fluctuations that exceed gas velocity fluctuations, which are observed experimentally.

2.2.1.2 *Gidaspow And Co-Workers*

Gidaspow actively pursues CFB modeling using a generalization of the inviscid

model for two fluids, which requires knowledge of the solids viscosity. Ding and Gidaspow (1990) use the KTGF to predict the viscosity by solving the fluctuating energy equation for the particulate phase. Their simulation results for a bubbling fluidized bed containing an obstacle match the time-averaged voidage well.

Tsuo and Gidaspow (1990) apply the generalization of the Navier-Stokes equations for two fluids to circulating fluidized beds. Their model requires input of the solids viscosity and is able to predict the formation of clusters. Simulation run time on a Cray X-MP supercomputer is not mentioned but simulation real-time is limited to less than 20 s indicating that run time is exorbitant. The comparison between simulation results and experimental observations is fair.

Through a digital video technique, Gidaspow and Huilin (1996) verify the use of the KTGF for calculating the particle viscosity, which is equal to the product of the mean free path and the random oscillating velocity of a particle. The verification strengthens the argument for the KTGF approach.

2.2.1.3 *Nieuwland, Kuipers, And Van Swaaij*

The models in Sections 2.2.1 and 2.2.1 are continuum models that generalize the Navier-Stokes equations for interacting continua. An alternative approach is discrete particle modeling (DPM), which solves the Newtonian equations of motion for every single particle in a system. Nieuwland, Kuipers, van Swaaij, and co-workers pursue both of the techniques because they regard the two as complimentary. In discrete particle modeling, state-of-the-art computational techniques allow for simultaneous hydrodynamic simulation of up to 2×10^5 particles (Hoomans, 1998), which is impressive; however, the order of 10^{12} particles typically populate an industrial scale riser. Clearly, DPM does not have even laboratory scale application at this time. Nonetheless, its merit is as a "learning model" (Kuipers et al., 1998) that tests closure laws for phenomena, such as solids stresses and fluid-particle drag, in two-fluid models.

Of the CFD models presented in this Section, Nieuwland et al. (1998) are the only researchers that couple hydrodynamics with a kinetic reaction model. The hy-

drodynamic model they employ is from Nieuwland et al. (1996) and the kinetics are first-order and model fictitious reactions a catalytic cracking riser. The results qualitatively demonstrate that the effects of radial solids segregation are negative as far as yield of the desired product is concerned.

2.2.2 Cluster Models

Clusters, or streamers, are agglomerations of particles with relatively low interparticle voidage that coalesce and disintegrate throughout the riser with preferential tendency at the wall. Controversy over clusters exists because of their highly transient nature. Soong et al. (1995) standardize the definition of a cluster so that effective comparisons between independently obtained experimental data are possible. However, no trend in adhering to the definition appears in recent literature.

Cluster models are analogous to emulsion phase-bubble phase models for conventional fluidized beds, with the lean phase in an LDCFB corresponding to the bubble phase. In bubbling bed models, reactions do not occur in the bubble phase because it is devoid of catalyst, but in cluster models, the lean phase contains catalyst and reactions occur. Moreover, some cluster models are stochastic.

2.2.2.1 *Schoenfelder, Kruse, And Werther*

Schoenfelder, Kruse, and Werther published a series of papers (Schoenfelder et al., 1996ab; Kruse et al., 1995; Kruse and Werther, 1995) that describe an outstanding cluster model for an LDCFB. The only factor that detracts from their work is that the model is not predictive. Inputs to the model include riser geometry, superficial gas velocity, inlet solids mass flux, solids concentration in the clusters, the axial pressure profile, and the radial solids mass flux profile at a specific axial location in the riser. The radial mass flux profile must include both the upward and downward components, not just the net profile, over the entire radial domain.

Hydrodynamically and kinetically, a CSTR represents the lower dense zone, which is comprised of the bottom and splash zones. The model does not radially segregate

the upper dilute zone, as in core-annulus models. Instead, a continuous phase of relatively low solids concentration, the lean phase, ascends over all r and dense agglomerations of particles (clusters), the dense phase, descends over all r.

The gas velocity in the lean phase is a function of the radial and axial co-ordinate while a correlation specifies the gas velocity in the dense phase relative to the cluster velocity. The axial pressure profile and cluster solids concentration gives the cluster velocity, which is invariant with radial position. The solids velocity in the lean phase is equal to the gas velocity in the lean phase plus the (negative) terminal velocity of a single particle. The solids concentration in the lean phase is invariant with radial position; it varies radially in the dense phase based on the radial profile input.

Kruse et al. (1995) present data and calculations from extensive gas mixing experimentation. The model includes radial dispersion of the gas phase in both the lean and dense phases with mass transfer between the two given by a mass transfer coefficient. To maintain some degree of tractability, the radial dispersion coefficient in each of the phases is equal and is determined from experimental data.

In coupling the hydrodynamic and kinetic reaction models (Schoenfelder et al., 1996ab), some simplifying assumptions are made and certain restrictions are implied. Contributions to the pressure profile by acceleration and friction are neglected, as is the ascent of particles at the wall. Furthermore, the model only applies to reactions that do not cause a change in the molar gas flux since it would alter the flow structure in the riser. The mass transfer coefficient that characterizes the material interchange between the lean and dense phases is set at the value Kruse et al. (1995) calculate experimentally.

2.2.3 Core-Annulus Models

The most common and practical LDCFB models employ a time-averaged approach and assume a core-annulus flow structure. The popularity of these models is based

on their functional capabilities and relative simplicity.

2.2.3.1 *Brereton, Grace, And Yu*

After performing tracer experiments in a 9.3 m tall, 0.152 m diameter cold model CFB unit fluidizing sand ($\rho_p = 2650\,\mathrm{kg\,m^{-3}}$, $D_p = 148\,\mu\mathrm{m}$) and a rigorous RTD analysis, Brereton et al. (1988) conclude that a simple plug flow model is severely erroneous in describing the gas phase in an LDCFB. They were among the first to propose a two-zone, core-annulus type model for the gas phase using the assumptions that all of the gas flows upward in the core only and is stagnant in the annulus. Additionally, the model postulates that the gas is well mixed radially in both zones, respectively, and cross-flow between the core and annulus is characterized by a mass transfer coefficient. The values of the coefficient and core radius, which are invariant with height, are determined using experimental data.

The model performs well only when continuity conditions are relaxed.

Brereton et al. (1988) fully acknowledge that their model is oversimplified and suggest that including axial dispersion and velocity gradients in the model, as well as an axially varying mass transfer coefficient and core radius, would improve the accuracy.

2.2.3.2 *Patience And Chaouki*

Research by Patience and Chaouki (1993, 1995) greatly extends the work of Brereton et al. (1988) by making the model predictive and incorporating the solids phase. The assumptions used in the Patience-Chaouki Model for the gas phase are identical to those used by their predecessors but neither the cross-flow coefficient nor the core radius are determined by fitting experimental data. Instead, the cross-flow coefficient is based on an analogy between LDCFBs and wetted wall towers and the gas phase core radius is based on an empirical correlation.

A modified form of the Gilliland-Sherwood correlation (McCabe and Smith, 1976) provides the basis for the cross-flow coefficient (k) analogy. The modification is nec-

essary to account for the increase in k with solids mass flux. Consequently, the cross-flow coefficient is calculated using:

$$\mathrm{Sh}_c = 0.25\mathrm{Sc}_c^{1/2}\mathrm{Re}_c^{3/4}\left(\frac{G_{sin}}{\rho_p u_{gin}}\right)^{1/4} \tag{3}$$

and predicts that $0.03 \leq k \leq 0.10$ for $1 \times 10^{-4} < G_{sin}/\rho_p u_{gin} < 9 \times 10^{-3}$, $3 \times 10^4 < \mathrm{Re}_c < 1 \times 10^5$, and $0.19 < \mathrm{Sc} < 0.76$.

Both radioactive tracer studies and solids center-line velocity measurements form the basis for the gas phase core radius. Patience and Chaouki (1993) calculate the gas velocity in the core from the solids data by assuming that the center-line solids velocity is equal to the gas velocity plus the (negative) terminal settling velocity of a single particle. A two parameter correlation,

$$\phi_g = \frac{1}{1 + 1.1\mathrm{Fr}(G_{sin}/\rho_p u_{gin})^{0.083\mathrm{Fr}}}, \tag{4}$$

is the result of correlating a wide range of operating conditions, particle characteristics, and riser geometries.

In an effort to provide a design and scaling mechanism for circulating fluidized beds, Patience et al. (1992) present a correlation for the slip factor, the ratio of interstitial gas velocity over solids velocity,

$$\psi = 1 + \frac{5.6}{\mathrm{Fr}} + 0.47\mathrm{Fr}_t^{0.41}, \tag{5}$$

that can be used to calculate the plug flow voidage in the "fully developed zone" of a riser. The plug flow voidage is:

$$\epsilon_{\mathrm{pf}} = \frac{1}{1 + \frac{\psi G_{sin}}{\rho_p u_{gin}}} \tag{6}$$

and provides one of the keys for the solids phase modeling.

The Patience-Chaouki Model prescribes the radial voidage profile using the plug flow voidage:

$$\frac{{\epsilon_{\mathrm{pf}}}^{0.4} - \epsilon(r)}{{\epsilon_{\mathrm{pf}}}^{0.4} - \epsilon_{\mathrm{pf}}} = 4\hat{r}^6, \tag{7}$$

and a parabolic radial solids velocity:

$$u_s(r) = u_s(0)\left(1 - \frac{\hat{r}^2}{\phi_s}\right), \tag{8}$$

where ϕ_s is equal to the square of the solids phase core radius over the square of the riser radius. Using Equation 5 to calculate the slip factor for a given riser, the center-line voidage can be calculated using Equation 7. Then, invoking the assumption that, at the center-line, the absolute value of the slip velocity is equal to the terminal velocity of a particle, the center-line solids velocity can be calculated using $u_s(0) = u_{gin}/[\phi_g \epsilon(0)] + u_t$. Finally, ϕ_s can be calculated by performing a mass balance on the radial solids mass flux profile. All the inputs to the model, for both phases, consist of the superficial velocity of the gas and its thermodynamic properties, particle characteristics, inlet solids mass flux, and riser geometry, which are always known a priori. Note that the core radii for both phases are not necessarily coincidental and are invariant with height.

2.2.3.3 *Pugsley*

Notwithstanding the errors in the model for the "fully developed zone" that Pugsley (1995) presents (see Appendix C for details), the concept he uses to determine the length of the "acceleration zone" is noteworthy.

The procedure begins with the force balance on a single particle, consisting of the force of drag that the gas exerts on the particle, the force of gravity acting on the particle, and the buoyant force of the fluid on the particle:

$$\frac{du_p}{dt} = \frac{3}{4} C_d \frac{\rho_g {u_{\text{slip}}}^2}{D_p \rho_p} + \frac{g(\rho_g - \rho_p)}{\rho_p}. \tag{9}$$

The value of the drag coefficient for a sphere from the standard drag curve (Flemmer and Banks, 1986),

$$C_d = \frac{18.5}{\text{Re}_p^{0.6}}, \tag{10}$$

is highly idealized and cannot be used in Equation 9 with confidence. Pugsley replaces the constant 18.5 in Equation 9 with a variable, K, and uses consistent and reasonable

assumptions to determine its value. By definition of the "acceleration zone", $du_p/dt = 0$ at $L = L_{\text{acceleration}}$; therefore, the left hand size of Equation 9 is zero at the end of the "acceleration zone". Using the invariant solids velocity in the "fully developed zone", which is determined prior to "acceleration zone" calculations, and specifying the voidage at the base of the riser, an iterative procedure is employed to calculate K and, subsequently, $L_{\text{acceleration}}$.

2.2.3.4 *Ouyang, Li, And Potter*

Accounting for the downward flow of gas and solids in the annular region is of utmost importance in LDCFB riser reactor modeling because the back-mixing can have profoundly negative effects on conversion. Ouyang et al. (1995) are the first to develop a model that does so (in a non-predictive fashion).

The model employs the following assumptions:

- A core-annulus flow structure exists in the riser with both phases ascending in the core and descending in the annulus.
- The density of both phases is constant throughout the riser.
- The mass of gas and solids introduced into the annulus at the top of the riser is determined by maintaining the overall mass balance.
- Both phases are re-introduced into the core from the annulus at the base of the riser.
- A mass transfer coefficient characterizes the cross-flow of gas between the core and annulus. (Gas present in the intra-particle voids does not contribute to the exchange of matter between the core and annulus.)
- The core and annular regions are radially well mixed, respectively.
- The slip velocity in both regions is equal to the absolute value of the terminal velocity of a single particle.

Ozone decomposition in a 10.5 m tall, 0.254 m diameter riser fluidizing activated FCC catalyst ($D_p = 65\,\mu m, \rho_p = 1380\,\mathrm{kg\,m^{-3}}$) is the system that Ouyang et al. (1996) use to test their model. (User specification of the solids concentration and velocity in the annulus, as well as the cross-flow coefficient, make the model non-predictive. These values may be known a posteriori but restrict the model from use as a design tool.) With a single, simple kinetic reaction, an analytical solution for the model is available because the solids hold-up is invariant with height. The analytical solution to the ozone decomposition system over predicts the conversion in the riser, which, in actuality, is less than the conversion attainable in a CSTR. Ouyang et al. (1996) attribute the poor reactor performance at high solids mass fluxes to the formation of clusters, which derogatorily affect gas-solids contacting and, hence, reaction rates.

As with all fluidized bed models, the models reviewed in this Section have imperfections. The objective of the model presented in this dissertation is to eliminate some of the more significant shortcomings of existing models, predict the solid phase axial and radial non-homogeneities within an LDCFB riser, and couple LDCFB hydrodynamic and kinetic reaction equations in riser reactor using only design variables as inputs, i.e. develop a fully predictive model.

Everything should be made as simple as possible, but not simpler.
Albert Einstein

3 Hydrodynamic Model

The hydrodynamic model presented in this dissertation is the result of an iterative process that adds additional realism and predictive capabilities to existing models. It is worthwhile to expound upon how the complexities of the model were introduced so that, should further development occur, numerous pitfalls can be avoided.

3.1 Evolution Of The Model

In the late 1980s and early 1990s, there was no distinction between LDCFBs and HDCFBs and all models suffered from various shortcomings, the most notable being their non-predictive nature and the assumption of stagnant gas in the annulus. Clearly, a predictive model is required for design purposes so engineers can simulate the performance of a CFB before any pilot-scale construction begins. And, through experimental observation, Kruse et al. (1995) irrefutably prove that there is indeed downward flow of gas in the annulus. The first generation of the model (Puchyr et al., 1997) overcomes these shortcomings but has some of its own, including a constant core radius and restricted application to the so called "fully-developed zone".

The basis for the second generation of the model is the work of Rhodes et al. (1992) and Werther (1994). Rhodes et al. (1992) validated the findings of Monceaux et al. (1986) by observing that the solids mass flux profiles of risers exhibit similarity and can be reasonably represented with a function of the form:

$$\hat{G}_s(\hat{r}) = a\left(1 - \hat{r}^b\right) + c. \tag{11}$$

They performed experiments using two risers ($H = 6.600\,\mathrm{m}$, $D = 0.305\,\mathrm{m}$ and $H = 5.825\,\mathrm{m}$, $D = 0.152\,\mathrm{m}$, respectively), FRF5 powder (ρ_p=2456 $\mathrm{kg\,m^{-3}}$, D_p=75 μm),

and various superficial gas velocities ($3 - 5\,\mathrm{m\,s^{-1}}$) and solids mass fluxes ($G_s = 2 - 111\,\mathrm{kg\,m^{-2}s^{-1}}$) and found that a constant value of $b = 5$ correlates their data most effectively. (The values of the parameters a and c depend on the riser operating conditions.) The model Rhodes et al. (1992) present suffers from the assumption of a constant core radius.

Werther (1994) presents an empirical correlation, based on riser height, diameter, and Reynolds number, that allows the calculation of the wall layer thickness as a function of axial position; simple manipulations of the equation allow direct calculation of the dimensionless core radius:

$$\hat{r}_c = 1 - 1.1\mathrm{Re}_t^{-0.22}\left(\frac{L}{D}\right)^{0.21}\left(\frac{L-z}{L}\right)^{0.73}. \tag{12}$$

Intuitively, the lack of dependence of Equation 12 on the imposed solids mass flux would seem to be an oversight. However, Rhodes et al. (1992) state that "...the thickness of the region of solids downflow is independent of imposed solids flux and, for a given riser, is determined only by the superficial gas velocity.". Therefore, the two independent research bodies corroborate each other.

For the reason stated above, Equations 11 and 12 can be combined consistently and formed the foundation of the second generation of the model presented in this dissertation. Equation 11 has three unknowns, the parameters a, b, and c, and therefore requires three independent equations to solve the system. The first equation in the system is the mass balance on the solids. The second equation stems from Equation 12 whereby the solids mass flux at the core radius is zero, by definition. The third equation presumes that the center-line solids mass flux, as a function of axial location, is available a priori in the form of a semi-empirical correlation based upon the plethora of published solids mass flux data. The resulting model is simple yet vastly improves the realism of the situation other models represent. However, even without formulating the center-line solids mass flux correlation, the model fails.

Assuming the solids mass flux profile of Equation 11, as $z \to 1$, $\hat{r}_c \to 1$, which forces $b \to \infty$, meaning that the solids are in plug flow at the exit of the riser. For a

sufficiently tall riser with a smooth exit this is exactly the case and the model appears to be successful. Unfortunately, Equation 12, which indirectly states that the solids mass flux at $z = 1$ and $\hat{r} = 1$ is zero, is contradicted. Near the top of the riser, closing the mass balance with the monotonic decrease of the center-line solids mass flux and the increase in the core radius forces the mass flux at $\hat{r} = 1$ to decrease with height—a trend opposite to reality. Figure 4 graphically illustrates this fatal flaw. The three curves in Figure 4 correspond to reduced core radii of $\hat{r}_c = [0.85, 0.9, 0.999]$ and reduced centerline solids mass fluxes of $\hat{G}_s(0) = [3.75, 2, 1.0055]$, respectively. (The calculated values of b are $b = [1.45, 4.28, 879]$.) Figure 4 clearly shows that the reduced solids mass fluxes at the wall are decreasing, $\hat{G}_s(1) = [-1, -1.14, -1.42]$, as the core radius goes to one, which contradicts experimental observation and Equation 12 at $z = 1$.

The third generation of the model attempts to correct the flaw of the second generation model by describing the solids mass flux profile in the annulus with another equation similar to Equation 11, which obviously adds complexity. Inverting and translating Equation 11 to apply to the annular region of the riser yields:

$$\hat{G}_a(\hat{r}) = d\left[(1-\hat{r})^e - 1\right] + f, \tag{13}$$

which is valid in the domain $\hat{r} = [\hat{r}_c, 1]$, thereby making Equation 11 valid in the domain $\hat{r} = [0, \hat{r}_c]$.

Using Equations 11 and 13 to describe the solids mass flux profiles across the entire domain, $\hat{r} = [0, 1]$, results in six unknown parameters. The first three equations in the system that solves for the parameters are the same as those in the second generation of the model. The remaining three equations are based on the continuity of the mass flux profile at $\hat{r} = \hat{r}_c$:

$$\hat{G}_{sc}\Big|_{\hat{r}=\hat{r}_c} = \hat{G}_{sa}\Big|_{\hat{r}=\hat{r}_c}, \tag{14}$$

$$\left.\frac{d\hat{G}_{sc}}{d\hat{r}}\right|_{\hat{r}=\hat{r}_c} = \left.\frac{d\hat{G}_{sa}}{d\hat{r}}\right|_{\hat{r}=\hat{r}_c}, \tag{15}$$

Figure 4: Demonstration Of The Failure Of The Second Generation Of The Proposed LDCFB Model

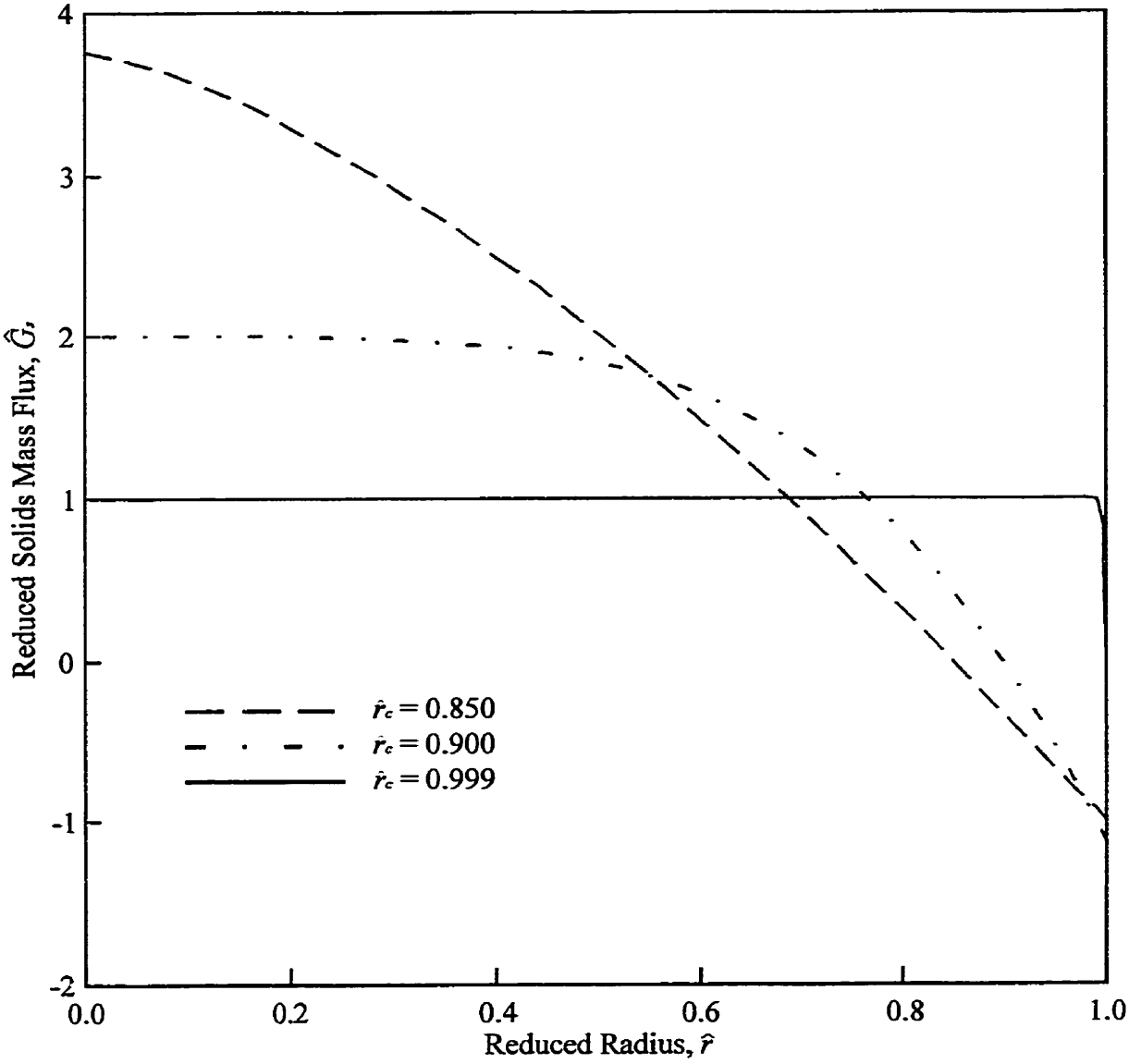

and

$$\left.\frac{d^2\hat{G}_{sc}}{d\hat{r}^2}\right|_{\hat{r}=\hat{r}_c} = \left.\frac{d^2\hat{G}_{sa}}{d\hat{r}^2}\right|_{\hat{r}=\hat{r}_c}. \tag{16}$$

Woefully, the third generation of the model suffers exactly the same fate as the second generation of the model, as Figure 5 illustrates. Thankfully, the failures of the second and third generations of the model sparked the idea for the basis of the final generation of the model.

The novel idea for the final generation of the model, i.e. the model proposed in this dissertation, is: *Prescribe the axial profiles at both the center-line and wall of the riser based on fundamental laws or entirely reasonable assumptions.* What follows is a totally unique hydrodynamic model for an LDCFB with downward flow of gas and solids near the wall.

Before describing the axial profiles, it is useful to elaborate on general characteristics of the model. Figure 6 shows the physical and conceptual boundaries in the model presented in this dissertation. The boundary between the core and annulus is a physical one and is demarcated by the radial location at which the solids mass flux is zero. In order to keep the model as simple as possible, the model assumes that all material in the core, both gas and solids, flows in the upward, positive direction. Similarly, all material in the annulus flows in the downward, negative direction. In Figure 6, the core is blue, the annulus is red, and the shading in the figure is indicative of the solids concentration at a particular axial location. The darker the color, the higher the concentration of the solids. The radial variation of the solids concentration is not evident even though the hydrodynamic model has the capability to predict it.

The axial location at which the core radius is a minimum specifies the conceptual boundary, shown in Figure 6, that divides the riser into lower and upper zones. This boundary is required for the determination of the mass flux and solids velocity axial profiles only. It does not indicate a change in the assumed flow structure in the riser; all material ascends in the core and descends in the annulus in both the lower and upper zones. Physically, the model assumes that the boundary represents the axial

Figure 5: Demonstration Of The Failure Of The Third Generation Of The Proposed LDCFB Model

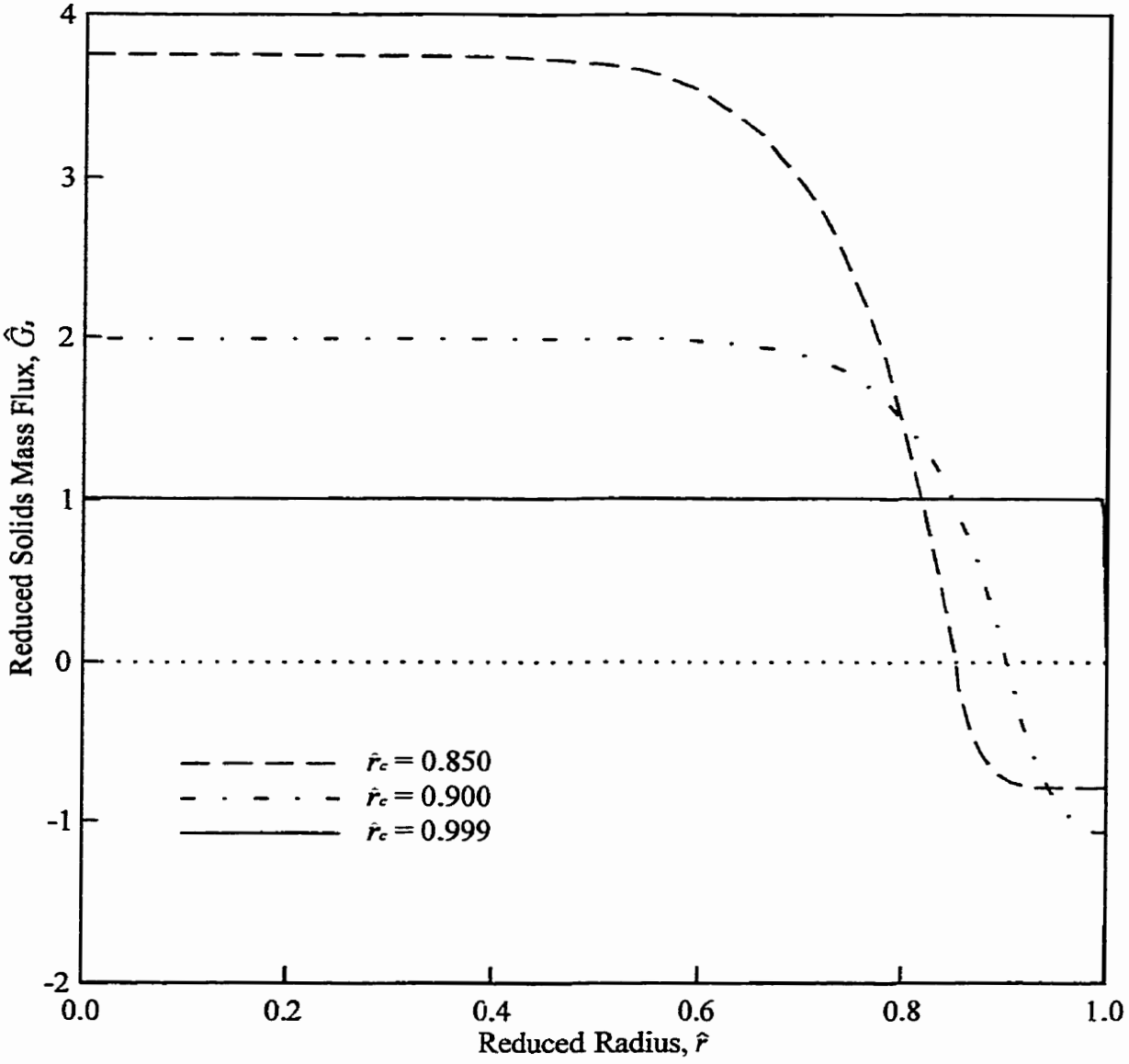

Figure 6: Physical And Conceptual Zones Of The Proposed LDCFB Model

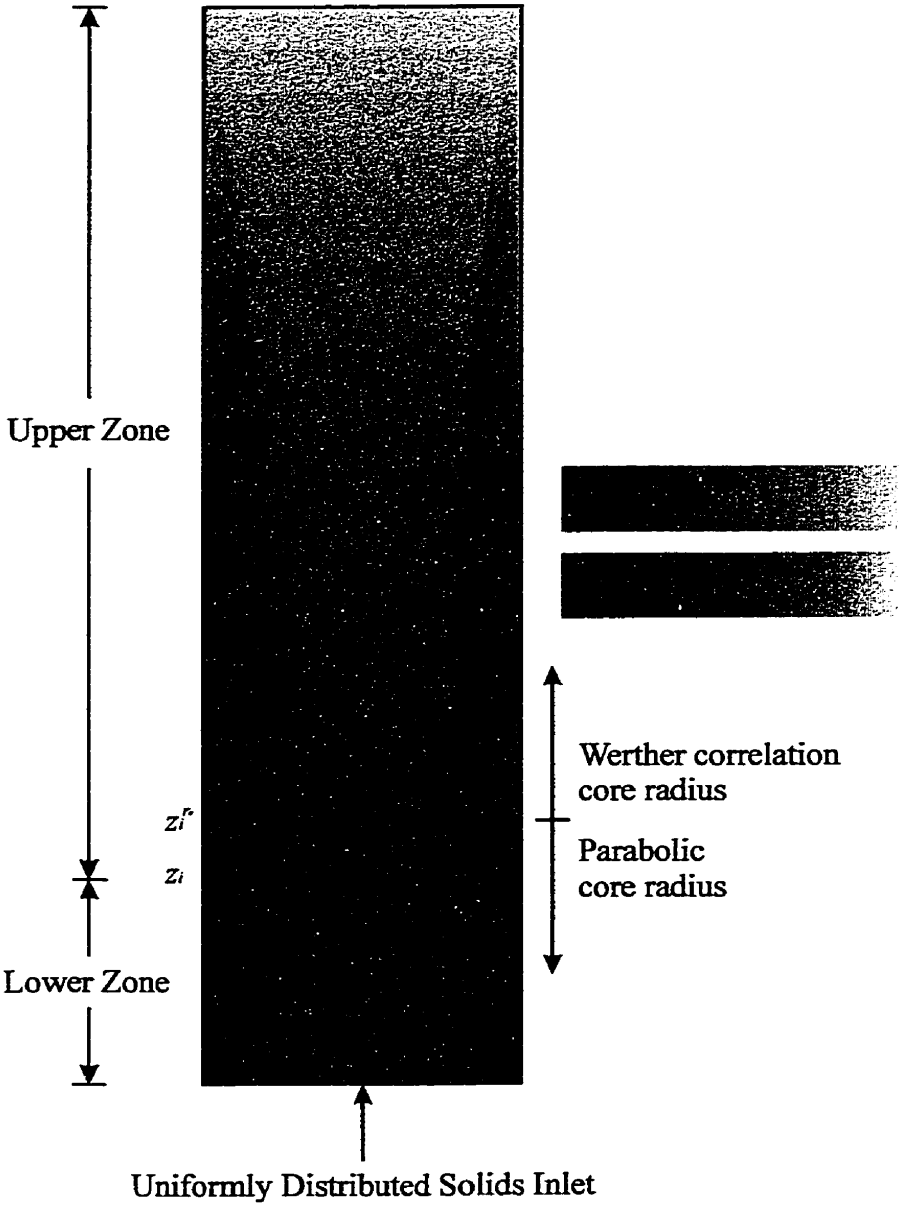

location where the center-line mass flux is at a maximum and the wall mass flux and solids velocity are at a minimum.

The lack of densification of the solids at the top of the riser, as seen in Figure 6, indicates that the model only applies to risers with smooth exits. The solids concentration is greatest at the base of the riser.

As will become evident, the model presented in this dissertation is fairly complicated. A summary of the important ideas in each section is tabulated at the end of each section to emphasize the major points. Table 1 outlines the important general characteristics of the model.

Table 1: Summary Of The General Characteristics Of The Proposed LDCFB Model

• The core radius is the radial location at which the axial solids mass flux is zero.
• The gas and solids ascend in the core.
• The gas and solids descend in the annulus.
• The lower zone-upper zone interface is a conceptual boundary at the axial location of the minimum core radius.
• The model only applies to risers with smooth exits.

3.2 Core-Annulus Boundary

As previously noted, one of the shortcomings of other LDCFB models is that they rely on a fixed radial location for the core-annulus boundary (core radius). By design, an axially varying core radius correlation is one of the fundamental keys to the hydrodynamic model developed in this dissertation, which is obviously an improvement over existing models. Moreover, formulation of the proposed model is modular so that incorporation of refined correlations or improved ideas to achieve greater accuracy is simple.

Throughout the remainder of this dissertation, any reference to the core radius actually denotes the dimensionless core radius, unless otherwise noted.

In the upper portion of the riser, the state-of-the-art equation developed by Werther (1994), Equation 12, based on both pilot scale and industrial scale rigs, is the correlation that specifies the core radius. It is superior to other correlations (Yang, 1998; Bi et al., 1996) because its inputs are design variables and the data set generating the constants in the correlation include riser reactors that incur a change in moles. Strictly speaking, Equation 12 only applies to the solids phase; however, because the minimization of the complexity of the model is a concern, Equation 12 is also used to specify the gas phase core radius.

The base of the riser, where both externally and internally re-circulated solids undergo a radical change in momentum, is the most chaotic region in the riser and is the most difficult to model. Simplifying assumptions, such as representing the region as a bubbling bed (Werther and Wein, 1994; Svensson et al., 1993) or extending the core-annulus structure from the upper portion of the riser into the base (Pugsley, 1995; Patience and Chaouki, 1995; Brereton et al., 1988), are always employed. The proposed model uses the latter assumption, with some unique modifications.

In the model, the axially varying core radius is continuous throughout the length of the riser. As mentioned, in the upper portion, the location of $\hat{r}_c$ is given by Equation 12. In the lower portion, the function representing the core radius is assumed

to be parabolic; therefore, it has three coefficients and requires a system of three equations to determine the value of the coefficients. The first two equations are based on the continuity at the point where the two core radius functions intersect, z_i^{rc}:

$$\hat{r}_c|_{z_i^{rc}}^{-} = \hat{r}_c|_{z_i^{rc}}^{+} \tag{17}$$

and

$$\left.\frac{d\hat{r}_c}{dz}\right|_{z_i^{rc}}^{-} = \left.\frac{d\hat{r}_c}{dz}\right|_{z_i^{rc}}^{+}. \tag{18}$$

The third equation is based upon the assumption that

$$\hat{r}_c(0) = 1. \tag{19}$$

This assumption is analogous to the formation of a boundary layer in fluid flowing from a reservoir into a pipe. In a pipe, the boundary layer is defined as the radial location where the fluid velocity is some specified fraction of the main stream velocity; in the proposed LDCFB model, it is where the solids velocity is zero.

Figure 6 provides an example of the shape of the core radius over the entire length of the riser. Note that the minimum core radius does not occur at z_i^{rc}; it occurs at the lower zone-upper zone interface, z_i, which is below z_i^{rc}, because Equation 12 does not have an extremum in $z = [0, 1]$.

Characteristics of the core radius are summarized in Table 2.

Table 2: Summary Of The Core-Annulus Boundary In The Proposed LDCFB Model

• Equation 12 defines the core radius in the upper portion of the riser.
• The core radius is continuous throughout the length of the riser.
• The core radius is parabolic in the lower portion of the riser.
• The core radius is one at the base of the riser.
• The core radius for the gas is equal to the core radius for the solids.

3.3 Lower Zone-Upper Zone Interface Location

The boundary between the lower zone and upper zone, which is the axial location where the core radius is a minimum,

$$\frac{d\hat{r}_c}{dz} = 0, \tag{20}$$

must be determined a priori in order for the proposed model to be predictive. Values of the solids and gas mass fluxes and solids velocity at the lower zone-upper zone interface (LZUZI) are used to seed the appropriate axial profiles, which form the basis of the model. At the LZUZI, it is assumed that the mass flux profiles take the form of Equation 11 over the entire radial domain, $\hat{r} = [0, 1]$, and that the center-line solids mass flux is at the minimum that allows for the closure of the mass balance. (For further details see Appendix A.) These assumptions allow for the calculation of the re-circulation ratio, the mass flow rate in the core over the mass flow rate in the annulus ($|\dot{m}_{sc}/\dot{m}_{sa}|$), at the LZUZI. Werther (1994) gives indications that the re-circulation ratio might aid in the description of LDCFB fluid mechanics; the proposed model subscribes to his suggestion.

An assumption of the model presented in this dissertation is that a particular re-circulation ratio, based on riser geometry, operating conditions, and particle characteristics, correlates to a specific axial location in the riser. Since knowledge of all quantities other than the axial location are always known at the onset of CFB designs, formulation of an empirical re-circulation ratio is possible, which the next Section elaborates upon, and allows for the determination of z_i a priori.

3.3.1 Re-Circulation Ratio Correlation

Development of the re-circulation ratio correlation in this dissertation relies on various dimensionless groups that undoubtedly affect the hydrodynamics in an LDCFB riser (Farrell et al., 1998; Glicksman, 1984). The form of the correlation is:

$$\left|\frac{\dot{m}_{sc}}{\dot{m}_{sa}}\right| = \alpha \left(\frac{G_{sin}}{G_{gin}}\right)^{\beta} \left(\frac{L}{D}\right)^{\gamma} \mathrm{Re}_p{}^{\delta}. \tag{21}$$

Because the correlation is empirical, experimental data obviously determine the parameters. Calculation of the parameters and a detailed description of the process involved, including the data set, are presented in Appendix A. The result of the least squares regression gives $[\alpha, \beta, \gamma, \delta] = [0.9825, 0.5644, 0.0366, -0.2225]$; Figure 7 is a parity plot of the correlation.

Figure 7: Comparison Of Calculated And Predicted Solids Re-Circulation Ratio In An LDCFB

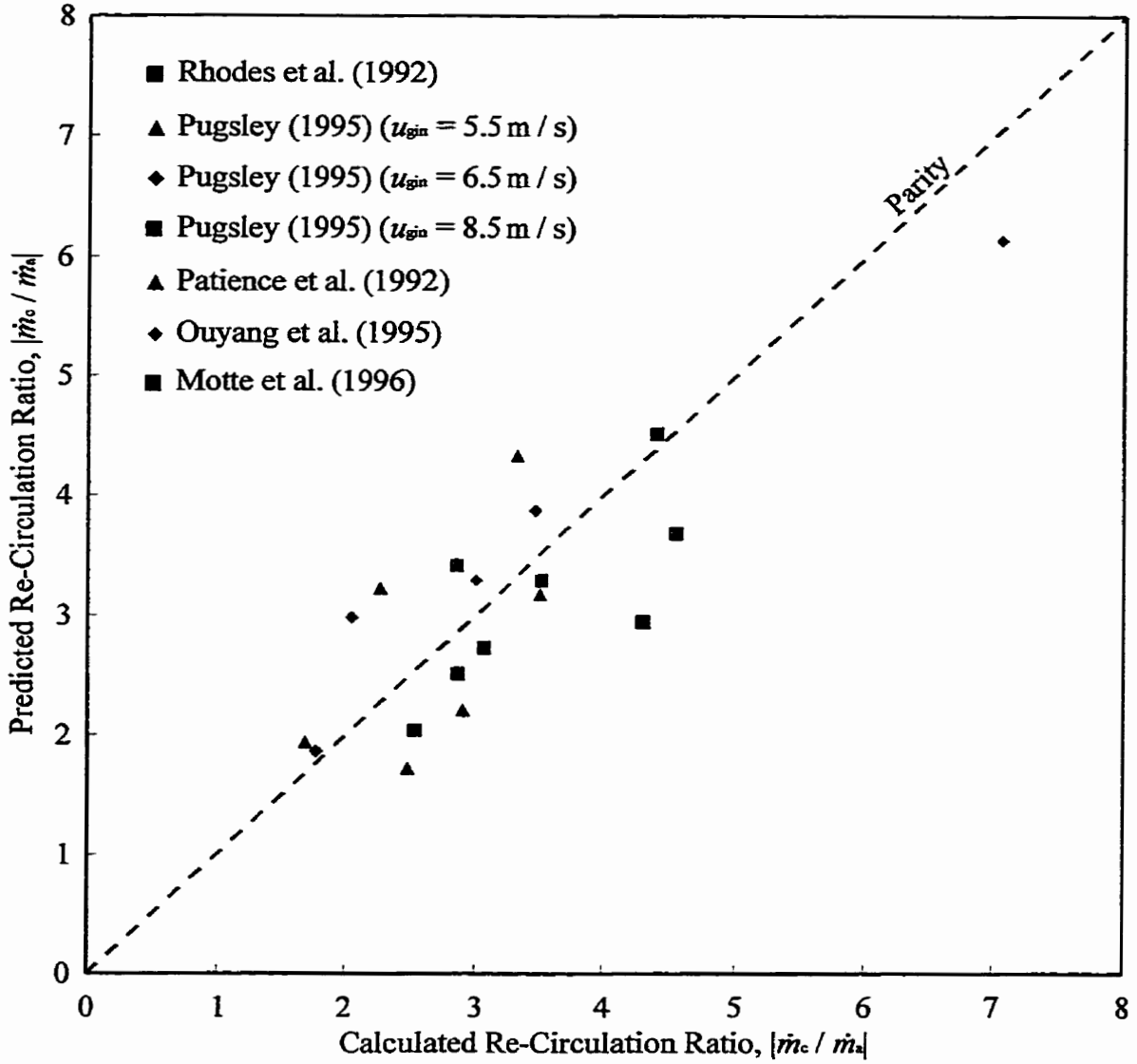

3.4 Axial Mass Flux Profiles

Prescribing the axial mass flux profiles at the center-line and wall of the riser are two of the most profound ideas presented in this dissertation. Each of the mass flux profiles are based on both fundamental laws derived from constitutive equations and the re-circulation ratio presented in Section 3.3.

3.4.1 Axial Mass Flux Profile At The Center-Line

The assumption of a perfectly uniform radial and angular distribution of matter at the entrance ($z = 0$) and the exit ($z = 1$) of a riser provides two values for the center-line mass flux profile. Conservation of matter clearly dictates that the reduced mass flux at these two locations is one over both the entire radial and angular domains. (Note that the hydrodynamic model presented in this dissertation is two-dimensional and angular uniformity is assumed throughout the riser.) At the LZUZI, the center-line mass flux, $\hat{G}(0, z_i)$, is assumed to be the minimum that will close the local mass balance in the radial domain using Equation 11. That minimum value is greater than one because the mass flux is zero at the core radius and is negative in the annulus. Therefore, the center-line mass flux profile starts at one at the base of the riser, increases to $\hat{G}(0, z_i)$, and decreases to one at the top of the riser. It is assumed that $\hat{G}(0, z_i)$ is a maximum in the axial domain and that the initial increase in $\hat{G}(0, z)$ and subsequent decrease in $\hat{G}(0, z)$ are monotonic in $z = [0, z_i)$ and $z = (z_i, 1]$, respectively. The leftmost and upper right profiles in Figure 8 (Page 42) depict the scenario.

The function chosen to represent the profile described above is a critically damped second order response:

$$\hat{G}(0, z) = K_0 \left[1 - (1 + \omega_0(z - h_0)) \exp\left(-\omega_0(z - h_0)\right)\right] + k_0. \tag{22}$$

It looks somewhat onerous because of the number of coefficients and terms it contains; however, dissecting it and examining the meaning of each coefficient indi-

vidually reveals that it is not overly complex. The first coefficient, K, is the gain, which, in the context of an LDCFB, scales the response appropriately. The second coefficient, ω, is the natural frequency, which is equal to the inverse of the characteristic time constant for a given system. The third and fourth coefficients, h and k, translate the function in the horizontal and vertical directions, respectively. The center-line mass flux profile is always translated vertically by $\hat{G}(0, z_i)$ and horizontally by z_i. The function never overshoots $\hat{G}(0, z_i)$ and does not exhibit oscillatory behavior because of the critical damping. The subscripts on the coefficients in Equation 22 merely denote the radial location of its applicability.

In order to minimize complexity in the model, the reduced gas mass flux profile and reduced solids mass flux profiles are coincidental. Multiplying the reduced mass flux profile by the appropriate inlet mass flux differentiates the specific values of the local gas and solids mass flux profiles, respectively.

Table 3 summarizes the characteristics of the center-line mass flux profiles.

Table 3: Summary Of The Center-Line Mass Flux Profiles In The Proposed LDCFB Model

- The reduced gas and solids mass flux profiles are coincidental.
- Equation 22 gives the form of the center-line mass fluxes.
- At the entrance of the riser, the mass fluxes are one, $\hat{G}(r, 0) = 1$.
- At the exit of the riser, the mass fluxes are one, $\hat{G}(r, 1) = 1$.
- At the LZUZI, the mass fluxes are equal to the minimum center-line mass flux required to close the local mass balance using Equation 11, $\hat{G}(0, z_i) = a + c$.
- At the LZUZI, the mass fluxes exhibit a maximum.

3.4.2 Axial Mass Flux Profile At The Wall

The form of the solids and gas mass flux profiles at the wall, which the model specifies as coincidental, is identical to Equation 22 but different parameters govern its

behavior, which invert, translate, and scale the profile appropriately. The wall mass flux profile is

$$\hat{G}(1,z) = K_1 \left[1 - (1 + \omega_1(z - h_1)) \exp\left(-\omega_1(z - h_1)\right)\right] + k_1. \tag{23}$$

It requires four points or characteristics for the determination of the parameters. Two points are known based on the assumed core radius presented in Section 3.2. They are $\hat{G}(1,0) = 0$ and $\hat{G}(1,1) = 0$ since the solids velocity, and, therefore, the solids mass flux, is zero at the core radius for all z. The third point on the profile, $\hat{G}(1,z_i) = c$, is calculated by closing the local mass balance at the LZUZI. The fourth equation that dictates a characteristic of the profile is based on the assumption that the wall mass flux profile exhibits a minimum at the LZUZI.

Table 4 summarizes the characteristics of the wall mass flux profiles.

Table 4: Summary Of The Wall Mass Flux Profiles In The Proposed LDCFB Model

- The reduced gas and solids profiles are coincidental.
- Equation 23 gives the form of the wall mass fluxes.
- At the entrance of the riser, the mass fluxes are zero, $\hat{G}(1,0) = 0$.
- At the exit of the riser, the mass fluxes are zero, $\hat{G}(1,1) = 0$.
- At the LZUZI, the mass fluxes correspond to the value calculated by closing the local mass balance using Equation 11, $\hat{G}(1,z_i) = c$.
- At the LZUZI, the mass fluxes exhibit a minimum.

Figure 8 shows the graphical representation of the mathematical assumptions presented in Sections 3.4.1 and 3.4.2. The center-line mass flux at the LZUZI, $\hat{G}(0,z_i)$, is the minimum center-line mass flux that allows for closure of the local mass balance and the wall mass flux, $\hat{G}(1,z_i)$, stems directly from the mass balance. The axial location of the extremum of each profile is coincidental at z_i but the absolute values of the extrema are not necessarily equal. The re-circulation ratio correlation, Equation 21, which relies on design variables, determines the location of z_i.

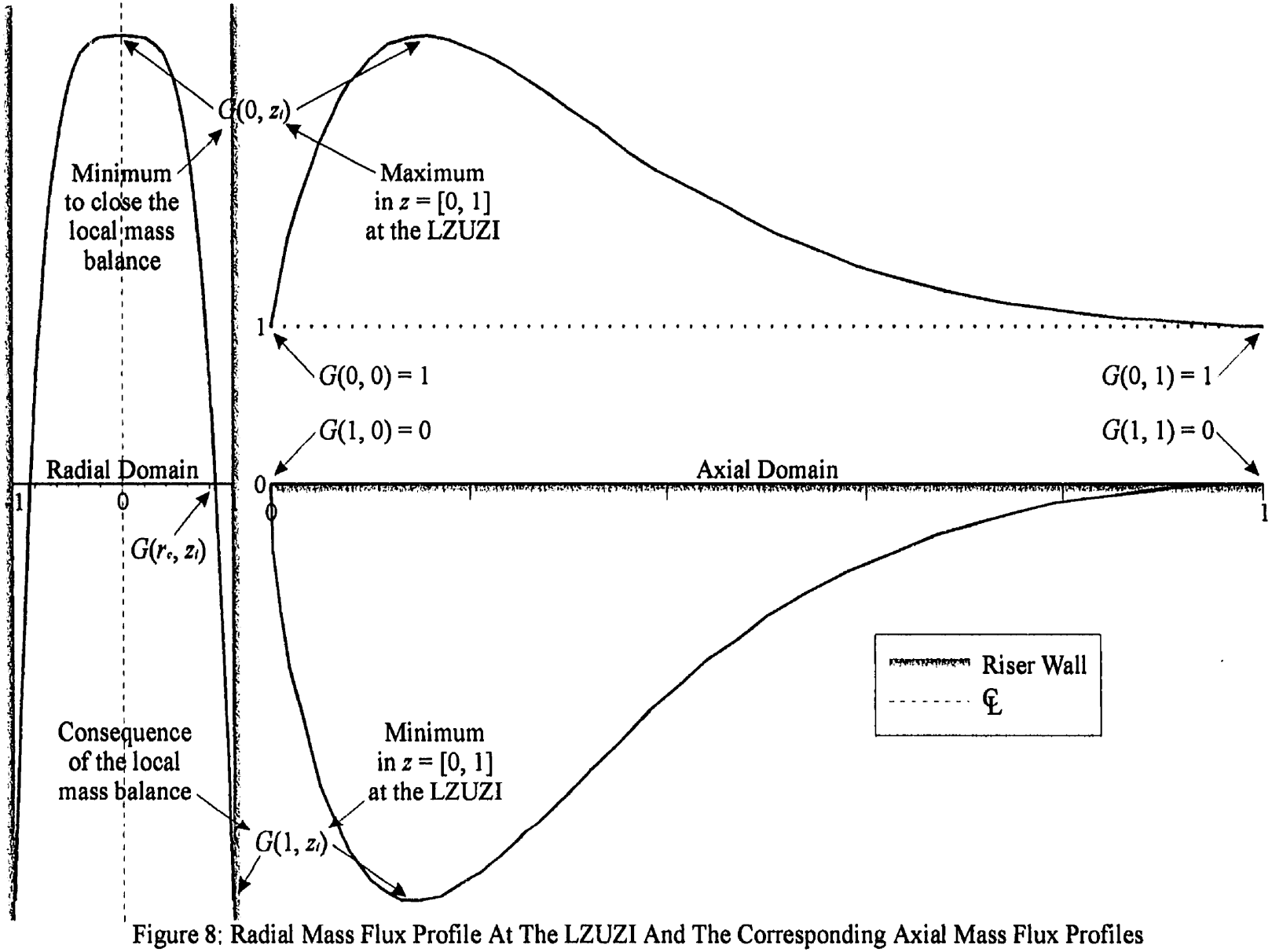

Figure 8: Radial Mass Flux Profile At The LZUZI And The Corresponding Axial Mass Flux Profiles

3.5 Axial Solids Velocity Profiles

Assuming the flow structure illustrated in Figure 6 (Page 32) and accounting for the expansion of the gas phase due to the pressure drop in the riser suggests that particles on the center-line of the riser accelerate over its entire length. Additionally, the influence of internally re-circulated solids is least on particles at the center-line. Therefore, prescribing a monotonically increasing function for the center-line solids velocity profile is reasonable. Conversely, both internal and external re-circulation of solids is greatest near the wall, which warrants the prescription of a more complicated profile function at $\hat{r} = 1$.

3.5.1 Axial Solids Velocity Profile At The Center-Line

At the center-line, the solids velocity is assumed to increase monotonically from the inlet solids velocity, u_{sin}, at $z = 0$ to the outlet gas velocity plus the (negative) terminal velocity of a particle, $u_g(0,1) + u_t$, at $z = 1$. The value of u_{sin} is determined by the inlet solids mass flux, the particle density, and the voidage at the base of the riser, $\epsilon(r,0)$, which is specified by the user and is typically the minimum fluidization voidage. By design, the voidage at the base of the riser is not fixed so that the proposed model is able to account for a particle acceleration apparatus, should one exist upstream of the riser being modeled.

Maintaining the process control undertones of Section 3.4, the prescribed profile for the center-line solids velocity is a first-order response:

$$u_s(0,z) = K_0^{u_s}\left[1 - \exp\left(\frac{-z}{\tau}\right)\right] + k_0^{u_s}. \tag{24}$$

The first coefficient, K^{u_s}, is the gain, which scales the response, the second coefficient, τ, is the time constant for the system and the third coefficient, k^{u_s}, translates the function in the vertical direction. In the model presented in this dissertation, k^{u_s} is always equal to $u_s(0,0)$.

As mentioned, two values for the center-line solids velocity profile are presumed

at $z = 0$ and $z = 1$; one more value is required to solve for the three parameters in Equation 24. It stems from the assumption that at the LZUZI, the solids velocity is equal to the inlet superficial gas velocity plus the (negative) terminal velocity of a single particle, $u_s(0, z_i) = u_{gin} + u_t$.

Table 5 summarizes the characteristics of the center-line solids velocity profile.

Table 5: Summary Of The Center-Line Solids Velocity Profile In The Proposed LD-CFB Model

- Equation 24 gives the form of the center-line solids velocity profile.
- The voidage at the entrance of the riser, $\epsilon(r, 0)$, is specifiable, with a default value of the minimum fluidization voidage.
- At the entrance of the riser, the solids velocity is calculated based upon operating conditions and particle characteristics,

$$u_s(0, 0) = \frac{G_{sin}}{\rho_p[1 - \epsilon(r, 0)]}. \tag{25}$$

- At the LZUZI, the solids velocity is assumed to be the inlet superficial gas velocity plus the (negative) terminal velocity of a particle, $u_s(0, z_i) = u_{gin} + u_t$.
- At the exit of the riser, the solids velocity is assumed to be the gas velocity plus the (negative) terminal velocity of a particle, $u_s(0, 1) = u_g(0, 1) + u_t$.

3.5.2 Axial Solids Velocity Profile At The Wall

The wall solids velocity profile mimics the wall solids mass flux profile and, consequently, the two prescribed profiles have identical forms.

$$u_s(1, z) = K_1^{u_s}\left[1 - (1 + \omega_1^{u_s}(z - h_1^{u_s}))\exp\left(-\omega_1^{u_s}(z - h_1^{u_s})\right)\right] + k_1^{u_s} \tag{26}$$

The lower right curve in Figure 9 (Page 47) displays the shape of the wall solids velocity profile.

The motif of calculating profile parameters based on fundamental laws or reasonable assumptions continues. Again, by definition of the core radius, the solids

velocities at $z = 0$ and $z = 1$ are both zero. The radial solids velocity profile at the LZUZI is assumed to be parabolic which, when coupled with the solids velocity at the center-line and LZUZI, allows for the calculation of the solids velocity at the wall. It is:

$$u_s(1, z_i) = u_s(0, z_i)\left(1 - \frac{1}{\hat{r}_c^2}\right). \tag{27}$$

The proposed model assumes that the particles descend most rapidly at the wall and LZUZI. The physical meaning of this assumption is that, just below the LZUZI, ascending gas and solids start to impede the descent of particles at the wall.

Because all of the second order profiles exhibit an extremum at the LZUZI, the horizontal translation parameter, h, and the natural frequency, ω, for each profile, respectively, are equal for a given riser (i.e. $h_0 = h_1 = h_1^{u_s} = z_i$ and $\omega_0 = \omega_1 = \omega_1^{u_s}$).

Table 6 summarizes the characteristics of the wall solids velocity profile.

Table 6: Summary Of The Wall Solids Velocity Profile In The Proposed LDCFB Model

- Equation 26 gives the form of the wall solids velocity profile.
- At the entrance of the riser, the solids velocity is zero.
- At the LZUZI, the radial solids velocity profile is assumed to be parabolic and the solids velocity at the wall is calculated,

$$u_s(1, z_i) = u_s(0, z_i)\left(1 - \frac{1}{\hat{r}_c^2}\right). \tag{28}$$

- At the LZUZI, the solids velocity is at a minimum.
- At the exit of the riser, the solids velocity is zero.

Figure 9 shows the graphical representation of the mathematical assumptions presented in Sections 3.5.1 and 3.5.2. The center-line solids velocity at the LZUZI, $u_s(0, z_i)$, is equal to the inlet superficial gas velocity plus the (negative) terminal velocity of a single particle. The wall solids velocity at the LZUZI, $u_s(1, z_i)$, stems from the assumption that the radial solids velocity is parabolic at the LZUZI. The

center-line solids velocity increases monotonically from the inlet velocity, $u_s(0,0) = G_{s\text{in}}/[\rho_p(1-\epsilon)]$, to the outlet velocity of the gas plus the (negative) terminal velocity of a single particle. The wall solids velocity is zero at the base of the riser, decreases to $u_s(1,z_i)$ at the LZUZI, and increases to zero at the exit of the riser.

The prescription of the axial profiles at the center-line and wall is the essence of the model proposed in this dissertation. Sections 3.6 to 3.8 describe the radial profiles, which make the hydrodynamic model two-dimensional.

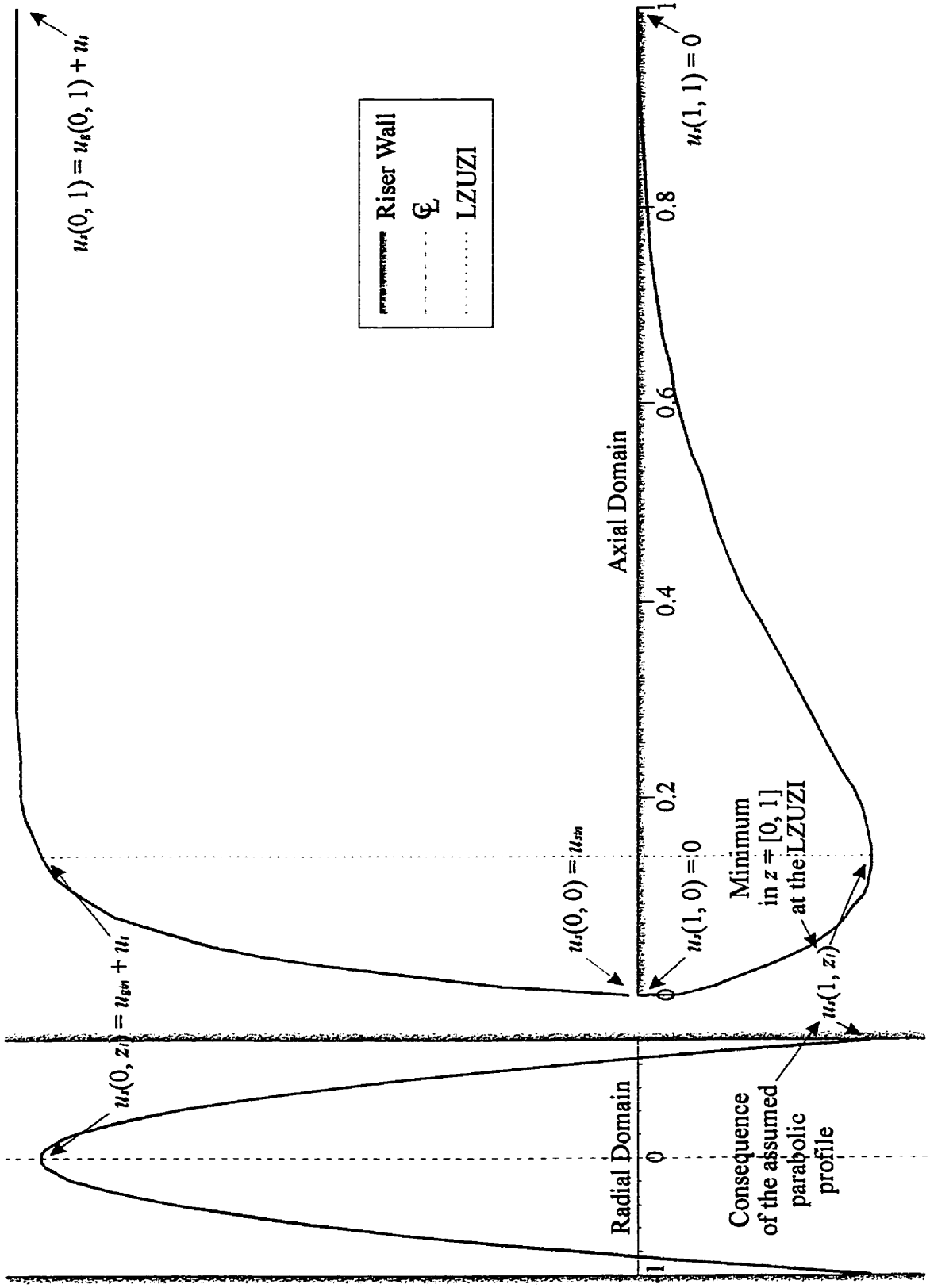

Figure 9: Radial Solids Velocity Profile At The LZUZI And The Corresponding Axial Solids Velocity Profiles

3.6 Radial Mass Flux Profiles

The model proposed in this dissertation invokes the simplifying assumption that the reduced radial gas and solids mass flux profiles are coincidental, as is the case with the axial profiles. Of course, the absolute mass flux profiles are not coincidental since the inlet solids mass flux is typically two or three orders of magnitude greater than the inlet gas mass flux.

The model uses Equations 11 and 13 for the mass flux profiles in the core and annular regions respectively. A total of six parameters define the behavior of the two equations and, therefore, a system of six equations is required to solve for them. At the center-line, Equation 22 determines the reduced mass flux at any axial location, which forms the first of the six equations. Similarly, at the wall, Equation 23 provides the reduced mass flux at any particular z. Even though the core radius is fixed at a single point for a given axial location, it provides another two of the six required equations because it applies to both Equation 11 and Equation 13. Additionally, continuity at the core radius,

$$\left.\frac{d\hat{G}_c}{d\hat{r}}\right|_{\hat{r}_c} = \left.\frac{d\hat{G}_a}{d\hat{r}}\right|_{\hat{r}_c}, \tag{29}$$

provides another equation. Lastly, the local mass balance,

$$\frac{1}{2} = \int_0^{\hat{r}_c} \hat{G}_c(\hat{r})\hat{r}d\hat{r} + \int_{\hat{r}_c}^1 \hat{G}_a(\hat{r})\hat{r}d\hat{r}, \tag{30}$$

must be satisfied, which is the sixth and final equation.

Algebraic manipulation of the system of six equations yields a cubic in the parameter e:

$$\psi_3 e^3 + \psi_2 e^2 + \psi_1 e + \psi_0 = 0, \tag{31}$$

where

$$\begin{aligned} \psi_3 &= \frac{\hat{G}(1,z)}{2}\left\{\left[\hat{G}(0,z) - \hat{G}(1,z)\right]\hat{r}_c{}^3 + \left[\hat{G}(1,z) - 1\right]\hat{r}_c\right\}, \qquad (32) \\ \psi_2 &= \frac{\hat{G}(1,z)}{2}\left[\hat{G}(0,z) - \hat{G}(1,z)\right]\hat{r}_c{}^3 \end{aligned}$$

$$+ \hat{G}(1,z)\left[\hat{G}(0,z) - \hat{G}(1,z)\right]\hat{r}_c{}^2$$
$$+ \left\{\frac{3\hat{G}(1,z)}{2}\left[\hat{G}(1,z) - 1\right] + \hat{G}(0,z)\left[\hat{G}(1,z) - 1\right]\right\}\hat{r}_c$$
$$+ \hat{G}(0,1)\left[1 - \hat{G}(1,z)\right], \tag{33}$$

$$\psi_1 = -\hat{G}(0,z)\hat{G}(1,z)\hat{r}_c{}^2$$
$$+ \left[5\hat{G}(0,z)\hat{G}(1,z) - 3\hat{G}(0,z) - \hat{G}(1,z)\right]\hat{r}_c$$
$$+ 3\hat{G}(0,z)\left[1 - \hat{G}(1,z)\right], \text{ and} \tag{34}$$

$$\psi_0 = 2\hat{G}(0,z)\left[1 - \hat{r}_c\right]. \tag{35}$$

The values of $\hat{r}_c$, $\hat{G}(0,z)$, and $\hat{G}(1,z)$ are known for all z once the parameters in the axial mass flux profiles are calculated. Ordinarily, Equation 31 has three roots, two negative and one positive. The negative roots invert Equation 13 and, therefore, are nonsensical in this case. The positive root determines the five remaining parameters:

$$d = \frac{-\hat{G}(1,z)}{(1-\hat{r}_c)^e}, \tag{36}$$

$$f = \hat{G}(1,z) + d, \tag{37}$$

$$a = \frac{\hat{G}(0,z)}{\hat{r}_c^b}, \tag{38}$$

$$b = \frac{-e\hat{G}(1,z)\hat{r}_c}{\hat{G}(0,z)\left[1-\hat{r}_c\right]}, \tag{39}$$

$$c = \hat{G}(0,z) - a. \tag{40}$$

On a computational note, even using objects with 15 digits of accuracy, loss of numerical precision can wreak havoc on the calculated profile in the annulus. This phenomenon occurs with relatively large values of e and is further expounded upon in Section 6. When e is large, b is very large and the profiles are nearly in plug flow in each of the respective regions, as the smooth curve in Figure 10 (Page 51) shows. Therefore, in order to circumvent the numerical precision problem, it is reasonable to assume that the profiles are fully in plug flow when a catastrophic loss of precision occurs. Since it is imperative not to violate the local mass balance, two scenarios exist as far as maintaining the balance and the plug flow condition are concerned:

1. Use the calculated value of the center-line mass flux and adjust the wall mass flux, or

2. Use the calculated value of the wall mass flux and adjust the center-line mass flux.

The latter option minimizes the discontinuity in the average voidage, and, hence, pressure drop and provides resolution to a different, contingent problem that arises, which is expounded upon in Section 6. So, in order to minimize the impact of the catastrophic loss of precision and to make the model as robust as possible, Equation 23 always determines the wall mass flux and the center-line mass flux is adjusted when necessary.

Table 7 summarizes the characteristics of the radial solids mass flux profiles.

Table 7: Summary Of The Radial Mass Flux Profiles In The Proposed LDCFB Model

- The reduced gas and solids mass flux profiles are coincidental.
- Equation 11 gives the form of the mass fluxes in the core.
- Equation 13 gives the form of the mass fluxes in the annulus.
- At the center-line, Equation 22 determines the axial value of the reduced mass fluxes.
- At the wall, Equation 23 determines the axial value of the reduced mass fluxes.
- At the core radius, the reduced mass fluxes are zero and continuous in the first derivative.
- The local and overall mass balances are always maintained.
- When a catastrophic loss of numerical precision occurs, plug flow in each of the core and annular regions, respectively, is assumed.

Figure 10: Reduced Radial Mass Flux Profile Options When A Catastrophic Loss Of Numerical Precision Occurs In The Proposed LDCFB Model

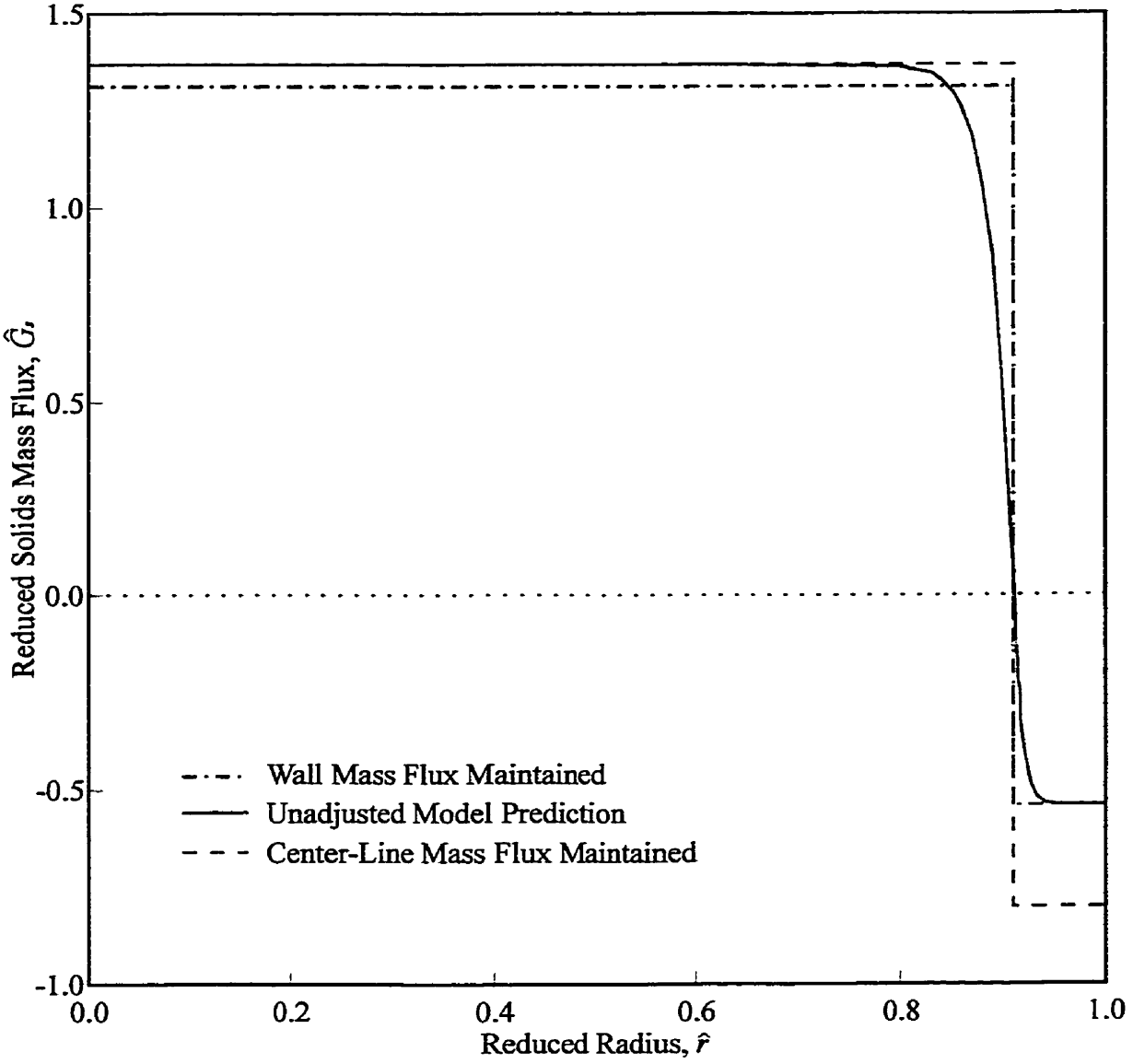

3.7 Radial Gas Velocity Profiles

Unlike the mass flux profiles, the gas and solids velocity profiles are not coincidental. An equation of state (EOS), such as the Peng-Robinson EOS or Ideal Gas Law, combined with the gas mass flux profiles and composition and local voidage allows for direct calculation of the radial gas velocity profile.

3.8 Radial Solids Velocity Profiles

Determination of the parameters in the radial solids velocity profiles,

$$u_{sc} = a^{u_s}\left(1 - \hat{r}^{b^{u_s}}\right) + c^{u_s} \tag{41}$$

and

$$u_{sa} = d^{u_s}\left[(1-\hat{r})^{e^{u_s}} - 1\right] + f^{u_s} \tag{42}$$

in the core and annulus, respectively, is analogous to the radial mass flux profiles, with one exception: No conservation equation applies to the solids velocity alone. Consequently, an equation must replace the mass balance in the system of six equations that solves for the parameters. Forcing continuity in the second derivatives at the core radius,

$$\left.\frac{d^2u_{sc}}{d\hat{r}^2}\right|_{\hat{r}_c} = \left.\frac{d^2u_{sa}}{d\hat{r}^2}\right|_{\hat{r}_c}, \tag{43}$$

seems like a good choice; however, it is not because using Equation 43 results in a massive discontinuity in the radial voidage profile at the core radius. A much more clever choice, substantiated by physical observation, is to force continuity in the first derivative of the voidage profile at the core radius.

The voidage at any point in the riser is:

$$\epsilon(r,z) = 1 - \frac{G_s(r,z)}{\rho_p u_s(r,z)}, \tag{44}$$

and, since unique profiles describe the radial variation in the core and annular regions,

respectively, continuity at the core radius is:

$$\left.\frac{d\epsilon_c}{d\hat{r}}\right|_{\hat{r}_c} = \left.\frac{d\epsilon_a}{d\hat{r}}\right|_{\hat{r}_c}. \tag{45}$$

By definition, both the solids mass flux and velocity are zero at the core radius, rendering Equation 44 indeterminate, so Equation 45 is properly expressed as:

$$\lim_{\hat{r}\to\hat{r}_c^-} \frac{d\epsilon_c}{d\hat{r}} = \lim_{\hat{r}\to\hat{r}_c^+} \frac{d\epsilon_a}{d\hat{r}}. \tag{46}$$

The derivative of the radial voidage profile exists at $\hat{r}_c$. Algebraic manipulation of Equations 41, 42, and 46 yields the solutions to the six parameters of interest:

$$e^{u_s} = \frac{u_s(0,z)\left[\hat{G}(0,z)b^2\left(\hat{r}_c-1\right)^2 - e^2\hat{G}(1,z)\hat{r}_c{}^2\right]}{\hat{r}_c\left[b\left(\hat{r}_c-1\right)u_s(1,z)\hat{G}(0,z) - \hat{r}_c e\hat{G}(1,z)u_s(0,z)\right]}, \tag{47}$$

$$d^{u_s} = \frac{-u_s(1,z)}{\left(1-\hat{r}_c\right)^{e^{u_s}}}, \tag{48}$$

$$f^{u_s} = u_s(1,z) + d^{u_s}, \tag{49}$$

$$b^{u_s} = \frac{-e^{u_s}u_s(1,z)\hat{r}_c}{u_s(0,z)\left(1-\hat{r}_c\right)}, \tag{50}$$

$$a^{u_s} = \frac{u_s(0,z)}{\hat{r}_c{}^{b^{u_s}}}, \text{ and} \tag{51}$$

$$c^{u_s} = u_s(0,z) - a^{u_s}. \tag{52}$$

The parameters e and b, from the radial mass flux profiles, are known, as are the quantities $\hat{r}_c$, $u_s(0,1)$, $u_s(1,z)$, $\hat{G}(0,z)$, and $\hat{G}(1,z)$.

Table 8 summarizes the characteristics of the radial solids velocity profiles.

Table 8: Summary Of The Radial Solids Velocity Profile In The Proposed LDCFB Model

- Equation 41 gives the form of the solids velocity profile in the core.
- Equation 42 gives the form of the solids velocity profile in the annulus.
- At the center-line, Equation 24 determines the axial value of the solids velocity.
- At the wall, Equation 26 determines the axial value of the solids velocity.
- At the core radius, Equations 41 and 42 are continuous up to the first derivative,

$$u_{sc}|_{\hat{r}_c} = u_{sa}|_{\hat{r}_c}, \text{ and} \tag{53}$$

$$\left.\frac{du_{sc}}{d\hat{r}}\right|_{\hat{r}_c} = \left.\frac{du_{sa}}{d\hat{r}}\right|_{\hat{r}_c}. \tag{54}$$

- At the core radius, the radial voidage profile, Equation 44 at a particular z, is continuous in the first derivative,

$$\lim_{\hat{r}\to\hat{r}_c} \frac{d\epsilon_c}{d\hat{r}} = \lim_{\hat{r}\to\hat{r}_c} \frac{d\epsilon_a}{d\hat{r}}. \tag{55}$$

3.9 Core-Annulus Material Interchange

In an LDCFB hydrodynamic model with an axially varying core radius and mass flux, a differential mass balance on the core provides a mechanism for the exchange of matter between the core and annulus. Figure 11 depicts the net radial flow of matter as the difference between the mass flow rate at z and $z + dz$, which is $\Delta\dot{m} = \dot{m}|_{z+dz} - \dot{m}|_z$. In the upper zone, where the core radius increases with height and the center-line mass flux profiles decrease, the net radial flow is from the core to annulus and $\Delta m < 0$. Conversely, in the lower zone, where the core radius decreases with height and the center-line mass fluxes increase, the net radial flow is in the opposite direction and $\Delta m > 0$. It is important to include this exchange of matter in a hydrodynamic model since it affects heat transfer and reaction rates when the riser is a reactor.

Figure 11: Differential Solids Mass Balance In The Core

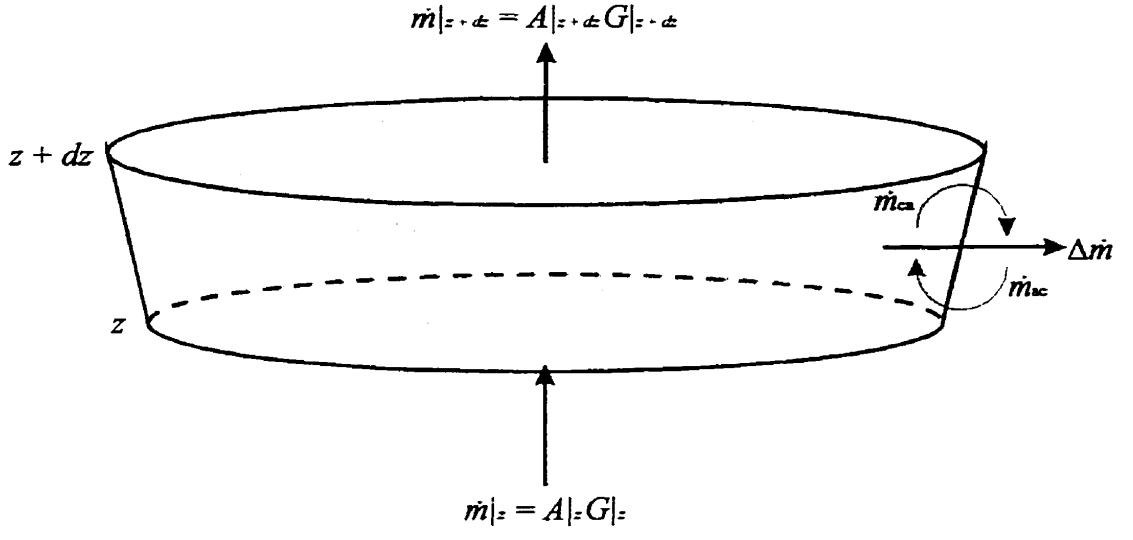

To facilitate the interchange of matter between the core and annulus without using a mass transfer coefficient, the definition of two points, x_{ic} and x_{ia}, on opposite sides of the core radius, is necessary. The model proposed in this dissertation postulates that the net interchange of matter is given by:

$$\Delta\hat{m} = \hat{m}_{ca} + \hat{m}_{ac} \tag{56}$$

$$\frac{\dot{m}|_{z+dz} - \dot{m}|_z}{2\dot{m}_{\text{in}}} = \int_{\hat{r}_c - x_{ic}}^{\hat{r}_c} \hat{G}_c(\hat{r})\hat{r}d\hat{r} + \int_{\hat{r}_c}^{\hat{r}_c + x_{ia}} \hat{G}_a(\hat{r})\hat{r}d\hat{r}, \tag{57}$$

which exploits the difference in gradients between the mass flux profiles in the core and annulus as well as the rate of change of area with respect to radius. (The mass flux gradients are equal at the core radius for continuity but diverge as $\hat{r} - \hat{r}_c \neq 0$ in $0 \leq \hat{r} \leq 1$.) Note that $\dot{m}_{ca}$ is always negative because matter descends in the annulus.

Up to this point, the assumed flow structure in the lower dense zone—all matter ascending in the core and descending in the annulus—is quite oversimplified. The material interchange scheme provides a means to more realistically represent the chaotic, intense mixing in the lower dense zone and less prevalent mixing in the upper dilute zone by dictating one of the interchange points, x_{ia} or x_{ic}, and calculating the other using Equation 57. In the lower dense zone, the model assumes that all the material in the annulus is exchanged with the appropriate amount of material from the core, i.e. $x_{ia} = 1 - \hat{r}_c$. In the upper dilute zone, x_{ia} varies linearly with the core radius location, which necessitates two values of x_{ia} for the calculation of the slope and intercept of the line. At the LZUZI, $x_{ia} = 1 - \hat{r}_c$, which gives continuity between the lower and upper zones, and at the exit of the riser, $x_{ia} = 0$ since there is not exchange of matter between the core and annulus at $z = 1$.

Expressing the idea behind Equation 57 mathematically is much easier than expressing it verbally. Physically, the premise is that shear at the core radius, caused by the ascending material in the core and descending material in the annulus, gives the material in the core momentum toward the wall and gives the material in the annulus momentum toward the center-line. The radial co-ordinates x_{ic} and x_{ia} delimit the influence of the shear force in the core and annular regions respectively. The formation of a moment of a couple at the core radius results in the interchange of matter—all the material in $x_{ic} \leq \hat{r} \leq \hat{r}_c$ is exchanged with all the material in $\hat{r}_c \leq \hat{r} \leq x_{ia}$. Figure 12 shows the exchange graphically. The mass flow rate vectors at x_{ic} and x_{ia} stem from the respective (different) mass flux profiles in the core and annulus. If they

Figure 12: Graphical Representation Of Material Interchange Between The Core And Annulus

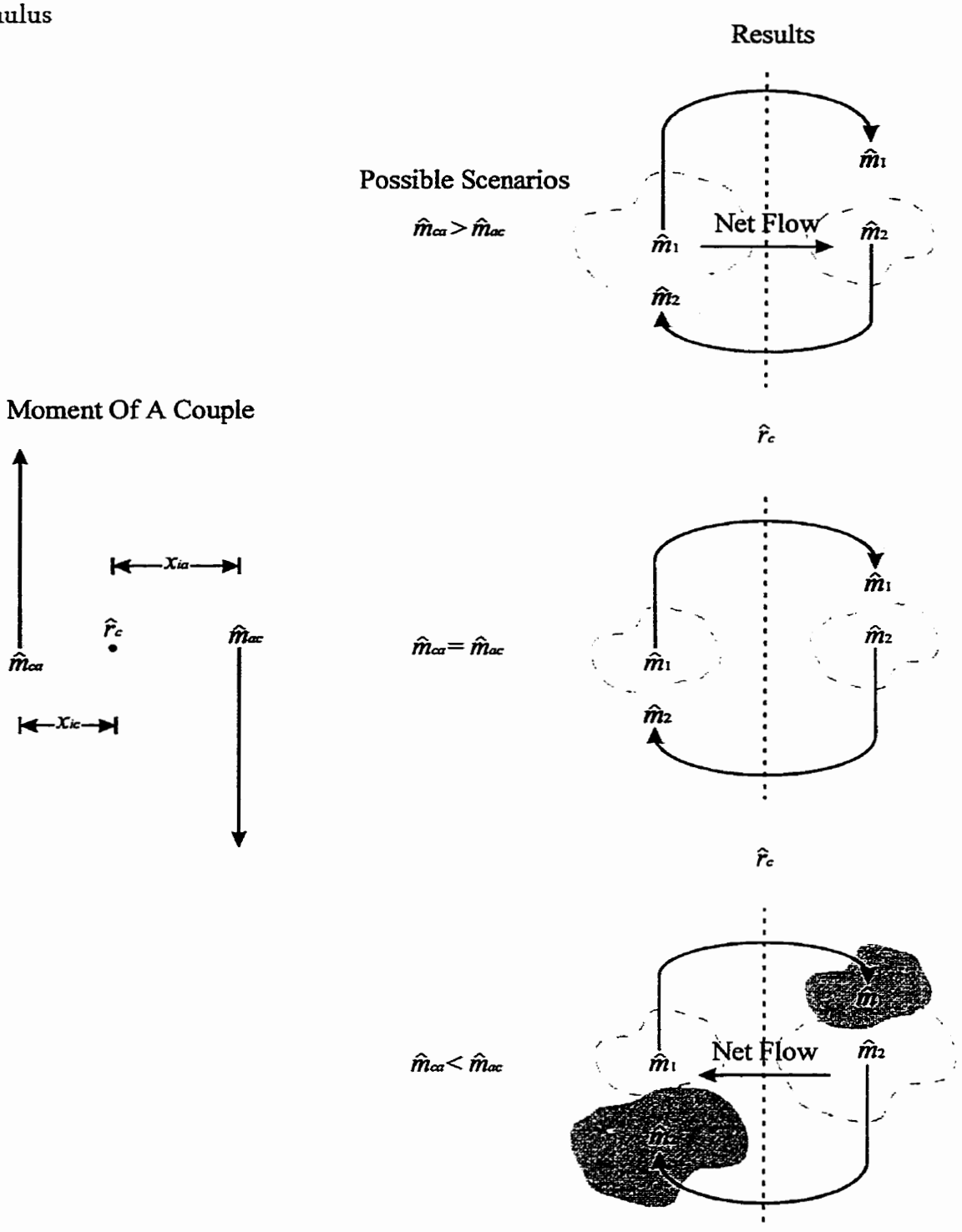

are equal, there is no net radial flow but exchange of matter does occur; when they are not equal, the difference in magnitude of the vectors dictates the direction of the net flow.

Table 9 summarizes the characteristics of the interchange of matter between the core and annular regions.

Table 9: Summary Of The Core-Annulus Material Interchange In The Proposed LDCFB Model

- The interchange of matter between the core and annulus stems from the differential mass balance on the core.
- The axially varying points x_{ia} and x_{ic}, on opposite sides of the core radius, delimit the exchange of material.
- The annulus interchange length, $x_{ia} - \hat{r}_c$, is equal to the wall layer thickness in the lower dense zone and is a linear function of axial location in the upper dilute zone.
- The core interchange length, $\hat{r}_c - x_{ic}$, is calculated using Equation 57.
- Equation 57 governs the interchange of both gas and solids.

Figure 13 illustrates the interchange lengths for a 5.825 m tall, 0.152 m diameter riser fluidizing FCC catalyst ($D_p = 74.9\,\mu$m, $\rho_p = 2456\,\mathrm{kg\,m^{-3}}$) at a rate of $47.8\,\mathrm{kg\,m^{-2}s^{-1}}$ with air at 110 kPa and 300 K.

Figure 13: Material Interchange Lengths As A Function Of Axial Position

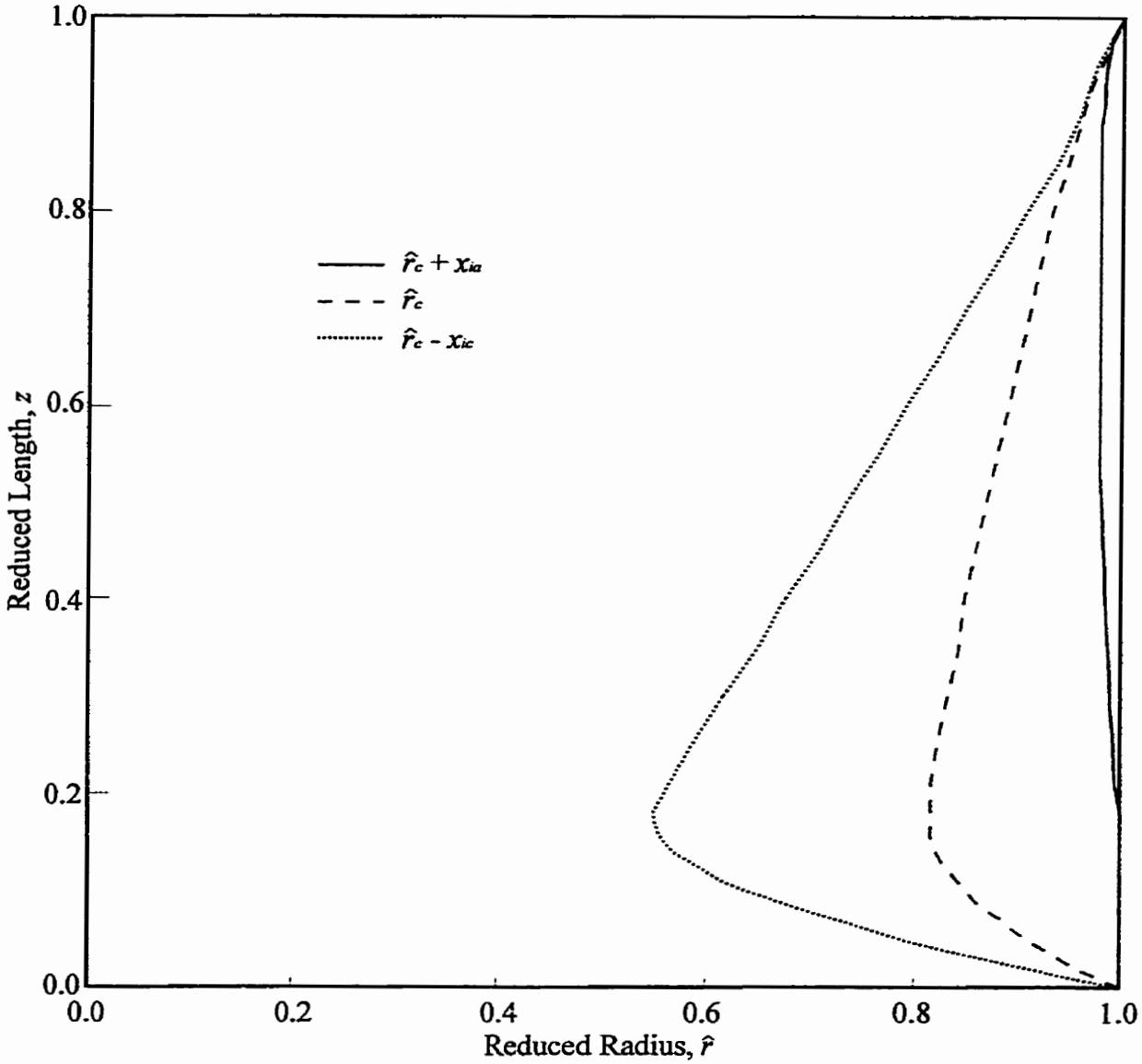

3.10 Pressure Drop

Contributions to the pressure drop in an LDCFB riser include the acceleration of solids, the hydrostatic head, gas-particle friction, particle-particle friction, and more. Of the quantities mentioned, the acceleration of solids and the hydrostatic head are the dominant contributors to the pressure drop; both frictional components typically contribute less the 5% (Pugsley, 1995) to the total pressure drop.

Due to the compressibility of the gas phase, the solids exhibit acceleration throughout the entire length of the riser. (Only under extremely contrived circumstances can the solids have a constant axial velocity.) A differential force balance and application of Newton's Second Law allow for calculation of the pressure drop in a riser. Figure 14 shows the vector quantities in Newton's Second Law. The sum of the forces,

Figure 14: Differential Force And Momentum Balance

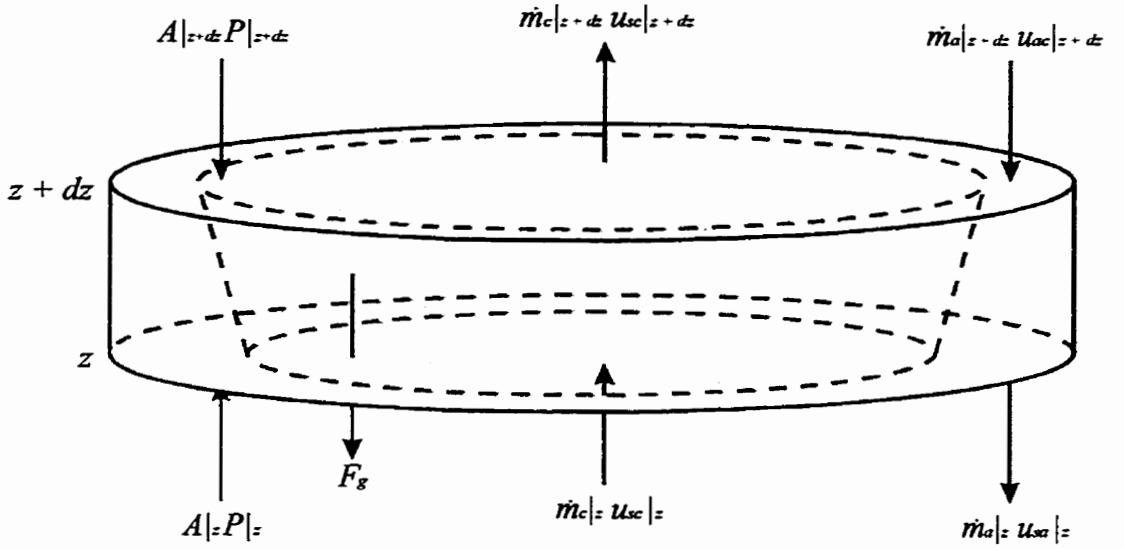

neglecting the gas phase contribution to the differential weight, are:

$$\sum F = -A\frac{\partial P}{\partial z}dz - ALg\rho_p\left(1-\epsilon\right)dz \tag{58}$$

and the rate of change of momentum, neglecting gas phase contributions, is:

$$\Delta\Lambda = \frac{\partial}{\partial z}\left(A_c\bar{G}_{sc}\bar{u_{sc}}\right)dz - \frac{\partial}{\partial z}\left(A_a\bar{G}_{sa}\bar{u_{sa}}\right)dz. \tag{59}$$

The solids mass fluxes, areas, and solids velocities are all functions of z.

In this case, the partial derivatives are equal to the total derivatives since the model development is at steady-state and the vectors of interest act in the axial direction only. Expanding the derivatives in Equation 59 and combining the result with Equation 58 yields the differential pressure drop:

$$\begin{aligned}\frac{dP}{dz} &= -Lg\rho_p(1-\epsilon) - \hat{r}_c^{\,2}\left(\bar{u_{sc}}\frac{d\bar{G_{sc}}}{dz} + \bar{G_{sc}}\frac{d\bar{u_{sc}}}{dz}\right) \\ &\quad - \left(\bar{G_{sc}}\bar{u_{sc}} + \bar{G_{sa}}\bar{u_{sa}}\right)\frac{d\hat{r}_c^{\,2}}{dz} + \left(1-\hat{r}_c^{\,2}\right)\left(\bar{u_{sa}}\frac{d\bar{G_{sa}}}{dz} + \bar{G_{sa}}\frac{d\bar{u_{sa}}}{dz}\right), \qquad (60)\end{aligned}$$

which includes contributions from the static head and particle acceleration throughout the length of the riser. All other previous core-annulus modeling efforts cannot/do not possess this level of sophistication because of their oversimplifying assumptions. Typically, they simply account for the static head.

3.11 Solution Methodology

The overall solution methodology for the hydrodynamic model presented in this dissertation, implemented in a simulator, is comprised of two iterative procedures in succession. Within each of the procedures reside other iterative procedures for calculating the center-line solids velocity at the LZUZI, solving the exchange of matter between the core and annulus, and solving various systems of non-linear equations. Brief and detailed descriptions of the methodology follow.

3.11.1 Brief Description

Steps 2 through 5, which are solved using the Newton-Raphson Method, form the first distinct iterative procedure and Steps 8 through 11, which are solved using successive substitution, form the second procedure.

1. Calculate $|\dot{m}_{sc}/\dot{m}_{sa}|_{\text{correlation}}$ using Equation 21.
2. Guess the axial position of the intersection of core radius functions and, subsequently, z_i.
3. Calculate $\hat{r}_c$ at z_i using Equation 12.
4. Calculate $|\dot{m}_{sc}/\dot{m}_{sa}|_{\text{calculated}}$ at z_i using Equation 11.
5. Go to Step 2 if $|\dot{m}_{sc}/\dot{m}_{sa}|_{\text{correlation}} - |\dot{m}_{sc}/\dot{m}_{sa}|_{\text{calculated}}$ does not meet the convergence criterion.
6. Calculate the axial mass flux profiles and wall solids velocity profile coefficients.
7. Seed the outlet pressure ($P(1)_{\text{calculated}}$).
8. Set $P(1)_{\text{last}} = P(1)_{\text{calculated}}$.
9. Calculate the center-line solids velocity profile coefficients.
10. Calculate $P(1)_{\text{calculated}}$ using Equation 60.

11. Go to Step 8 if $|P(1)_{\text{last}} - P(1)_{\text{calculated}}|/P(1)_{\text{calculated}}$ does not meet the convergence criterion.

3.11.2 Detailed Description

1. Calculate $|\dot{m}_{sc}/\dot{m}_{sa}|_{\text{correlation}}$ using Equation 21.

   - All of the variables in Equation 21 are known at the onset of any LDCFB calculation and can be used directly to determine the correlated value of the re-circulation ratio for a given riser.

2. Guess the axial position of the intersection of core radius functions and subsequently calculate the axial position of the LZUZI.

   - Experience shows that guessing high in the domain $0 \leq z \leq 1$ consistently converges the first iterative procedure. Once the location of the intersection of the parabolic core radius function and the core radius function Werther (1994) presents is known, algebraic manipulations allow for the determination of the location of z_i.

3. Calculate $\hat{r}_c$ at z_i using Equation 12.

   - The core radius, $\hat{r}_c$, is a function of design variables and axial location in the riser. Having calculated z_i in Step 2, all the variables in Equation 12 are known and $\hat{r}_c$ can be calculated.

4. Calculate $|\dot{m}_{sc}/\dot{m}_{sa}|_{\text{calculated}}$ at z_i using Equation 11.

   - One of the model assumptions is that the $\hat{G}(0, z_i)$ is the minimum center-line mass flux that allows for closure of the local mass balance. The minimum center-line mass flux corresponds to Ω (Equation 107) having a maximum value, which occurs when:

$$b = \frac{-1}{\ln(\hat{r}_c)} - 2. \tag{61}$$

Appendix A gives details on the derivation of Equation 61 and other related equations.

5. Go to Step 2 if $|\dot{m}_{sc}/\dot{m}_{sa}|_{\text{correlation}} - |\dot{m}_{sc}/\dot{m}_{sa}|_{\text{calculated}}$ does not meet the convergence criterion.

   - The re-circulation ratio correlation allows for $|\dot{m}_{sc}/\dot{m}_{sa}|_{\text{correlation}}$ to be calculated given the design variables. Integration and manipulation of Equation 11 gives

$$\dot{m}_{sc} = 2\pi \left[\frac{\hat{G}(0, z_i)_{\text{minimum}} \hat{r}_c^2}{2} - \frac{a \hat{r}_c^{b+2}}{b+2} \right] \tag{62}$$

   and

$$\dot{m}_{sa} = 2\pi \left[\frac{\hat{G}(0, z_i)_{\text{minimum}}}{2} - \frac{a}{b+2} - \dot{m}_{sc} \right], \tag{63}$$

   which are used to calculate $|\dot{m}_{sc}/\dot{m}_{sa}|_{\text{calculated}}$. The simulator uses a convergence criterion of 10^{-10} on the difference between the re-circulation ratios. Typically, about five Newton- Raphson iterations of Steps 2 through 5 are required to meet the criterion.

6. Calculate the axial mass flux profiles and wall solids velocity profile coefficients.

   - Equations 22, 23, and 26 each have four parameters and, therefore, each require a system of four equations to solve for the parameters. The equations for the center-line mass flux profile are:

$$\hat{G}(0,0) = 1, \tag{64}$$

$$\hat{G}(0,1) = 1, \tag{65}$$

$$\hat{G}(0, z_i) = \hat{G}(0, z_i)_{\text{minimum}}, \text{ and} \tag{66}$$

$$\frac{d\hat{G}}{dz}(0, z_i) = 0. \tag{67}$$

   The equations for the wall mass flux profile are:

$$\hat{G}(1,0) = 0, \tag{68}$$

$$\hat{G}(1,1) = 0, \tag{69}$$

$$\hat{G}(1,z_i) = c, \text{ and} \tag{70}$$

$$\frac{d\hat{G}}{dz}(1,z_i) = 0. \tag{71}$$

The equations for the wall solids velocity profile are:

$$u_s(1,0) = 0, \tag{72}$$

$$u_s(1,1) = 0, \tag{73}$$

$$u_s(1,z_i) = (u_{gin} + u_t)\left(1 - \frac{1}{\hat{r}_c^2}\right), \text{ and} \tag{74}$$

$$\frac{du_s}{dz}(1,z_i) = 0. \tag{75}$$

- The three systems of equations presented above can each be manipulated into a single non-linear function of the natural frequency, ω. Less than 10 iterations of the Newton-Raphson Method determines ω to an accuracy of 10 digits. It turns out that ω is the same for all of the second order responses used to model a given riser, i.e. $\omega_0 = \omega_1 = \omega_1^{u_s}$.

7. Seed the outlet pressure ($P(1)_{\text{calculated}}$).

   - The simulator simply uses the hydrostatic head of solids as an initial estimate of the pressure drop through the riser, which determines the associated outlet pressure. The slip factor correlation presented by Patience et al. (1992), Equation 5, is employed to calculate the average voidage in the riser, which is used in the determination of the hydrostatic head of solids.

8. Set $P(1)_{\text{last}} = P(1)_{\text{calculated}}$.

   - This step is the crux of successive substitution.

9. Calculate the center-line solids velocity profile coefficients.

- Fixing the outlet pressure enables the outlet gas velocity to be calculated, which, in turn, allows for $u_s(0,1)$ to be calculated based upon the assumption that $u_s(0,1) = u_g(0,1) + u_t$. Additionally, having calculated z_i in Steps 2 through 5, the center-line solids velocity at z_i is known based upon the assumption that $u_s(0,z_i) = u_{gin} + u_t$. Moreover, $u_s(0,0)$ can be calculated based upon the voidage at the base of the riser, the inlet solids mass flux, and the particle density. The three prescribed values of the center-line solids velocity are used to determine the parameters in Equation 24. They can be manipulated into a single non-linear function of $k_0^{u_s}$ and solved to an accuracy of 10^{-10} with less than 10 iterations of the Newton-Raphson Method.

10. Calculate $P(1)_{\text{calculated}}$ using Equation 60.

    - Because the axial profiles at the center-line and wall are prescribed and the radial profiles can be calculated at any z, all of the variables on the right hand side of Equation 60 are known. Calculating $P(1)_{\text{calculated}}$ is simply a matter of numerically integrating Equation 60 from $z = 0$ to $z = 1$. The simulator uses routines presented by Press et al. (1992) to perform the integration.

11. Go to Step 8 if $|P(1)_{\text{last}} - P(1)_{\text{calculated}}|/P(1)_{\text{calculated}}$ does not meet the convergence criterion.

    - The simulator uses a tolerance of 10^{-4} for the outlet pressure convergence criterion. Typically, about five iterations of Steps 8 through 10 are required to meet the criterion.

4 Kinetic Reaction Model

Coupling the advanced hydrodynamic model presented in Section 3 with a kinetic reaction model is one of the major objectives of the research presented in this dissertation. The obvious reactor modeling strategies for the two-dimensional hydrodynamic model would be to model the areas under the influence of the material interchange lengths as a continuous stirred tank reactor (CSTR) and the remaining core area as a plug flow reactor (PFR) with upward flow and the remaining annular area as a PFR with downward flow. Additionally, incorporation of radial diffusion and both radial and axial dispersion is possible. However, such sophistication is unwarranted due to the degree of uncertainty in the hydrodynamic model as far as key components such as the core radius and re-circulation ratio correlations are concerned. Moreover, even after developing the aforementioned, unwieldy reactor model, unreasonable simulation durations would render it impractical. Simplification of the hydrodynamic model, as presented in the next Section, yields a reasonable facsimile of reality and makes the coupled model viable.

Invocation of the Pseudo-Homogeneous Assumption for the development of the coupled hydrodynamic and kinetic reaction model requires that reactions be under kinetic control. Typically, this requirement restricts application to slow reactions; however, because particles in CFB reactors are small, the effectiveness factor is one and application of the Pseudo-Homogeneous Assumption is valid even for fast reactions. Therefore, the model development in this Section has general applicability.

4.1 Simplified Hydrodynamics

Although they do not explicitly note Peclet Numbers, Kruse et al. (1995) state that "In agreement with other researchers, the axial dispersion in the core zone was found to be negligible.". Additionally, Weinstein et al. (1989) indicate that gas phase backmixing is attributable to the downward flow of matter in the annular region. These

two findings justify the use of a PFR model for both the core and annular regions with material ascending in the core and descending in the annulus. The material interchange scheme presented in Section 3.9, which maintains the local and overall mass balances, provides the mechanism for exchange of matter between the core and annulus.

Invocation of the Pseudo-Homogeneous Assumption implicitly includes the assumption of perfect mixing within the control volume of interest. Consequently, the mole balance on component i in the core is:

$$\frac{dF_{ic}}{dz} = \pi r_c^2 L \rho_p (1-\epsilon_c) \sum_{j=1}^{n_r} \nu_{ij} r_j + 2\pi r_c L \left(\frac{y_{ia}}{MW_a} G_{gac} - \frac{y_{ic}}{MW_c} G_{gca} \right), \qquad (76)$$

where ν_{ij} is the stoichiometric coefficient of component i for reaction j, r_j is the jth reaction rate, y_i is the mole fraction of component i, MW is the average molecular weight, and the subscripts a and c denote the core and annular regions, respectively. The quantities G_{gac} and G_{gca} are the gas mass fluxes from the annulus to core and core to annulus, respectively. The material interchange scheme dictates their values, which maintains closure of the local mass balance. The average voidage in the core, ϵ_c, at any axial location is:

$$\epsilon_c = \frac{2 \int_0^{\hat{r}_c} \epsilon(\hat{r}, z) \hat{r} d\hat{r}}{\hat{r}_c^{\,2}}. \qquad (77)$$

Similarly, the mole balance on component i in annulus is:

$$\frac{dF_{ia}}{dz^\star} = \pi (R^2 - r_c^2) L \rho_p (1-\epsilon_a) \sum_{j=1}^{n_r} \nu_{ij} r_j - 2\pi r_c L \left(\frac{y_{ia}}{MW_a} G_{gac} - \frac{y_{ic}}{MW_c} G_{gca} \right), \qquad (78)$$

with the average voidage in the annulus,

$$\epsilon_a = \frac{2 \int_{\hat{r}_c}^{1} \epsilon(\hat{r}, z) \hat{r} d\hat{r}}{1 - \hat{r}_c^{\,2}}. \qquad (79)$$

The symbol $z^\star$ indicates that integration proceeds from $z = 1$ to $z = 0$.

Typically, the heat carrying capacity of the solids feed to an LDCFB riser reactor is orders of magnitude greater than that of the gas feed, so near isothermal operation may be possible, even for highly exothermic reactions. However, the effects of the

internal re-circulation of matter may have profound consequences on reactor operation and warrant investigations into the thermal behavior of a riser reactor.

For each region in the simplified hydrodynamic model, the differential energy balance is comprised of three general terms: net axial input, net radial input, and generation. The convective terms, the net axial and radial inputs, apply to both phases of matter, which tends to make presentation of the energy balance equation cumbersome. Therefore, piecemeal development of the conservation of energy for both the core and annular regions in an adiabatic riser reactor follows.

The differential generation of energy in the core due to chemical reactions is relatively simple:

$$E_{\text{generation}} = \pi r_c^2 L dz \rho_p (1 - \epsilon_c) \sum_{j=1}^{n_r} r_j \mathcal{H}_j, \tag{80}$$

where j varies from one to the number of reactions and $\mathcal{H}_j$ is the enthalpy of the jth reaction.

The net axial input of energy into the core control volume, including the temperature dependence of the heat capacity of both solids and gas, is:

$$\Delta E_{\text{axial}} = \sum_{i=1}^{n_c} c_{p_i} F_{ic} \frac{\partial T_c}{\partial z} dz + \sum_{i=1}^{n_c} \mathcal{H}_i(T_c) \frac{\partial F_{ic}}{\partial z} dz + c_{p_s} \dot{m}_{sc} \frac{\partial T_c}{\partial z} dz + \mathcal{H}_s(T_c) \frac{\partial \dot{m}_{sc}}{\partial z} dz, \tag{81}$$

where i varies from one to the number of components, c_{p_i}, F_i, and $\mathcal{H}_i$ are the heat capacity, mole flow rate, and enthalpy of component i, respectively and c_{p_s} and $\dot{m}_{sc}$ are the heat capacity and mass flow rate of the solids, respectively. The component enthalpies and heat capacities for both phases are functions of the core temperature, T_c.

The net radial input of energy into the core control volume is:

$$\Delta E_{\text{radial}} = \tag{82}$$
$$2\pi r_c L dz \left(\sum_{i=1}^{n_c} \mathcal{H}_i(T_c) \frac{y_{ic}}{MW_c} G_{gca} - \sum_{i=1}^{n_c} \mathcal{H}_i(T_a) \frac{y_{ia}}{MW_a} G_{gac} + \mathcal{H}_s(T_c) G_{sca} - \mathcal{H}_s(T_a) G_{sac} \right).$$

Combining Equations 80, 81, and 82 appropriately, dividing by dz, re-arranging, and acknowledging that, in this case, the partial derivative is equal to the total

derivative, yields the differential equation describing the temperature in the core:

$$\frac{dT_c}{dz} = \frac{\pi r_c^2 L \rho_p (1-\epsilon_c) \sum_{j=1}^{n_r} r_j \mathcal{H}_j - \sum_{i=1}^{n_c} \mathcal{H}_i(T_c) \frac{\partial F_{ic}}{\partial z} - \mathcal{H}_s(T_c) \frac{\partial \dot{m}_{sc}}{\partial z} - \mathcal{H}_{\text{radial}}}{\sum_{i=1}^{n_c} c_{p_i} F_{ic} + c_{p_s} \dot{m}_{sc}} \quad (83)$$

where

$$\mathcal{H}_{\text{radial}} = \quad (84)$$
$$2\pi r_c L \left(\sum_{i=1}^{n_c} \mathcal{H}_i(T_c) \frac{y_{ic}}{MW_c} G_{gca} - \sum_{i=1}^{n_c} \mathcal{H}_i(T_a) \frac{y_{ia}}{MW_a} G_{gac} + \mathcal{H}_s(T_c) G_{sca} - \mathcal{H}_s(T_a) G_{sac} \right).$$

Development of the energy balance for the corresponding annular control volume is analogous to that presented above. The result is:

$$\frac{dT_a}{dz^*} = \quad (85)$$
$$\frac{\pi (R^2 - r_c^2) L \rho_p (1-\epsilon_a) \sum_{j=1}^{n_r} r_j \mathcal{H}_j - \sum_{i=1}^{n_c} \mathcal{H}_i(T_a) \frac{\partial F_{ia}}{\partial z^*} - \mathcal{H}_s(T_a) \frac{\partial |\dot{m}_{sa}|}{\partial z^*} + \mathcal{H}_{\text{radial}}}{\sum_{i=1}^{n_c} c_{p_i} F_{ia} + c_{p_s} |\dot{m}_{sa}|}$$

with the net radial flow of energy in the opposite direction with respect to Equation 86 and the direction of integration from $z = 1$ to $z = 0$.

Equations 83 and 86 appear intimidating but, in fact, coding them into a computer program is not difficult at all and adds significant capabilities to the model.

4.2 Solution Methodology

From a gross perspective, the solution methodology for the couple hydrodynamic-kinetic reaction model is quite simple and only the implementation makes it seem burdensome. Brief and detailed descriptions of the methodology follow.

4.2.1 Brief Description

After solving the complex hydrodynamic model, the general procedure for solving the couple hydrodynamic-kinetic reaction model is to solve for the state properties in the

annular region and, subsequently, solve for the state properties in the core region.

1. Solve the complex hydrodynamic model presented in Section 3.

2. Generate splines for the average solids mass flow, derivative of the solids mass flow with respect to the axial co-ordinate, radial mass fluxes, and voidage for both the core and annular regions.

3. Generate a spline for the pressure in the riser reactor.

4. Integrate Equations 76 and 83 (the core) storing the temperature at each node. For the material interchange scheme, assume the composition at node i in the annulus is the same as the composition at node i in the core. Neglect the radial flow of energy contributions to the differential energy balance.

5. Integrate Equations 78 and 86 (the annulus) storing the composition and temperature at each node. For the material interchange scheme, assume the composition at node i in the core is the same as the composition at node i in the annulus. Neglect the radial flow of energy contributions to the differential energy balance.

6. Generate splines for the composition and temperature in the annulus.

7. Integrate the core storing the composition and temperature at each node.

8. Generate splines for the composition and temperature in the core.

9. Set $u_{gout}^{\text{last}} = u_{gout}^{\text{calculated}}$.

10. Calculate the outlet composition and temperature.

11. Use the result of Step 10 with the complex hydrodynamic model to calculate $u_{gout}^{\text{calculated}}$.

12. Generate splines for the average solids mass flow, derivative of the solids mass flow with respect to the axial co-ordinate, radial mass fluxes, and voidage for both the core and annular regions.

13. Generate a spline for the pressure in the riser reactor.

14. Go to Step 9 if $\left|u_{gout}^{last} - u_{gout}^{calculated}\right| / u_{gout}^{calculated}$ does not meet the convergence criterion.

4.2.2 Detailed Description

1. Solve the complex hydrodynamic model presented in Section 3.

   - The entire basis for the simplified hydrodynamic model presented in Section 4.1, which the coupled hydrodynamic-kinetic reaction model uses, is the complex hydrodynamic model. The solution for the complex hydrodynamic model is presented in Section 3.11.

2. Generate splines for the average solids mass flow, derivative of the solids mass flow with respect to the axial co-ordinate, radial mass fluxes, and voidage for both the core and annular regions.

   - The simplified hydrodynamic model uses average values for the variables in the core and annular regions, which stem from the complex hydrodynamic model. Calculating the average values "on the fly" is possible but greatly encumbers the overall calculation process and is unnecessary. Generating splines for the average values reduces the overall computational requirements and expedites the solution procedure, particularly since integration routines use variable, unpredictable step-sizes.

3. Generate a spline for the pressure in the riser reactor.

- Using a spline to determine the pressure at any location in the riser reduces the number of differential equations that describe the system by one, which reduces calculation time, and avoids potentially introducing stiffness into the system of differential equations.

4. Integrate Equations 76 and 83 (the core) storing the temperature at each node. For the material interchange scheme, assume the composition at node i in the annulus is the same as the composition at node i in the core. Neglect the radial flow of energy contributions to the differential energy balance.

   - When integrating the core, the feed to the riser reactor fully specifies the initial values since the core radius is one at the base of the reactor.
   - At this point in the solution methodology, the composition in the annulus is not known but net radial transfer of matter between the core and annulus must occur in order to satisfy the local and, ultimately, overall mass balance. Assuming equal compositions in the two regions closes the mass balance(s).
   - Neglect the radial contributions,

     $$\mathcal{H}_s \frac{d\dot{m}_{sc}}{dz} \text{ and } \mathcal{H}_{\text{radial}},$$

     to the energy balance in the core. Failure to do so results in a decrease in temperature, even for highly exothermic reactions, in the lower zone and increase in temperature, even for highly endothermic reactions, in the upper zone since the rate of change of solids mass flow in the core is the dominant term in Equation 83 at the base and exit of the riser reactor. It must be counteracted by the radial flow of energy but, because the temperature in the annulus is not known at this point in the solution methodology, $\mathcal{H}_{\text{radial}}$ is indeterminate.

5. Integrate Equations 78 and 86 (the annulus) storing the composition and temperature at each node. For the material interchange scheme, assume the composition at node i in the core is the same as the composition at node i in the annulus. Neglect the radial flow of energy contributions to the differential energy balance.

   - At $z = 1$, the starting point for integration of the annulus, the flow of matter is zero by definition of the radius of the core—the interchange of matter is the means by which flow starts in the annulus. However, from a numerical standpoint, initial values for the mole flow rates in the annulus are necessary. Therefore, initialize the flow rates in the annulus with the corresponding composition from the core, at $z = 1$, and multiply them by a very small number to effectively make the flow zero; the simulator uses 10^{-30} as a scaling factor.
   - Closure of the local mass balance is accomplished via material interchange between the core and annulus. During the first integration of the annulus, by nature of the interchange scheme, it is possible that negative mole flows occur by using the core composition of Step 4. Therefore, to avoid negative mole flows and maintain the local mass balance, use a core composition equal to the annulus composition for the material interchange scheme.

6. Generate splines for the composition and temperature in the annulus.

7. Integrate the core storing the composition and temperature at each node.

   - Subsequent integration iterations cycle through integrating the annulus and then the core, which requires integration of the core prior to starting the cycle.
   - Radial contributions to the equations describing the core rely on values in the annulus, which are calculated from the splines generated in the last

Step.

8. Generate splines for the composition and temperature in the core.

9. Set $u_{gout}^{\text{last}} = u_{gout}^{\text{calculated}}$.

   - This is the crux of successive substitution.
   - The first time through, $u_{gout}^{\text{calculated}}$ is the outlet gas velocity, determined by the complex hydrodynamic model, without accounting for reactions. Reactions may induce changes in moles or temperature that substantially affect the overall hydrodynamic structure in the riser reactor, according to the model presented in this dissertation, since the center-line solids velocity and pressure drop are functions of the outlet gas velocity, which is a function of mole density and temperature.

10. Calculate the outlet composition and temperature.

    - This Step consists of several steps:
      (a) Store the state property vector for the core at the reactor exit ($z = 1$).
          – Only the state properties of the core determine convergence because the core radius is one at the riser exit.
      (b) Integrate Equations 78 and 86 (the annulus) storing compositions and temperatures at each node.
      (c) Generate splines for the composition and temperature in the annulus.
      (d) Integrate Equations 76 and 83 (the core) storing compositions and temperatures at each node.
      (e) Generate splines for the composition and temperature in the core.
      (f) Go to Step 10a if the convergence criteria on the state vector at the riser reactor exit ($z = 1$) are not met.

- The number of iterations necessary to meet a convergence criterion of 10^{-4} on all the elements in the state vector varies from hundreds to thousands depending on the number of components and reactions.

11. Use the result of Step 10 with the complex hydrodynamic model to calculate $u_{gout}^{calculated}$.

    - In order to determine the hydrodynamic parameters of the proposed model, Step 1 sets the composition and temperature of the reactor outlet equal to the reactor inlet. However, after passing through the reactor, the composition and temperature at the outlet undoubtedly differ from the inlet. Therefore, re-calculate the hydrodynamic parameters, which determine the outlet gas velocity, using the calculated outlet conditions.

12. Generate splines for the average solids mass flow, derivative of the solids mass flow with respect to the axial co-ordinate, radial mass fluxes, and voidage for both the core and annular regions.

13. Generate a spline for the pressure in the riser reactor.

14. Go to Step 9 if $\left|u_{gout}^{last} - u_{gout}^{calculated}\right| / u_{gout}^{calculated}$ does not meet the convergence criterion.

    - Step 10 is so computationally intensive that the simulator uses a convergence criterion of 1% to limit the duration of a simulation, which is strongly dependent on the number of reactions and components in the system, to hours.

Comparing the predictions of the models presented in Sections 3 and 4 with experimental data demonstrates the merits of the ideas put forth in this dissertation. The

next Section presents extensive comparisons using data from 10 independent research groups.

5 Model Validation

The culmination of the research presented in this dissertation manifests itself in the form of a fully object-oriented, multi-threaded simulator written in C++. The simulator includes a Microsoft Foundation Classes (MFC) graphical user interface supporting drag-and-drop process flow diagram construction, novel object persistence design, and generic flash calculations. The object design is superior to the design commercial simulators, such as HYSYS, use because it maintains clearly distinct interface and engineering objects. As a result, any interface, including textual or graphical, written in any language, including C++, Visual Basic, or Java, can be "put on top of" the engineering kernel, which does not have to be re-written. Additionally, the generic, robust solution algorithms for a coupled hydrodynamic and kinetic reaction model allow for the simulator's application to any kinetically limited LDCFB riser reactor. The simulator expedites the model validation process considerably and allows for future validations.

Admittedly, it is highly unlikely that an all encompassing, predictive LDCFB model can be formulated due to the many factors affecting CFB operation, such as solids feeder mechanism, exit geometry, variable gas molar density, heat transfer, wall roughness, particle size distribution, roughness, sphericity, and so on. With that in mind, the results presented in Sections 5.1 through 5.7 are remarkably good and justify the use of the model for at least preliminary design and economic evaluations. Sections 5.6 through 5.8 examine the capabilities of the coupled hydrodynamic-kinetic reaction model while Sections 5.1 through 5.5 scrutinize the model strictly from a hydrodynamic point of view.

Typically, a chi-squared distribution,

$$\chi^2 = \sum_{i=1}^{n} \frac{(\text{Predicted Value}_i - \text{Experimental Value}_i)^2}{\text{Experimental Value}_i}, \tag{86}$$

quantifies the goodness of fit between model predictions and experimental data. However, for mass flux and solids velocity profiles, it fails to provide an adequate indication

of the goodness of fit because Equation 86 is singular at the core radius. For example, qualitatively, Figure 22 (Page 92) shows an absolutely outstanding fit; however, the average percent error between model predictions and experimental observations is a whopping 119% because the point at $\hat{r}_c = 0.93$ is close to zero, which results in a 736% error locally and amplifies the average error enormously. Obviously, an alternative method of quantification of the goodness of fit is necessary.

Eliminating the singularity in Equation 86 is the solution to the apparent problem. Therefore, choosing a normalizing factor other than the observation value itself is necessary. The range of the experimental observations has physical meaning in the system of interest and allows for the definition of the "relative error":

$$\text{Relative Error} = \frac{\text{Predicted Value}_i - \text{Experimental Value}_i}{\text{Maximum Experimental Value - Minimum Experimental Value}}, \tag{87}$$

which is used to quantify the goodness of fit throughout this dissertation. This measure is only useful when comparing the model presented in this dissertation to other models. Comparisons between the model presented in this dissertation and the renowned Pugsley Model are pointless because of fundamental errors in the Pugsley Model, which Appendix C demonstrates. So, comparisons in this Section are with the empirical Patience-Chaouki Model, which is also touted as one of the best core-annulus type models in the world.

Note that all reports of parametric values for the radial profiles are truncated at six digits, which may not provide sufficient accuracy for reproduction of the figures.

5.1 Radial Solids Mass Flux Profiles

One of the strengths of the model presented in this dissertation is that the core radius and all functions of the core radius vary axially in accordance with physical observations. Figure 15 (Page 81) demonstrates this capability by depicting the reduced mass flux profile at various axial locations in the riser. At $z = 0$, the profile

is flat and has a value of one. At $z = 0.1$, the effects of internal refluxing are apparent with downward flow at the wall and an increase in the center-line mass flux. The center-line mass flux continues to increase until $z = z_i$, as does the magnitude of the downward flow at the wall. In the upper zone, $z > z_i$, the center-line mass flux decreases from its maximum value. Similarly, the wall mass flux increases from its minimum value. This phenomenon tends to flatten the profiles until they converge to unity at $z = 1$.

The model inputs for the pseudo-animation in Figure 15 are from Rhodes et al. (1992), who provide an abundance of reduced solids mass flux data profiles.

Figure 15: Predicted Reduced Radial Mass Flux Profile Pseudo-Animation

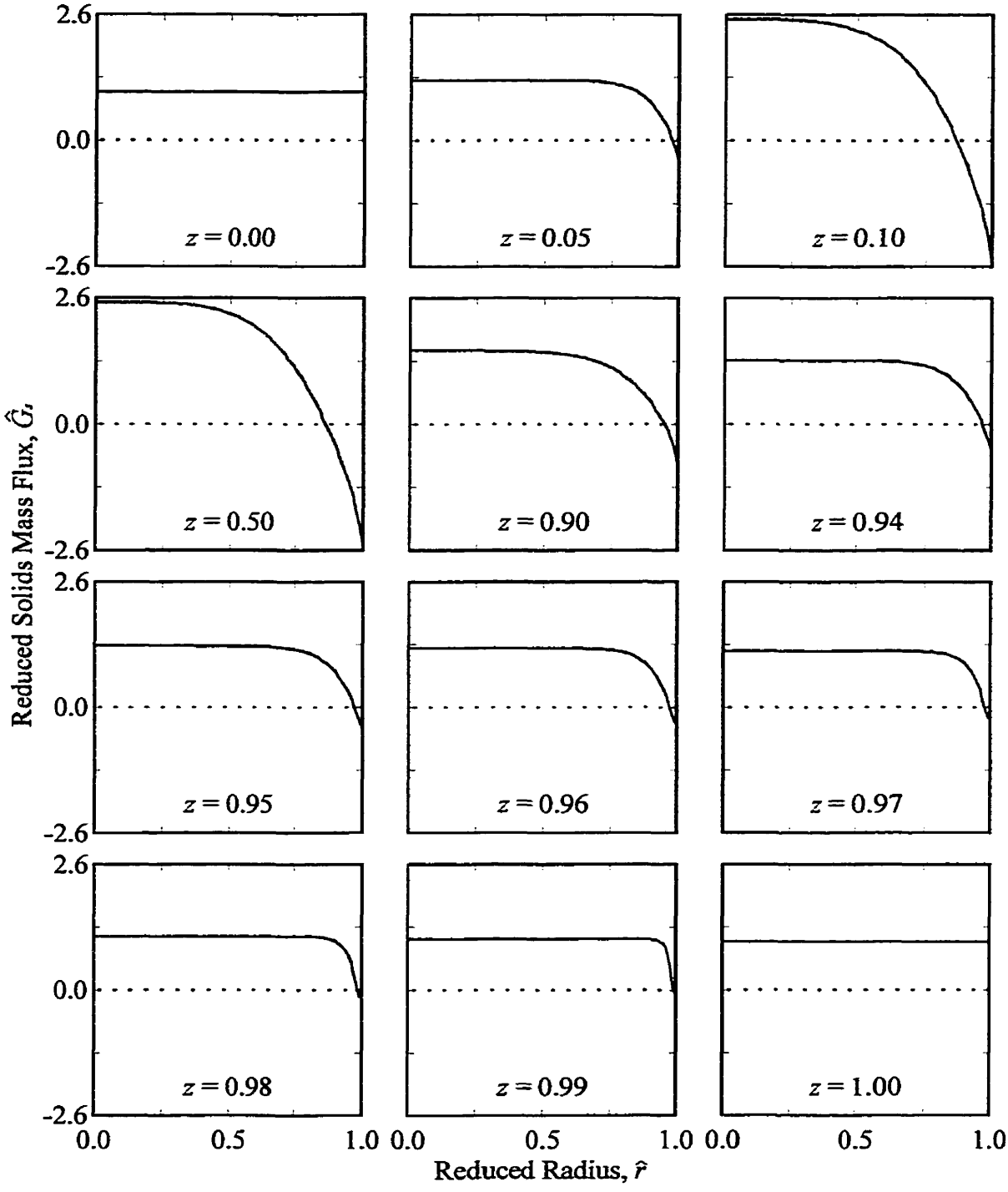

5.1.1 Rhodes et al., 1992

Rhodes et al. (1992) used two risers and fluid catalytic cracking catalyst (D_p = 74.9 μm, $\rho_p = 2456\,\mathrm{kg\,m^{-3}}$) to obtain 26 radial solids mass flux profiles. The smaller of the two risers had a height of 5.825 m and a diameter of 0.152 m while the larger one had a height of 6.600 m and a diameter of 0.305 m. The researchers do not report the inlet pressure to the risers; the simulations use a value of 110 kPa for all comparisons, which allows for adequate pressure for cyclonic gas-solids separation at the riser outlet.

Rhodes et al. (1992) employed a non-isokinetic sampling probe to measure the solids mass flux at various radial locations. Calculations of the local mass balance, based on probe measurements, are accurate within 10%. In this Section, the scope of examination is arbitrarily restricted to inlet solids mass fluxes greater than $30\,\mathrm{kg\,m^{-2}s^{-1}}$. The first 10 comparisons are between model predictions and experimental observations from the small riser at a fixed axial sampling location of $z = 0.33$.

The data in Figure 16 (Page 83) correspond to an inlet superficial gas velocity of $3\,\mathrm{m\,s^{-1}}$ and an inlet solids mass flux of $63.5\,\mathrm{kg\,m^{-2}s^{-1}}$. The calculated location of the LZUZI, based on the re-circulation ratio, is $z_i = 0.48$ and the calculated outlet pressure is 104.4 kPa. The relative error between the model predictions and experimental data is 16%. (The Patience-Chaouki Model exhibits a 11% relative error.) Clearly, the magnitude of both the center-line and wall mass fluxes are under predicted. Because the sampling location is below the LZUZI, the assumed parabolic core radius function predicts $\hat{r}_c$; it is erroneous by approximately +3%. If Equation 12, based on experimental observation, is employed at the sampling location, the error increases to -5%. The shape of the predicted profile is extremely sensitive to the location of the core radius, so it is critical to predict $\hat{r}_c$as accurately as possible.

The data in Figure 17 (Page 85) correspond to an inlet superficial gas velocity of $3\,\mathrm{m\,s^{-1}}$ and an inlet solids mass flux of $46.1\,\mathrm{kg\,m^{-2}s^{-1}}$. The LZUZI is $z_i = 0.42$ and outlet pressure is 105.8 kPa. The relative error is 12% with the model predicting the

Figure 16: Reduced Radial Solids Mass Flux Profile Comparison With Experimental Data From Rhodes et al., 1992 ($z = 0.33$, $u_{gin} = 3\,\mathrm{m\,s^{-1}}$, $G_{sin} = 63.5\,\mathrm{kg\,m^{-2}s^{-1}}$, $H = 5.825\,\mathrm{m}$, $D = 0.152\,\mathrm{m}$, $\rho_p = 2456\,\mathrm{kg\,m^{-3}}$, $D_p = 74.9\,\mu\mathrm{m}$)

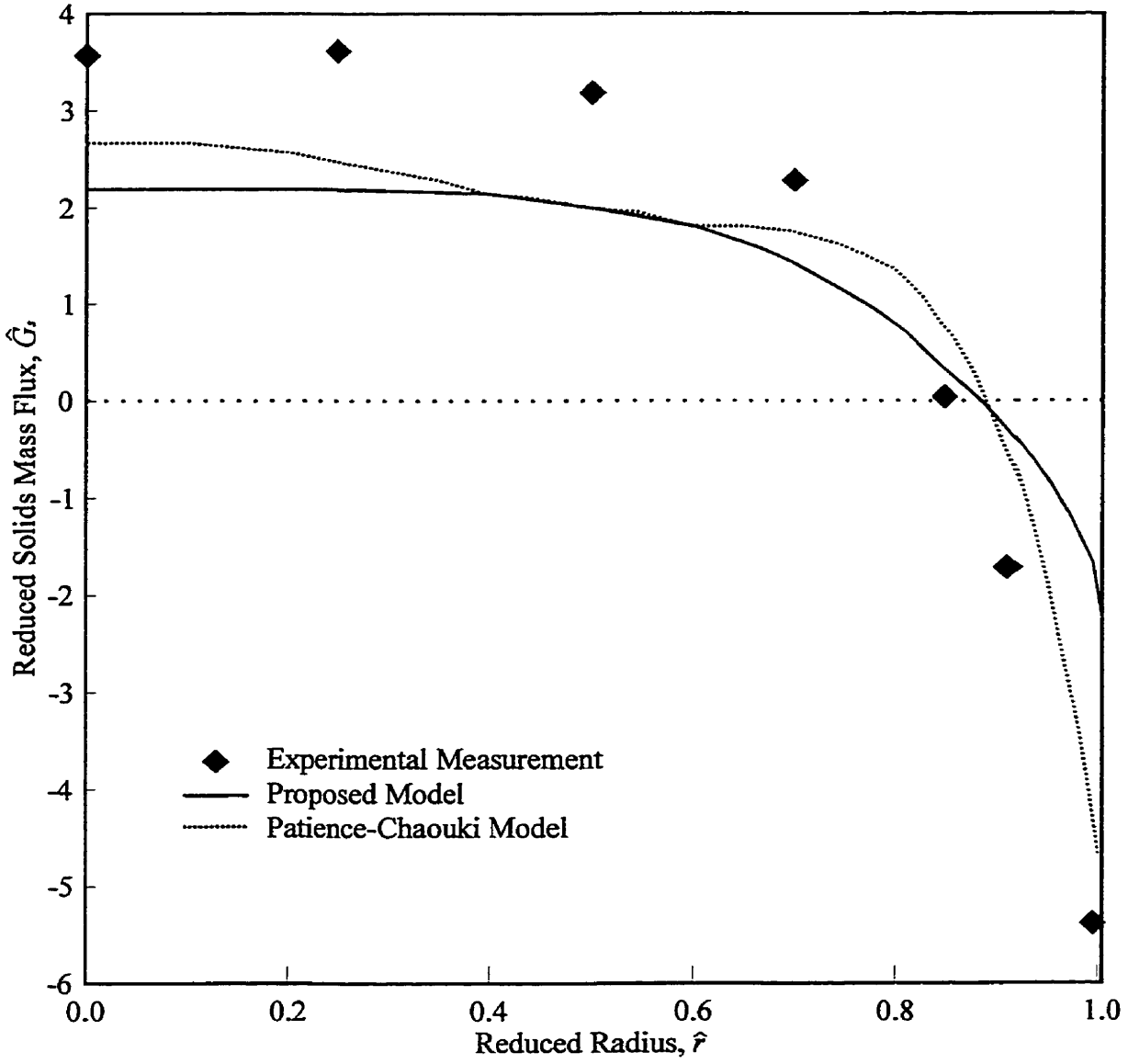

Radial Profile Parameters For The Predicted Values In Figure 16

$\hat{r}_c$=0.884	a	b	c	d	e	f
$\hat{G}$	3.79556	4.46265	-1.60517	7.68645	0.572410	5.44769
u_s	3.05922	2.12948	-0.70589	4.96488	0.878288	4.21685

core radius nearly perfectly. (The Patience-Chaouki Model exhibits a 12% relative error.) Once again, the parabolic function determines the core radius and is more accurate than using Equation 12. The center-line mass flux prediction is satisfactory but the wall mass flux prediction is not. In this case, the LZUZI is less than in the first case and the outlet pressure is greater than in the first case, which adheres to intuition and observation since the inlet solids mass flux is greater in the first case.

The data in Figure 18 (Page 86) correspond to an inlet superficial gas velocity of $3\,\mathrm{m\,s^{-1}}$ and an inlet solids mass flux of $31.4\,\mathrm{kg\,m^{-2}s^{-1}}$. The LZUZI is $z_i = 0.31$ and outlet pressure is 107.0 kPa. The relative error is a mere 9% and the goodness of fit is superb with the exception of the points nearest to the wall. (The Patience-Chaouki Model exhibits a 15% relative error.) Even though the sampling location is above the LZUZI, the parabolic function determines the core radius because the core radius function intersection point is greater than the sampling location. Once again, the parabolic core radius function is more accurate than using Equation 12. The center-line mass flux prediction is excellent, exhibiting a 1% relative error, but the wall mass flux is under predicted by 19%.

The data in Figure 19 (Page 87) correspond to an inlet superficial gas velocity of $4\,\mathrm{m\,s^{-1}}$, $1\,\mathrm{m\,s^{-1}}$ greater than the previous three comparisons, and an inlet solids mass flux of $62.7\,\mathrm{kg\,m^{-2}s^{-1}}$. The LZUZI is $z_i = 0.39$ and outlet pressure is 105.9 kPa. The relative error is a 8% and, qualitatively, the goodness of fit is excellent. (The Patience-Chaouki Model exhibits a 9% relative error.) The predicted core radius, determined by the parabolic function, matches the interpolated experimental core radius almost exactly and, since the center-line mass flux prediction is good, the overall shape of the profile is very good. The under prediction of the magnitude of the wall mass flux has a relative error of 17%.

The data in Figure 20 (Page 89) correspond to an inlet superficial gas velocity of $4\,\mathrm{m\,s^{-1}}$ and an inlet solids mass flux of $49.7\,\mathrm{kg\,m^{-2}s^{-1}}$. The LZUZI is $z_i = 0.33$ and outlet pressure is 106.7 kPa. The relative error is a 10% due to the over prediction of

Figure 17: Reduced Radial Solids Mass Flux Profile Comparison With Experimental Data From Rhodes et al., 1992 ($z = 0.33$, $u_{gin} = 3\,\mathrm{m\,s^{-1}}$, $G_{sin} = 46.1\,\mathrm{kg\,m^{-2}s^{-1}}$, $H = 5.825\,\mathrm{m}$, $D = 0.152\,\mathrm{m}$, $\rho_p = 2456\,\mathrm{kg\,m^{-3}}$, $D_p = 74.9\,\mu\mathrm{m}$)

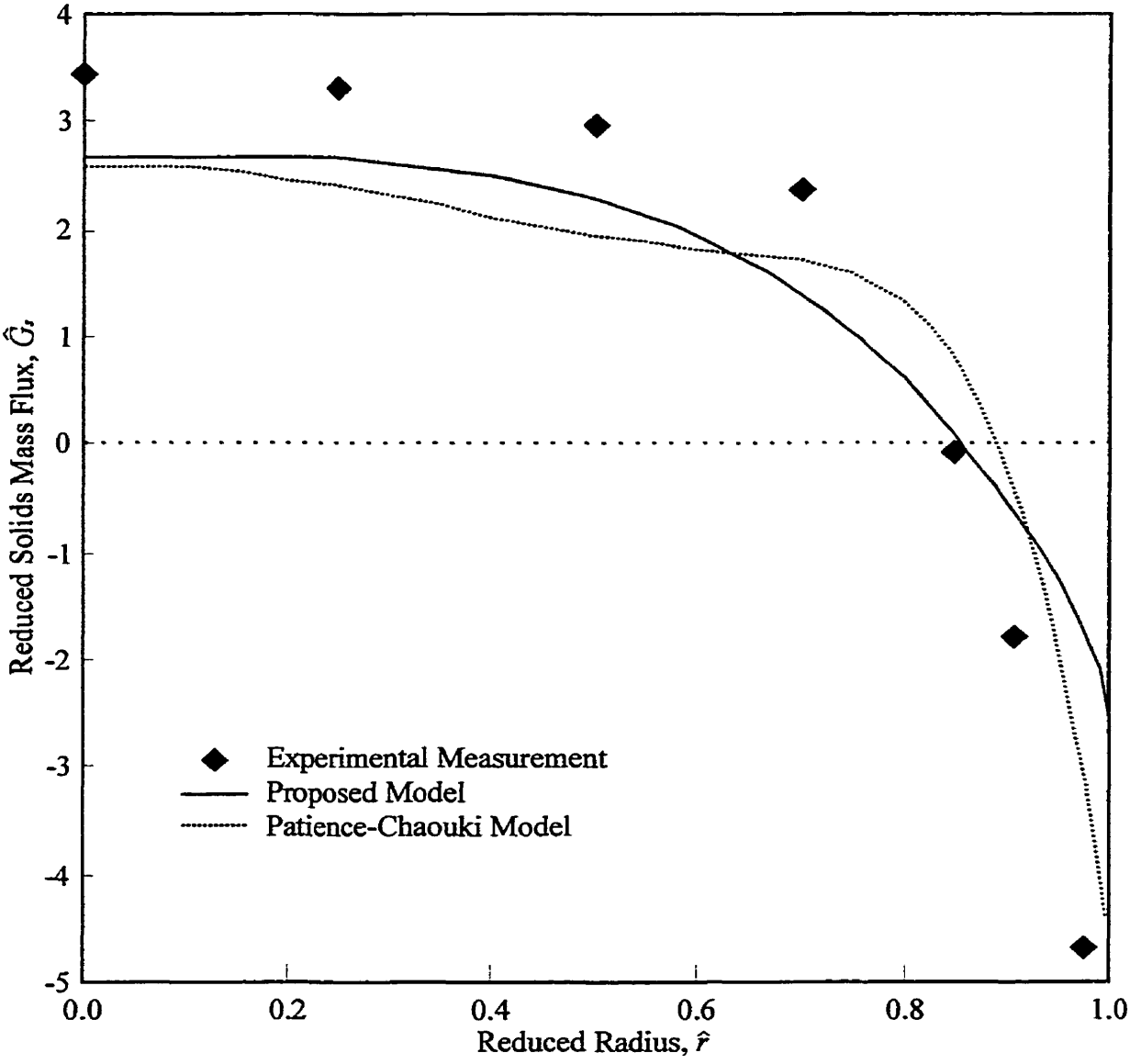

Radial Profile Parameters For The Predicted Values In Figure 17

$\hat{r}_c$=0.857	a	b	c	d	e	f
$\hat{G}$	4.66508	3.59291	-1.979678	8.67281	0.626109	6.11234
u_s	3.39765	2.05261	-0.919350	5.34447	0.882038	4.38620

Figure 18: Reduced Radial Solids Mass Flux Profile Comparison With Experimental Data From Rhodes et al., 1992 ($z = 0.33$, $u_{gin} = 3\,\mathrm{m\,s^{-1}}$, $G_{sin} = 31.4\,\mathrm{kg\,m^{-2}s^{-1}}$, $H = 5.825\,\mathrm{m}$, $D = 0.152\,\mathrm{m}$, $\rho_p = 2456\,\mathrm{kg\,m^{-3}}$, $D_p = 74.9\,\mu\mathrm{m}$)

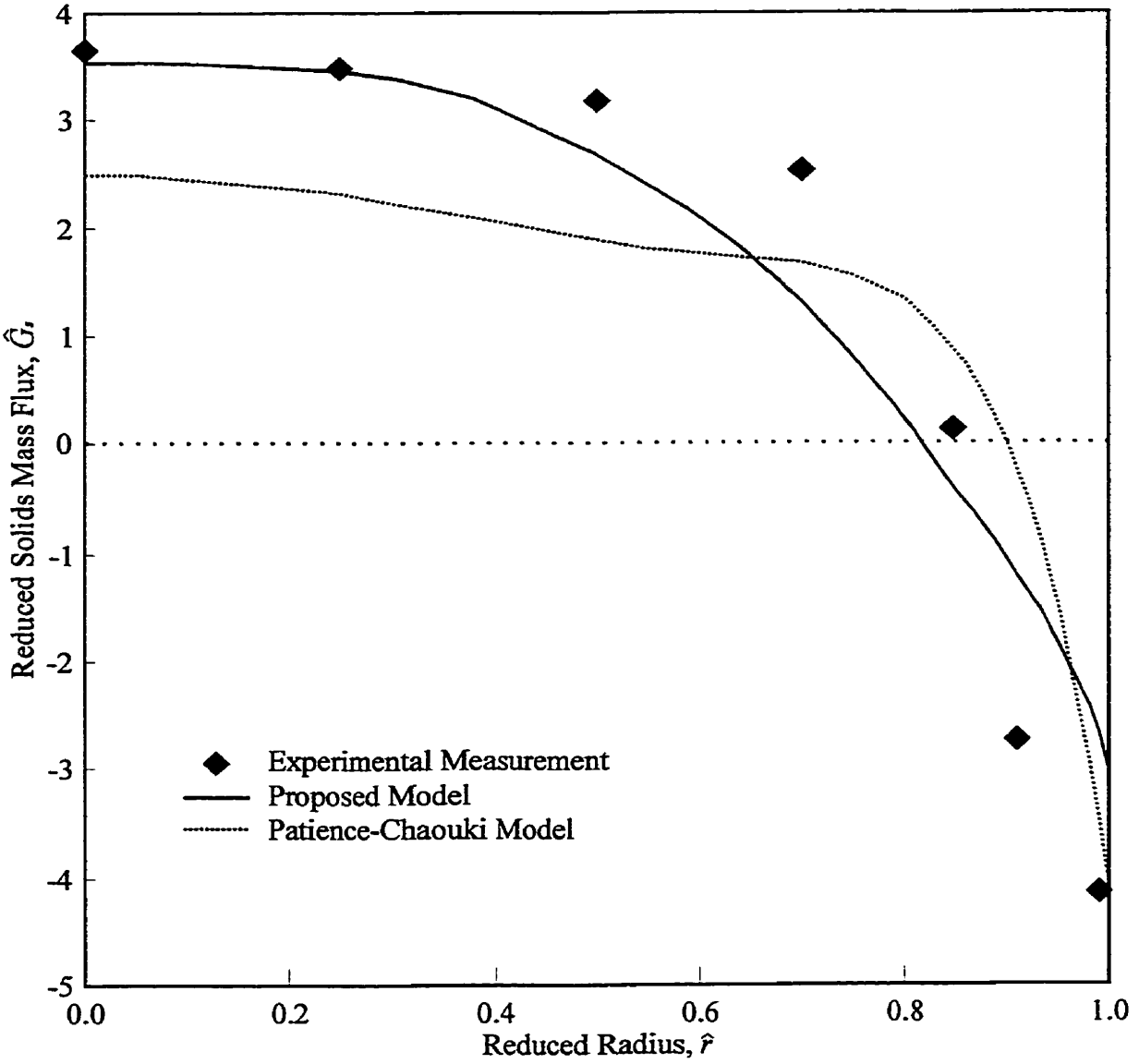

Radial Profile Parameters For The Predicted Values In Figure 18

$\hat{r}_c$=0.822	a	b	c	d	e	f
$\hat{G}$	6.30447	2.88577	-2.72284	10.88109	0.748394	7.89171
u_s	3.91603	2.05121	-1.29607	6.22541	0.929038	4.97330

Figure 19: Reduced Radial Solids Mass Flux Profile Comparison With Experimental Data From Rhodes et al., 1992 ($z = 0.33$, $u_{gin} = 4\,\mathrm{m\,s^{-1}}$, $G_{sin} = 62.7\,\mathrm{kg\,m^{-2}s^{-1}}$, $H = 5.825\,\mathrm{m}$, $D = 0.152\,\mathrm{m}$, $\rho_p = 2456\,\mathrm{kg\,m^{-3}}$, $D_p = 74.9\,\mu\mathrm{m}$)

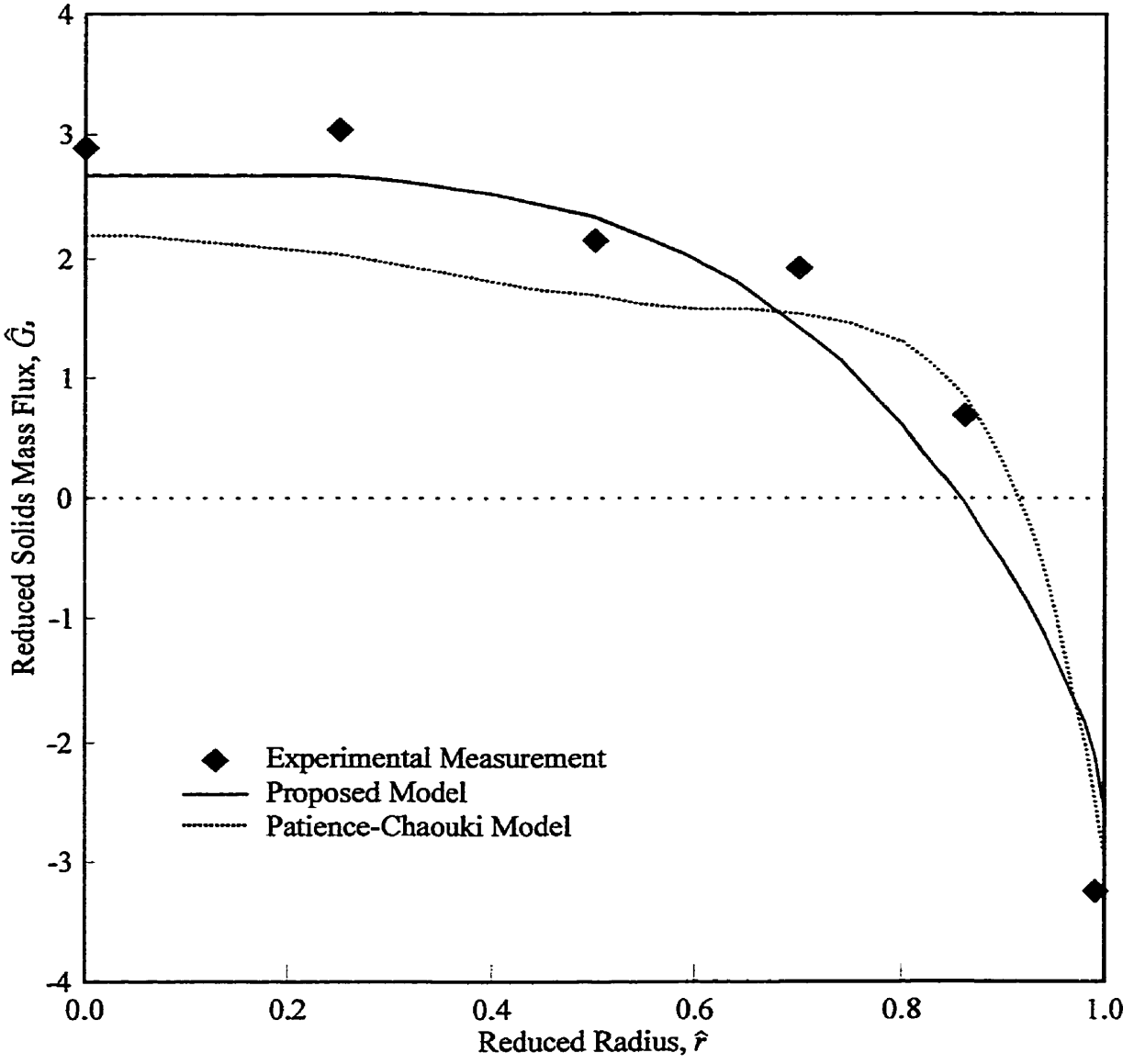

Radial Profile Parameters For The Predicted Values In Figure 19

$\hat{r}_c$=0.855	a	b	c	d	e	f
$\hat{G}$	4.81410	3.74992	-2.12911	9.20350	0.653762	6.60878
u_s	4.84781	2.11145	-1.35828	8.08240	0.929809	6.74733

the center-line mass flux and the under prediction of the magnitude of wall mass flux. The predicted core radius is fairly good. Translating the predicted curve vertically by -0.65 reduces the relative error to 7% and matches the experimental values at the center-line and wall perfectly. (The Patience-Chaouki Model exhibits a 10% relative error.)

The data in Figure 21 (Page 90) correspond to an inlet superficial gas velocity of $4\,\mathrm{m\,s^{-1}}$ and an inlet solids mass flux of $30.7\,\mathrm{kg\,m^{-2}s^{-1}}$. The LZUZI is $z_i = 0.13$ and outlet pressure is 108.3 kPa. The relative error is a only 11% due to the excellent fit of the interior points; however, the magnitude of the wall mass flux is severely under predicted. (The Patience-Chaouki Model exhibits a 15% relative error.) Typically, with all other variables held constant, the trend is for the magnitude of the wall mass flux to decrease with inlet solids mass flux. In this case, the experimental wall mass flux is anomalous because it is one and a half times greater than for the case with an inlet solids mass flux of $62.7\,\mathrm{kg\,m^{-2}s^{-1}}$ and, therefore, the point can justifiably be dismissed as flawed.

The data in Figure 22 (Page 92) mark another increase in the inlet superficial gas velocity, to $5\,\mathrm{m\,s^{-1}}$, and correspond to an inlet solids mass flux of $111.0\,\mathrm{kg\,m^{-2}s^{-1}}$. The LZUZI is $z_i = 0.45$ and outlet pressure is 104.3 kPa. The relative error is a 11%. (The Patience-Chaouki Model exhibits a 9% relative error.) As Figure 22 shows, the interior and wall mass flux predictions are excellent and exhibit relative errors of less than 3%. The overall relative error is amplified tremendously by the erroneous predictions near the core radius. Even though there isn't a singularity in the relative error at the core radius, it is hypersensitive to error near $\hat{r}_c$ because the profile gradient is very large at that location thereby making potential differences between predicted and experimental values large. Experimental error, evidenced by the violation in the mass balance calculable from the data, prohibits localizing the root of the overall error and contributes significantly to the relative error.

This case is of particular importance because riser reactors operate with an inlet

Figure 20: Reduced Radial Solids Mass Flux Profile Comparison With Experimental Data From Rhodes et al., 1992 ($z = 0.33$, $u_{gin} = 4\,\mathrm{m\,s^{-1}}$, $G_{sin} = 49.7\,\mathrm{kg\,m^{-2}s^{-1}}$, $H = 5.825\,\mathrm{m}$, $D = 0.152\,\mathrm{m}$, $\rho_p = 2456\,\mathrm{kg\,m^{-3}}$, $D_p = 74.9\,\mu\mathrm{m}$)

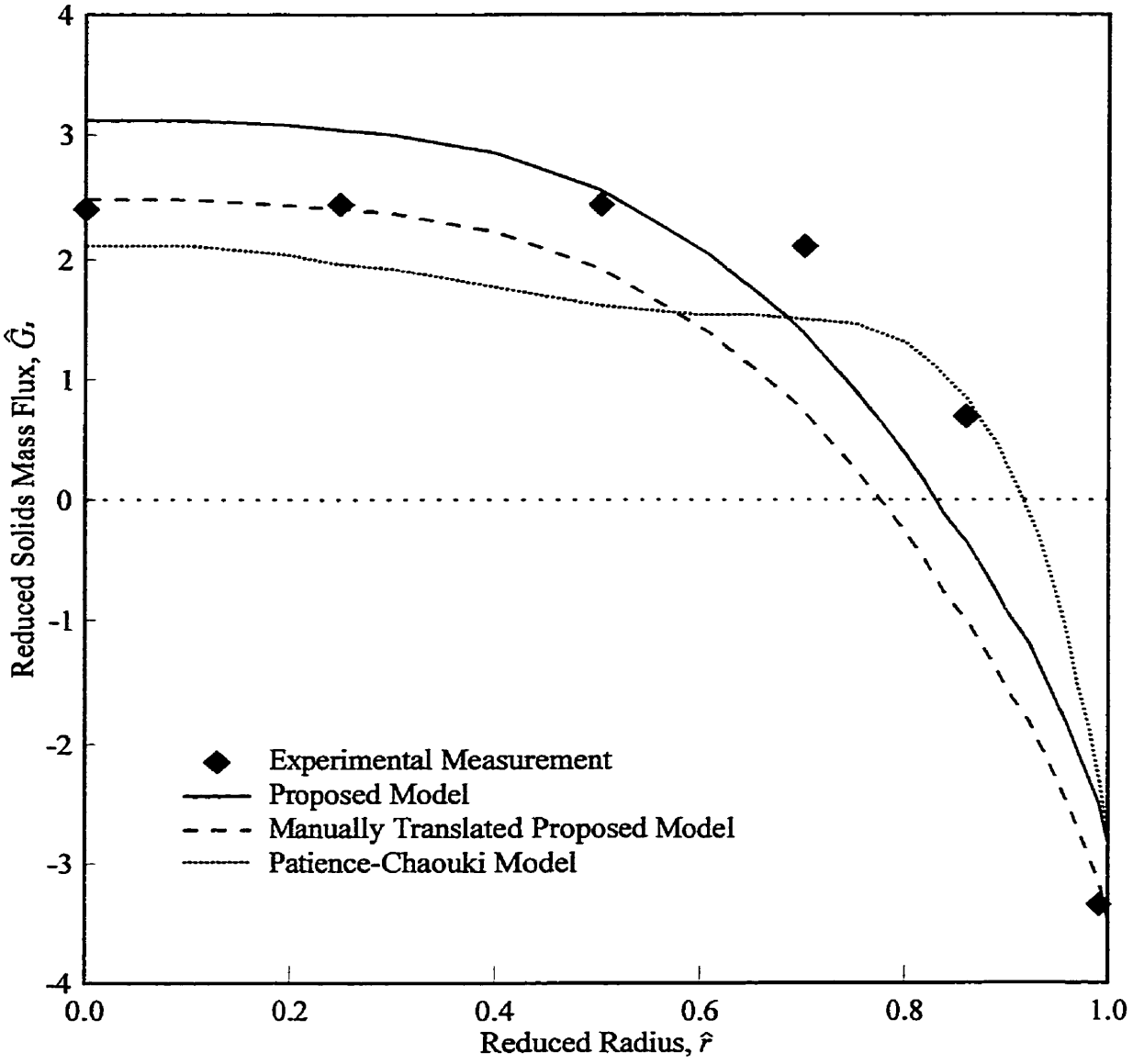

Radial Profile Parameters For The Predicted Values In Figure 20

$\hat{r}_c$=0.835	a	b	c	d	e	f
$\hat{G}$	5.73574	3.31265	-2.57825	10.5482	0.730415	7.72065
u_s	5.29141	2.11916	-1.67958	8.92451	0.966078	7.36011

Figure 21: Reduced Radial Solids Mass Flux Profile Comparison With Experimental Data From Rhodes et al., 1992 ($z = 0.33$, $u_{gin} = 4\,\mathrm{m\,s^{-1}}$, $G_{sin} = 30.7\,\mathrm{kg\,m^{-2}s^{-1}}$, $H = 5.825\,\mathrm{m}$, $D = 0.152\,\mathrm{m}$, $\rho_p = 2456\,\mathrm{kg\,m^{-3}}$, $D_p = 74.9\,\mu\mathrm{m}$)

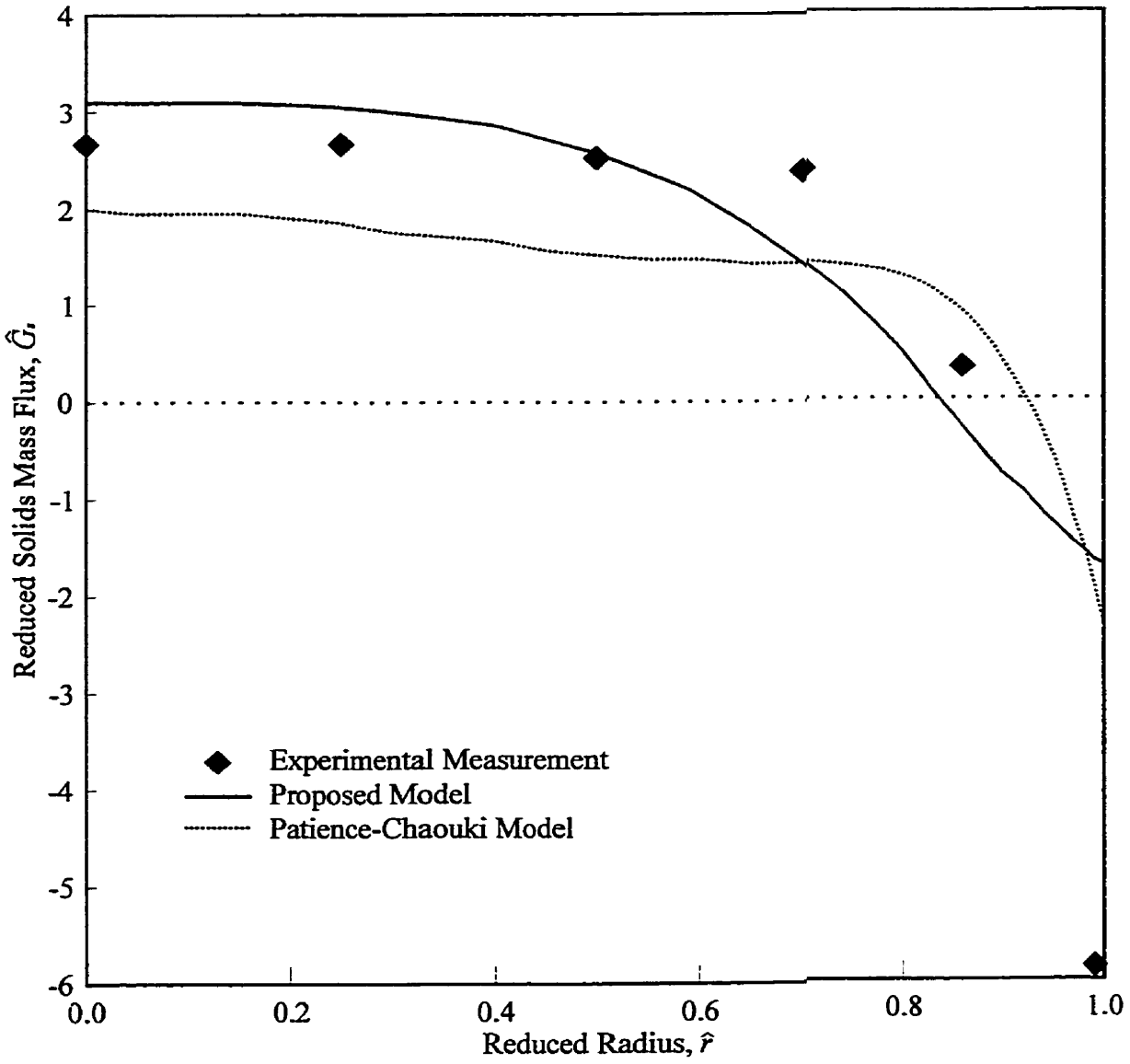

Radial Profile Parameters For The Predicted Values In Figure 21

$\hat{r}_c$=0.830	a	b	c	d	e	f
$\hat{G}$	5.74056	3.49506	-2.74286	14.6340	1.17398	12.8108
u_s	5.51306	2.16521	-1.82677	14.6598	1.44566	13.5319

solids mass flux of the same magnitude. The outstanding match of the model prediction of the mass flux profile, which directly affects voidage and reaction rates, bolsters confidence in the model's application to riser reactor simulations.

The data in Figure 23 (Page 93) correspond to an inlet superficial gas velocity of $5\,\mathrm{m\,s^{-1}}$ and an inlet solids mass flux of $94.4\,\mathrm{kg\,m^{-2}s^{-1}}$. The LZUZI is $z_i = 0.41$ and outlet pressure is 105.1 kPa. The relative error is 12%, which is, once again, amplified by the errors near the core radius. (The Patience-Chaouki Model exhibits an 8% relative error.) Discounting the experimental points at $\hat{r} = 0.87$ and $\hat{r} = 0.93$, the overall relative error decreases to 9%. Although the center-line mass flux is under predicted, it is acceptable. The wall mass flux prediction is very good. The predicted core radius is unsatisfactory considering its impact on the overall scheme. It is predicted by the parabolic function, which is better than the prediction by Equation 12 at the sampling location.

The data in Figure 24 (Page 94) correspond to an inlet superficial gas velocity of $5\,\mathrm{m\,s^{-1}}$ and an inlet solids mass flux of $47.8\,\mathrm{kg\,m^{-2}s^{-1}}$. The LZUZI is $z_i = 0.18$ and outlet pressure is 107.7 kPa. The model over predicts the mass flux in the core, which results in a 15% relative error. (The Patience-Chaouki Model exhibits a 14% relative error.) The relative error between the predicted and measured wall mass flux is just 4%. Equation 12 defines the predicted core radius in this case because the core radius function intersection is at $z = 0.19$, which is less than the sampling location.

The data in Figure 25 (Page 96) correspond to an inlet superficial gas velocity of $5\,\mathrm{m\,s^{-1}}$ and an inlet solids mass flux of $36.3\,\mathrm{kg\,m^{-2}s^{-1}}$. The LZUZI is $z_i = 0.41$ and outlet pressure is 108.7 kPa. The model under predicts the mass flux in the core resulting in a relative error of 7% in that region; the overall relative error is 20% due to the severe under prediction of the magnitude of the wall mass flux. (The Patience-Chaouki Model exhibits a 15% relative error.) The predicted core radius, calculated with the parabolic function, is in error by approximately 7%. This is the first case in which a catastrophic loss of precision occurs below the sampling location.

Figure 22: Reduced Radial Solids Mass Flux Profile Comparison With Experimental Data From Rhodes et al., 1992 ($z = 0.33$, $u_{gin} = 5\,\mathrm{m\,s^{-1}}$, $G_{sin} = 111\,\mathrm{kg\,m^{-2}s^{-1}}$, $H = 5.825\,\mathrm{m}$, $D = 0.152\,\mathrm{m}$, $\rho_p = 2456\,\mathrm{kg\,m^{-3}}$, $D_p = 74.9\,\mu\mathrm{m}$)

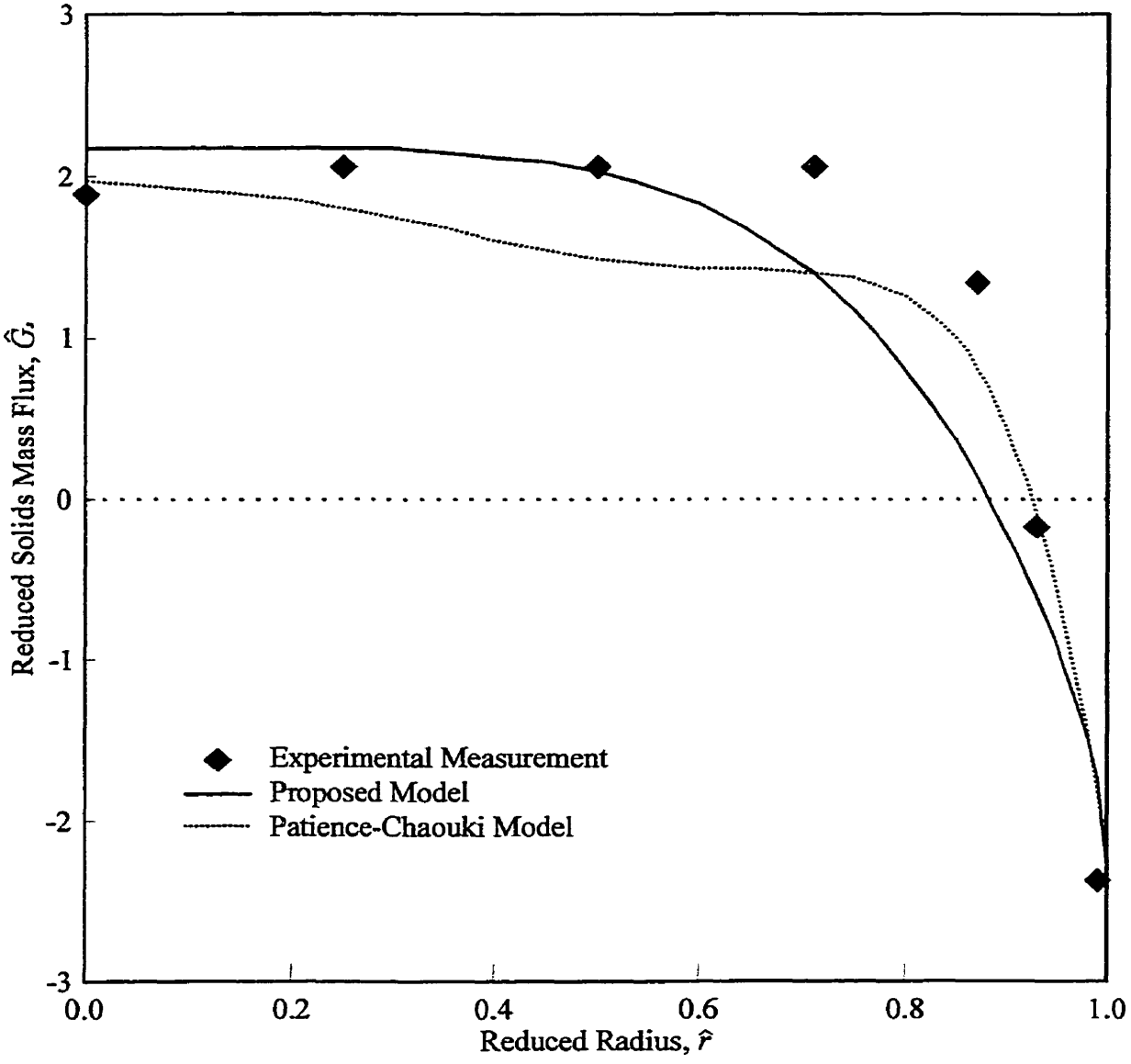

Radial Profile Parameters For The Predicted Values In Figure 22

$\hat{r}_c$=0.883	a	b	c	d	e	f
$\hat{G}$	3.88127	4.65169	-1.70091	8.04293	0.584581	5.75306
u_s	5.57127	2.15687	-1.30715	9.46704	0.913852	8.13875

Figure 23: Reduced Radial Solids Mass Flux Profile Comparison With Experimental Data From Rhodes et al., 1992 ($z = 0.33$, $u_{gin} = 5\,\mathrm{m\,s^{-1}}$, $G_{sin} = 94.4\,\mathrm{kg\,m^{-2}s^{-1}}$, $H = 5.825\,\mathrm{m}$, $D = 0.152\,\mathrm{m}$, $\rho_p = 2456\,\mathrm{kg\,m^{-3}}$, $D_p = 74.9\,\mu\mathrm{m}$)

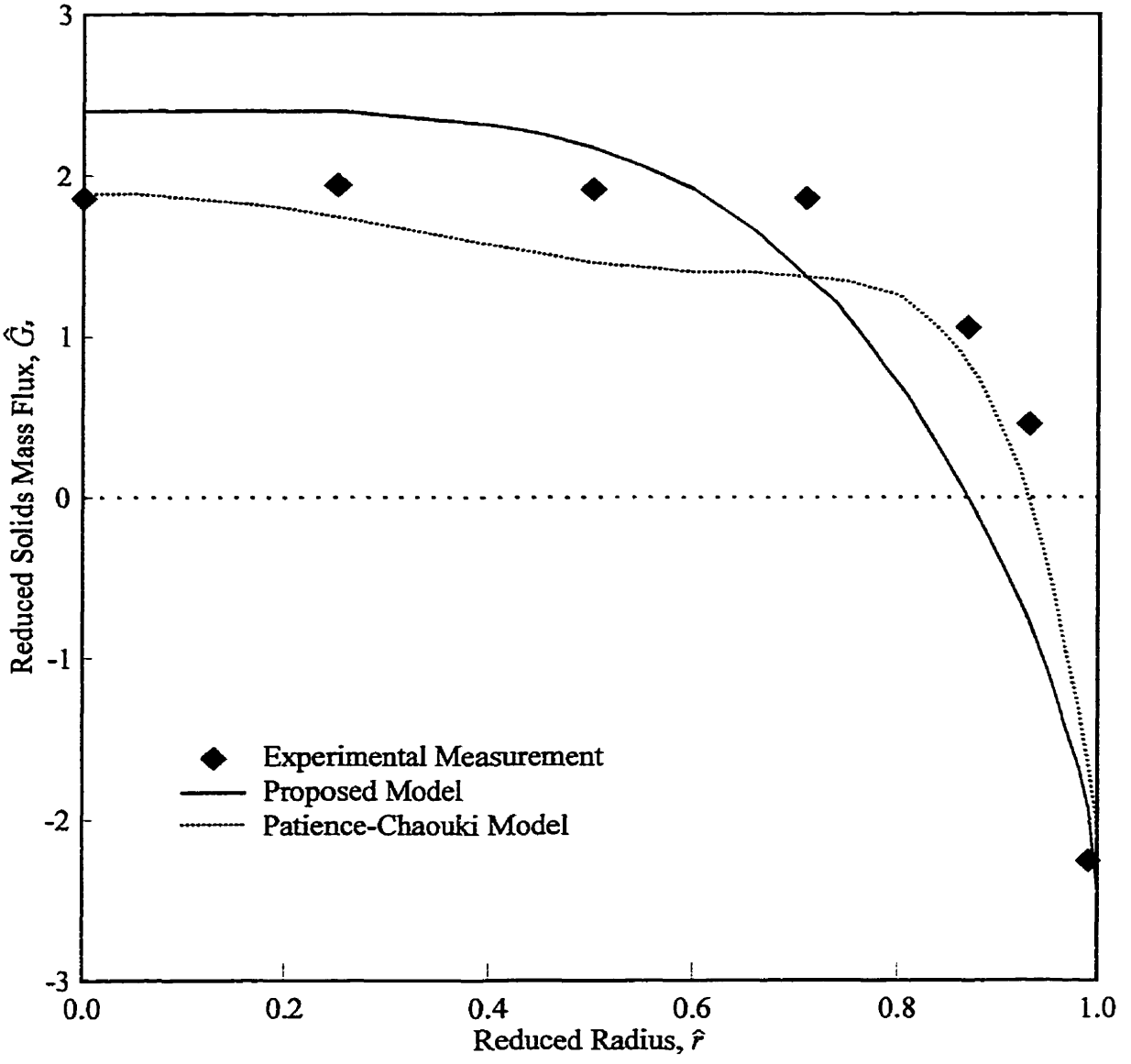

Radial Profile Parameters For The Predicted Values In Figure 23

$\hat{r}_c$=0.870	a	b	c	d	e	f
$\hat{G}$	4.31976	4.21898	-1.91862	8.64393	0.618941	6.19953
u_s	5.90840	2.13688	-1.52014	10.0452	0.929896	8.53922

Figure 24: Reduced Radial Solids Mass Flux Profile Comparison With Experimental Data From Rhodes et al., 1992 ($z = 0.33$, $u_{gin} = 5\,\mathrm{m\,s^{-1}}$, $G_{sin} = 47.8\,\mathrm{kg\,m^{-2}s^{-1}}$, $H = 5.825\,\mathrm{m}$, $D = 0.152\,\mathrm{m}$, $\rho_p = 2456\,\mathrm{kg\,m^{-3}}$, $D_p = 74.9\,\mu\mathrm{m}$)

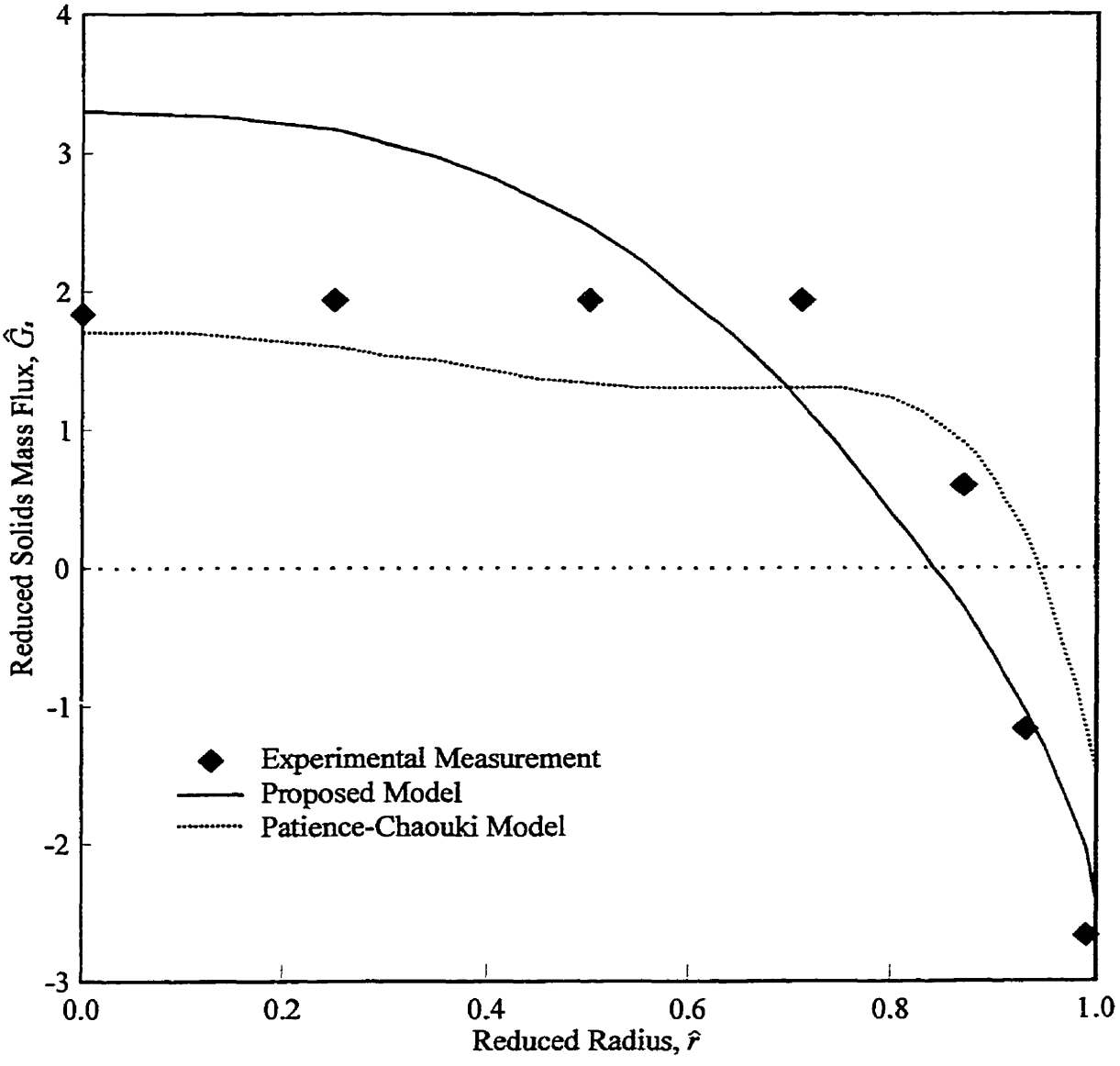

Radial Profile Parameters For The Predicted Values In Figure 24

$\hat{r}_c$=0.838	a	b	c	d	e	f
$\hat{G}$	5.18203	2.61634	-1.91358	8.34243	0.67083	5.88699
u_s	6.40302	1.72049	-1.67410	8.64746	0.84339	6.78926

Consequently, as evident in Figure 25, the model invokes the contingency measure of plug flow in the core and annular regions. The assumption is not bad in the core but, for this case, is not good in the annulus even if the wall mass flux is adequately predicted.

The data in Figure 26 (Page 97) stems from the larger of the two columns Rhodes et al. (1992) describe and correspond to an inlet superficial gas velocity of $4\,\mathrm{m\,s^{-1}}$ and an inlet solids mass flux of $60.0\,\mathrm{kg\,m^{-2}s^{-1}}$. The LZUZI is $z_i = 0.14$ and outlet pressure is 106.7 kPa. Even though the model predicts the center-line mass flux with a relative error of a meagre 0.5% and the wall mass flux with a phenomenal 0.02% relative error, the overall relative error is 11% because of the poor prediction of the core radius. Manually setting the core radius to 0.95 reduces the relative error to 7%, which is show in Figure 26. (The Patience-Chaouki Model exhibits a 38% relative error.)

Several trends are apparent in the comparisons in this Subsection:

- In every single case, at the axial sampling location of interest, the predicted core radius calculated by the parabolic function is more accurate than the predicted core radius calculated by Equation 12. This occurrence indicates that restricting the application of Equation 12 to the upper zone, as the model presented in this dissertation does, is sound.

- The model tends to under predict the magnitude of the wall mass flux with risers operating at a relatively low inlet solids mass flux.

Figure 25: Reduced Radial Solids Mass Flux Profile Comparison With Experimental Data From Rhodes et al., 1992 ($z = 0.33$, $u_{gin} = 5\,\mathrm{m\,s^{-1}}$, $G_{sin} = 36.3\,\mathrm{kg\,m^{-2}s^{-1}}$, $H = 5.825\,\mathrm{m}$, $D = 0.152\,\mathrm{m}$, $\rho_p = 2456\,\mathrm{kg\,m^{-3}}$, $D_p = 74.9\,\mu\mathrm{m}$)

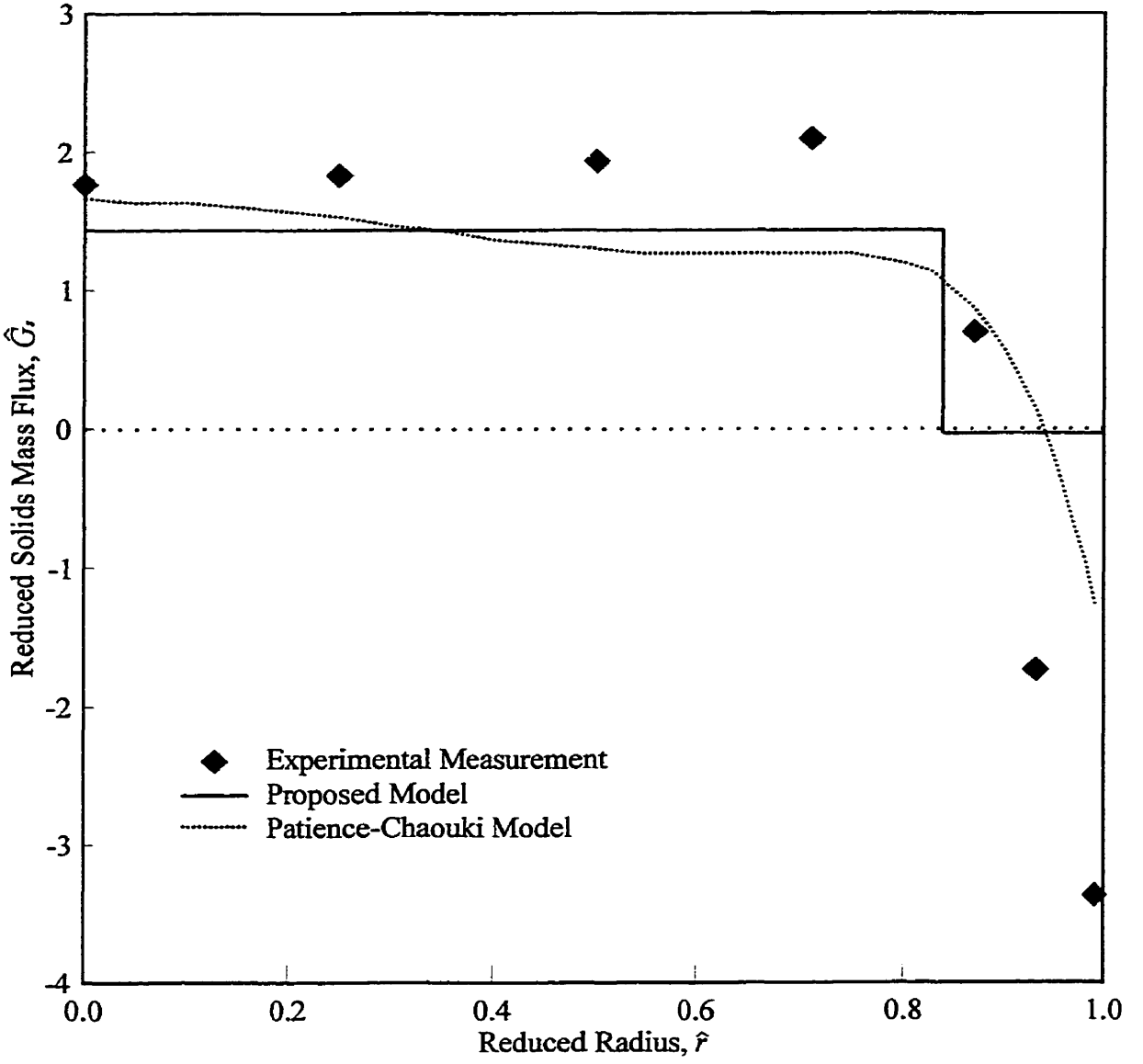

Radial Profile Parameters For The Predicted Values In Figure 25

$\hat{r}_c$=0.838	a	b	c	d	e	f
$\hat{G}$	0.0000	0.0000	1.43259	0.0000	0.0000	-0.024267
u_s	0.0000	0.0000	4.68939	0.0000	0.0000	-0.019341

Figure 26: Reduced Radial Solids Mass Flux Profile Comparison With Experimental Data From Rhodes et al., 1992 ($z = 0.40$, $u_{gin} = 4\,\mathrm{m\,s^{-1}}$, $G_{sin} = 60\,\mathrm{kg\,m^{-2}s^{-1}}$, $H = 6.6\,\mathrm{m}$, $D = 0.305\,\mathrm{m}$, $\rho_p = 2456\,\mathrm{kg\,m^{-3}}$, $D_p = 74.9\,\mu\mathrm{m}$)

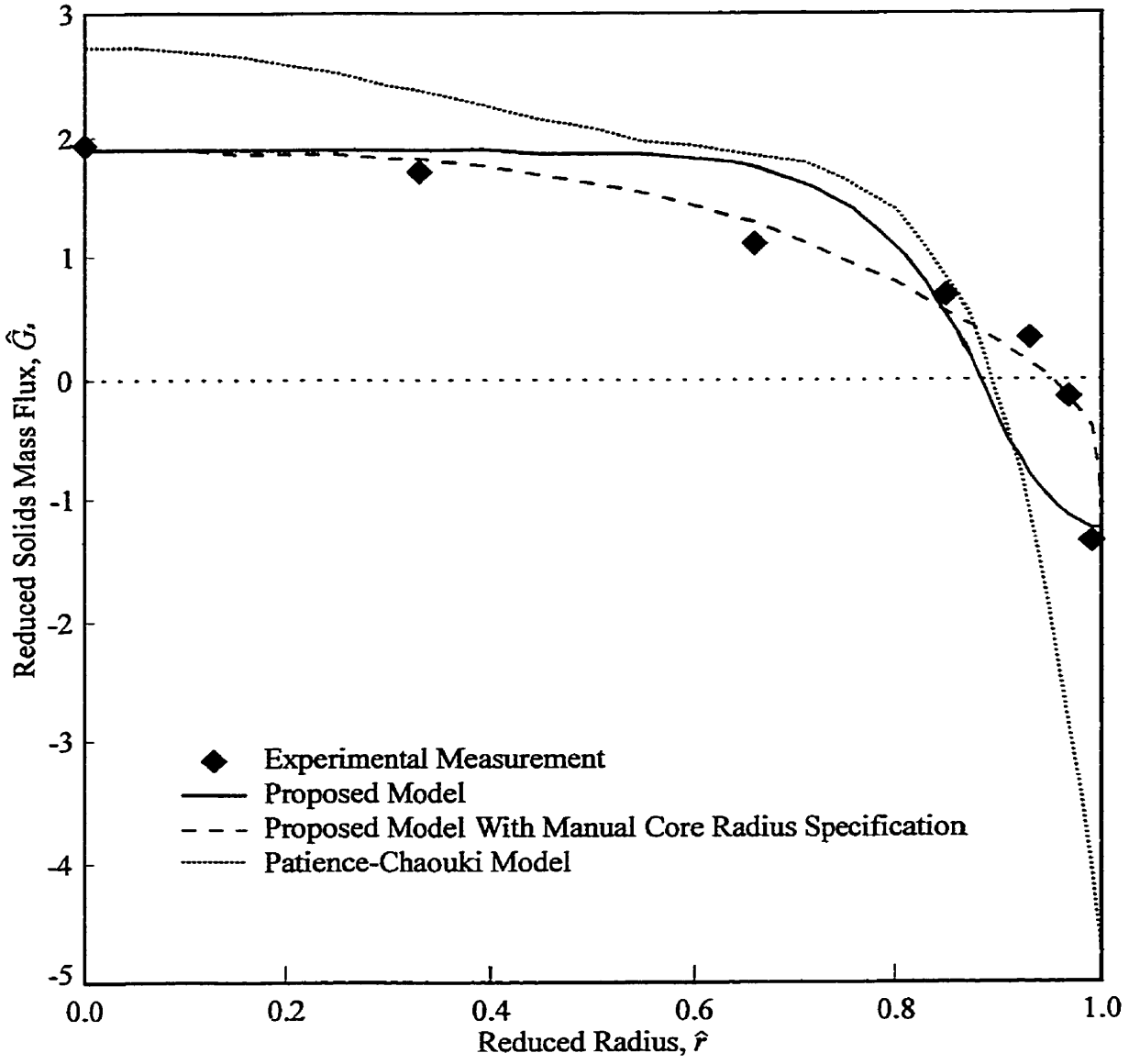

Radial Profile Parameters For The Predicted Values In Figure 26

$\hat{r}_c$=0.880	a	b	c	d	e	f
$\hat{G}$	5.89576	9.08662	-4.03302	60.5040	1.82065	59.2472
u_s	5.77554	3.38517	-2.01564	164.804	2.59143	164.140

5.1.2 Miller And Gidaspow, 1992

Miller and Gidaspow (1992) performed experiments in a 6.58 m tall, 0.075 m diameter acrylic riser with FCC catalyst ($D_p = 75\,\mu$m, $\rho_p = 1500\,\mathrm{kg\,m^{-3}}$) using air as the fluidizing agent. An X-ray densitometer was used to obtain the radial voidage profiles and a non-isokinetic sampling probe was used to measure the local solids mass flux. They used the two measured profiles to calculate the radial solids velocity profile directly by algebraically manipulating Equation 44. This Subsection presents comparisons between the model presented in this dissertation and experimental data the researchers obtained at three axial locations in the column while operating it with an invariant inlet solids mass flux of $32.8\,\mathrm{kg\,m^{-2}s^{-1}}$ and superficial gas velocity of $2.89\,\mathrm{m\,s^{-1}}$. The inlet pressure at the base of the riser is 118.6 kPa.

The specified operating conditions result in a outlet pressure of 115.0 kPa and LZUZI of $z_i = 0.5$ for Figures 27 through 29, which correspond to axial sampling locations of $z = [0.28, 0.64, 0.84]$, respectively.

The data in Figure 27 (Page 99) correspond to an axial location of 1.86 m ($z = 0.28$) and shows that Miller and Gidaspow (1992) traversed the entire radial domain with the sampling probe. As a result, it is apparent that the solids distribution in the riser is not symmetric about the axis. The relative error at the center-line approaches 20%, is 50% at $\hat{r} = -0.92$, and is 3% at $\hat{r} = 0.78$. The huge range of data, varying from -6.65 to 4.85, has the tendency to dampen the overall relative error to 15%. (The Patience-Chaouki Model exhibits a 19% relative error.)

The massive discrepancy between the model and experimental data at $\hat{r} = -1$ is probably due to non-uniform distribution of the solids at the base of the riser. Both air and particles enter the riser from a U-tube and, with the inlet solids mass flux so relatively low, centrifugal force may play a part in causing the solids to preferentially ascend near the wall farthest from the centroid of the U-tube and descend near the wall closest to the centroid.

The data in Figure 28 (Page 101) correspond to an axial location of 4.18 m ($z =$

Figure 27: Reduced Radial Solids Mass Flux Profile Comparison With Experimental Data From Miller And Gidaspow, 1992 ($z = 0.28$, $u_{gin} = 2.89\,\mathrm{m\,s^{-1}}$, $G_{sin} = 32.8\,\mathrm{kg\,m^{-2}s^{-1}}$, $H = 6.58\,\mathrm{m}$, $D = 0.075\,\mathrm{m}$, $\rho_p = 1500\,\mathrm{kg\,m^{-3}}$, $D_p = 75\,\mu\mathrm{m}$)

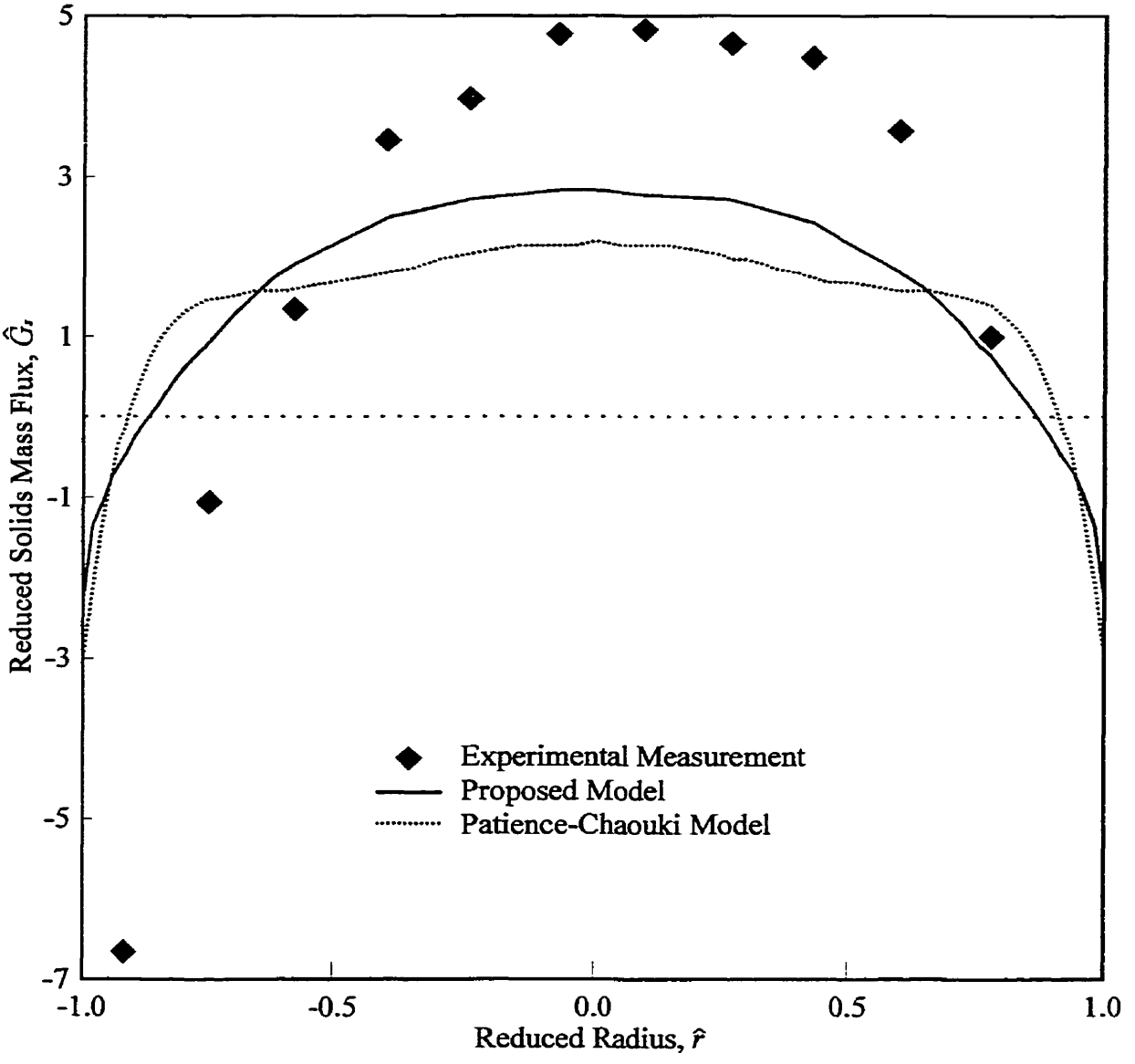

Radial Profile Parameters For The Predicted Values In Figure 27

$\hat{r}_c$=0.866	a	b	c	d	e	f
$\hat{G}$	4.08947	2.77994	-1.34340	6.43999	0.512286	4.14475
u_s	2.92634	1.76003	-0.65216	3.54584	0.669378	2.62483

0.64). The symmetry about the riser axis is much greater at $z = 0.64$ than $z = 0.28$ and, consequently, the model prediction is much better. The relative error is 8% and the goodness of fit is excellent. (The Patience-Chaouki Model exhibits a 17% relative error.) There is some skewing in the core, which significantly contributes to the relative error. The experimental error between the magnitude of the predicted mass flux at the wall and the measured mass flux at the point closest to the wall is only 3%.

The data in Figure 29 (Page 102) correspond to an axial location of 5.52 m ($z = 0.84$). The profile at $z = 0.84$ shows remarkably little difference from the profile at $z = 0.64$. The similarity of the profiles could be due to any number of exit effects. One of the premises of the model presented in this dissertation is that there is variation in all radial profiles with height. Hence, since the predicted profile at $z = 0.64$ is excellent, the prediction at this location is poor. However, near the wall, at both $\hat{r} = -1$ and $\hat{r} = 1$, the predictions are good; near the center-line they are not. The relative error is 17%. (The Patience-Chaouki Model exhibits a 19% relative error.)

Figure 28: Reduced Radial Solids Mass Flux Profile Comparison With Experimental Data From Miller And Gidaspow, 1992 ($z = 0.64$, $u_{gin} = 2.89\,\mathrm{m\,s^{-1}}$, $G_{sin} = 32.8\,\mathrm{kg\,m^{-2}s^{-1}}$, $H = 6.58\,\mathrm{m}$, $D = 0.075\,\mathrm{m}$, $\rho_p = 1500\,\mathrm{kg\,m^{-3}}$, $D_p = 75\,\mu\mathrm{m}$)

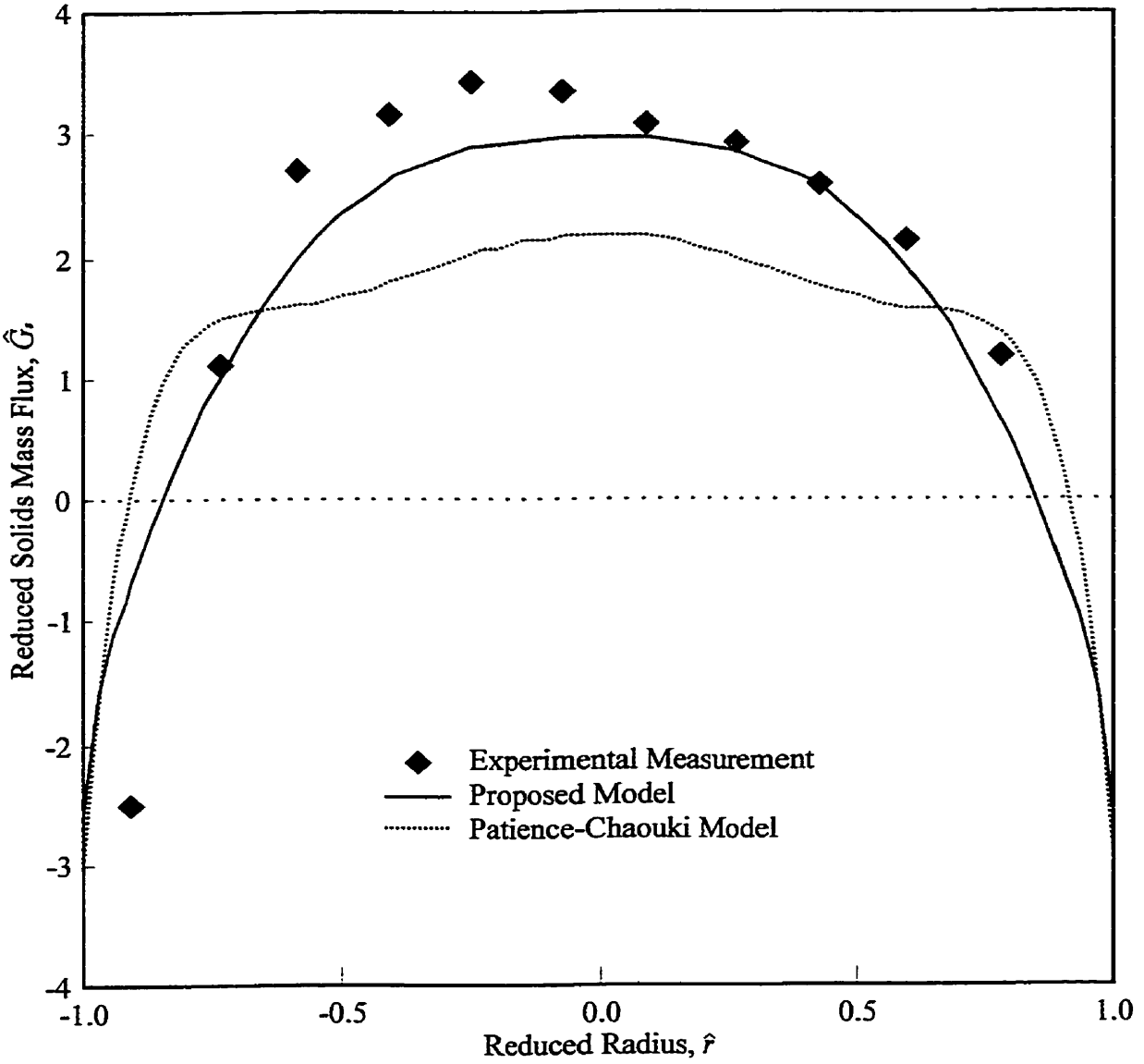

Radial Profile Parameters For The Predicted Values In Figure 28

$\hat{r}_c$=0.849	a	b	c	d	e	f
$\hat{G}$	4.82117	2.96732	-1.85109	8.11695	0.603504	5.52725
u_s	3.59314	1.77572	-0.90424	4.85906	0.814818	3.81988

Figure 29: Reduced Radial Solids Mass Flux Profile Comparison With Experimental Data From Miller And Gidaspow, 1992 ($z = 0.84$, $u_{gin} = 2.89\,\mathrm{m\,s^{-1}}$, $G_{sin} = 32.8\,\mathrm{kg\,m^{-2}s^{-1}}$, $H = 6.58\,\mathrm{m}$, $D = 0.075\,\mathrm{m}$, $\rho_p = 1500\,\mathrm{kg\,m^{-3}}$, $D_p = 75\,\mu\mathrm{m}$)

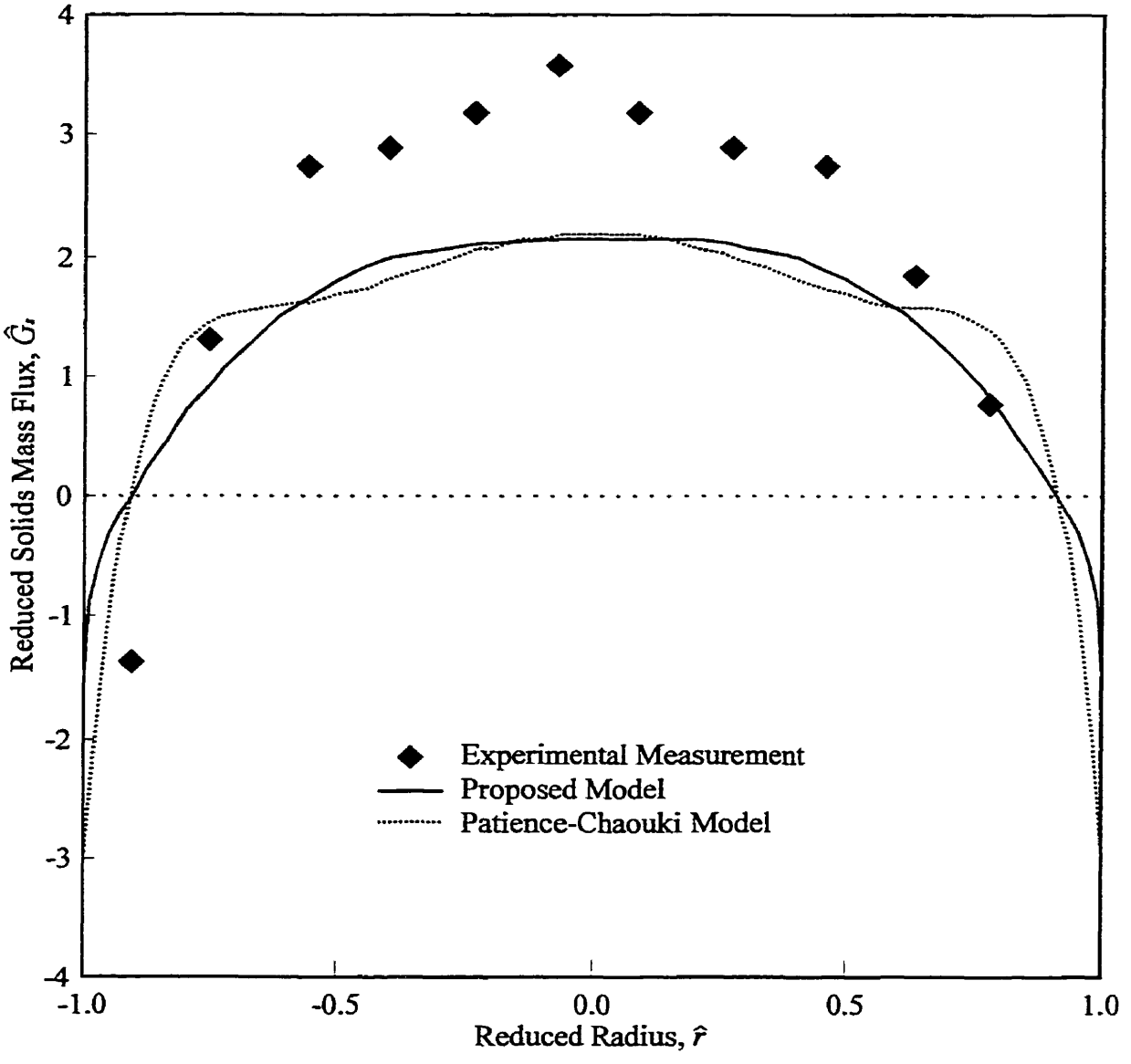

Radial Profile Parameters For The Predicted Values In Figure 29

$\hat{r}_c$=0.912	a	b	c	d	e	f
$\hat{G}$	2.82921	3.04093	-0.688149	4.13714	0.416617	2.63719
u_s	3.07801	1.33615	-0.354756	2.47280	0.580240	1.87092

5.1.3 Motte et al., 1996

Motte et al. (1996) measured solids mass flux profiles in a 10 m tall, 0.144 m diameter riser with an iron base powder ($D_p = 80\,\mu$m, $\rho_p = 5200\,\mathrm{kg\,m^{-3}}$) using air as the fluidizing agent. Two profiles, measured with a non-isokinetic sampling probe at heights of 4.55 m and 6.30 m, were obtained with the riser operating at a fixed inlet superficial gas velocity and solids mass flux of $5.3\,\mathrm{m\,s^{-1}}$ and $52.9\,\mathrm{kg\,m^{-2}s^{-1}}$ respectively. The researchers do not state the exact inlet pressure to the riser; the simulation specifies an inlet pressure of 110.0 kPa.

The specified operating conditions result in a outlet pressure of 105.4 kPa and LZUZI of $z_i = 0.21$ for both Figures 31 and 30. The data in Figure 30 (Page 104), representing the higher of the two axial sampling locations ($z = 0.63$), yield a relative error of a mere 6%. (The Patience-Chaouki Model exhibits a 23% relative error.) However, the data in Figure 31 (Page 105), representing the lower of the two axial sampling locations ($z = 0.46$), yield a relative error of 19% due to the large over prediction of the magnitude of both the center-line and wall mass fluxes. (The Patience-Chaouki Model exhibits a 23% relative error.) The shape of the predicted curve in Figure 31 is good if the entire curve is scaled down by 70%, which results in a relative error of 4%.

The reason for the large discrepancy between the two relative errors is that the experimental data shows very little variation with axial position. So, as was the case with the second and third comparisons in Subsection 5.1.2, outstanding prediction of the solids mass flux profile at one height results in a poor prediction at another height. This phenomenon suggests that further refinement of the axial profiles at the center-line and wall and/or the core radius functions in the model presented in this dissertation might be required.

Figure 30: Reduced Radial Solids Mass Flux Profile Comparison With Experimental Data From Motte et al., 1996 ($z = 0.63$, $u_{gin} = 5.3\,\mathrm{m\,s^{-1}}$, $G_{sin} = 52.9\,\mathrm{kg\,m^{-2}s^{-1}}$, $H = 10\,\mathrm{m}$, $D = 0.144\,\mathrm{m}$, $\rho_p = 5200\,\mathrm{kg\,m^{-3}}$, $D_p = 80\,\mu\mathrm{m}$)

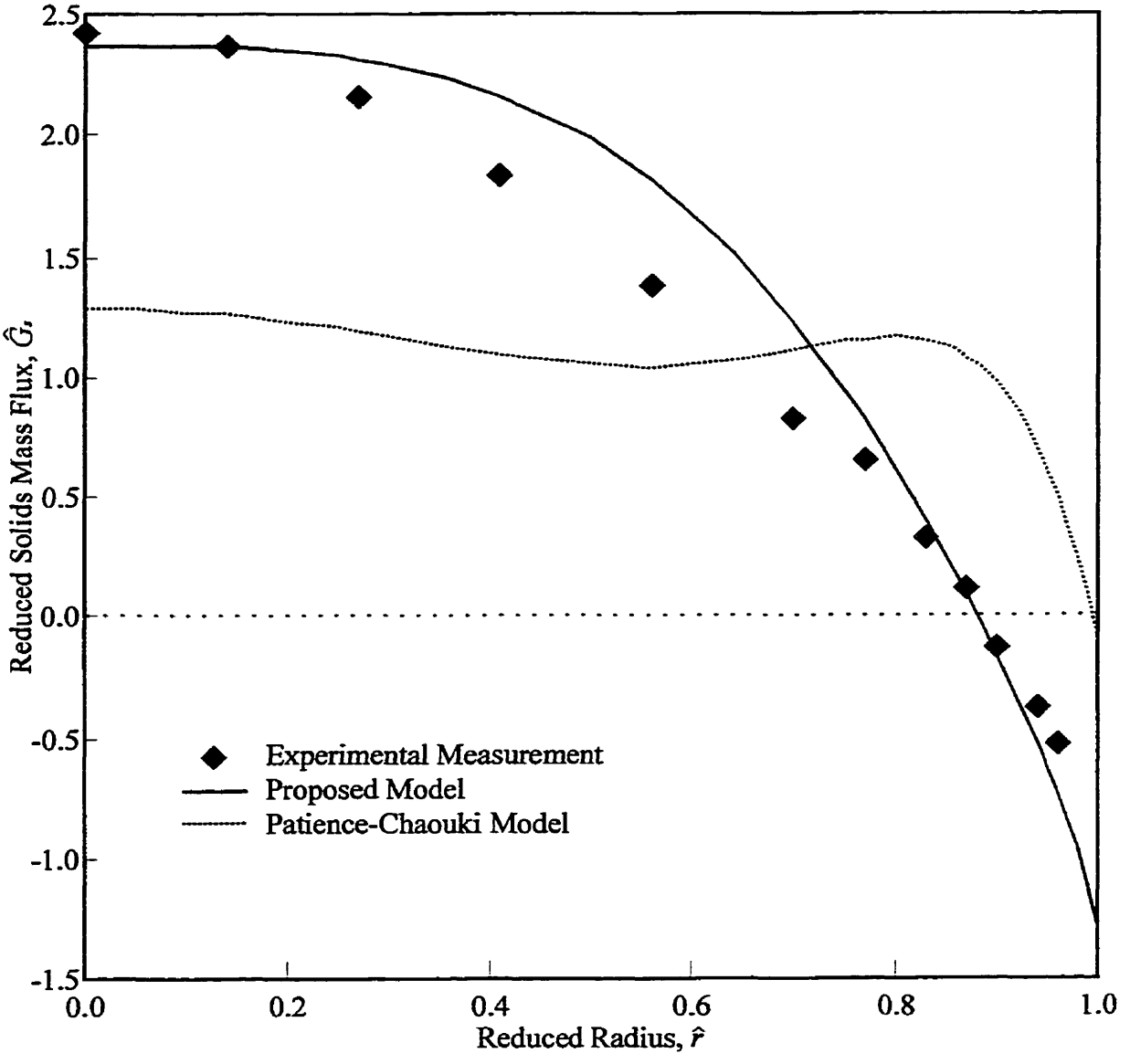

Radial Profile Parameters For The Predicted Values In Figure 30

$\hat{r}_c$=0.881	a	b	c	d	e	f
$\hat{G}$	3.53419	3.14816	-1.15834	6.79980	0.779192	5.50921
u_s	5.88591	1.53789	-1.03794	8.41699	0.995691	7.41023

Figure 31: Reduced Radial Solids Mass Flux Profile Comparison With Experimental Data From Motte et al., 1996 ($z = 0.46$, $u_{gin} = 5.3\,\mathrm{m\,s^{-1}}$, $G_{sin} = 52.9\,\mathrm{kg\,m^{-2}s^{-1}}$, $H = 10\,\mathrm{m}$, $D = 0.144\,\mathrm{m}$, $\rho_p = 5200\,\mathrm{kg\,m^{-3}}$, $D_p = 80\,\mu\mathrm{m}$)

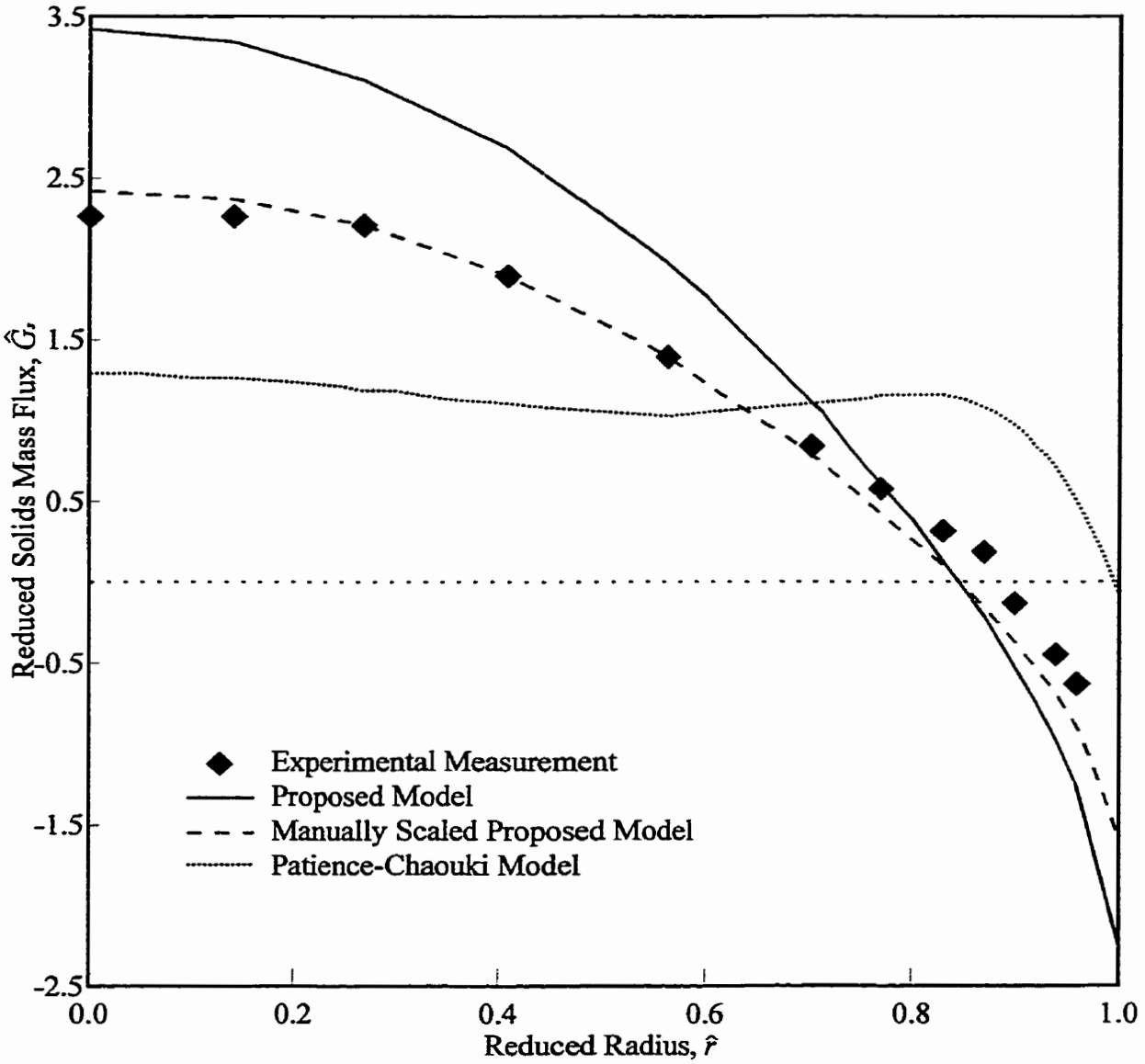

Radial Profile Parameters For The Predicted Values In Figure 31

$\hat{r}_c$=0.843	a	b	c	d	e	f
$\hat{G}$	4.89519	2.10315	-1.47021	6.75392	0.586119	4.47919
u_s	6.14973	1.41445	-1.31316	6.67542	0.713592	4.90097

The following table gives a qualitative assessment of the goodness of fit, based on the relative error between experimental data and the predictions of the proposed model, for the comparisons presented in this Subsection.

Table 10: Qualitative Assessment Of The Comparisons Between Experimental Radial Solids Mass Flux Profiles And Predictions By The Proposed LDCFB Model

	Relative Error	Number Of Cases
Very Good	<10%	5
Good	10–15%	7
Satisfactory	15–18%	2
Poor	>18%	2

Based on the distribution of the qualitative goodness of fit for the comparisons presented in this Subsection, the model is successful, especially considering that Equation 12 is only accurate within ±20% and has such profound effects on the radial predictions.

5.2 Radial Solids Velocity Profiles

In the model presented in this dissertation, the radial solids velocity profiles are also a function of axial position, as Figure 32 (Page 108) illustrates.

5.2.1 Miller And Gidaspow, 1992

As mentioned in the previous Section, Miller and Gidaspow (1992) indirectly measured radial solids velocity profiles by measuring solid mass flux and voidage profiles. Figures 33 through 35 are directly associated with Figures 27 through 29, respectively. Obviously, the experimental conditions are identical for the two sets of figures.

The profile in Figure 33 (Page 109), which corresponds to Figure 27, occurs at $z = 0.28$. The overall relative error is 15% and is largely attributable to the skewing in the measured profile. (The Patience-Chaouki Model exhibits a 58% relative error.) The range of the predicted profile is fairly accurate but the shape of the profile would be better if it was flatter.

The profile in Figure 34 (Page 110), which corresponds to Figure 28, occurs at $z = 0.64$. The solids velocity predictions in $|\hat{r}| > 0.6$ are outstanding but are totally unsatisfactory in $-0.6 < \hat{r} < 0.6$. The average relative error in the domains $|\hat{r}| > 0.5$ is 7%; it is 44% in $-0.5 < \hat{r} < 0.5$. The overall relative error is 31%. (The Patience-Chaouki Model exhibits a 11% relative error.) The enormous acceleration of solids in the core between the first two sampling locations in the riser is difficult to explain, particularly after examining Figure 35.

The profile in Figure 35 (Page 112), which corresponds to Figure 29, occurs at $z = 0.84$ and has an overall relative error of 19%. (The Patience-Chaouki Model exhibits a 36% relative error.) The velocity in the core at this axial location is half of the velocity at the previous location, which is very bizarre because the riser has a smooth exit geometry. Miller and Gidaspow (1992) calculate the velocity profile from the mass flux and voidage profiles but do not report the voidage profile at $z = 0.64$; therefore, detailed analysis into the seemingly anomalous behavior cannot

Figure 32: Predicted Radial Solids Velocity Profile Pseudo-Animation

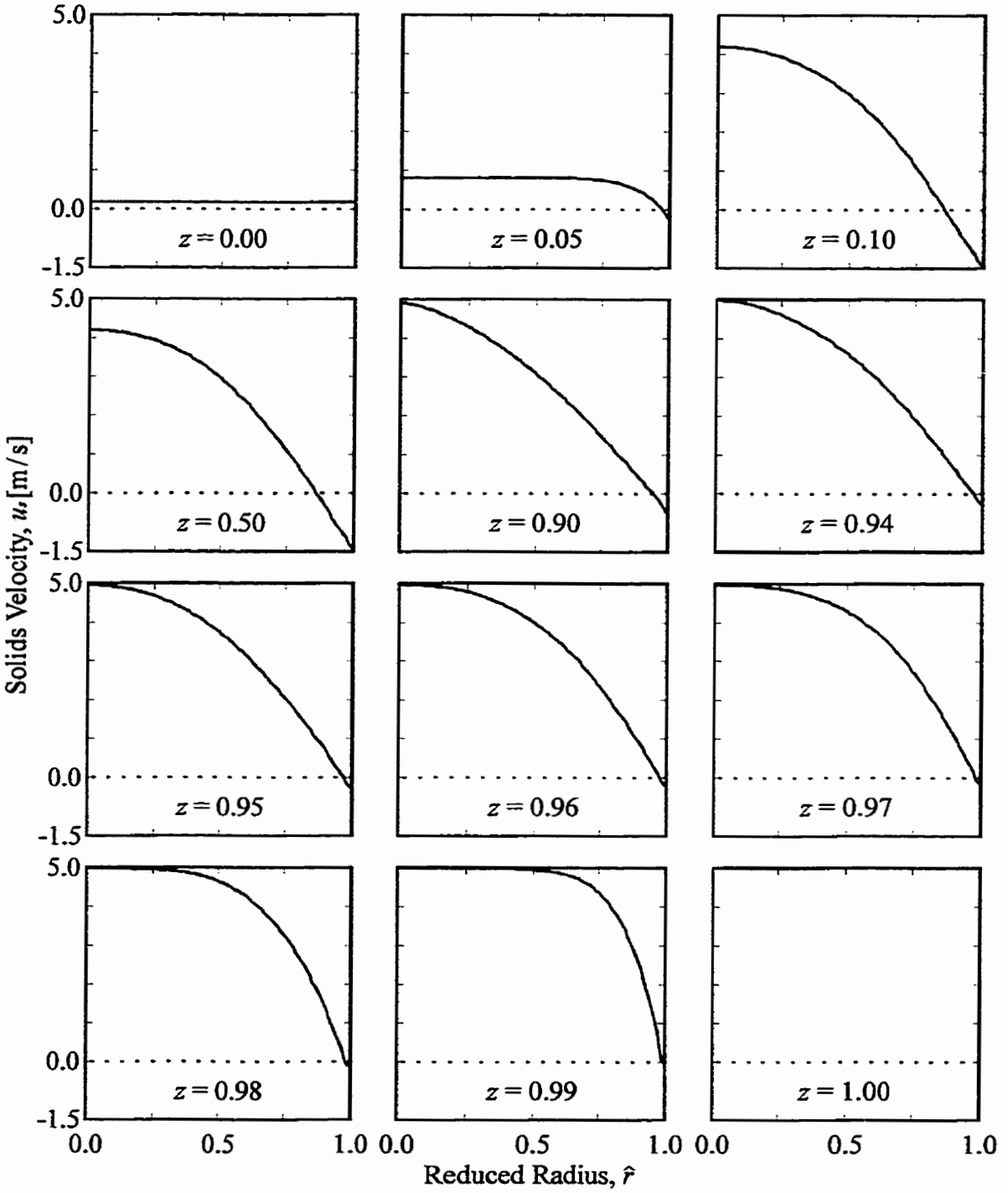

Figure 33: Radial Solids Velocity Profile Comparison With Experimental Data From Miller And Gidaspow, 1992 ($z = 0.28$, $u_{gin} = 2.89\,\mathrm{m\,s^{-1}}$, $G_{sin} = 32.8\,\mathrm{kg\,m^{-2}s^{-1}}$, $H = 6.58\,\mathrm{m}$, $D = 0.075\,\mathrm{m}$, $\rho_p = 1500\,\mathrm{kg\,m^{-3}}$, $D_p = 75\,\mu\mathrm{m}$)

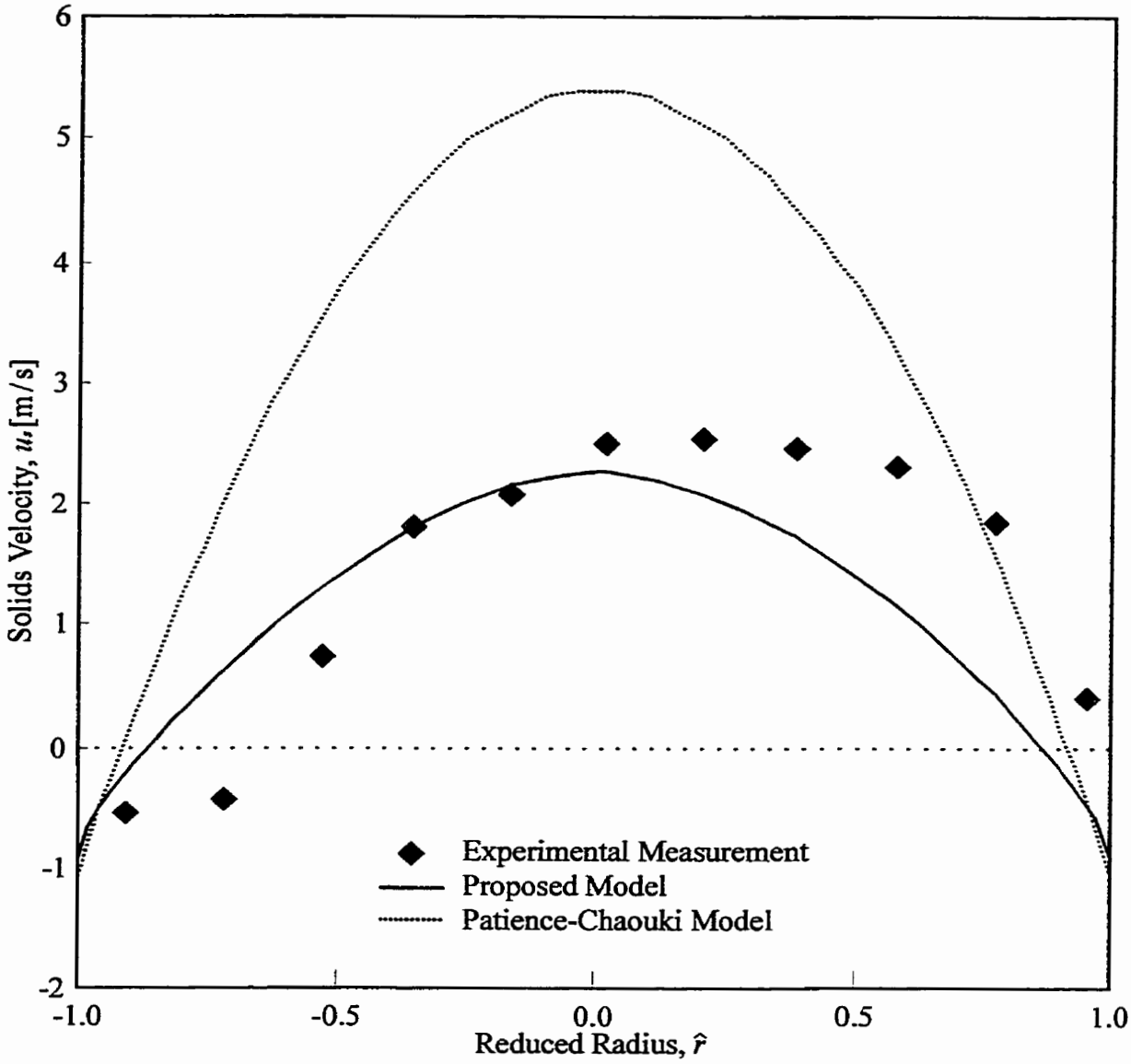

Radial Profile Parameters For The Predicted Values In Figure 33

$\hat{r}_c$=0.866	a	b	c	d	e	f
$\hat{G}$	4.08947	2.77994	-1.34340	6.43999	0.512286	4.14475
u_s	2.92634	1.76003	-0.65216	3.54584	0.669378	2.62483

Figure 34: Radial Solids Velocity Profile Comparison With Experimental Data From Miller And Gidaspow, 1992 ($z = 0.64$, $u_{gin} = 2.89\,\mathrm{m\,s^{-1}}$, $G_{sin} = 32.8\,\mathrm{kg\,m^{-2}s^{-1}}$, $H = 6.58\,\mathrm{m}$, $D = 0.075\,\mathrm{m}$, $\rho_p = 1500\,\mathrm{kg\,m^{-3}}$, $D_p = 75\,\mu\mathrm{m}$)

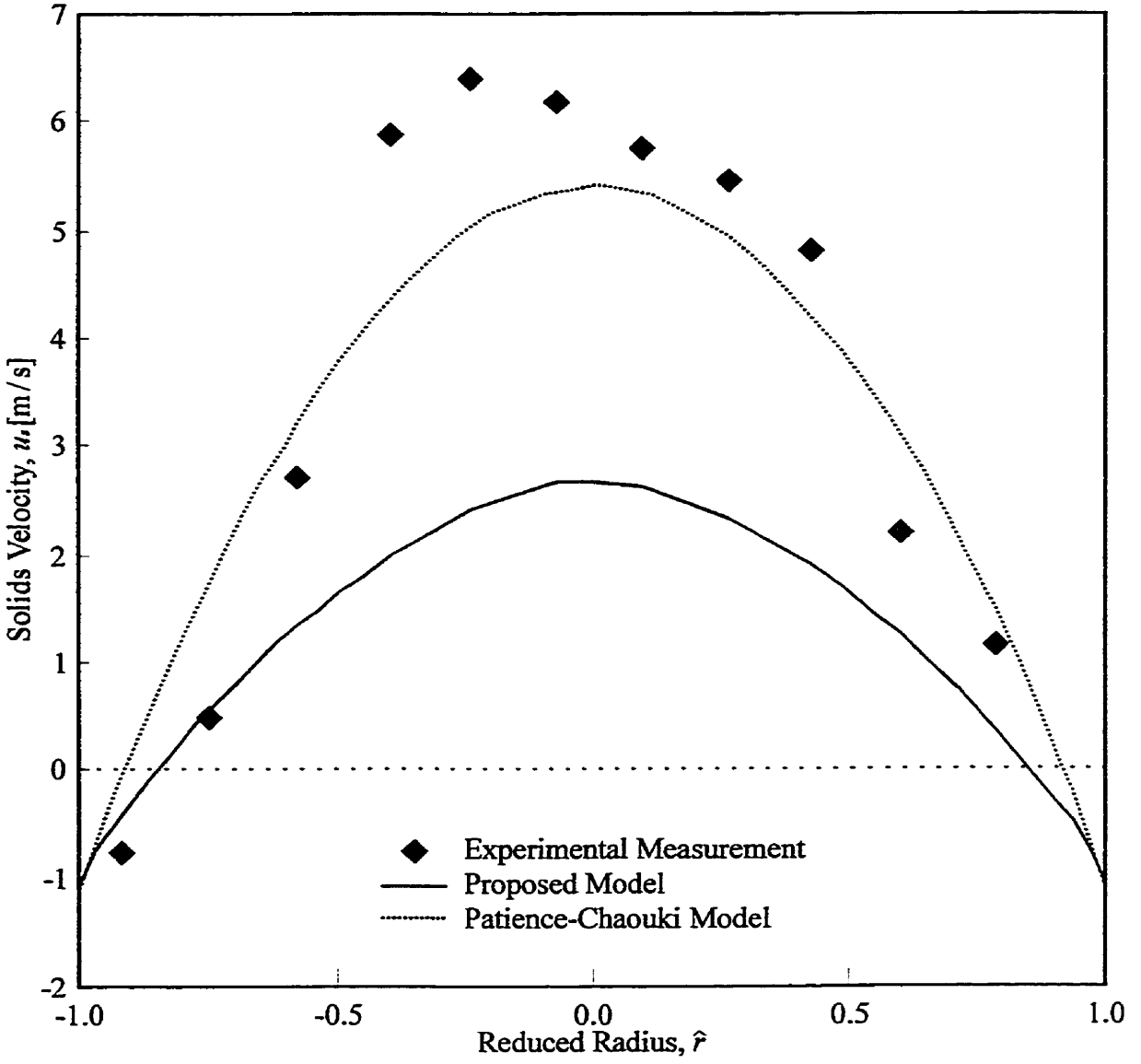

Radial Profile Parameters For The Predicted Values In Figure 34

$\hat{r}_c$=0.849	a	b	c	d	e	f
$\hat{G}$	4.82117	2.96732	-1.85109	8.11695	0.603504	5.52725
u_s	3.59314	1.77572	-0.90424	4.85906	0.814818	3.81988

occur. Considering the relatively low inlet solids mass flux and consequently small pressure drop through the riser, it is unlikely that the solids would attain a velocity more than twice the inlet superficial gas velocity at any location in the riser. In fact, based on the calculated pressure drop and experimental data, the slip velocity in $-0.6 < \hat{r} < 0.6$ at $z = 0.64$ is approximately -3 $\mathrm{m\,s^{-1}}$, meaning that the solids have a greater velocity than the gas, which is entirely impossible. It is reasonable to dismiss the data at $z = 0.64$ as flawed and doing so makes the model predictions for the solids velocity satisfactory.

Figure 35: Radial Solids Velocity Profile Comparison With Experimental Data From Miller And Gidaspow, 1992 ($z = 0.84$, $u_{gin} = 2.89\,\mathrm{m\,s^{-1}}$, $G_{sin} = 32.8\,\mathrm{kg\,m^{-2}s^{-1}}$, $H = 6.58\,\mathrm{m}$, $D = 0.075\,\mathrm{m}$, $\rho_p = 1500\,\mathrm{kg\,m^{-3}}$, $D_p = 75\,\mu\mathrm{m}$)

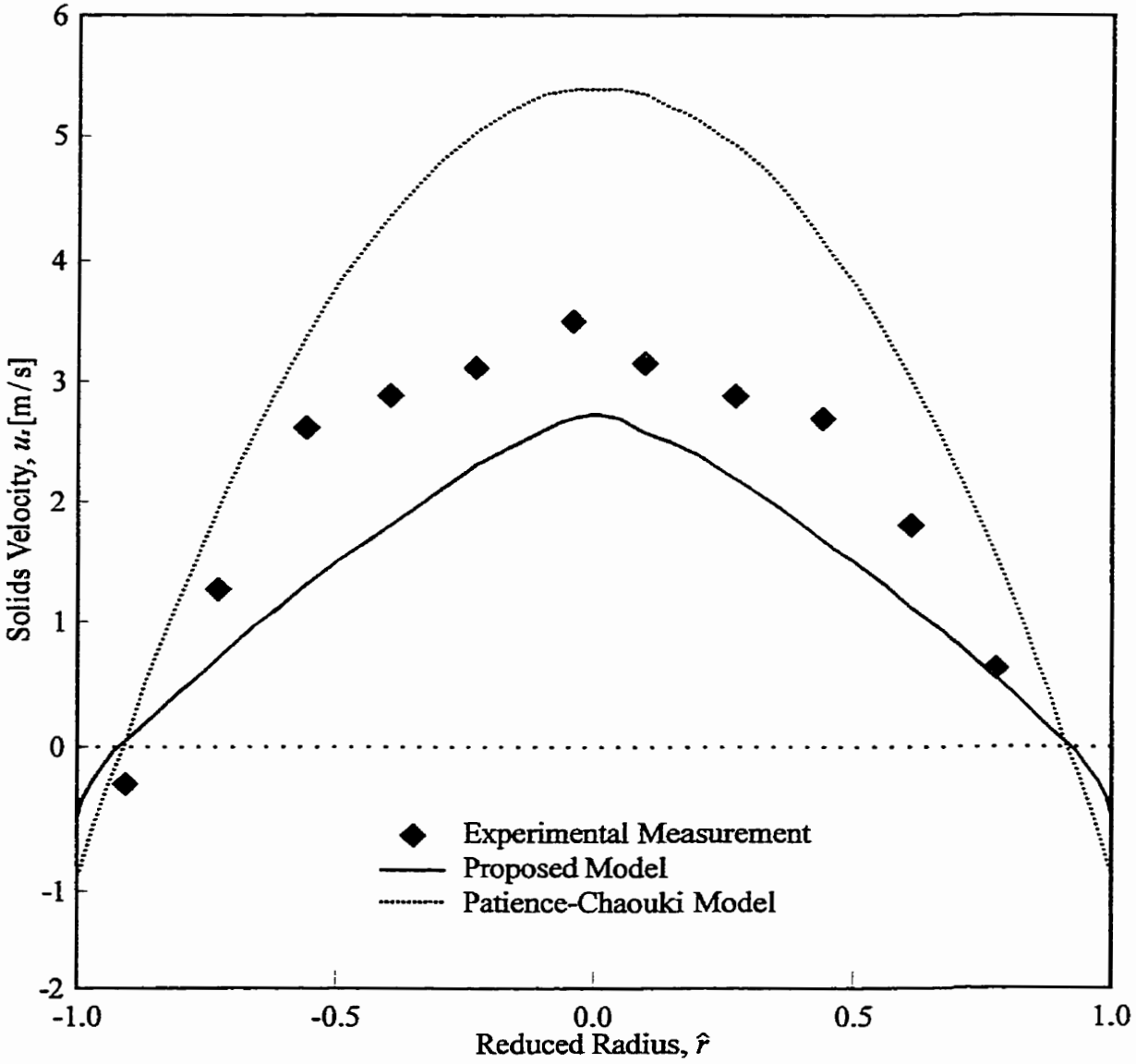

Radial Profile Parameters For The Predicted Values In Figure 35

$\hat{r}_c$=0.912	a	b	c	d	e	f
$\hat{G}$	2.82921	3.04093	-0.688149	4.13714	0.416617	2.63719
u_s	3.07801	1.33615	-0.354756	2.47280	0.580240	1.87092

5.2.2 Yang et al., 1992

Yang et al. (1992) measured solids velocity profiles in a 11 m tall, 0.14 m diameter riser fluidizing FCC catalyst ($D_p = 54\,\mu$m, $\rho_p = 1545\,\mathrm{kg\,m^{-3}}$) using air as the fluidizing agent. A fiber optic probe laser Doppler velocimetry optical system acquired the radial profiles at various axial locations. Examination of the effects of inlet superficial gas velocities and solids mass fluxes on local solids velocity profiles show that the center-line solids velocity is greater than the inlet superficial gas velocity at sampling locations sufficiently distant from the base of the riser. Figures 36 to 39 compare the predictions of the model presented in this dissertation with the selected experimental data.

The data in Figure 36 (Page 114) correspond to an inlet superficial gas velocity of $4.33\,\mathrm{m\,s^{-1}}$, an inlet solids mass flux of $15\,\mathrm{kg\,m^{-2}s^{-1}}$, and an inlet pressure of 103.0 kPa. The sampling location is $z = 0.6$. The LZUZI is $z_i = 0.19$ and outlet pressure is 101.2 kPa. The relative error is large, 28%, due to the severe under prediction of the model everywhere except near the wall; at the wall the prediction is good and exhibits a 4% relative error. (The Patience-Chaouki Model exhibits a 10% relative error.)

Figures 37 (Page 115) and 38 (Page 116) show comparisons between the model and experimental data at a sampling location of 3.3 m ($z = 0.3$) and inlet solids mass flux of $24.5\,\mathrm{kg\,m^{-2}s^{-1}}$. The data shown in the two figures correspond to inlet superficial gas velocities of $3.25\,\mathrm{m\,s^{-1}}$ and $4.33\,\mathrm{m\,s^{-1}}$ for Figures 37 and 38, respectively. In general, the model predictions are poor, except near the wall for the riser with the lesser of the two superficial gas velocities.

The data in Figure 39 (Page 118) correspond to an inlet superficial gas velocity of $4.33\,\mathrm{m\,s^{-1}}$, an inlet solids mass flux of $44.2\,\mathrm{kg\,m^{-2}s^{-1}}$, and an inlet pressure of 106.0 kPa. The sampling location is $z = 0.3$. The LZUZI is $z_i = 0.47$ and outlet pressure is 101.1 kPa. Again, the model prediction near the wall is good, within 6% in the domain $0.97 \leq \hat{r} \leq 1$, but the overall relative error is 33%, which is highly unsatisfactory. (The Patience-Chaouki Model exhibits a 13% relative error.)

Figure 36: Radial Solids Velocity Profile Comparison With Experimental Data From Yang et al., 1992 ($z = 0.6$, $u_{gin} = 4.33\,\mathrm{m\,s^{-1}}$, $G_{sin} = 15\,\mathrm{kg\,m^{-2}s^{-1}}$, $H = 11\,\mathrm{m}$, $D = 0.14\,\mathrm{m}$, $\rho_p = 1545\,\mathrm{kg\,m^{-3}}$, $D_p = 54\,\mu\mathrm{m}$)

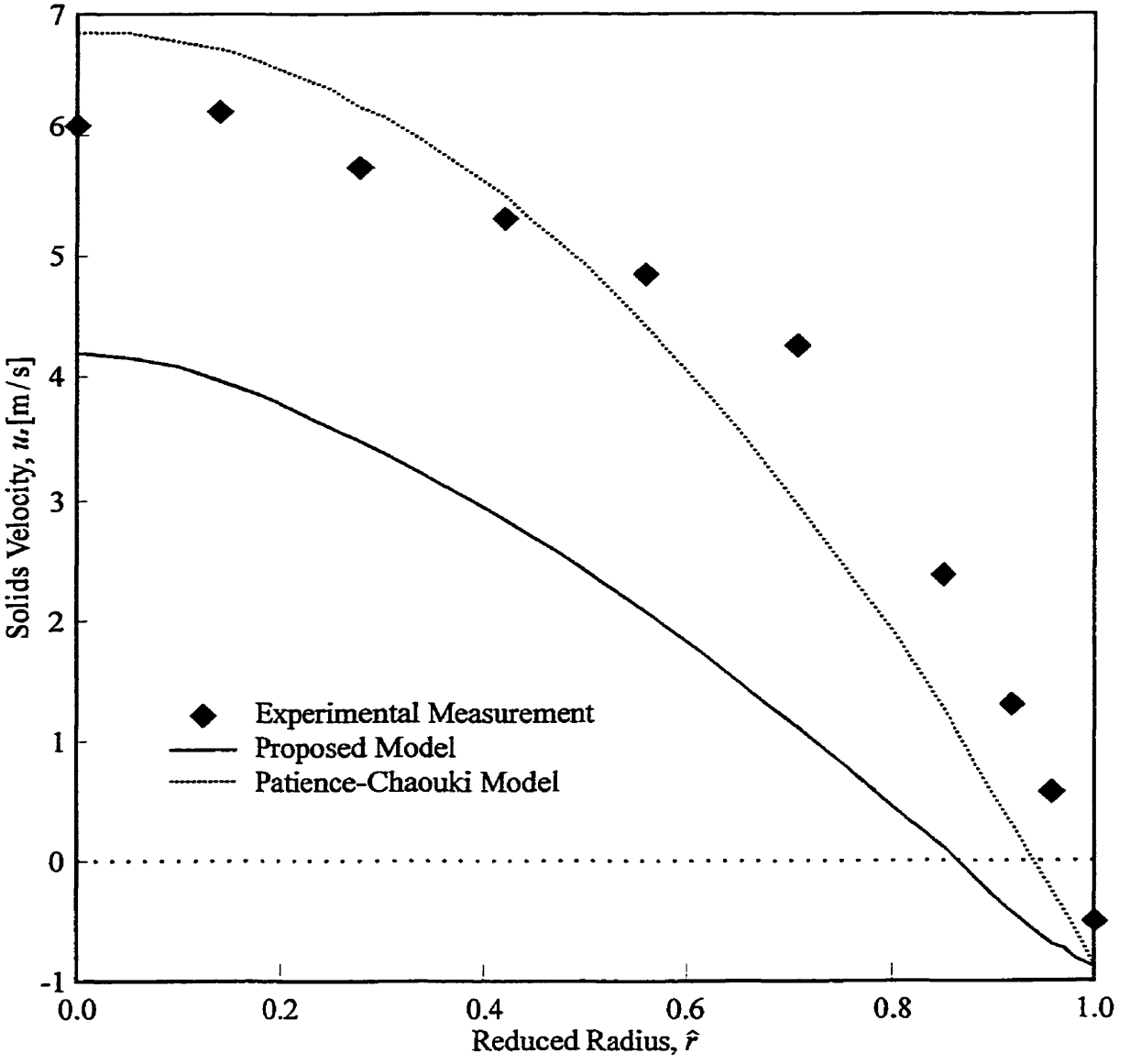

Radial Profile Parameters For The Predicted Values In Figure 36

$\hat{r}_c$=0.862	a	b	c	d	e	f
$\hat{G}$	4.03866	2.76843	-1.35648	8.25928	0.956970	7.02302
u_s	5.30820	1.54452	-1.08365	8.87821	1.151972	7.97577

Figure 37: Radial Solids Velocity Profile Comparison With Experimental Data From Yang et al., 1992 ($z = 0.3$, $u_{gin} = 3.25\,\mathrm{m\,s^{-1}}$, $G_{sin} = 24.5\,\mathrm{kg\,m^{-2}s^{-1}}$; $H = 11\,\mathrm{m}$, $D = 0.14\,\mathrm{m}$, $\rho_p = 1545\,\mathrm{kg\,m^{-3}}$, $D_p = 54\,\mu\mathrm{m}$)

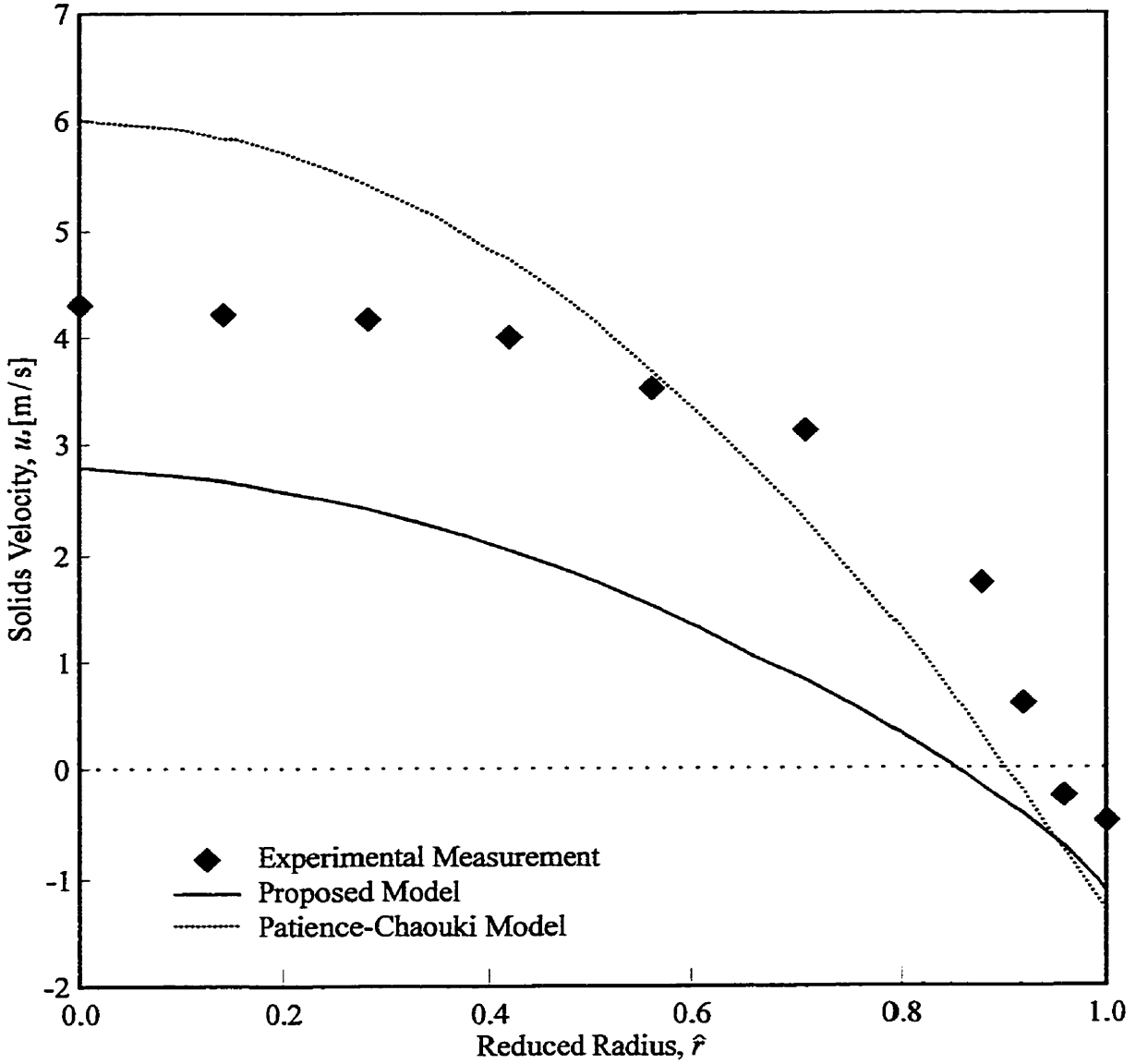

Radial Profile Parameters For The Predicted Values In Figure 37

$\hat{r}_c$=0.856	a	b	c	d	e	f
$\hat{G}$	4.48461	2.91743	-1.626818	7.38230	0.556534	4.88021
u_s	3.69146	1.83877	-0.912657	4.85134	0.736689	3.69292

Figure 38: Radial Solids Velocity Profile Comparison With Experimental Data From Yang et al., 1992 ($z = 0.3$, $u_{gin} = 4.33\,\mathrm{m\,s^{-1}}$, $G_{sin} = 24.5\,\mathrm{kg\,m^{-2}s^{-1}}$, $H = 11\,\mathrm{m}$, $D = 0.14\,\mathrm{m}$, $\rho_p = 1545\,\mathrm{kg\,m^{-3}}$, $D_p = 54\,\mu\mathrm{m}$)

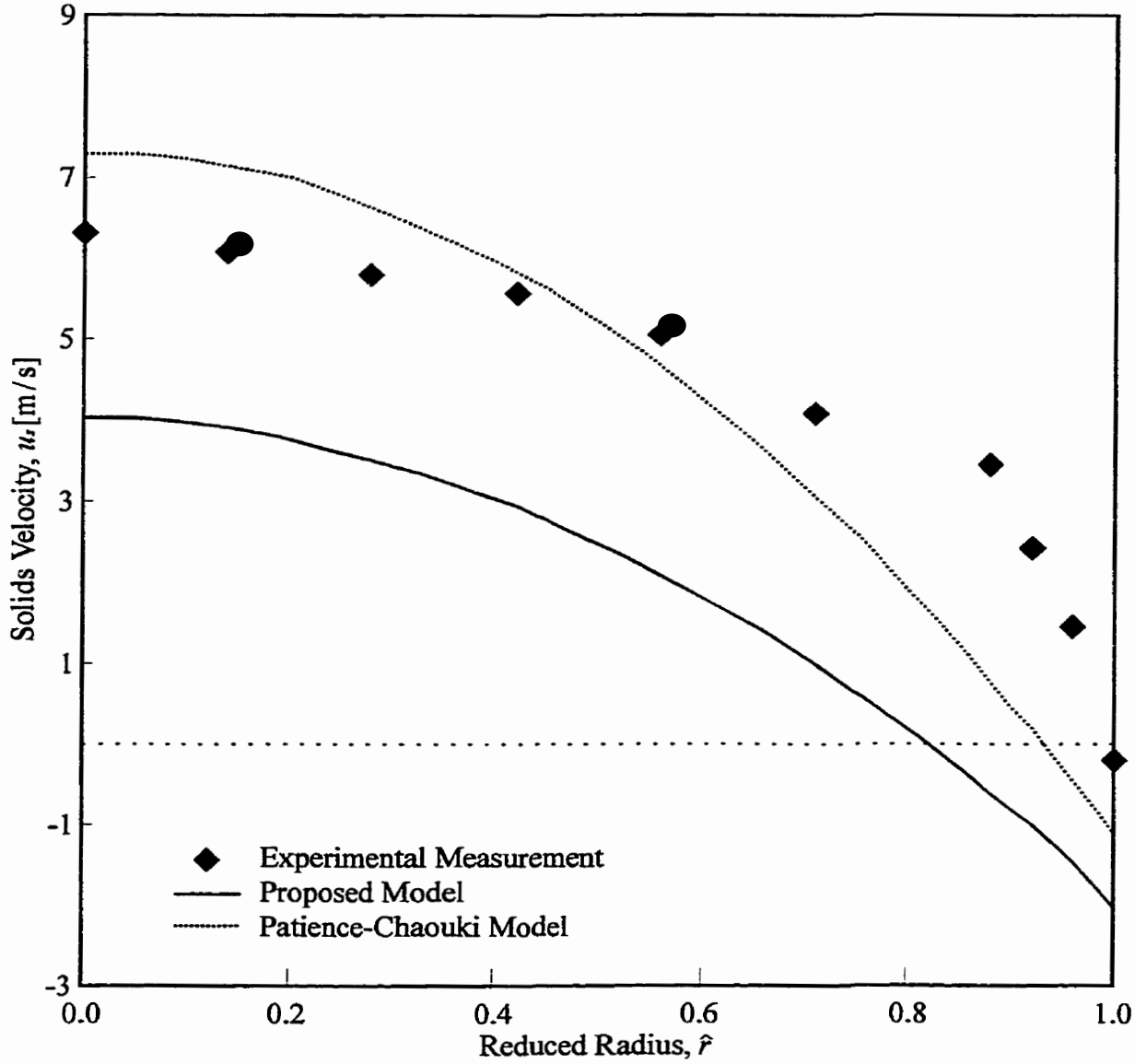

Radial Profile Parameters For The Predicted Values In Figure 38

$\hat{r}_c$=0.820	a	b	c	d	e	f
$\hat{G}$	6.22975	2.55329	-2.47027	9.97006	0.695659	6.95197
u_s	5.89014	1.93193	-1.87074	8.52137	0.831567	6.47890

Moreover, comparing Figures 38 and 39 shows that the model fails to predict the increase in center-line solids velocity with an increase in inlet solids mass flux while holding all other variables constant.

Figure 39: Radial Solids Velocity Profile Comparison With Experimental Data From Yang et al., 1992 ($z = 0.3$, $u_{gin} = 4.33\,\mathrm{m\,s^{-1}}$, $G_{sin} = 44.2\,\mathrm{kg\,m^{-2}s^{-1}}$; $H = 11\,\mathrm{m}$, $D = 0.14\,\mathrm{m}$, $\rho_p = 1545\,\mathrm{kg\,m^{-3}}$, $D_p = 54\,\mu\mathrm{m}$)

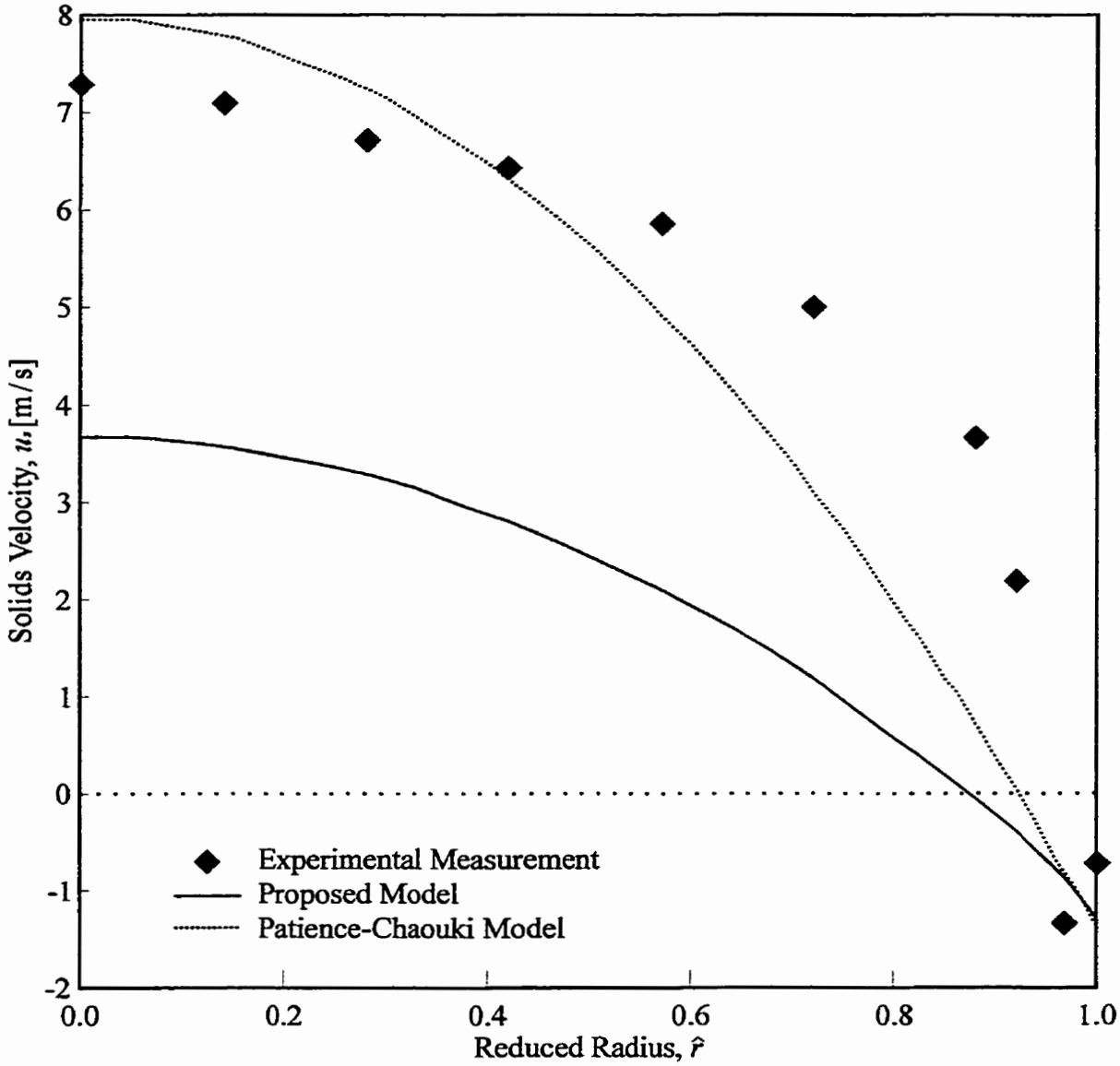

Radial Profile Parameters For The Predicted Values In Figure 39

$\hat{r}_c$=0.876	a	b	c	d	e	f
$\hat{G}$	3.88435	3.63935	-1.48231	7.07212	0.544359	4.80483
u_s	4.75829	1.96596	-1.08807	6.66929	0.780615	5.36427

5.2.3 Hartge et al., 1988

Like Miller and Gidaspow (1992), Hartge et al. (1988) present radial solids velocity profiles at three axial locations in a single riser operating with invariant inlet conditions. They used air flowing at $2.9\,\mathrm{m\,s^{-1}}$ to fluidize FCC catalyst ($D_p = 85\,\mu\mathrm{m}$, $\rho_p = 1500\,\mathrm{kg\,m^{-3}}$) at a rate of $49\,\mathrm{kg\,m^{-2}s^{-1}}$ in a 8.4 m tall, 0.4 m diameter riser. Hartge et al. (1988) do not report the inlet pressure nor temperature so assumed values of 106.0 kPa and 300 K, respectively, generate the model predictions throughout this Subsection.

The specified operating conditions result in a outlet pressure of 100.6 kPa and LZUZI of $z_i = 0.25$ for Figures 40 through 42, which correspond to axial sampling locations of $z = [0.11, 0.32, 0.56]$, respectively.

The data in Figure 40 (Page 120) correspond to an axial sampling location of 0.9 m ($z = 0.11$) and does not exhibit downward flow of solids near the wall. Additionally, it does not exhibit a monotonic decrease from the center-line to the wall, as all the previous experimental data does, which is a sound indicator that the sampling location is well within the chaotic lower dense region. Consequently, due to the relatively simplistic assumed flow structure in the model presented in this dissertation, the relative error between the model prediction and experimental data is 37%. (The Patience-Chaouki Model exhibits a 24% relative error.)

The data in Figure 41 (Page 121) corresponds to an axial sampling location of 2.7 m ($z = 0.32$). The model prediction at the wall is perfect, which makes the relative error in the annular region less than 5%. Unfortunately, the propensity of the severe under prediction of the solids velocity profile in the core continues. The relative error at the center-line is 53% which exaggerates the error in the core region to 40%. (The Patience-Chaouki Model exhibits a 24% relative error.)

The data in Figure 42 (Page 123) corresponds to an axial sampling location of 4.7 m ($z = 0.56$) and is the final comparison between the model presented in this dissertation and the experimental data that Hartge et al. (1988) present. Near the

Figure 40: Radial Solids Velocity Profile Comparison With Experimental Data From Hartge et al., 1988 ($z = 0.11$, $u_{gin} = 2.9\,\mathrm{m\,s^{-1}}$, $G_{sin} = 49\,\mathrm{kg\,m^{-2}s^{-1}}$; $H = 8.4\,\mathrm{m}$, $D = 0.4\,\mathrm{m}$, $\rho_p = 1500\,\mathrm{kg\,m^{-3}}$, $D_p = 85\,\mu\mathrm{m}$)

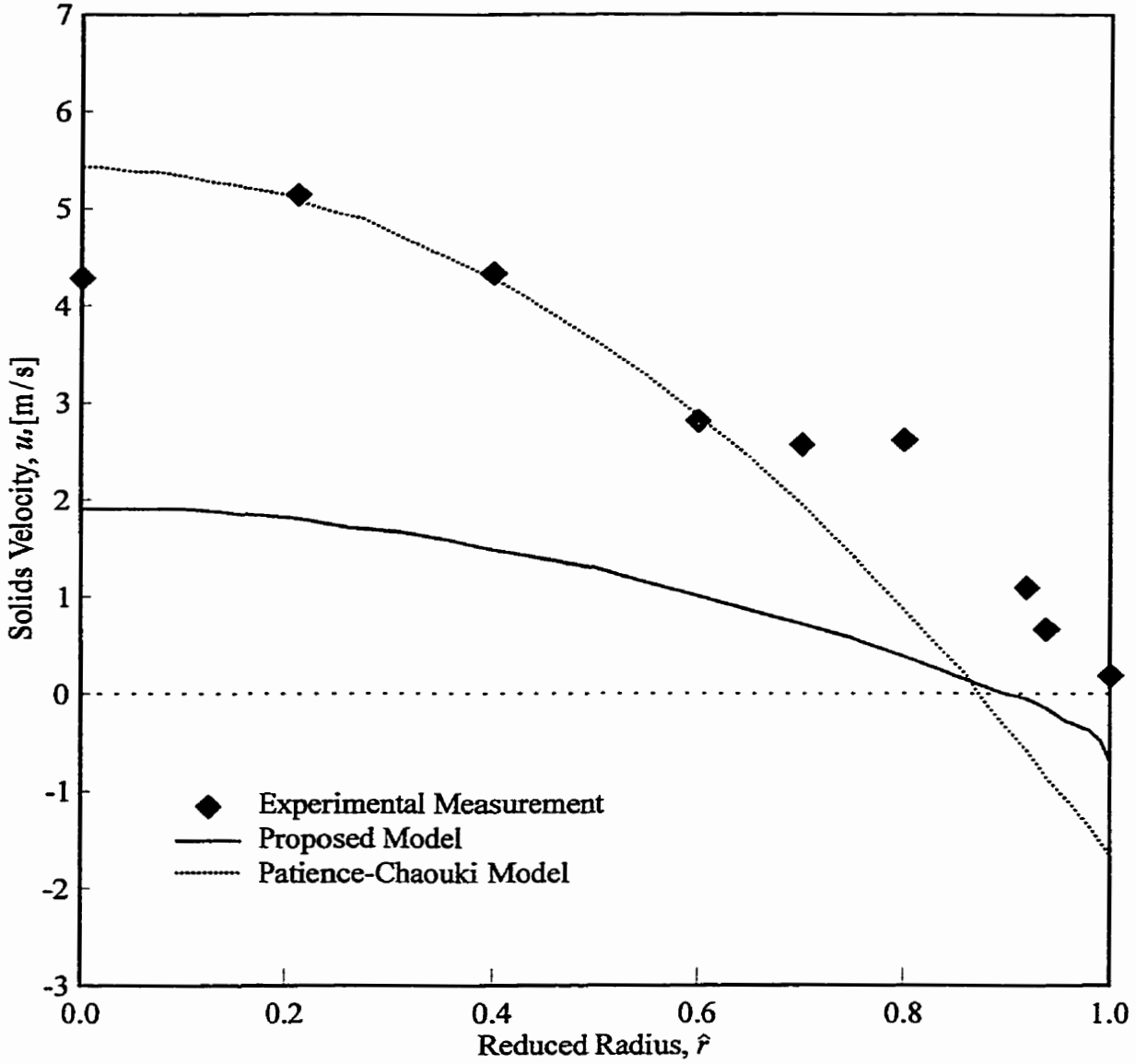

Radial Profile Parameters For The Predicted Values In Figure 40

$\hat{r}_c$=0.903	a	b	c	d	e	f
$\hat{G}$	3.03529	3.25856	-0.854983	4.84888	0.386316	2.88359
u_s	2.31784	1.82106	-0.391267	2.45344	0.539931	1.75905

Figure 41: Radial Solids Velocity Profile Comparison With Experimental Data From Hartge et al., 1988 ($z = 0.32$, $u_{gin} = 2.9\,\mathrm{m\,s^{-1}}$, $G_{sin} = 49\,\mathrm{kg\,m^{-2}s^{-1}}$; $H = 8.4\,\mathrm{m}$, $D = 0.4\,\mathrm{m}$, $\rho_p = 1500\,\mathrm{kg\,m^{-3}}$, $D_p = 85\,\mu\mathrm{m}$)

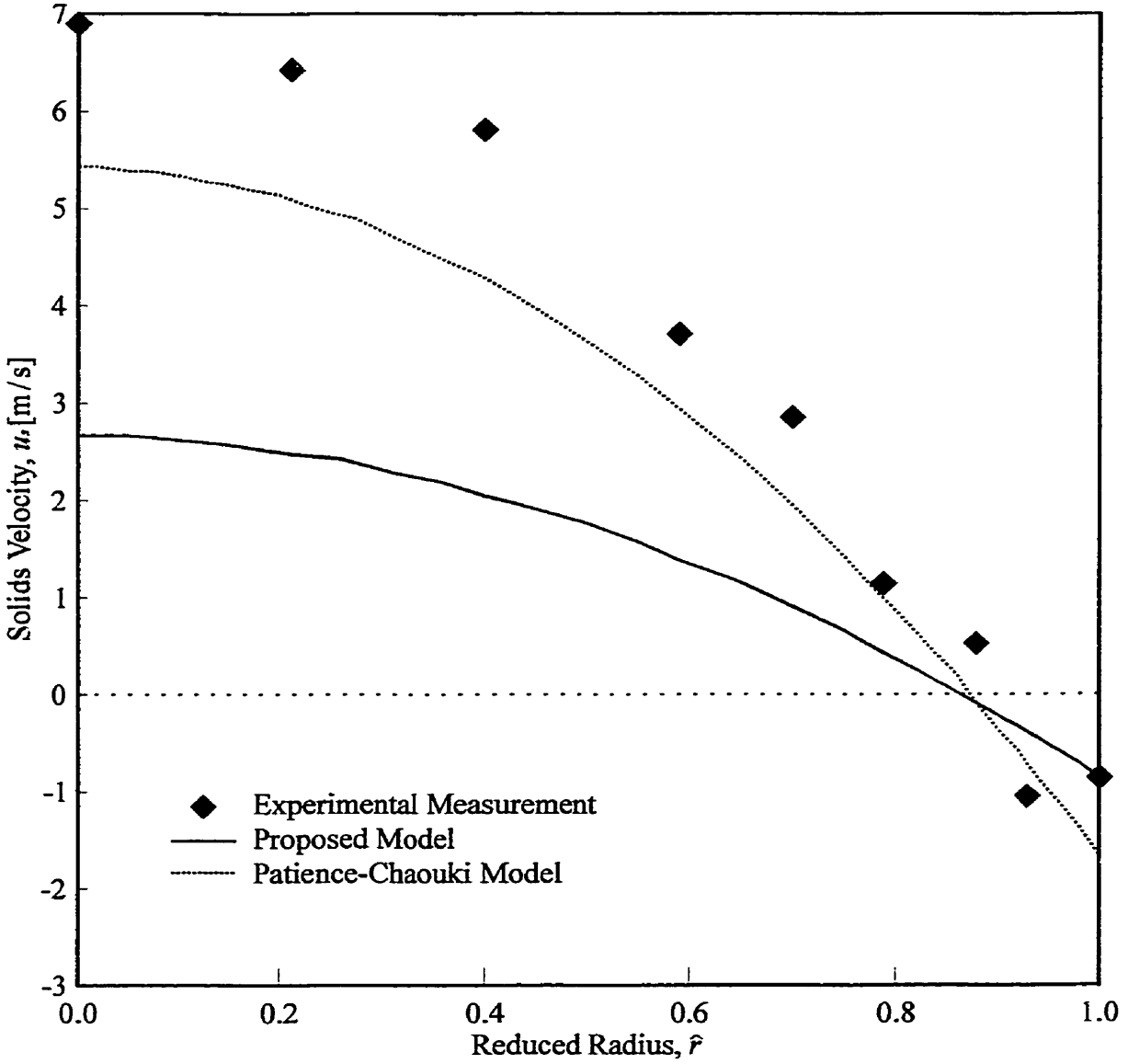

Radial Profile Parameters For The Predicted Values In Figure 41

$\hat{r}_c$=0.867	a	b	c	d	e	f
$\hat{G}$	4.29809	3.86539	-1.813471	8.18713	0.591813	5.71513
u_s	3.50947	1.90587	-0.831009	5.29195	0.890302	4.41854

wall, in the domain $0.9 \leq \hat{r} \leq 1$, the relative error is just over 6% but the relative error throughout the entire radial domain is 22%. (The Patience-Chaouki Model exhibits a 23% relative error.) Based on the assumption that the minimum solids velocity occurs at the wall and LZUZI ($\hat{r} = 1$ and $z = z_i$), Figures 41 and 42 clearly show that the calculated value of $z_i = 0.25$ is incorrect since $u_s(1, 0.56) < u_s(1, 0.32)$.

Figure 42: Radial Solids Velocity Profile Comparison With Experimental Data From Hartge et al., 1988 ($z = 0.56$, $u_{gin} = 2.9\,\mathrm{m\,s^{-1}}$, $G_{sin} = 49\,\mathrm{kg\,m^{-2}s^{-1}}$; $H = 8.4\,\mathrm{m}$, $D = 0.4\,\mathrm{m}$, $\rho_p = 1500\,\mathrm{kg\,m^{-3}}$, $D_p = 85\,\mu\mathrm{m}$)

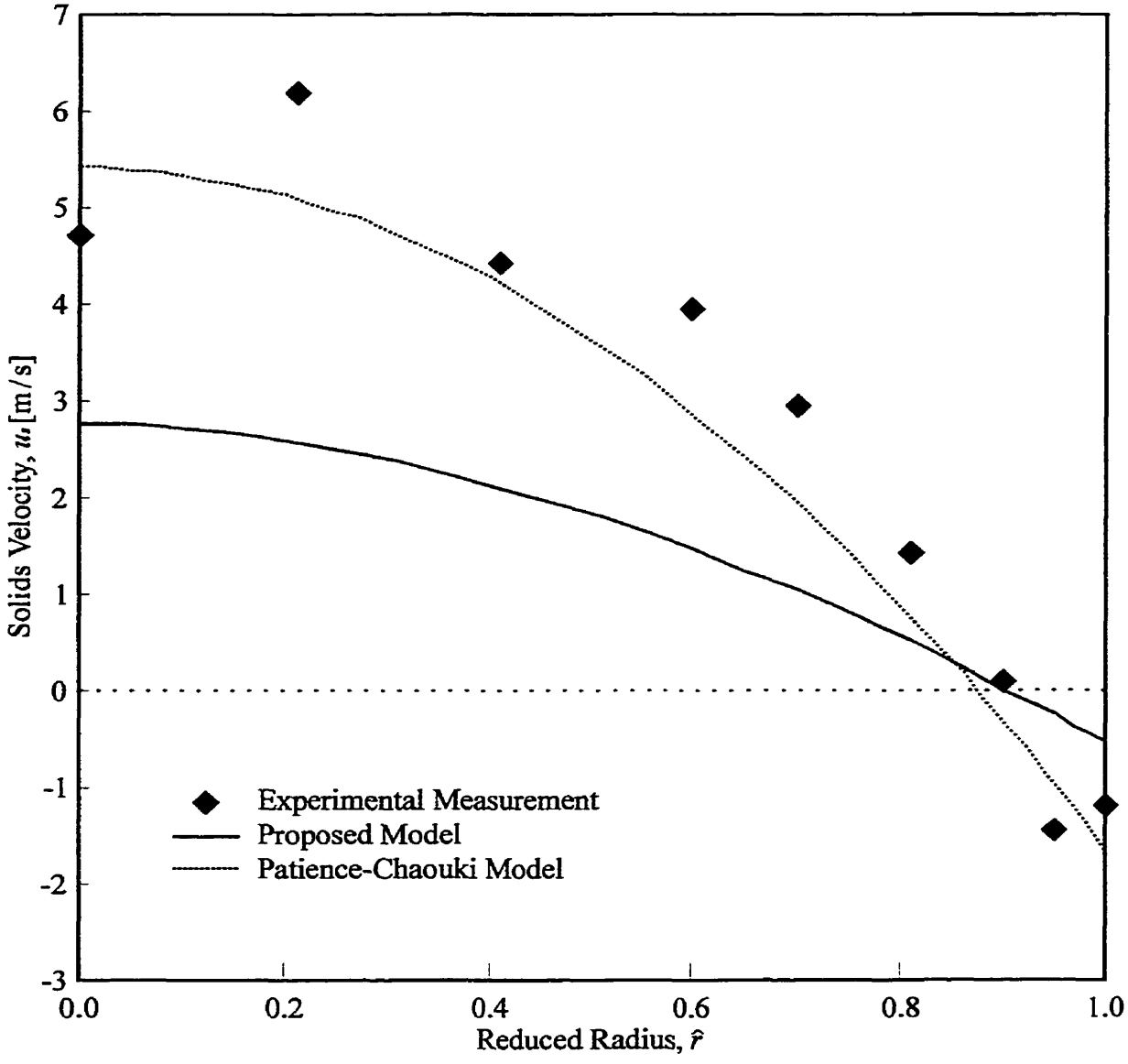

Radial Profile Parameters For The Predicted Values In Figure 42

$\hat{r}_c$=0.903	a	b	c	d	e	f
$\hat{G}$	3.16692	5.01705	-1.260407	7.32282	0.674531	5.81340
u_s	3.32612	1.83756	-0.564177	5.71449	1.012970	5.18118

A possible explanation for the relatively poor comparisons between model predictions and experimental data in the last two Subsections is that both the risers have abrupt exits, although it is more likely that there is a fundamental problem with an assumption that the model presented in this dissertation uses. The model tends to severely under predict the solids velocity in the core of the riser but adequately predicts the velocity near the wall, which is a trend that is useful to note. Section 6 elaborates on potential corrections to the model that may improve its capabilities as far as predicting the radial solids velocity profiles are concerned.

Table 11 presents a summary of the comparisons in this Subection.

Table 11: Qualitative Assessment Of The Comparisons Between Experimental Radial Solids Velocity Profiles And Predictions By The Proposed LDCFB Model

	Relative Error	Number Of Cases
Very Good	<10%	0
Good	10–15%	0
Satisfactory	15–18%	1
Poor	>18%	9

5.3 Radial Voidage Profiles

The radial solids mass flux and velocity profiles in the model presented in this dissertation are functions of axial position and, accordingly, so too is the radial voidage profile. Figure 43 demonstrates this attribute of the model.

The experimental error,

$$\text{Experimental Error} = \sum_{i=1}^{n} \frac{\text{Predicted Value}_i - \text{Experimental Value}_i}{\text{Experimental Value}_i}, \qquad (88)$$

is not singular for voidage measurements because it is not possible for any experimental value to equal zero. Therefore, Equation 88 is the measure of goodness of fit for the predicted profiles in this Subsection.

5.3.1 Miller And Gidaspow, 1992

Figure 44 (Page 127) shows the only voidage profile data that Miller and Gidaspow (1992) present for an inlet solids mass flux of $32.8\,\mathrm{kg\,m^{-2}s^{-1}}$. The profile corresponds to Figures 29 and 35, which represent the experimental data well. As a result, the predicted voidage profile is good and exhibits an experimental error of 2%. The voidage near the wall is under predicted but the voidage in the core, which occupies the vast majority of the riser cross-sectional area, is erroneous by a paltry 0.3%.

Figure 43: Predicted Radial Voidage Profile Pseudo-Animation

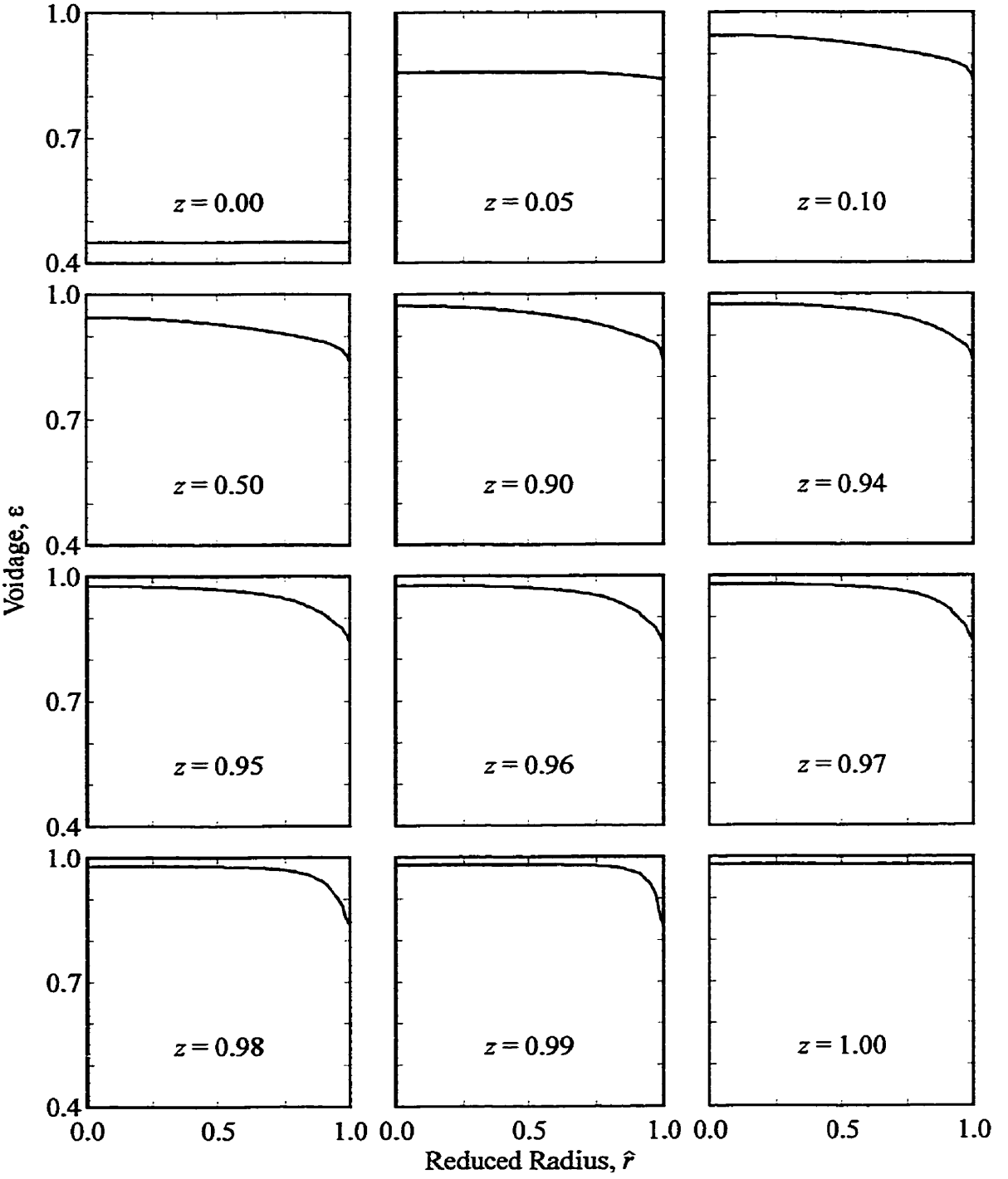

Figure 44: Radial Voidage Profile Comparison With Experimental Data From Miller And Gidaspow, 1992 ($z = 0.84$, $u_{gin} = 2.89\,\mathrm{m\,s^{-1}}$, $G_{sin} = 32.8\,\mathrm{kg\,m^{-2}s^{-1}}$, $H = 6.58\,\mathrm{m}$, $D = 0.075\,\mathrm{m}$, $\rho_p = 1500\,\mathrm{kg\,m^{-3}}$, $D_p = 75\,\mu\mathrm{m}$)

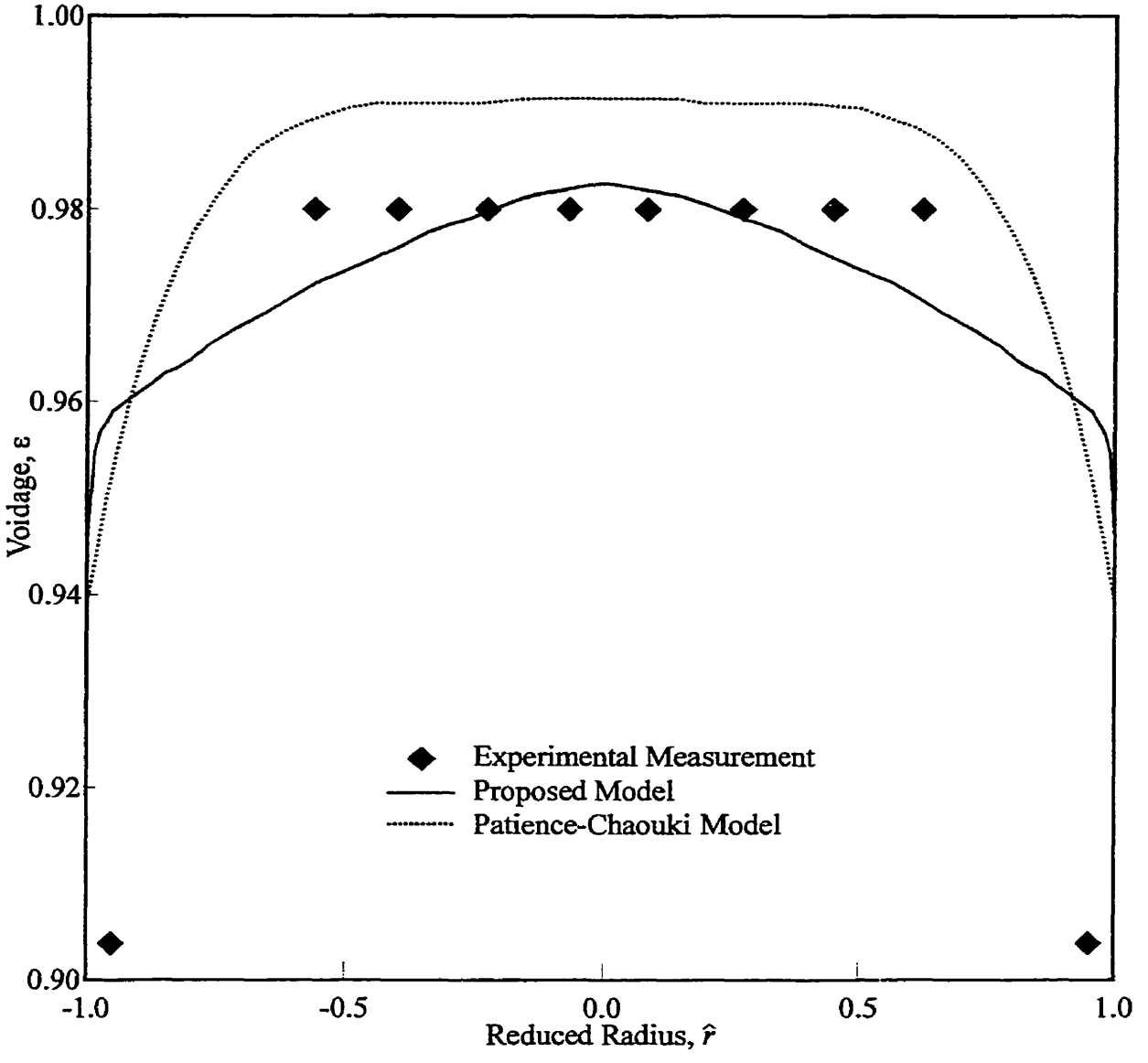

Radial Profile Parameters For The Predicted Values In Figure 44

$\hat{r}_c$=0.912	a	b	c	d	e	f
$\hat{G}$	2.82921	3.04093	- 0.688149	4.13714	0.416617	2.63719
u_s	3.07801	1.33615	- 0.354756	2.47280	0.580240	1.87092

5.3.2 Zhang et al., 1991

Zhang et al. (1991) performed experiments with three different risers and several different particles. They used a fiber-optic probe to measure the local voidage profiles at fixed axial locations in the respective risers. Only the larger two of the three risers are of interest because the small riser is a laboratory scale rig ($H = 2.8\,\mathrm{m}$, $D = 0.032\,\mathrm{m}$) and the target applications of the model presented in this dissertation are pilot-scale or industrial scale rigs.

The first comparison between the model and the experimental data obtained by Zhang et al. (1991) is for a 10 m tall, 0.09 m diameter riser fluidizing alumina particles ($D_p = 42.8\,\mu\mathrm{m}$, $\rho_p = 2003\,\mathrm{kg\,m^{-3}}$). The data in Figure 45 (Page 129) corresponds to sampling location of 4.27 m, an inlet superficial gas velocity of $2.16\,\mathrm{m\,s^{-1}}$, and an inlet solids mass flux of $10.2\,\mathrm{kg\,m^{-2}s^{-1}}$. Even though the inlet solids mass flux is small, this case demonstrates the capabilities of the model with respect to different particle characteristics. Using an inlet pressure of 110.0 kPa, the LZUZI is $z_i = 0.48$ and outlet pressure is 107.5 kPa. As was the case with the previous voidage profile comparison, the model prediction is nearly perfect in the core but exhibits a rather large experimental error, 18%, at the wall. The overall experimental error is 3%. The shape of the predicted profile is nearly flat while the experimental profile shows a marked decrease in the voidage near the wall. It is impossible to discern the location of the core radius from the experimental data and, consequently, detailed analysis into the discrepancy is not possible. However, an immediate deduction from Figure 45 is that either the solids mass flux or solids velocity profile is too flat, which renders the voidage profile too flat.

The next two comparisons use data gathered from a 12 m tall, 0.300 m diameter riser fluidizing FCC catalyst ($D_p = 54\,\mu\mathrm{m}$, $\rho_p = 929.5\,\mathrm{kg\,m^{-3}}$). The sampling location is constant for the two cases at 3.77 m ($z = 0.31$).

The data in Figure 46 (Page 131) correspond to an inlet superficial gas velocity of $2.60\,\mathrm{m\,s^{-1}}$ and an inlet solids mass flux of $45.0\,\mathrm{kg\,m^{-2}s^{-1}}$. The calculated

Figure 45: Radial Voidage Profile Comparison With Experimental Data From Zhang et al., 1991 ($z = 0.43$, $u_{gin} = 2.16\,\mathrm{m\,s^{-1}}$, $G_{sin} = 10.2\,\mathrm{kg\,m^{-2}s^{-1}}$, $H = 10\,\mathrm{m}$, $D = 0.09\,\mathrm{m}$, $\rho_p = 2003\,\mathrm{kg\,m^{-3}}$, $D_p = 42.8\,\mu\mathrm{m}$)

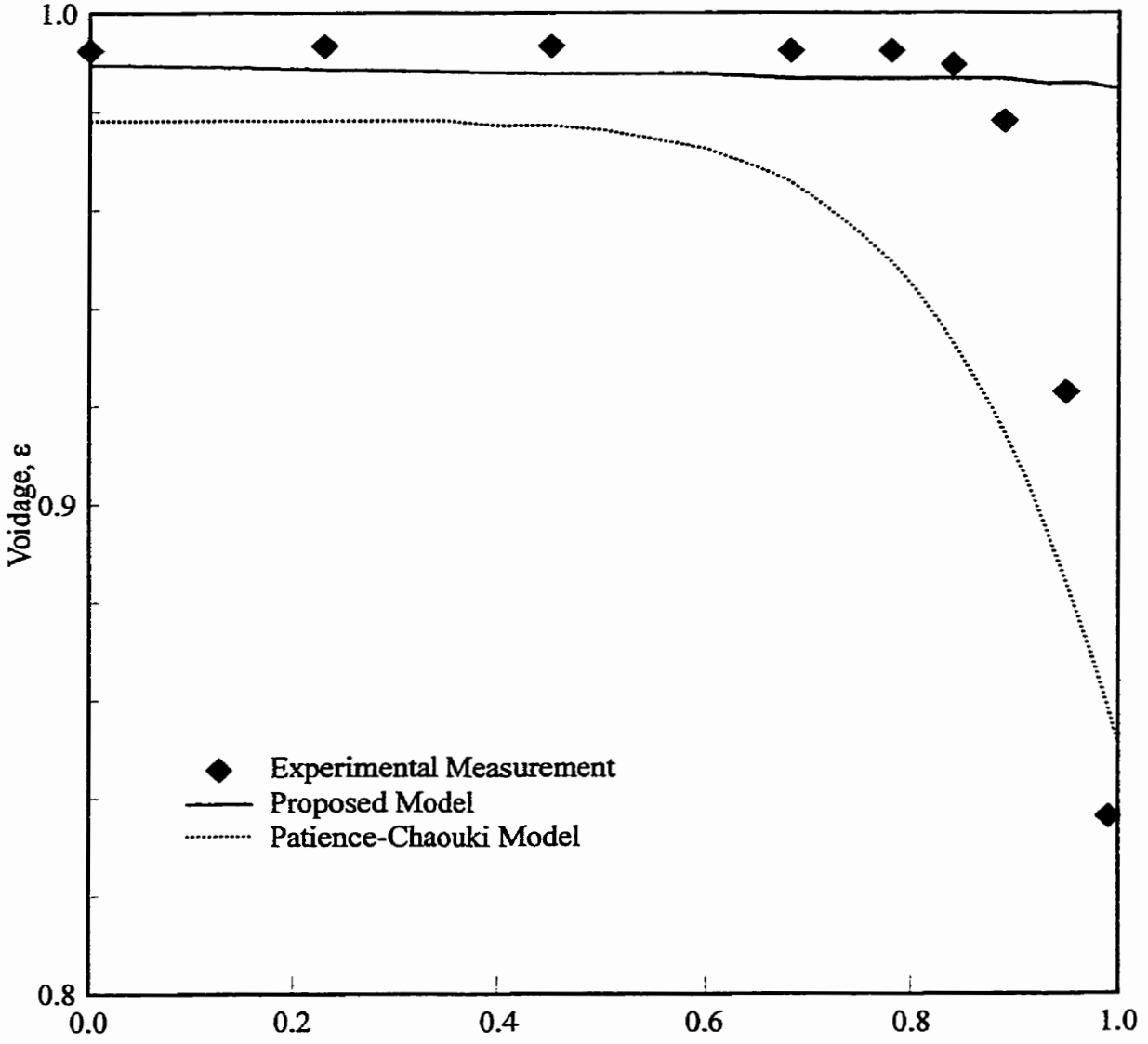

Radial Profile Parameters For The Predicted Values In Figure 45

$\hat{r}_c$=0.806	a	b	c	d	e	f
$\hat{G}$	7.07923	2.42855	-2.87393	11.2338	0.763562	8.03463
u_s	2.99135	1.98153	-1.03560	4.45826	0.870485	3.39339

location of the LZUZI is $z_i = 0.49$ and the calculated outlet pressure is 102.0 kPa. The experimental error between the model predictions and experimental data is 4%. The center-line voidage is under predicted while the wall voidage is over predicted. Nonetheless, the shape of the predicted profile mimics the experimental profile better in this case than in the previous two.

The data in Figure 47 (Page 132) correspond to an inlet superficial gas velocity of $3.11\,\mathrm{m\,s^{-1}}$ and an inlet solids mass flux of $22.0\,\mathrm{kg\,m^{-2}s^{-1}}$ and is the final comparison between the model and the experimental data of Zhang et al. (1991). The calculated location of the LZUZI is $z_i = 0.25$ and the calculated outlet pressure is 106.7 kPa. The experimental error in this case appears to be greater than that of the last because the scale is much smaller. In actuality, the experimental error is under 2%, which is 2% lower than the previous case. Once again, the center-line voidage is under predicted, the wall voidage is over predicted, and the predicted profile is too flat across the entire radial domain.

Although the shape of the predicted voidage profiles is not perfect, the average experimental error for the three comparisons in this Subsection is 3% and, therefore, the model is successful.

Figure 46: Radial Voidage Profile Comparison With Experimental Data From Zhang et al., 1991 ($z = 0.31$, $u_{gin} = 2.6\,\mathrm{m\,s^{-1}}$, $G_{sin} = 45\,\mathrm{kg\,m^{-2}s^{-1}}$, $H = 12\,\mathrm{m}$, $D = 0.3\,\mathrm{m}$, $\rho_p = 929.5\,\mathrm{kg\,m^{-3}}$, $D_p = 54\,\mu\mathrm{m}$)

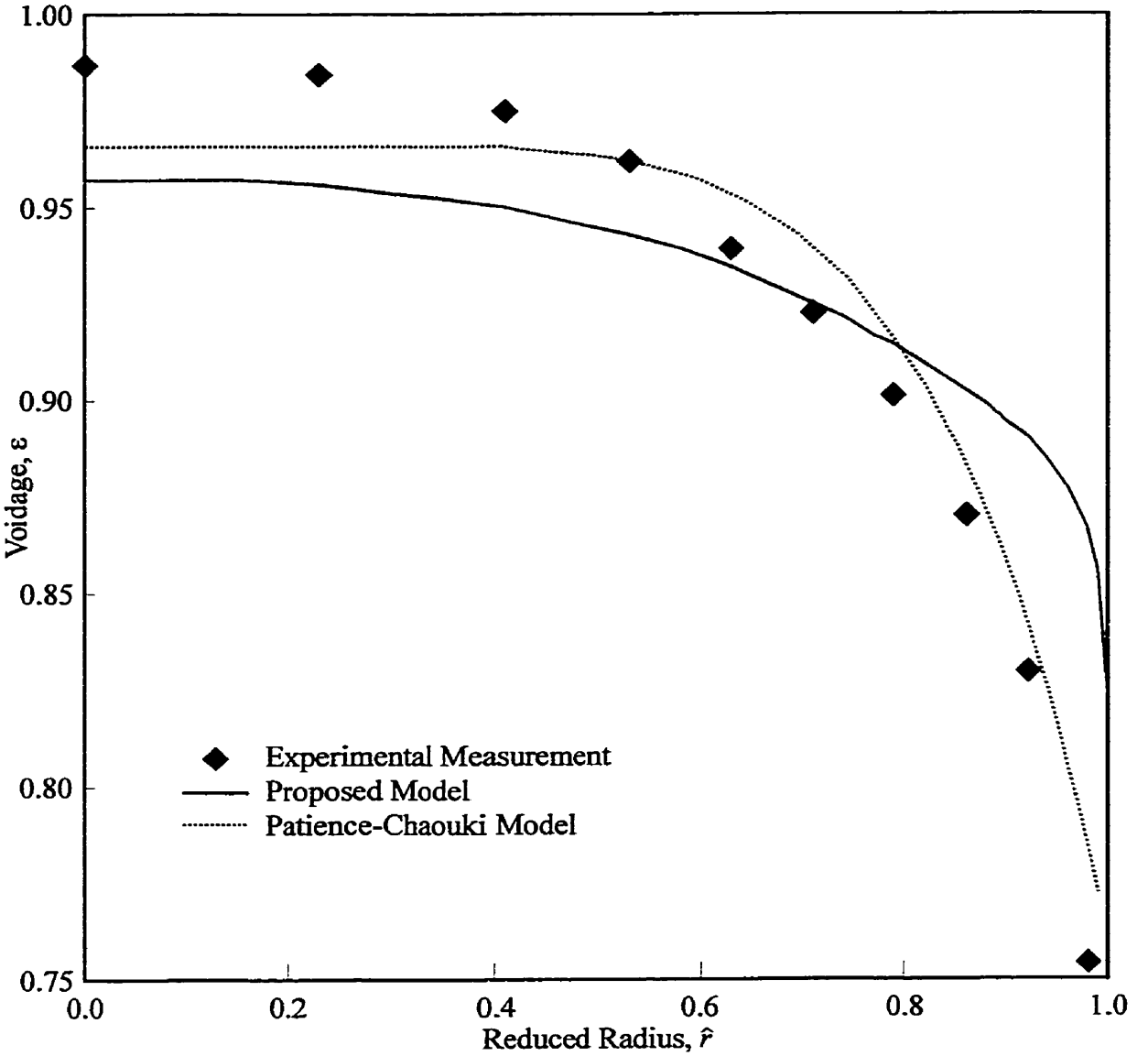

Radial Profile Parameters For The Predicted Values In Figure 46

$\hat{r}_c$=0.907	a	b	c	d	e	f
$\hat{G}$	3.24420	5.80202	-1.40171	7.36201	0.551669	5.37729
u_s	2.62534	2.31112	-0.52971	4.73295	0.909212	4.18736

Figure 47: Radial Voidage Profile Comparison With Experimental Data From Zhang et al., 1991 ($z = 0.31$, $u_{gin} = 3.11\,\mathrm{m\,s^{-1}}$, $G_{sin} = 22\,\mathrm{kg\,m^{-2}s^{-1}}$, $H = 12\,\mathrm{m}$, $D = 0.3\,\mathrm{m}$, $\rho_p = 929.5\,\mathrm{kg\,m^{-3}}$, $D_p = 54\,\mu\mathrm{m}$)

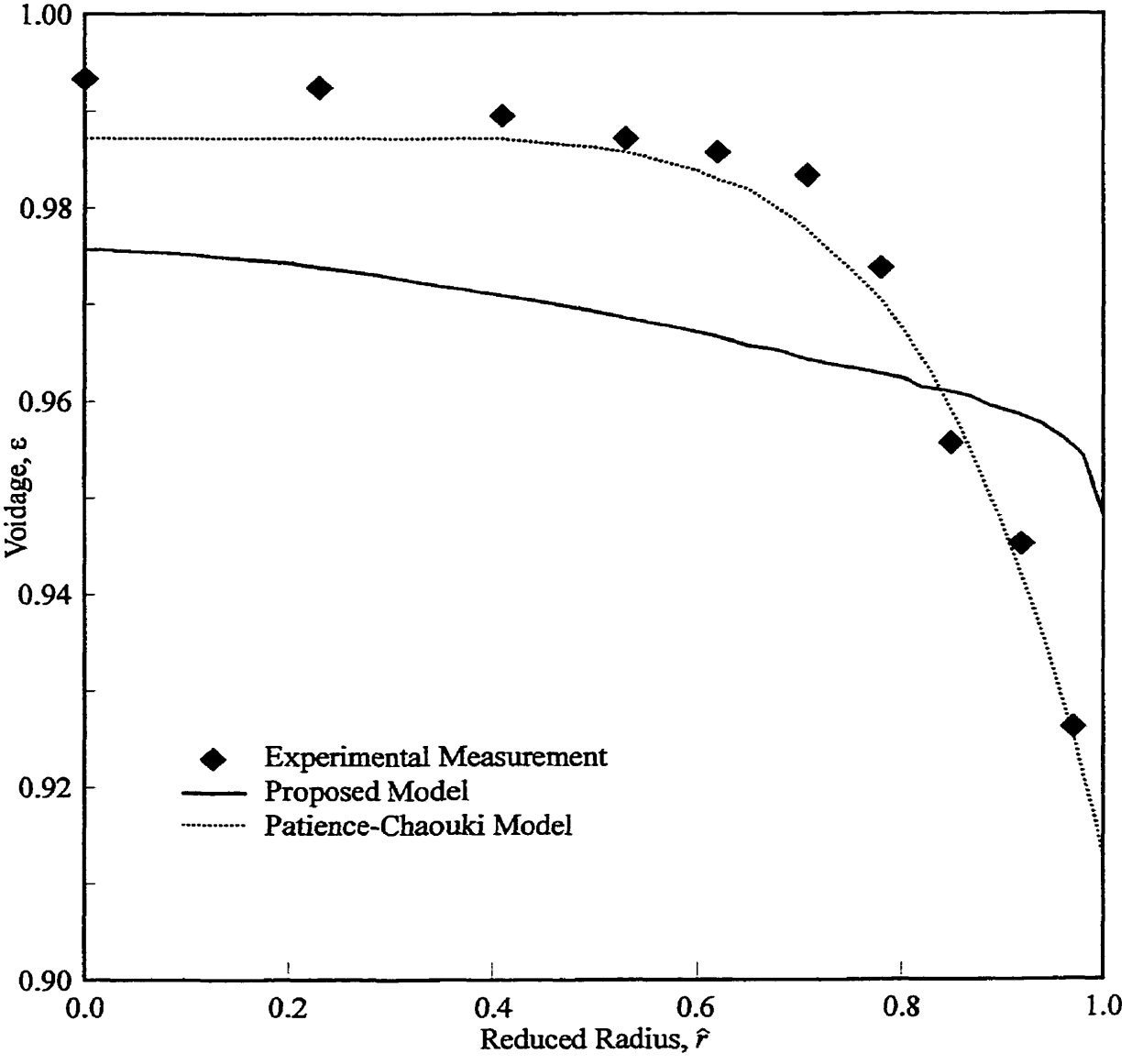

Radial Profile Parameters For The Predicted Values In Figure 47

$\hat{r}_c$=0.840	a	b	c	d	e	f
$\hat{G}$	5.26322	2.99528	-2.13179	8.99462	0.64026	6.22160
u_s	4.20598	1.88070	-1.17018	6.06870	0.85124	4.79909

5.3.3 Pugsley, 1995

Pugsley (1995) performed experiments with relatively large inlet solids mass fluxes that would be used in an LDCFB catalytic reactor; hence, the cases presented in this Subsection represent the opportunity for the model presented in this dissertation to simulate LDCFB reactors. He used a capacitance probe to measure radial voidage profiles in a 5 m tall, 0.083 m diameter riser fluidizing Lane Mount Silica Sand ($D_p = 208\,\mu$m, $\rho_p = 2580\,\mathrm{kg\,m^{-3}}$) with air. The riser had an abrupt exit but axial pressure gradient profiles indicate that densification at the exit was not too severe for several of the experiments, which is plausible (Pugsley et al., 1997). Therefore, comparisons between the predictions of the model presented in this dissertation and certain experimental data obtained by Pugsley (1995) can be made.

Unfortunately, there is no report of the operating temperature or inlet pressure so the inlet temperature is fixed 300 K for all simulations in this Subsection. Additionally, the inlet pressure is set to allow for an outlet pressure greater than atmospheric.

The data in Figure 48 (Page 134) correspond to an inlet superficial gas velocity of $5\,\mathrm{m\,s^{-1}}$ and an inlet solids mass flux of $240\,\mathrm{kg\,m^{-2}s^{-1}}$. The inlet pressure is set at 115.0 kPa and the resulting outlet pressure and LZUZI are 101.5 kPa and 0.49, respectively. The experimental error is 9% due to the poor fit of the data near the wall; the error in the core region is 2%. Out of all the comparisons of the radial voidage profiles, this case shows the greatest densification near the wall with the voidage of 0.62 approaching the particle minimum fluidization voidage of 0.45.

The data in Figure 49 (Page 135) correspond to an inlet superficial gas velocity of $6\,\mathrm{m\,s^{-1}}$ and an inlet solids mass flux of $360\,\mathrm{kg\,m^{-2}s^{-1}}$. An inlet pressure of 117.0 kPa results in an outlet pressure of 101.0 kPa and LZUZI of $z_i = 0.5$. Again, the model prediction for the voidage in the core is good but is quite over predicted at the wall. Clearly, the predicted curve should be flatter in the core and decrease more rapidly near the wall. Nonetheless, the overall experimental error is less than 5%.

The data in Figure 50 (Page 137) correspond to an inlet solids mass flux of

Figure 48: Voidage Profile Comparison With Experimental Data From Pugsley, 1995 ($z = 0.5$, $u_{gin} = 5\,\mathrm{m\,s^{-1}}$, $G_{sin} = 240\,\mathrm{kg\,m^{-2}s^{-1}}$, $H = 5\,\mathrm{m}$, $D = 0.083\,\mathrm{m}$, $\rho_p = 2580\,\mathrm{kg\,m^{-3}}$, $D_p = 208\,\mu\mathrm{m}$)

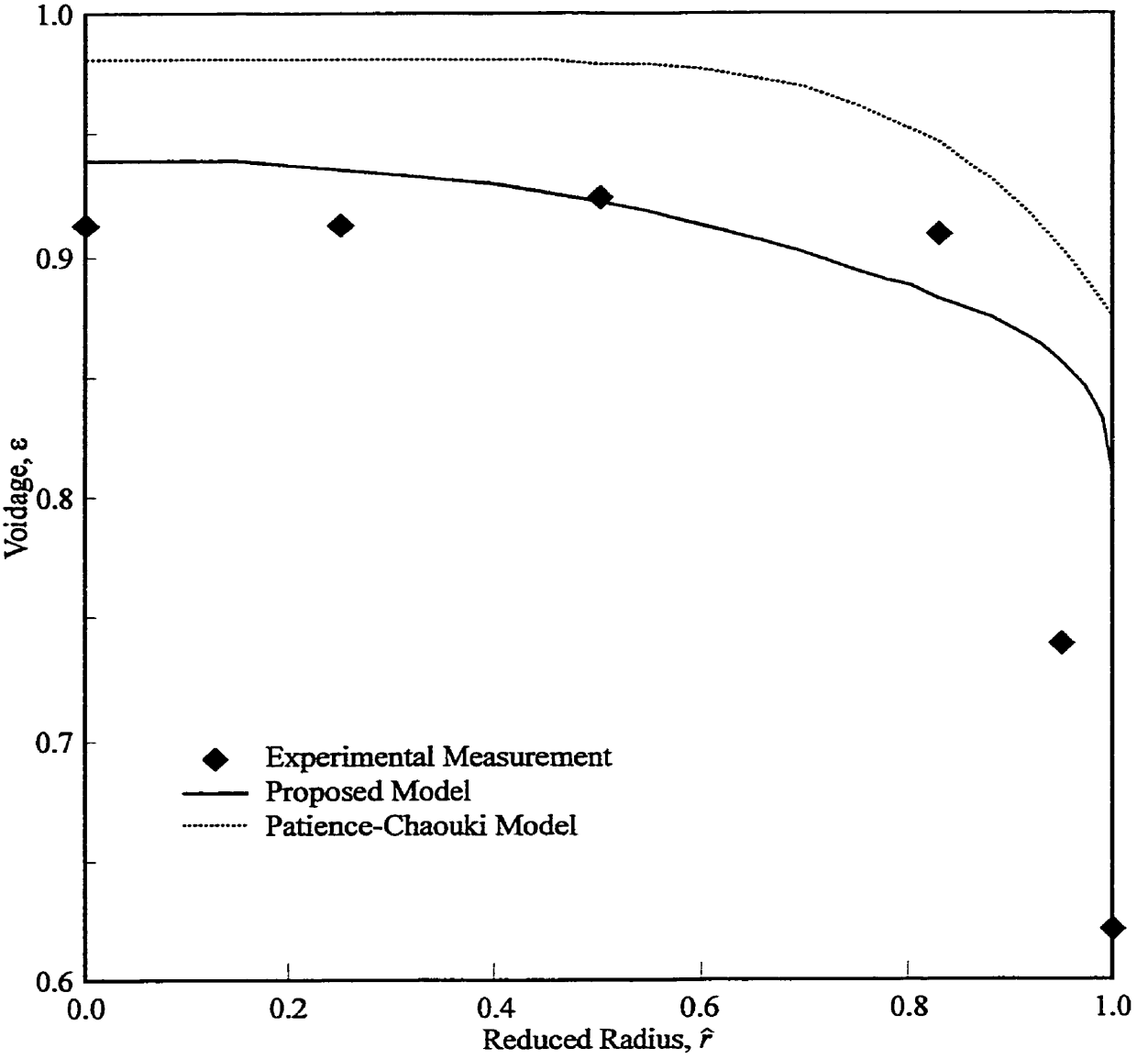

Radial Profile Parameters For The Predicted Values In Figure 48

$\hat{r}_c$=0.866	a	b	c	d	e	f
$\hat{G}$	4.64808	4.57728	-2.23700	9.82789	0.678393	7.31949
u_s	5.12102	2.23039	-1.40180	9.98086	1.040262	8.75130

Figure 49: Voidage Profile Comparison With Experimental Data From Pugsley, 1995 ($z = 0.5$, $u_{gin} = 6\,\mathrm{m\,s^{-1}}$, $G_{sin} = 360\,\mathrm{kg\,m^{-2}s^{-1}}$, $H = 5\,\mathrm{m}$, $D = 0.083\,\mathrm{m}$, $\rho_p = 2580\,\mathrm{kg\,m^{-3}}$, $D_p = 208\,\mu\mathrm{m}$)

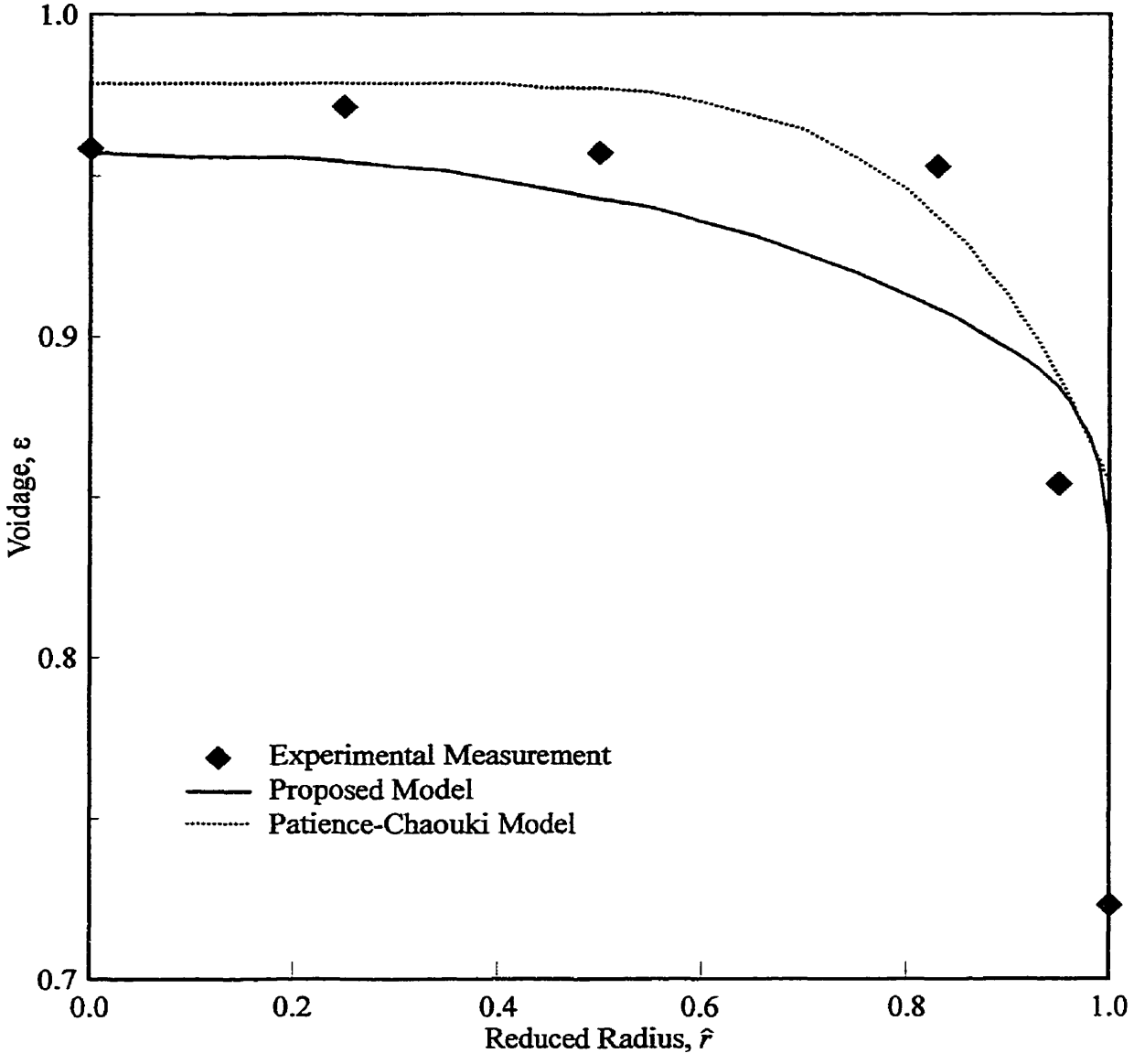

Radial Profile Parameters For The Predicted Values In Figure 49

$\hat{r}_c$=0.878	a	b	c	d	e	f
$\hat{G}$	4.31020	5.25558	-2.12449	9.66134	0.659448	7.25881
u_s	6.30755	2.29213	-1.61679	13.2261	1.068176	11.8378

$450\,\mathrm{kg\,m^{-2}s^{-1}}$. The experimental inlet superficial gas velocity is $6\,\mathrm{m\,s^{-1}}$ but the model presented in this dissertation fails to determine the LZUZI at that operating condition, likely because the inlet solids mass flux is outside the range of data used to generate the re-circulation ratio correlation. However, the model can calculate the LZUZI using an inlet superficial gas velocity of $6.5\,\mathrm{m\,s^{-1}}$, which generates the predicted curve in Figure 50. The LZUZI is $z_i = 0.51$ with an inlet pressure of 119.0 kPa. The resultant outlet pressure is 100.8 kPa. In this case the voidage at the wall is under predicted, which disrupts the trend of over prediction of the voidage at the wall.

Figure 50: Voidage Profile Comparison With Experimental Data From Pugsley, 1995 ($z = 0.5$, $u_{gin} = 6.5\,\mathrm{m\,s^{-1}}$, $G_{sin} = 450\,\mathrm{kg\,m^{-2}s^{-1}}$, $H = 5\,\mathrm{m}$, $D = 0.083\,\mathrm{m}$, $\rho_p = 2580\,\mathrm{kg\,m^{-3}}$, $D_p = 208\,\mu\mathrm{m}$)

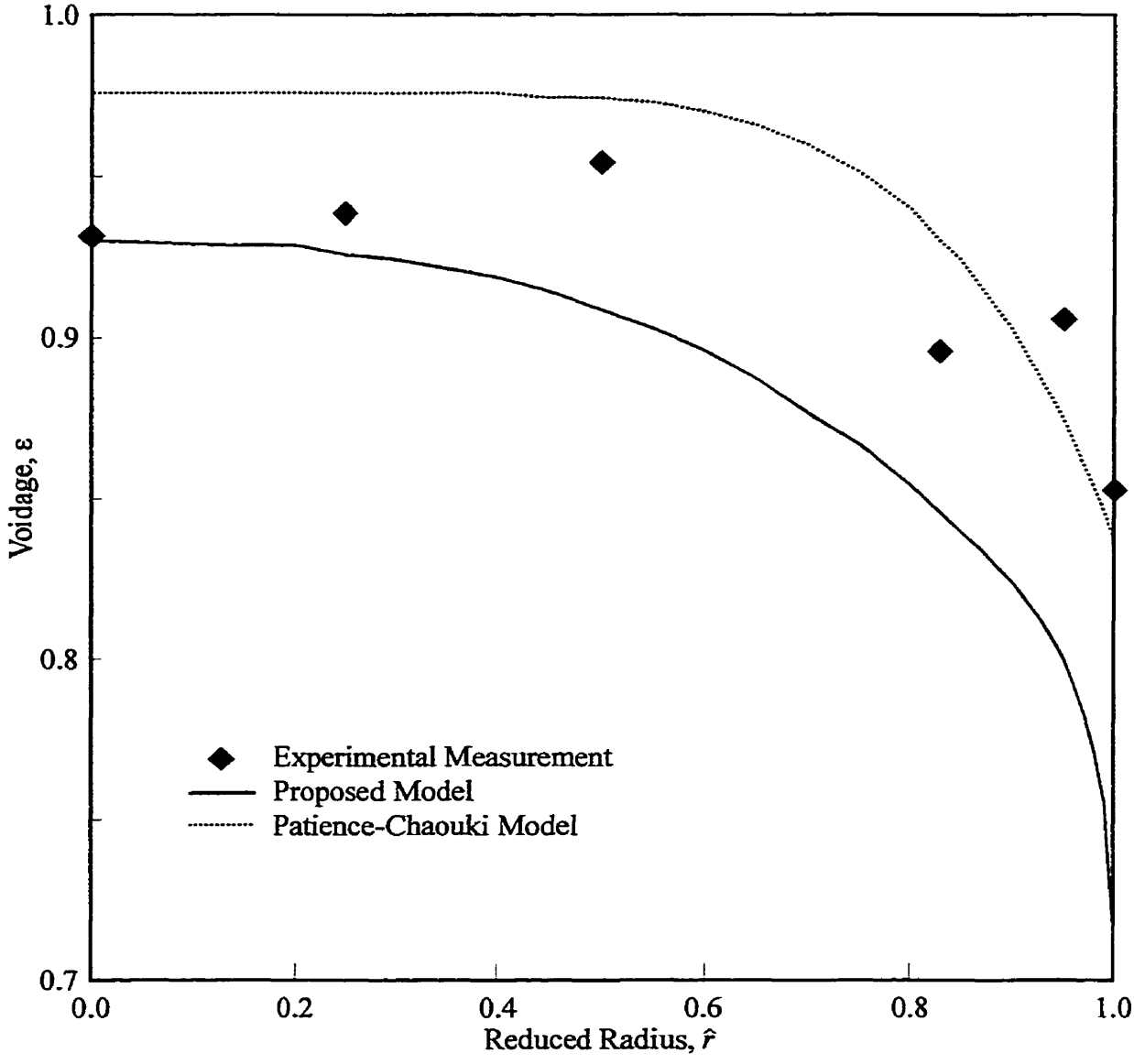

Radial Profile Parameters For The Predicted Values In Figure 50

$\hat{r}_c$=0.885	a	b	c	d	e	f
$\hat{G}$	4.13515	5.70153	-2.06365	9.59084	0.648855	7.24463
u_s	6.85489	2.32733	-1.68529	15.0307	1.083774	13.5998

5.3.4 Hartge et al., 1988

In addition to radial solids velocity profiles, Hartge et al. (1988) also present data for radial solids concentrations in the 8.4 m tall, 0.4 m diameter riser. The axial sampling locations for the radial profiles are coincidental with their solids velocity counterparts; however, the radial sampling locations are not. Consequently, indirect calculation of the solids mass flux profiles, with a reasonable degree of accuracy, is not possible. In this Subsection, the experimental solids concentration profiles are converted to voidage profiles.

To recapitulate the operating conditions that Hartge et al. (1988) use, the inlet superficial gas velocity is $2.9\,\mathrm{m\,s^{-1}}$, inlet solids mass flux is $49\,\mathrm{kg\,m^{-2}s^{-1}}$, and the inlet pressure and temperature are assumed to be 106.0 kPa and 300 K, respectively.

The axial sampling location for the voidage profile in Figure 51 (Page 139), which corresponds to the solids velocity profile in Figure 40, is $z = 0.11$. The overall error between the model prediction and experimental data is 18%. The axial sampling location is close to the base of the riser where the model specifies the voidage as the minimum fluidization voidage—0.45 in this case. Despite that, the average predicted voidage at $z = 0.11$ is approximately 0.95, which over predicts the experimental data substantially. This phenomenon suggests that either the prescribed center-line solids velocity profile increases too rapidly or the center-line solids mass flux profile does not increase rapidly enough.

The axial sampling location for the data in Figure 52 (Page 140), which corresponds to the solids velocity profile in Figure 41, is 0.32. The overall error between the model prediction and experimental data is only 1%. Near the wall, where the solids velocity profile prediction is excellent, the error is less than 0.1%.

The final comparison between the predictions of the model presented in this dissertation and the experimental radial voidage profiles that Hartge et al. (1988) present is shown in Figure 53 (Page 142). The corresponding radial solids velocity profile at $z = 0.56$ is shown in Figure 42. In this case, the voidage is under predicted through-

Figure 51: Radial Voidage Profile Comparison With Experimental Data From Hartge et al., 1988 ($z = 0.11$, $u_{gin} = 2.9\,\mathrm{m\,s^{-1}}$, $G_{sin} = 49\,\mathrm{kg\,m^{-2}s^{-1}}$, $H = 8.4\,\mathrm{m}$, $D = 0.4\,\mathrm{m}$, $\rho_p = 1500\,\mathrm{kg\,m^{-3}}$, $D_p = 85\,\mu\mathrm{m}$)

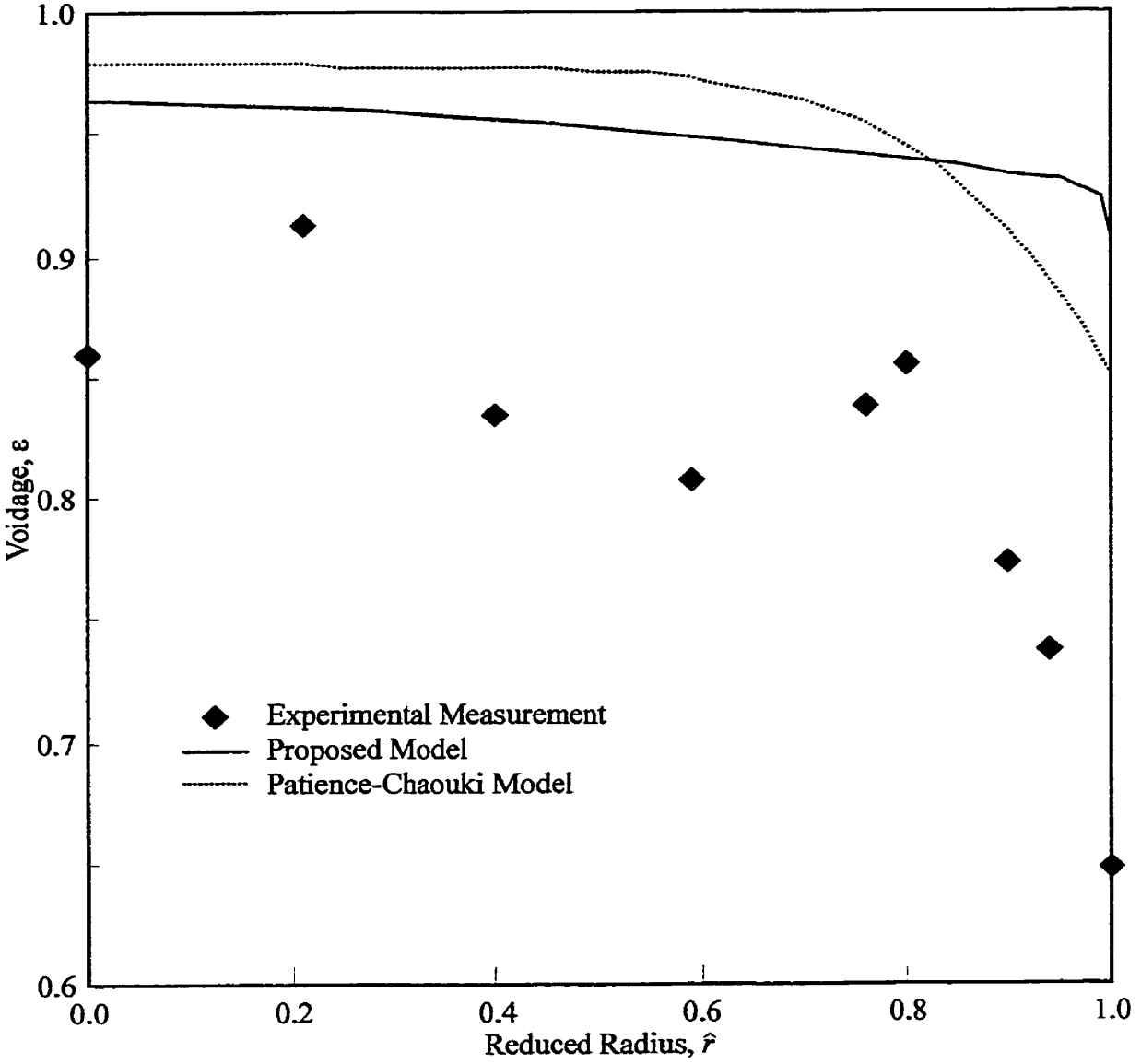

Radial Profile Parameters For The Predicted Values In Figure 51

$\hat{r}_c$=0.903	a	b	c	d	e	f
$\hat{G}$	3.03529	3.25856	-0.854983	4.84888	0.386316	2.88359
u_s	2.31784	1.82106	-0.391267	2.45344	0.539931	1.75905

Figure 52: Radial Voidage Profile Comparison With Experimental Data From Hartge et al., 1988 ($z = 0.32$, $u_{gin} = 2.9\,\mathrm{m\,s^{-1}}$, $G_{sin} = 49\,\mathrm{kg\,m^{-2}s^{-1}}$, $H = 8.4\,\mathrm{m}$, $D = 0.4\,\mathrm{m}$, $\rho_p = 1500\,\mathrm{kg\,m^{-3}}$, $D_p = 85\,\mu\mathrm{m}$)

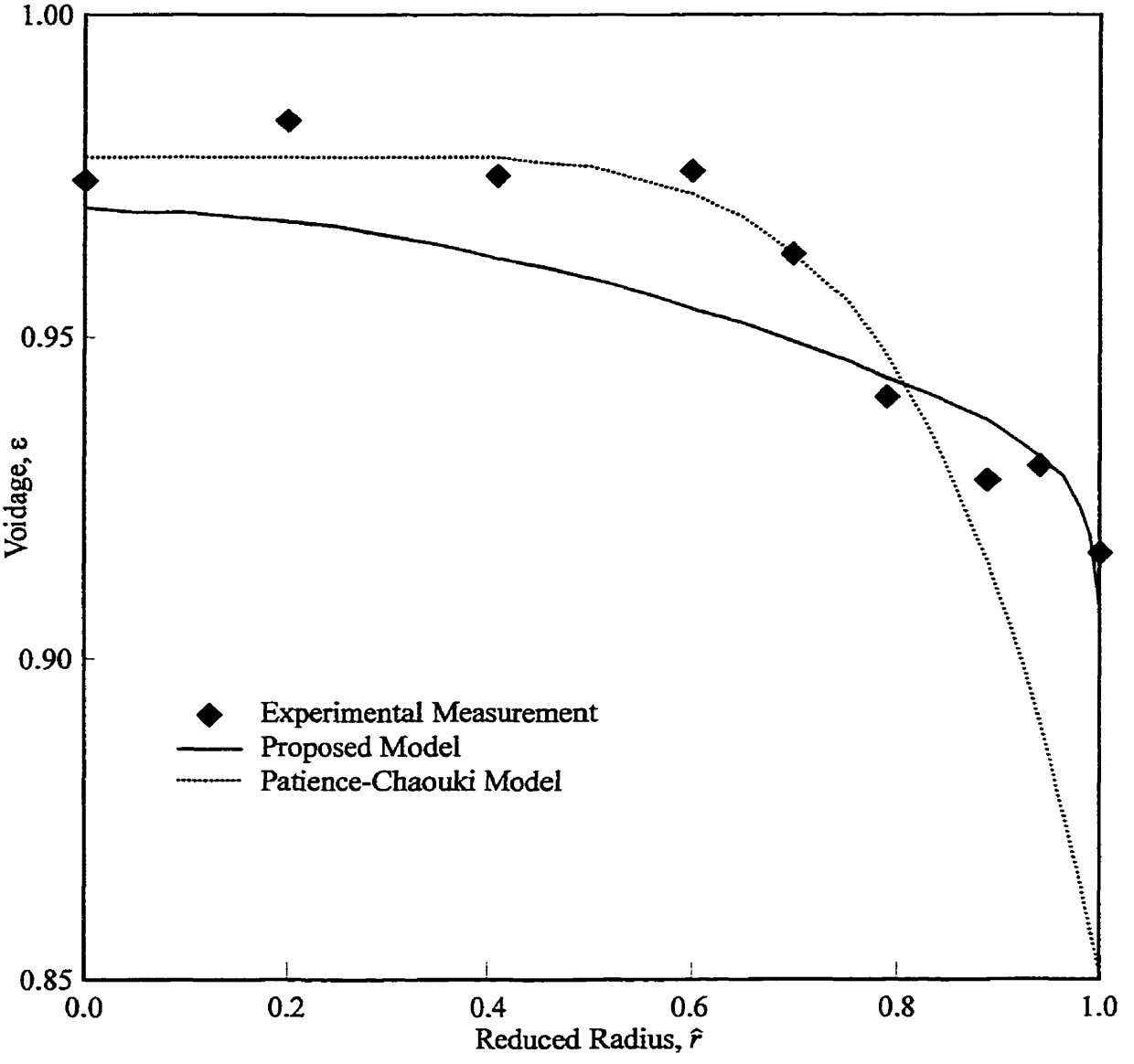

Radial Profile Parameters For The Predicted Values In Figure 52

$\hat{r}_c$=0.867	a	b	c	d	e	f
$\hat{G}$	4.29809	3.86539	-1.813471	8.18713	0.591813	5.71513
u_s	3.50947	1.90587	-0.831009	5.29195	0.890302	4.41854

out the radial domain but the shape of the predicted curve is good. This qualitative assessment is substantiated by translating the predicted voidage profile by +0.02 since the resulting error is less than 1%.

Table 12 presents a summary of the comparisons in this Subsection.

Table 12: Qualitative Assessment Of The Comparisons Between Experimental Radial Voidage Profiles And Predictions By The Proposed LDCFB Model

	Per Cent Error	Number Of Cases
Very Good	<3%	3
Good	3–4%	3
Satisfactory	5–6%	1
Poor	>6%	2

Figure 53: Radial Voidage Profile Comparison With Experimental Data From Hartge et al., 1988 ($z = 0.56$, $u_{gin} = 2.9\,\mathrm{m\,s^{-1}}$, $G_{sin} = 49\,\mathrm{kg\,m^{-2}s^{-1}}$, $H = 8.4\,\mathrm{m}$, $D = 0.4\,\mathrm{m}$, $\rho_p = 1500\,\mathrm{kg\,m^{-3}}$, $D_p = 85\,\mu\mathrm{m}$)

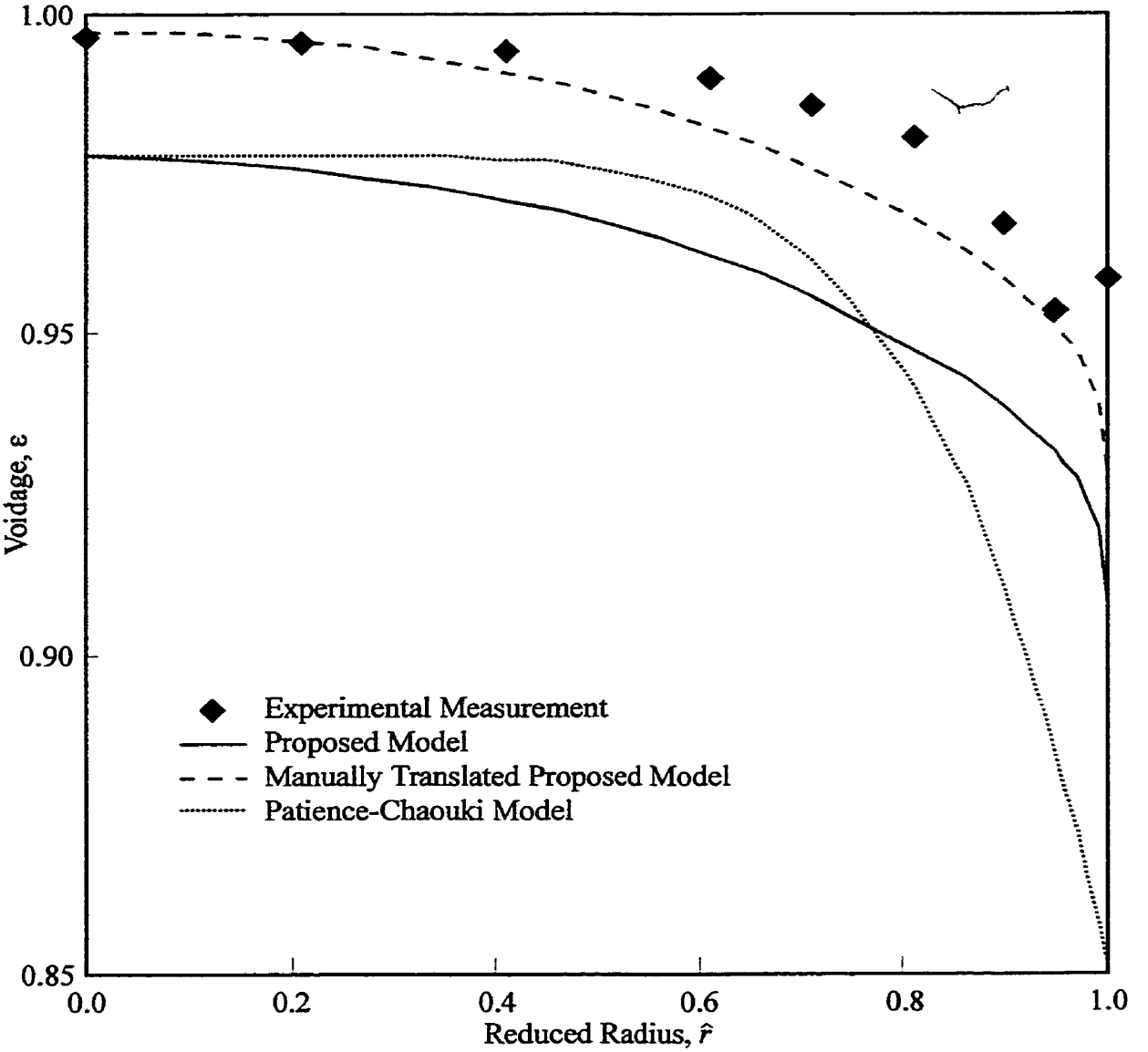

Radial Profile Parameters For The Predicted Values In Figure 53

$\hat{r}_c$=0.903	a	b	c	d	e	f
$\hat{G}$	3.16692	5.01705	-1.260407	7.32282	0.674531	5.81340
u_s	3.32612	1.83756	-0.564177	5.71449	1.012970	5.18118

5.4 Axial Voidage Profiles

Another quantitative measure of the applicability of a hydrodynamic model for an LDCFB riser is the axial voidage profile. Typically, researchers indirectly obtain the profile by measuring pressure differentials along the length of the riser and equating them with the static head of solids, which is proportional to the cross-sectional average of the voidage at a particular axial location. This calculation is erroneous, as shown by the development of Equation 60, because of the omission of the contribution of the solids acceleration to the pressure gradient. Though specious, the erroneous calculation method is a de facto standard for judging model capabilities and this Section provides three comparisons using this basis.

5.4.1 Hartge et al., 1988

The now familiar experiments of Hartge et al. (1988) form the first comparison in this Subsection. Figure 54 (Page 144) corresponds to an inlet superficial gas velocity of $2.9\,\mathrm{m\,s^{-1}}$ and inlet solids mass flux of $49\,\mathrm{kg\,m^{-2}s^{-1}}$ to their 8.4 m tall, 0.4 m diameter riser fluidizing FCC catalyst ($D_p = 85\,\mu\mathrm{m}$, $\rho_p = 1500\,\mathrm{kg\,m^{-3}}$) with air. The error between the predicted voidage, which is the weighted sum of the average voidage in the core and annular regions, respectively, and the experimental voidage is slightly greater than 3% over the length of the riser. The greatest discrepancy is at the base of the riser where the acceleration of the solids is greatest. As mentioned, neglecting the acceleration is erroneous and doing so results in artificially low voidages. In the upper portion of the riser, where acceleration effects are less prevalent, the difference between the prediction of the model presented in this dissertation and the experimental data is only 1%.

Figure 54: Axial Voidage Profile Comparison With Experimental Data From Hartge et al., 1988 ($u_{gin} = 2.9\,\mathrm{m\,s^{-1}}$, $G_{sin} = 49\,\mathrm{kg\,m^{-2}s^{-1}}$, $H = 8.4\,\mathrm{m}$, $D = 0.4\,\mathrm{m}$, $\rho_p = 1500\,\mathrm{kg\,m^{-3}}$, $D_p = 85\,\mu\mathrm{m}$)

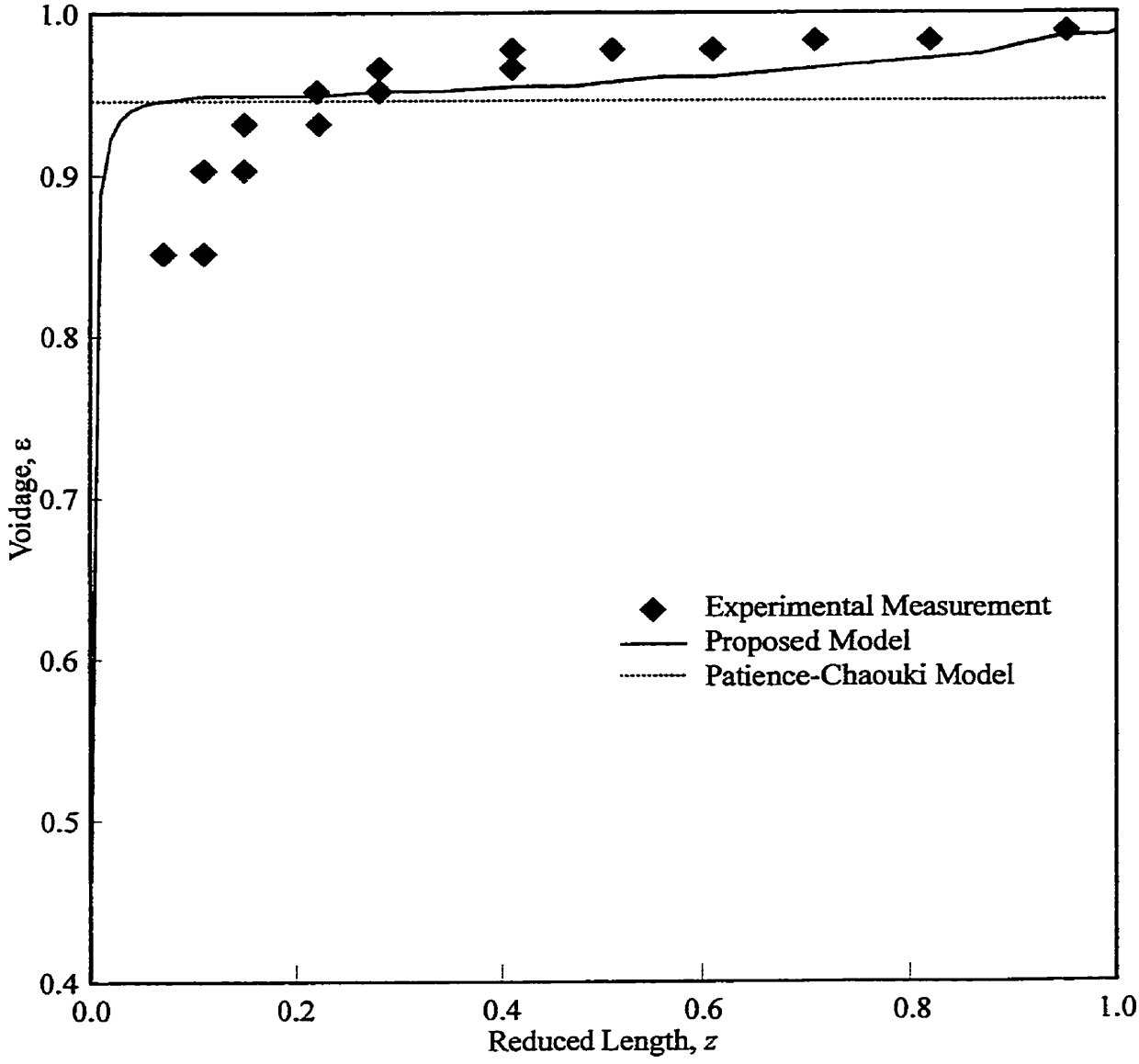

5.4.2 Ouyang et al., 1995

In an effort to minimize the effect of the omission of the acceleration of solids to the pressure gradient (and calculated axial voidage profile), Ouyang et al. (1995) approximate the acceleration contribution empirically. Consequently, both the qualitative and quantitative measures of the model presented in this dissertation are better than in the previous Subsection since the model implicitly includes the effects of the solids acceleration.

Ouyang et al. (1995) used a 10.85 m tall, 0.254 m diameter riser fluidizing spent FCC catalyst ($D_p = 65\,\mu$m, $\rho_p = 1380\,\mathrm{kg\,m^{-3}}$) with air and ozone.

The axial voidage profile data in Figure 55 (Page 146) correspond to an inlet superficial gas velocity of $3.9\,\mathrm{m\,s^{-1}}$ and an inlet solids mass flux of $34\,\mathrm{kg\,m^{-2}s^{-1}}$. The simulation that generates the predicted curve uses state properties at the base of the riser of 105.0 kPa and 300 K. The resulting outlet pressure is 101.1 kPa and LZUZI is $z_i = 0.27$. The comparison between the model prediction and experimental data is outstanding and exhibits an error of less than 1%.

The data in Figure 56 (Page 147) correspond to an inlet superficial gas velocity of $3.8\,\mathrm{m\,s^{-1}}$ and an inlet solids mass flux of $106\,\mathrm{kg\,m^{-2}s^{-1}}$. Specifying the inlet pressure at 113.0 kPa and inlet temperature at 300 K yields an outlet pressure of 101.3 kPa and LZUZI of $z_i = 0.5$. The error between the model prediction and data is less than 3%.

Figure 55: Axial Voidage Profile Comparison With Experimental Data From Ouyang et al., 1995 ($u_{gin} = 3.9\,\mathrm{m\,s^{-1}}$, $G_{sin} = 34\,\mathrm{kg\,m^{-2}s^{-1}}$, $H = 10.85\,\mathrm{m}$, $D = 0.254\,\mathrm{m}$, $\rho_p = 1380\,\mathrm{kg\,m^{-3}}$, $D_p = 65\,\mu\mathrm{m}$)

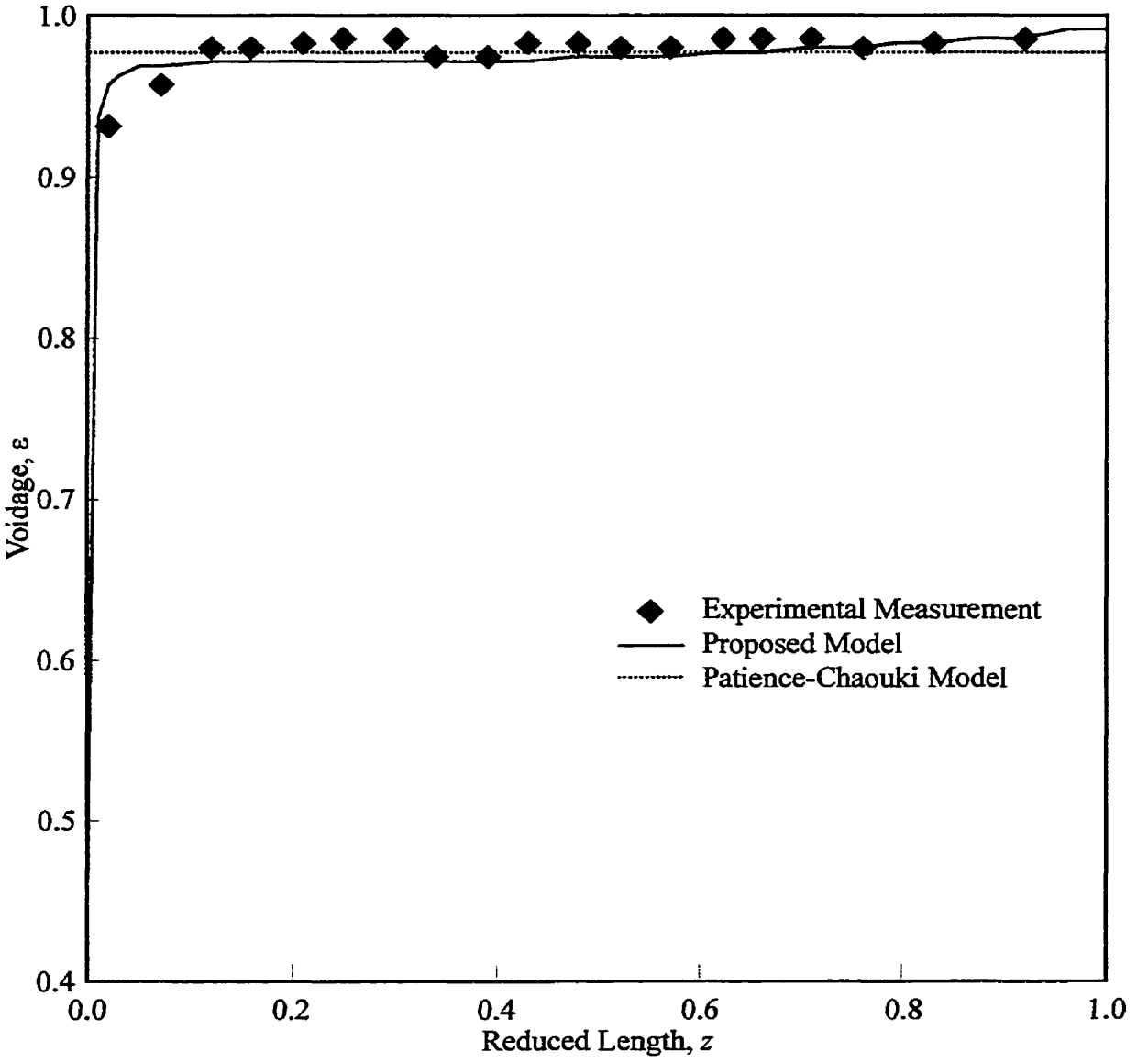

Figure 56: Axial Voidage Profile Comparison With Experimental Data From Ouyang et al., 1995 ($u_{gin} = 3.8\,\mathrm{m\,s^{-1}}$, $G_{sin} = 106\,\mathrm{kg\,m^{-2}s^{-1}}$, $H = 10.85\,\mathrm{m}$, $D = 0.254\,\mathrm{m}$, $\rho_p = 1380\,\mathrm{kg\,m^{-3}}$, $D_p = 65\,\mu\mathrm{m}$)

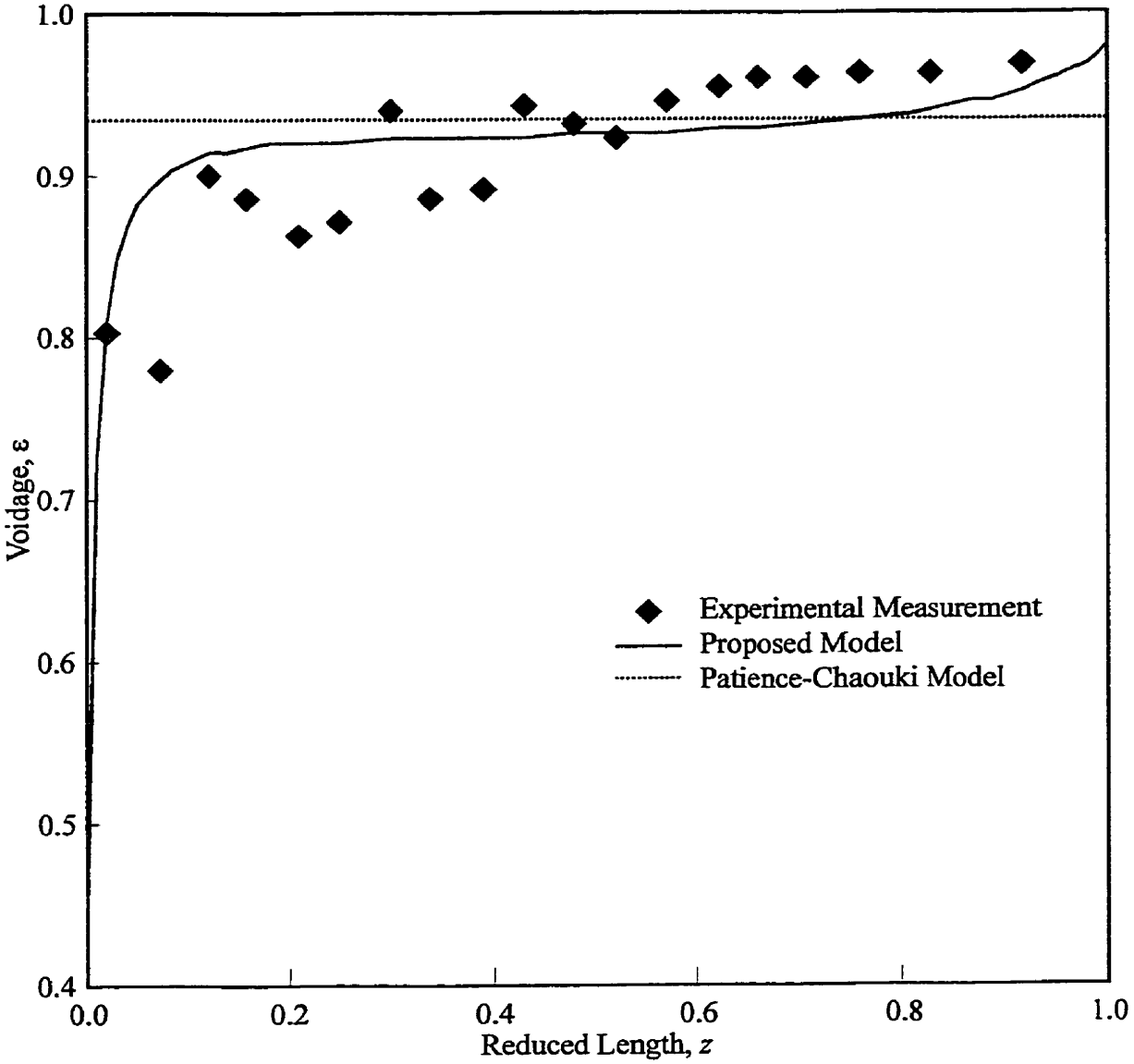

5.5 Axial Pressure Gradient Profiles

Technically, reporting measured axial pressure gradient profiles is more correct than calculated axial voidage profiles for reasons outlined in the previous Subsection. Even so, fluctuations in differential pressure measurements can wreak havoc on both profiles and, consequently, interpretation of the data should only be restricted to a macroscopic scale.

5.5.1 Pugsley, 1995

Pugsley (1995) presents several axial pressure gradient profiles for a 5 m tall, 0.083 m diameter riser fluidizing Lane Mount Silica Sand (D_p=208 μm, ρ_p=2580 kg m^{-3}) with air. Investigation of the effects of varying the inlet superficial gas velocity and solids mass flux are shown in Figures 57 to 62. The inlet superficial gas velocities range from 5.5 to 8.5 m s^{-1} and the inlet solids mass fluxes range from 140 to 400 kg m^{-2}s^{-1}.

Qualitatively, the predictions of the model presented in this dissertation are good for each of the six sets of experimental data. Rather than explicitly examining each of the axial pressure gradient profiles Pugsley (1995) presents, discussion is restricted to the trends in each of the figures because they are invariant.

The first trend to note is the model's over prediction of the magnitude of the pressure gradient. The overall pressure drop through the riser is equal to the area between the pressure gradient curve and the abscissa multiplied by the length of the riser. In these six cases, in a riser with a relatively large length to diameter ratio fluidizing relatively large, heavy particles, the pressure drop is over predicted. The error between the predictions and experimental data diminishes for a fixed inlet solids mass flux and increasing inlet superficial gas velocities as Figures 58, 60, and 61 show.

Interestingly, determination of the approximate location of the LZUZI is possible by inspection of the predicted pressure gradient profile. Recall that the center-line mass flux is a maximum at the LZUZI, which means that the most radical change in momentum in the riser occurs prior to the LZUZI. Since, by Newton's Second Law,

the pressure gradient is proportional to the rate of change of momentum, it is greatest below the LZUZI. Therefore, the location of the LZUZI is near the region where the predicted pressure gradient undergoes a significant decrease in absolute value, i.e. the rate of change of momentum decreases.

The final noteworthy trend in Figures 57 through 62 is the increase in magnitude of the pressure gradient at the exit of the riser, which is most apparent in Figures 61 and 62. Limiting the application of the model presented in this dissertation to risers with smooth exits should preclude predictions of densification at the riser exit, which is typically the cause for an increase in the pressure gradient. Indeed, the increase in the magnitude of the pressure gradient prediction is not a consequence of model development incorporating an abrupt exit, but is rather due to the prescription of the axial mass flux profiles at the center-line and wall and the core radius correlation. Further discussion of this attribute of the model is in Section 6.

Figure 57: Axial Pressure Gradient Profile Comparison With Experimental Data From Pugsley, 1995 ($u_{gin} = 5.5\,\mathrm{m\,s^{-1}}$, $G_{sin} = 140\,\mathrm{kg\,m^{-2}s^{-1}}$, $H = 5\,\mathrm{m}$, $D = 0.083\,\mathrm{m}$, $\rho_p = 2580\,\mathrm{kg\,m^{-3}}$, $D_p = 208\,\mu\mathrm{m}$)

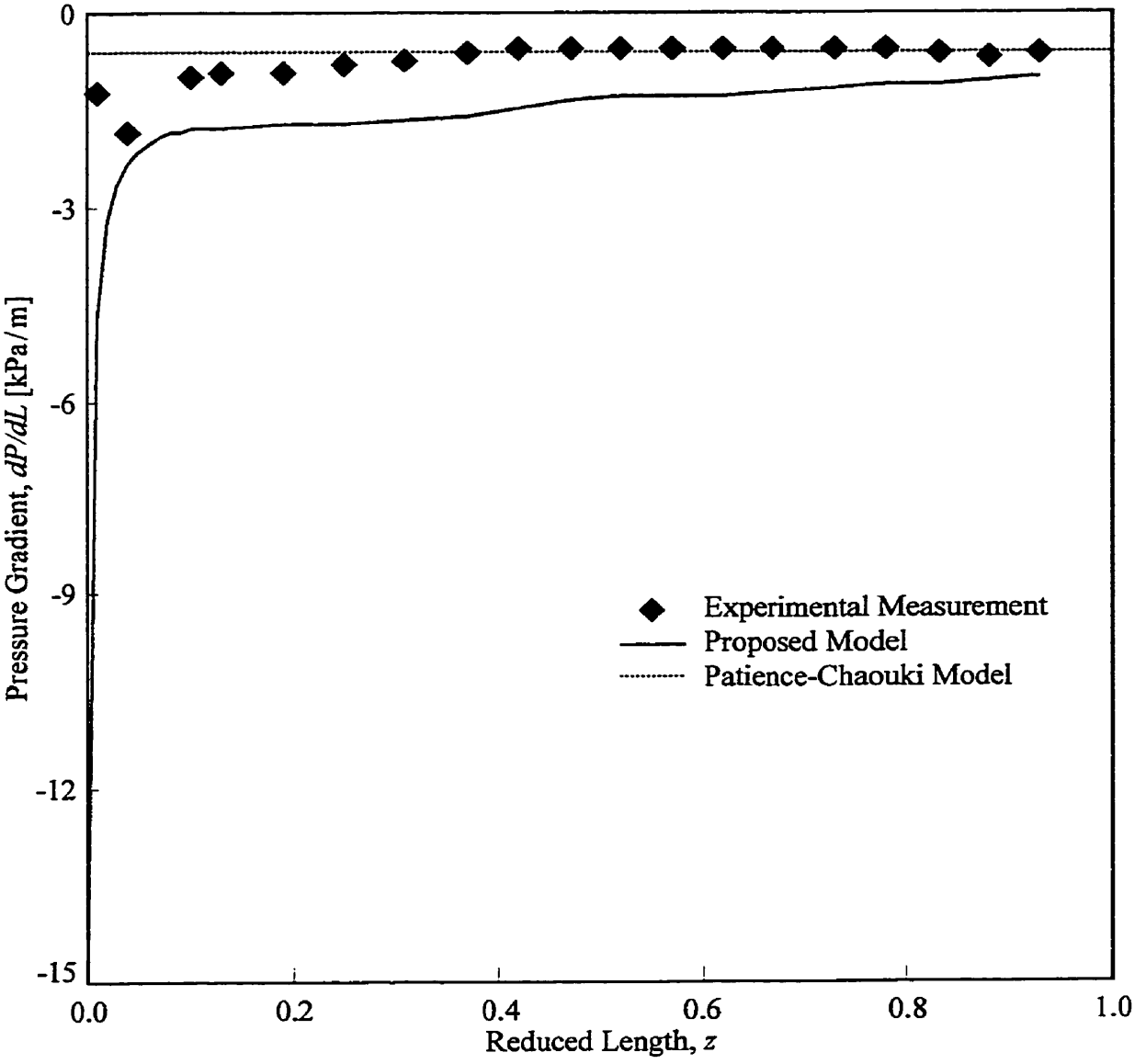

Figure 58: Axial Pressure Gradient Profile Comparison With Experimental Data From Pugsley, 1995 ($u_{gin} = 5.5\,\mathrm{m\,s^{-1}}$, $G_{sin} = 240\,\mathrm{kg\,m^{-2}s^{-1}}$, $H = 5\,\mathrm{m}$, $D = 0.083\,\mathrm{m}$, $\rho_p = 2580\,\mathrm{kg\,m^{-3}}$, $D_p = 208\,\mu\mathrm{m}$)

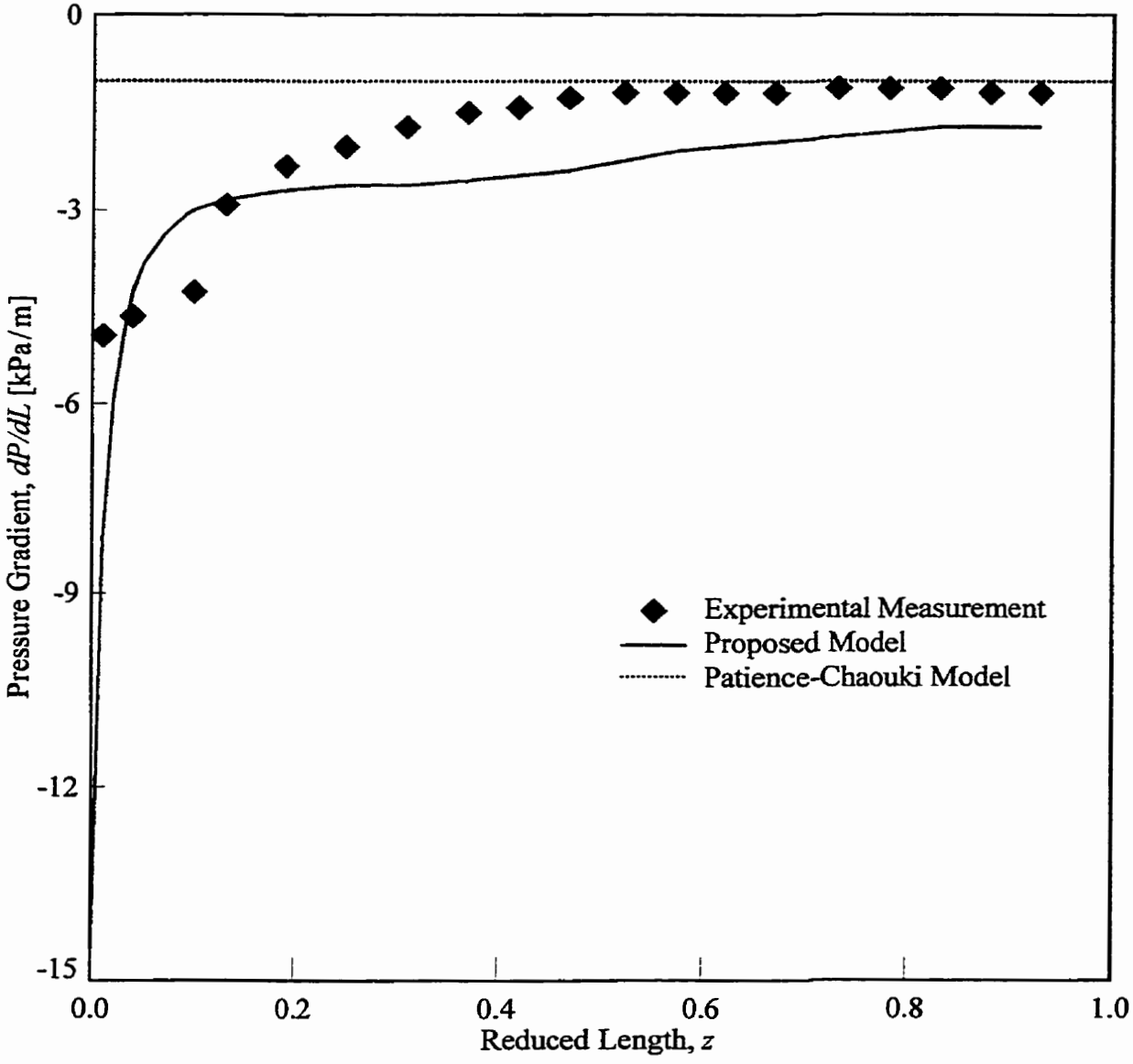

Figure 59: Axial Pressure Gradient Profile Comparison With Experimental Data From Pugsley, 1995 ($u_{gin} = 6.5\,\mathrm{m\,s^{-1}}$, $G_{sin} = 143\,\mathrm{kg\,m^{-2}s^{-1}}$, $H = 5\,\mathrm{m}$, $D = 0.083\,\mathrm{m}$, $\rho_p = 2580\,\mathrm{kg\,m^{-3}}$, $D_p = 208\,\mu\mathrm{m}$)

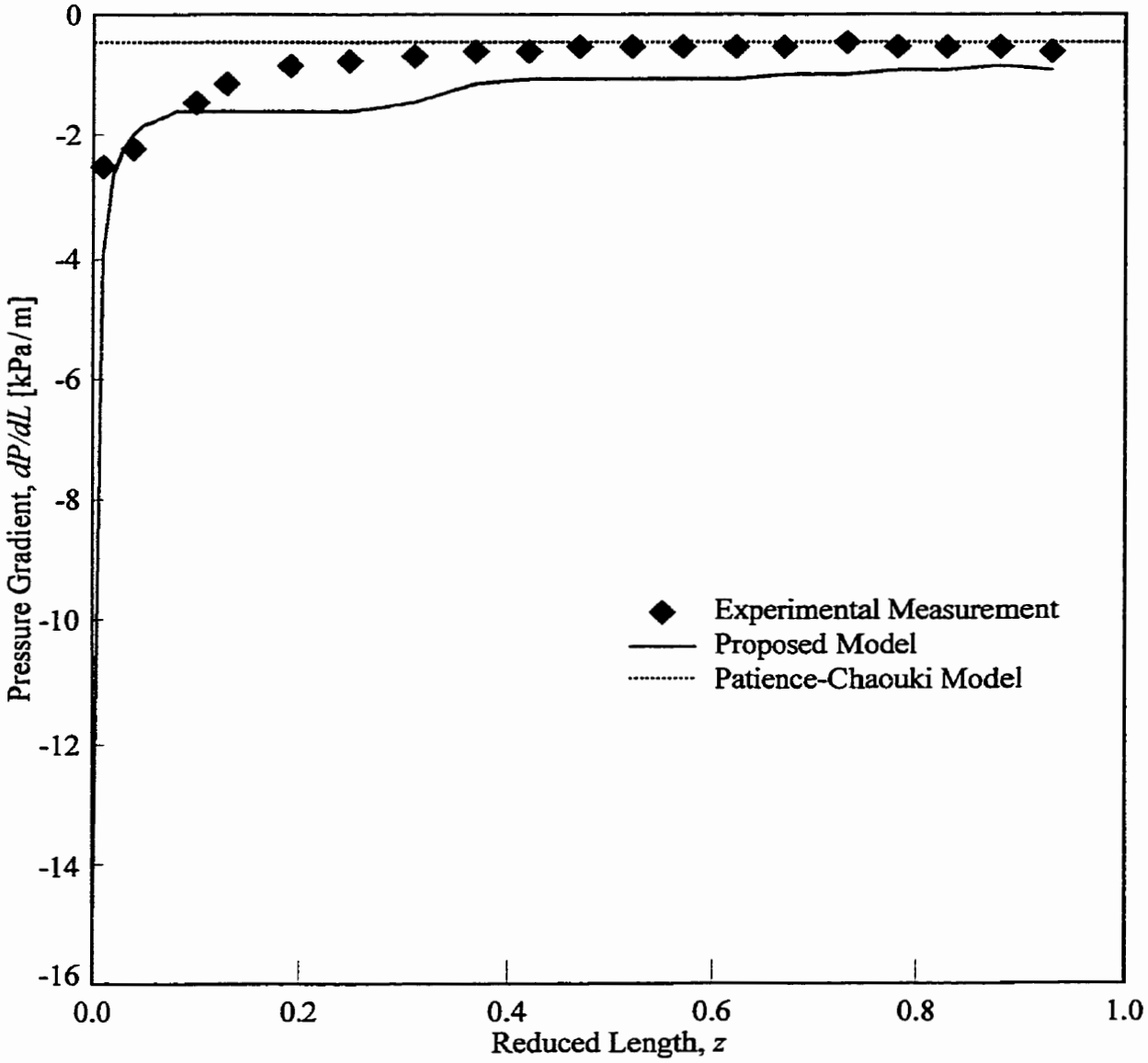

Figure 60: Axial Pressure Gradient Profile Comparison With Experimental Data From Pugsley, 1995 ($u_{gin} = 6.5\,\mathrm{m\,s^{-1}}$, $G_{sin} = 230\,\mathrm{kg\,m^{-2}s^{-1}}$, $H = 5\,\mathrm{m}$, $D = 0.083\,\mathrm{m}$, $\rho_p = 2580\,\mathrm{kg\,m^{-3}}$, $D_p = 208\,\mu\mathrm{m}$)

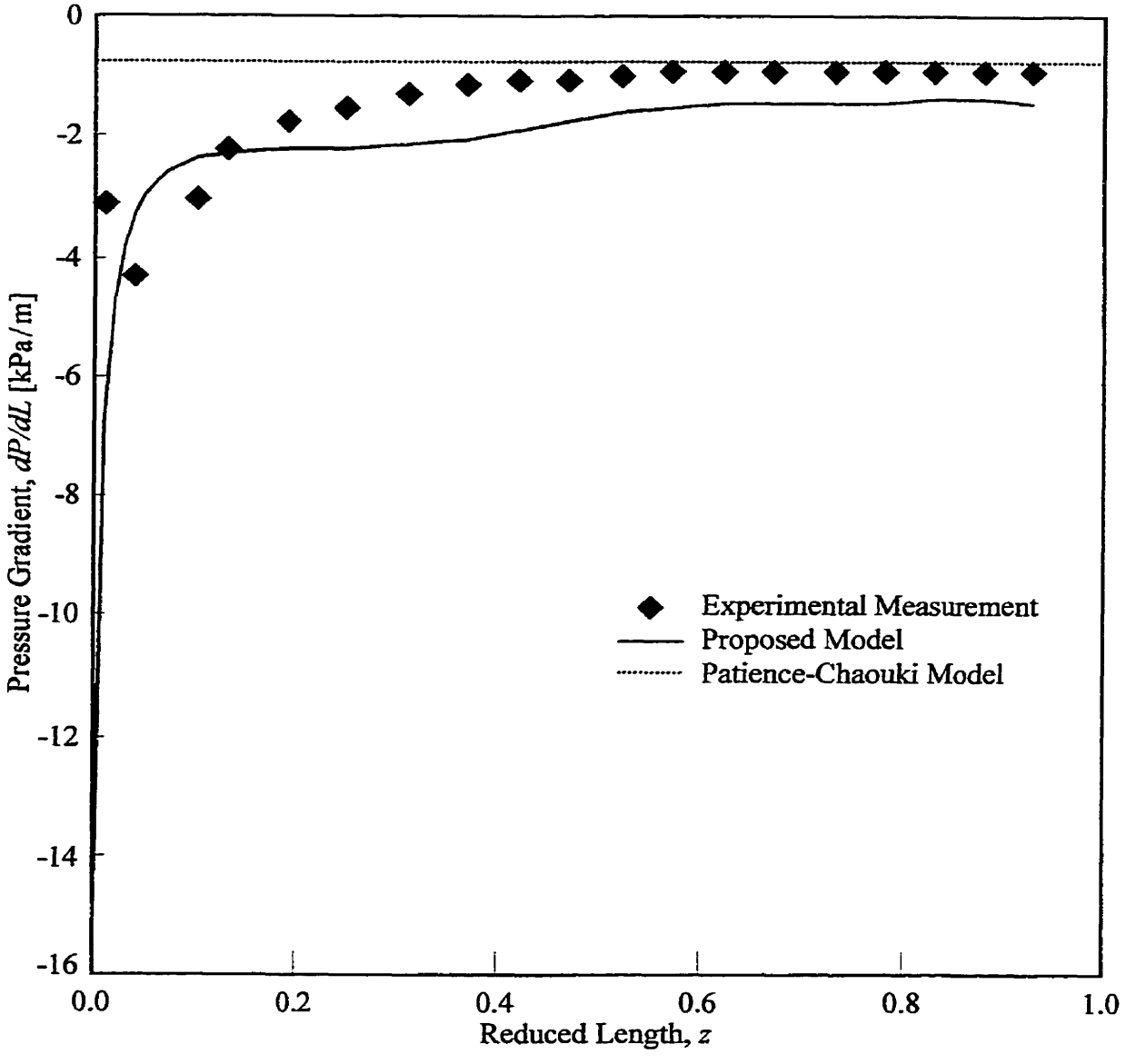

Figure 61: Axial Pressure Gradient Profile Comparison With Experimental Data From Pugsley, 1995 ($u_{gin} = 8.5\,\mathrm{m\,s^{-1}}$, $G_{sin} = 240\,\mathrm{kg\,m^{-2}s^{-1}}$, $H = 5\,\mathrm{m}$, $D = 0.083\,\mathrm{m}$, $\rho_p = 2580\,\mathrm{kg\,m^{-3}}$, $D_p = 208\,\mu\mathrm{m}$)

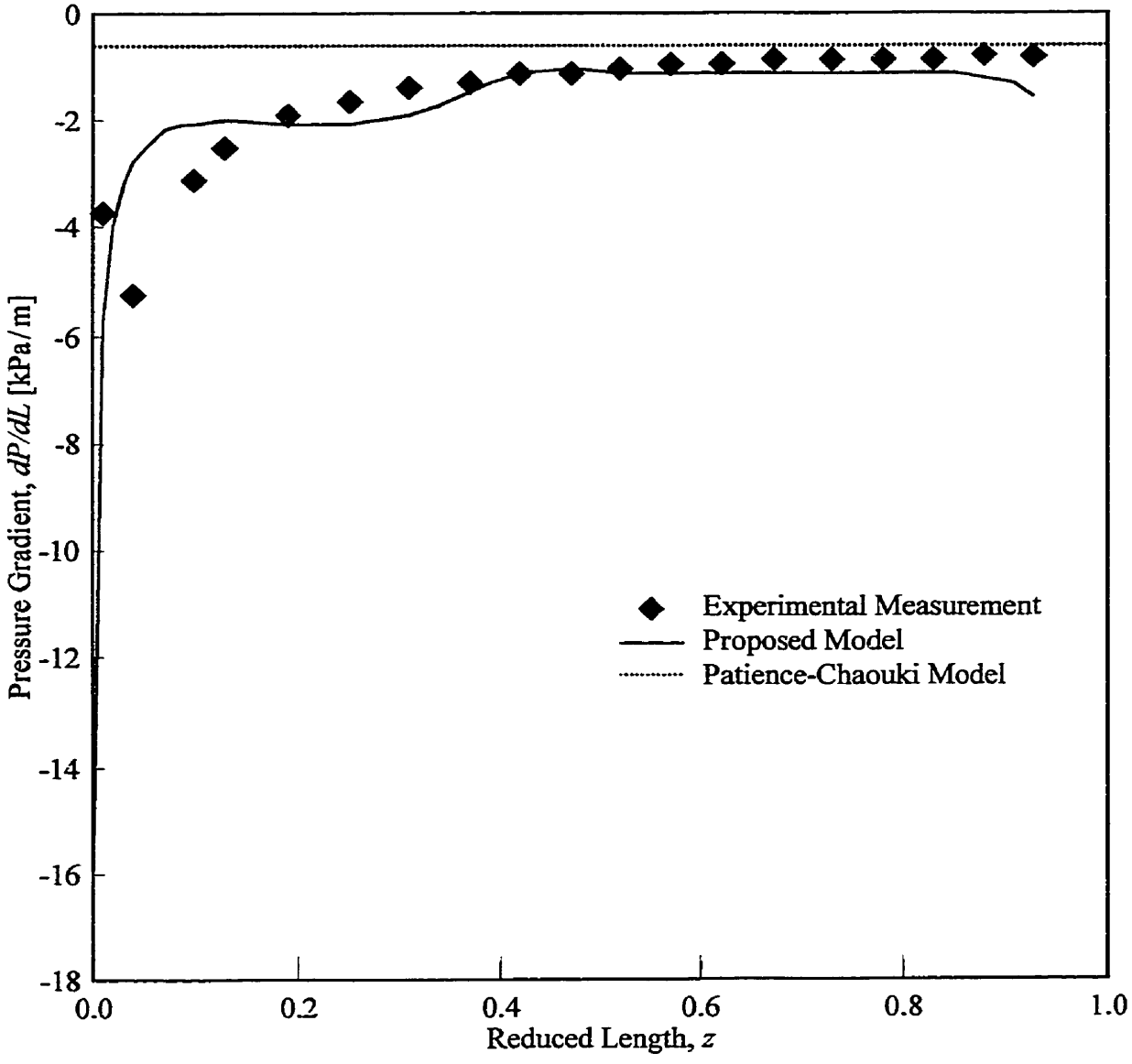

Figure 62: Axial Pressure Gradient Profile Comparison With Experimental Data From Pugsley, 1995 ($u_{gin} = 8.5\,\mathrm{m\,s^{-1}}$, $G_{sin} = 400\,\mathrm{kg\,m^{-2}s^{-1}}$, $H = 5\,\mathrm{m}$, $D = 0.083\,\mathrm{m}$, $\rho_p = 2580\,\mathrm{kg\,m^{-3}}$, $D_p = 208\,\mu\mathrm{m}$)

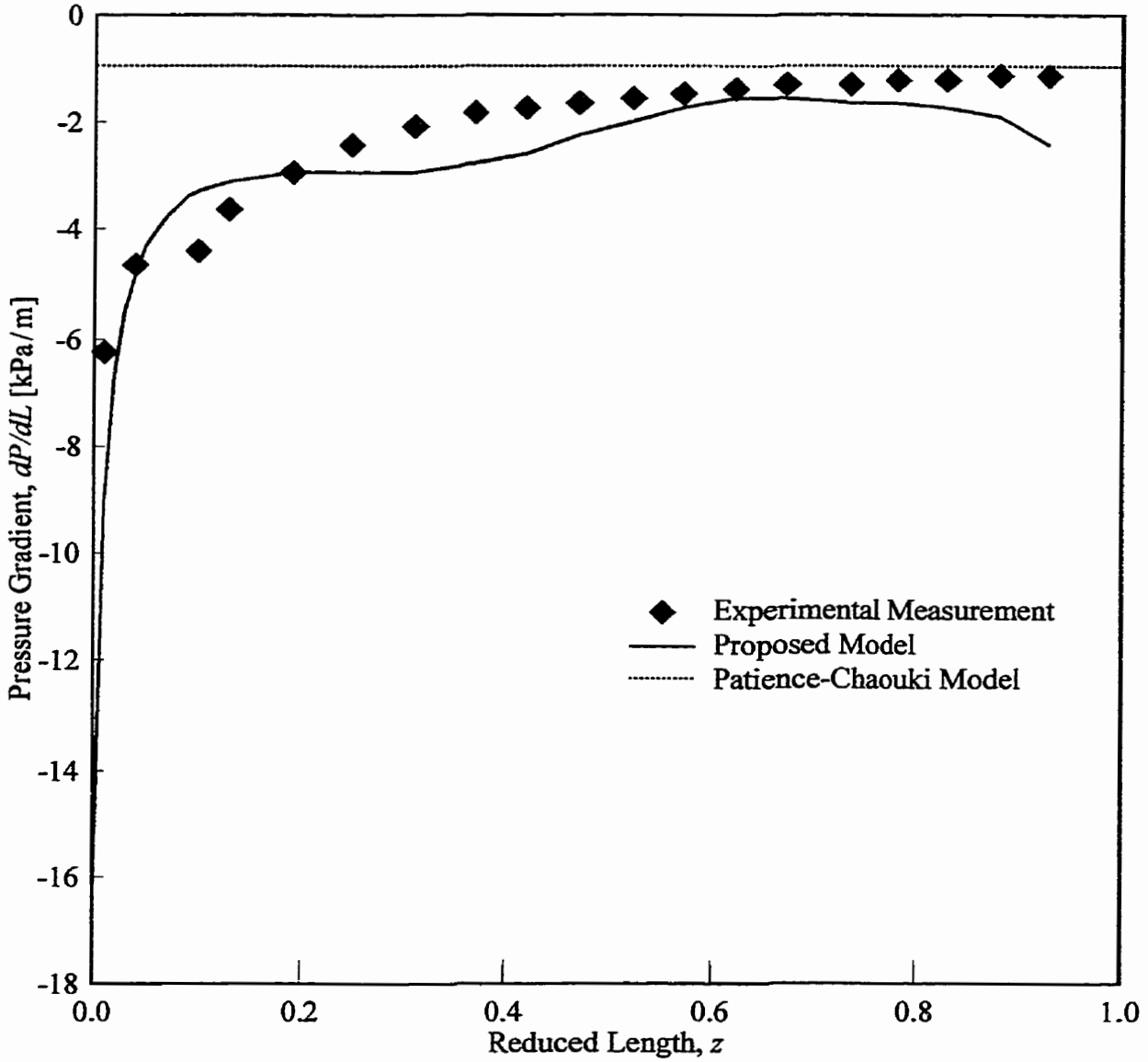

5.5.2 Pugsley et al., 1997

Pugsley et al. (1997) measured axial pressure gradient profiles in a 12 m tall, 0.2 m diameter riser fluidizing FCC catalyst ($D_p = 80\,\mu$m, $\rho_p = 1500\,\mathrm{kg\,m^{-3}}$) using air as the fluidizing agent. The researchers do not report the inlet temperature or pressure to the riser; the simulation uses values of 300 K and 105.0 kPa, respectively, for the state properties to generate the appropriate profile, which allows for adequate pressure for the necessary cyclonic gas-solids separation at the riser outlet.

The data in Figure 63 (Page 157) corresponds to an inlet superficial gas velocity of $5.5\,\mathrm{m\,s^{-1}}$ and an inlet solids mass flux of $46\,\mathrm{kg\,m^{-2}s^{-1}}$. The calculated location of the LZUZI is $z_i = 0.22$ and the calculated outlet pressure is 100.9 kPa. Although the magnitude of the pressure gradient is slightly over predicted, the shape of the predicted profile is excellent.

Figure 63: Axial Pressure Gradient Profile Comparison With Experimental Data From Pugsley et al., 1997 ($u_{gin} = 5.5\,\mathrm{m\,s^{-1}}$, $G_{sin} = 46\,\mathrm{kg\,m^{-2}s^{-1}}$, $H = 12\,\mathrm{m}$, $D = 0.2\,\mathrm{m}$, $\rho_p = 1500\,\mathrm{kg\,m^{-3}}$, $D_p = 80\,\mu\mathrm{m}$)

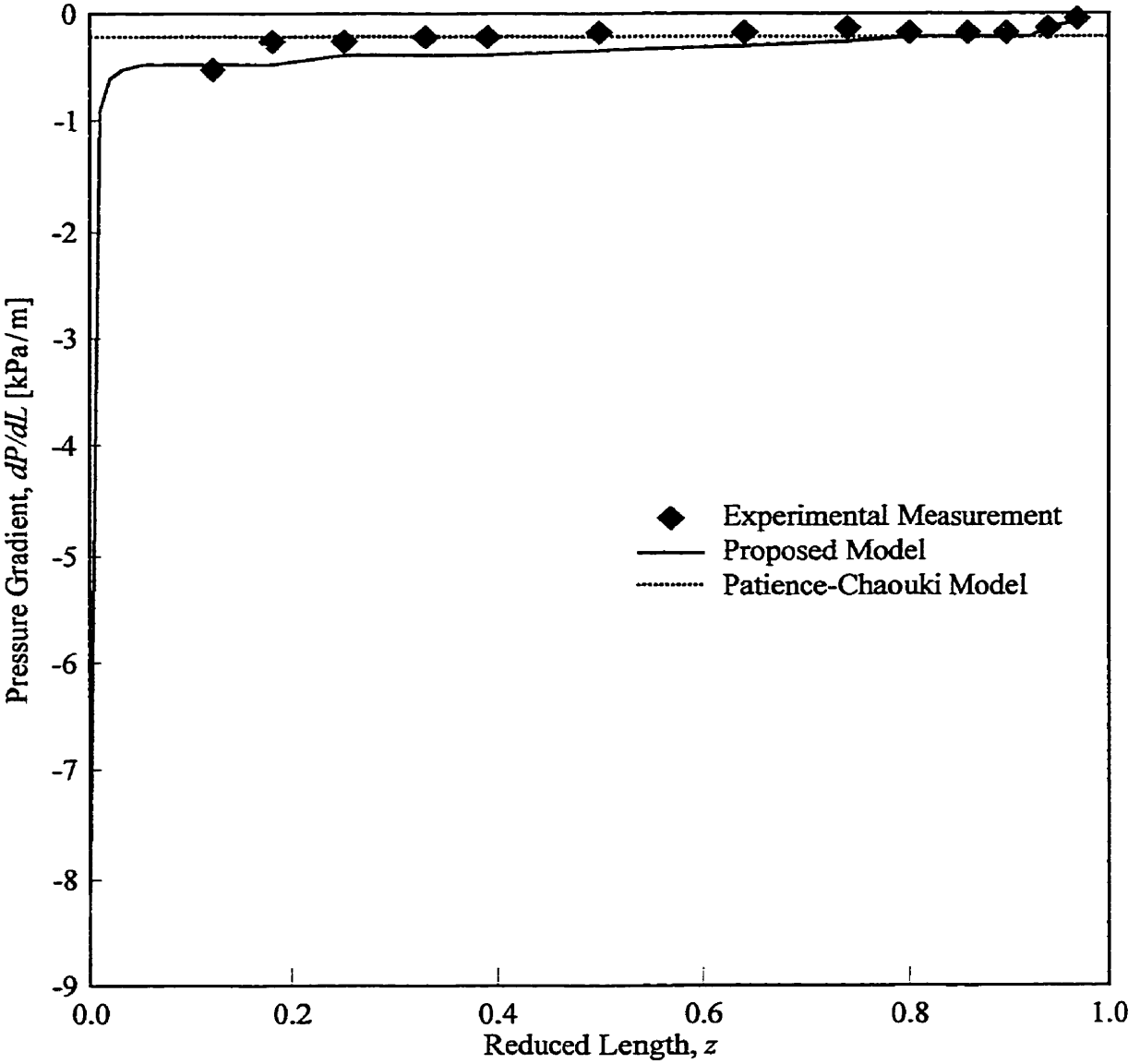

5.6 Residence Time Distributions

The residence time distribution (RTD) of a tracer flowing through a vessel indicates the degree of the mixing inside the vessel, which can affect reaction rates tremendously. Danckwerts (1953) was the first to popularize the use of RTDs to determine the performance of chemical reactors and the ideas presented in his landmark paper are still in use today. For an inert tracer, the fundamental conservation of matter equation,

$$\text{Accumulation} = \text{Input} - \text{Output}, \tag{89}$$

generates the RTD for any reactor. Of course, the complexity of the Input and Output terms can be exacting, particularly on a microscopic scale.

The purpose of this Section is to validate the kinetic reaction model presented in Section 4. Accordingly, the basis for the development of the conservation equation is the simplified hydrodynamic model outlined in Section 4.1. Additionally, the forthcoming equation development requires that the hydrodynamic flow structure in the riser does not vary with time, i.e. the riser is stationary from a hydrodynamic perspective. Application of Equation 89 to the core and annular regions constitutes the RTD for the model.

The terms on the right hand side of Equation 89 consist of axial and radial contributions. Performing a differential mass balance on an inert tracer in the core and grouping the spatial terms appropriately yields:

$$\text{Input} - \text{Output} = -\frac{\partial}{\partial z}\left(\mathcal{F}_c \dot{m}_c\right) dz - 2\pi r_c dz \left(\mathcal{F}_c G_{ca} - \mathcal{F}_a G_{ac}\right), \tag{90}$$

where $\mathcal{F}$ is the mass fraction of tracer and G_{ca} and G_{ac} are the mass fluxes from the core to annulus and annulus to core, respectively. The first term on the right hand side of Equation 90 represents the net axial flow of tracer into the core while the second term represents the net radial flow of tracer into the core.

For a hydrodynamically stationary riser, the temporal term, Accumulation, is the

simplest of the three terms in Equation 89 and is:

$$\text{Accumulation} = \frac{\partial}{\partial t}(\mathcal{F}_c m_c) = \pi r_c^2 dz \rho \frac{\partial \mathcal{F}_c}{\partial t}, \tag{91}$$

where ρ is the bulk density of the phase of interest. Combining Equations 90 and 91 and simplifying the result gives:

$$\pi r_c^2 \rho \frac{\partial \mathcal{F}_c}{\partial t} = -\frac{\partial}{\partial z}(\mathcal{F}_c \dot{m}_c) - 2\pi r_c (\mathcal{F}_c G_{ca} - \mathcal{F}_a G_{ac}), \tag{92}$$

which represents half of the differential equations for the RTD of a particular phase of the simplified hydrodynamic model.

Development of the annular region differential equation is analogous to the core region differential equation. Accounting for the downward flow of matter in the annulus, the mass balance is:

$$\pi(R^2 - r_c^2)\rho \frac{\partial \mathcal{F}_a}{\partial t} = \frac{\partial}{\partial z}(\mathcal{F}_a |\dot{m}_a|) + 2\pi r_c (\mathcal{F}_c G_{ca} - \mathcal{F}_a G_{ac}). \tag{93}$$

Equations 92 and 93 are non-linear, coupled partial differential equations and are the basis for the simplified hydrodynamic model RTD. The next two Subsections segregate the RTDs for the two phases in a riser reactor and describe details of the numerical solution to the resulting equations.

5.6.1 Gas Phase RTD

Equations 92 and 93 become

$$\frac{\partial \mathcal{F}_c}{\partial t} = \frac{-1}{\pi r_c^2 \rho_g \epsilon_c}\left[\dot{m}_c \frac{\partial \mathcal{F}_c}{\partial z} + \mathcal{F}_c \frac{\partial \dot{m}_c}{\partial z} + 2\pi r_c (\mathcal{F}_c G_{ca} - \mathcal{F}_a G_{ac})\right] \tag{94}$$

and

$$\frac{\partial \mathcal{F}_a}{\partial t} = \frac{-1}{\pi (R^2 - r_c^2) \rho_g \epsilon_a}\left[\dot{m}_a \frac{\partial \mathcal{F}_a}{\partial z} + \mathcal{F}_a \frac{\partial \dot{m}_a}{\partial z} - 2\pi r_c (\mathcal{F}_c G_{ca} - \mathcal{F}_a G_{ac})\right] \tag{95}$$

when applied to the gas phase. A convenient solution strategy for solving partial differential equations is to transform them into ordinary differential equations and then use any of a number of integration routines to solve the transformed equations.

Explicitly discretizing the spatial derivatives in Equations 94 and 95 creates a system of ordinary differential equations—two equations per axial node, one for the core and one for the annulus. At the ith node in the core the equation is:

$$\frac{d\mathcal{F}_c^i}{dt} = \frac{-1}{\pi r_c^2 \rho_g^i \epsilon_c^i} \times \left[\dot{m}_c \left(\frac{\mathcal{F}_c^i - \mathcal{F}_c^{i+1}}{\Delta z}\right) + \mathcal{F}_c^i \left(\frac{\dot{m}_c{}^i - \dot{m}_c{}^{i+1}}{\Delta z}\right) + 2\pi r_c \left(\mathcal{F}_c^i G_{ca}{}^i - \mathcal{F}_a^i G_{ac}{}^i\right)\right]. \tag{96}$$

Similarly, at the ith node in the annular region the equation is:

$$\frac{d\mathcal{F}_a^i}{dt} = \frac{-1}{\pi \left(R^2 - r_c^2\right) \rho_g^i \epsilon_a^i} \times \left[\dot{m}_a \left(\frac{\mathcal{F}_a^i - \mathcal{F}_a^{i+1}}{\Delta z}\right) + \mathcal{F}_a^i \left(\frac{\dot{m}_a{}^i - \dot{m}_a{}^{i+1}}{\Delta z}\right) - 2\pi r_c \left(\mathcal{F}_c^i G_{ca}{}^i - \mathcal{F}_a^i G_{ac}{}^i\right)\right]. \tag{97}$$

After solving the stationary hydrodynamics, Equations 97 and 98 describe the gas phase RTD. The data in Figure 64 (Page 162) are an example of the dynamic solution of the simplified hydrodynamic model. Patience and Chaouki (1993) obtained the experimental data shown in Figure 64 by injecting radioactive Argon into a 5 m tall, 0.083 m diameter riser fluidizing sand ($D_p = 277\,\mu$m, $\rho_p = 2630\,\mathrm{kg\,m^{-3}}$) with air. The data correspond to an inlet superficial gas velocity of $6.07\,\mathrm{m\,s^{-1}}$ and an inlet solids mass flux of $134\,\mathrm{kg\,m^{-2}s^{-1}}$. The pulse injection mechanism is a syringe protruding 2 mm into the riser 0.1 m above the gas distributor. The exact form of the input pulse is not known so the response curve from the first of two detectors, located 1 m above the distributor, is input to the second, located just after the riser exit. Suspension density profiles that Patience and Chaouki (1993) present incontrovertibly evidence the influence of the abrupt exit on the solids hydrodynamics. Undoubtedly, the exit geometry affects the gas phase too since the experimental data for the response curve in Figure 64 exhibits quite a lengthy tail that is many times greater than the tail on the input curve.

The detectors (scintillators) cannot differentiate between a signal from the core or annulus; therefore, the data in Figure 64 are the superposition of the tracer RTD

in both the regions. For the simulation, because the proposed model segregates the core and annular regions, the distribution of the tracer input pulse is proportional to the mass flow rate in each of the respective regions.

The leading edge of the predicted gas phase RTD generated by the model presented in this dissertation matches the steepness of the experimental response curve. The breakthrough times exhibit a difference of only 0.03 seconds. However, the abrupt exit causes significant spreading of the response curve and, consequently, the peak in the predicted curve is greater than the measured curve. There is a significant tail on the predicted curve but it fails to represent the experimental data because of the incongruence between the model restrictions and physical characteristics of the riser.

The differences between the predicted and measured RTDs in Figure 64 demonstrate that application of the model presented in this dissertation should be to risers that comply to the restrictions outlined in the model development.

Figure 64: Gas Phase RTD Comparison With Experimental Data From Patience And Chaouki, 1993 ($u_{gin} = 6.07\,\mathrm{m\,s^{-1}}$, $G_{sin} = 134\,\mathrm{kg\,m^{-2}s^{-1}}$, $H = 5\,\mathrm{m}$, $D = 0.083\,\mathrm{m}$, $\rho_p = 2630\,\mathrm{kg\,m^{-3}}$, $D_p = 277\,\mu\mathrm{m}$)

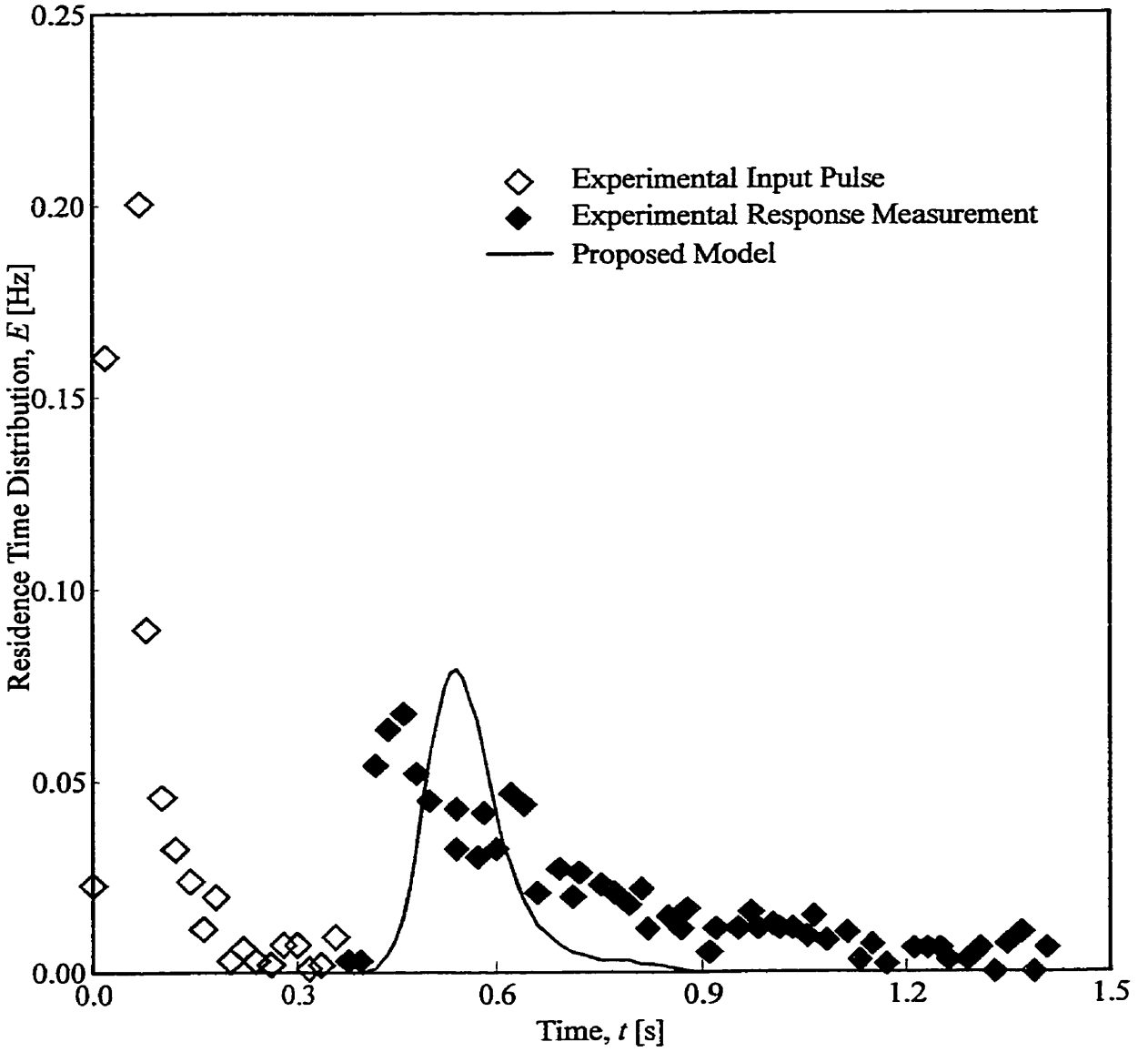

5.6.2 Solids Phase RTD

The spatially discretized versions of Equations 92 and 93 for the solids phase are:

$$\frac{d\mathcal{F}_c^i}{dt} = \frac{-1}{\pi r_c^2 \rho_p \left(1-\epsilon_c^i\right)} \times \left[\dot{m}_c \left(\frac{\mathcal{F}_c^i - \mathcal{F}_c^{i+1}}{\Delta z}\right) + \mathcal{F}_c^i \left(\frac{\dot{m}_c{}^i - \dot{m}_c{}^{i+1}}{\Delta z}\right) + 2\pi r_c \left(\mathcal{F}_c^i G_{ca}{}^i - \mathcal{F}_a^i G_{ac}{}^i\right)\right] \tag{98}$$

and

$$\frac{d\mathcal{F}_a^i}{dt} = \frac{-1}{\pi \left(R^2 - r_c^2\right) \rho_p \left(1-\epsilon_a^i\right)} \times \left[\dot{m}_a \left(\frac{\mathcal{F}_a^i - \mathcal{F}_a^{i+1}}{\Delta z}\right) + \mathcal{F}_a^i \left(\frac{\dot{m}_a{}^i - \dot{m}_a{}^{i+1}}{\Delta z}\right) - 2\pi r_c \left(\mathcal{F}_c^i G_{ca}{}^i - \mathcal{F}_a^i G_{ac}{}^i\right)\right]. \tag{99}$$

Patience and Chaouki (1995) present the data in Figure 65 (Page 164), which were obtained using the same riser and particles described in the previous Subsection. The data stems from the injection of 0.01 kg of irradiated sand at 1.75 m into the riser operating with an inlet superficial gas velocity of $8.2\,\mathrm{m\,s^{-1}}$ and inlet solids mass flux of $140\,\mathrm{kg\,m^{-2}s^{-1}}$. The effects of the abrupt exit are evident even with the scintillator at a height of 4 m, 1 m below the exit. The predicted curve exhibits a significant tail but it is not nearly as pronounced as the measured tail. The breakthrough time for the predicted curve is 0.15 s, which is almost half of the measured breakthrough time of 0.28 s. This phenomenon may be attributable to the abrupt exit since its effects can propagate to the base of the riser (Brereton and Grace, 1994; Pugsley et al., 1997). Additionally, the predicted curve's peak is approximately 33% greater than the measured curve because of the dampening effects of the abrupt exit.

All of the discrepancies between the model proposed in this dissertation and the experimental RTD data are attributable to the model's inapplicability to risers with abrupt exits. Nonetheless, the RTD comparisons indicate that the model has the potential to apply to riser reactors that conform to the assumptions inherent in the model.

Figure 65: Solids Phase RTD Comparison With Experimental Data From Patience And Chaouki, 1995 ($u_{gin} = 8.2\,\mathrm{m\,s^{-1}}$, $G_{sin} = 140\,\mathrm{kg\,m^{-2}s^{-1}}$, $H = 5\,\mathrm{m}$, $D = 0.083\,\mathrm{m}$, $\rho_p = 2630\,\mathrm{kg\,m^{-3}}$, $D_p = 277\,\mu\mathrm{m}$)

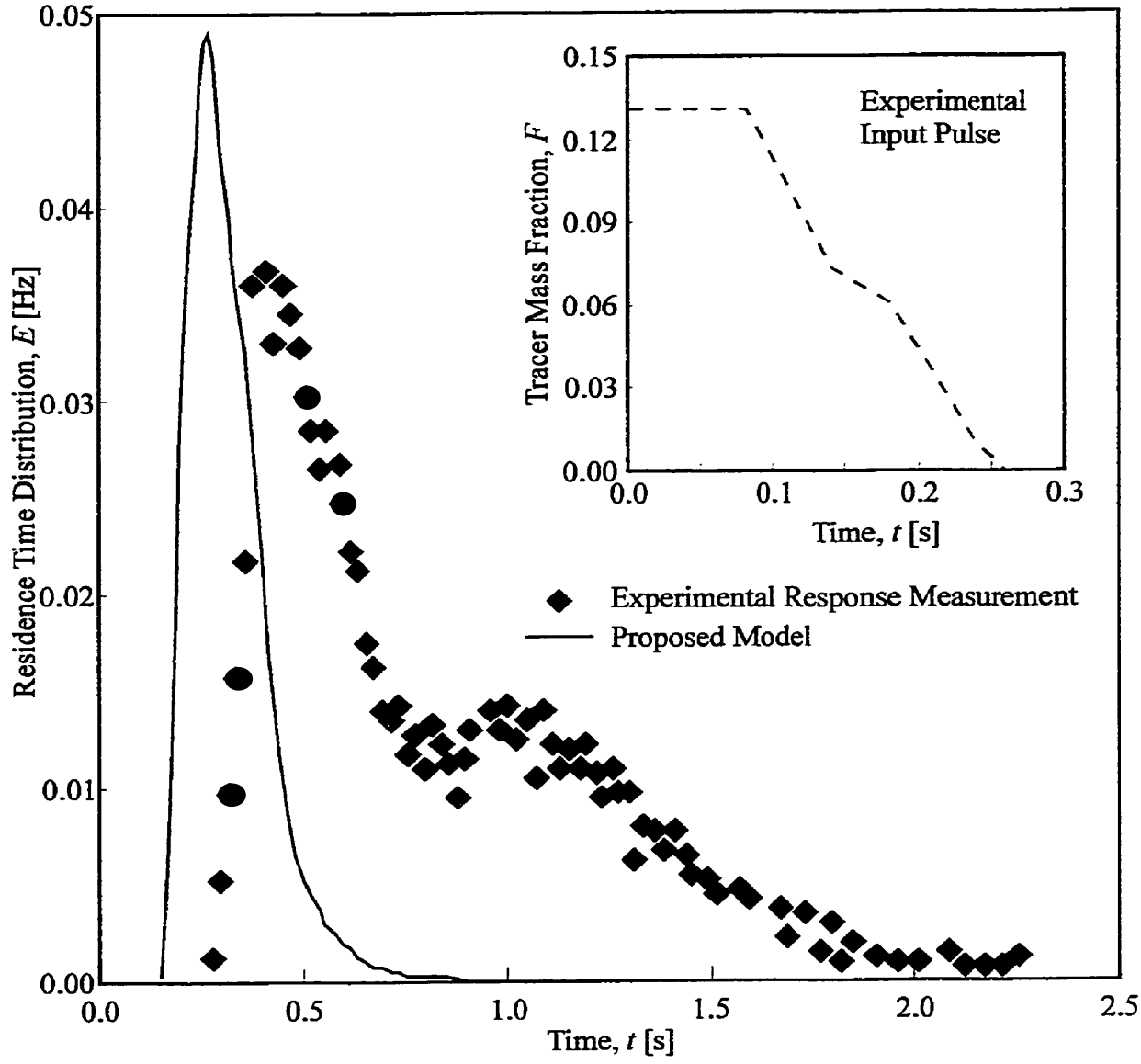

5.7 Ozone Decomposition

Ouyang et al. (1995) are among the few who report a set of experimental data for an LDCFB riser reactor. They measured ozone concentrations at various axial and radial sampling locations in the riser reactor described in Subsection 5.4.2. Although the researchers neglect to mention the several important variables in their experiments, this Subsection compares the data they obtained and predictions of the model presented in this dissertation.

Ouyang et al. (1995) do not report the inlet pressure, temperature, or ozone concentration to the riser reactor but merely mention that the inlet concentration is so low that the reactor operates virtually isothermally. This ambiguity limits comparisons to a qualitative nature.

The simplified hydrodynamic-kinetic reaction model presented in this dissertation does not have the capability to predict concentrations in two dimensions; it can only predict axially varying concentrations in each of the core and annular regions. Consequently, the two dimensional data that Ouyang et al. (1995) present are averaged for the comparisons in this Subsection.

The data in Figure 66 (Page 166) corresponds to an inlet superficial gas velocity of $3.9\,\mathrm{m\,s^{-1}}$ and an inlet solids mass flux of $34\,\mathrm{kg\,m^{-2}s^{-1}}$. Ouyang et al. (1995) indicate that the first-order ozone decomposition rate constant is 14.18 Hz. Inputs to the simulation that generate the predictions in Figure 66 are: $P(0) = 105.0\,\mathrm{kPa}$, $T_{\mathrm{in}} = 300\,\mathrm{K}$, $F_{O_2} = 1.75\,\mathrm{mol\,s^{-1}}$, $F_{O_3} = 0.02\,\mathrm{mol\,s^{-1}}$, and $F_{N_2} = 6.60\,\mathrm{mol\,s^{-1}}$. Hydrodynamic predictions from the proposed model are that the LZUZI is $z_i = 0.26$ and the outlet pressure is 101.0 kPa. The model prediction for the reduced ozone concentration in the annulus is low for all z, particularly at the top of the reactor. This indicates that the predicted quantity of gas descending in the annulus is low, which directly affects the prediction of the concentration in the core due to radial mixing. Accordingly, the predicted concentration in the core is too low. The uncertainty in the operating conditions undoubtedly affects the predictions.

Figure 66: Ozone Decomposition Comparison With Experimental Data From Ouyang et al., 1995 ($u_{gin} = 3.9\,\mathrm{m\,s^{-1}}$, $G_{sin} = 34\,\mathrm{kg\,m^{-2}s^{-1}}$, $H = 10.85\,\mathrm{m}$, $D = 0.254\,\mathrm{m}$, $\rho_p = 1380\,\mathrm{kg\,m^{-3}}$, $D_p = 65\,\mu\mathrm{m}$)

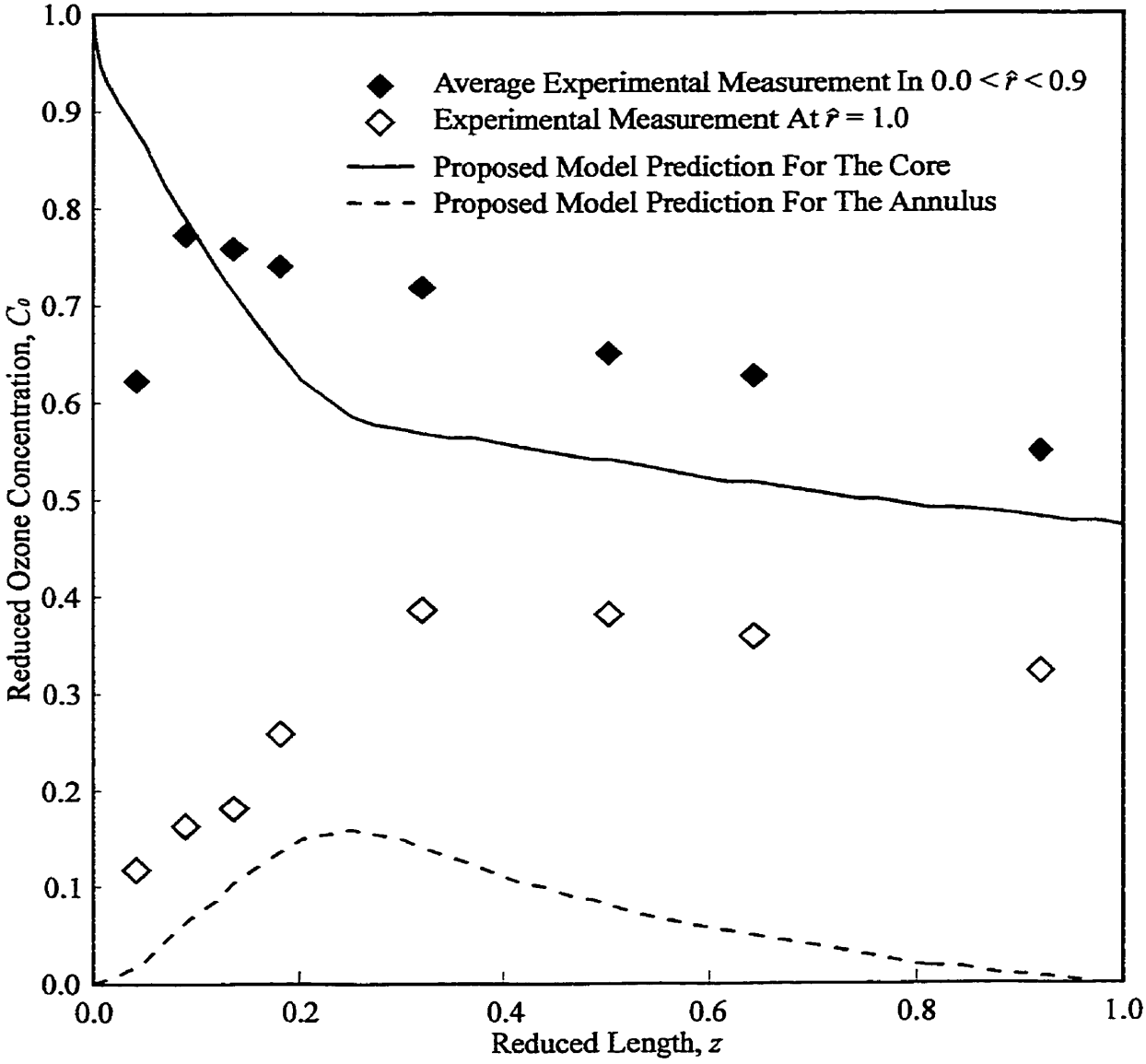

5.8 Adiabatic Reactor Operation

The last Subsection did not test the thermal predictive capabilities of the model presented in this dissertation because of the lack of information Ouyang et al. (1995) provide. The fast, reversible, exothermic Claus reaction,

$$H_2S + \frac{1}{2}SO_2 \rightleftharpoons \frac{3}{2\nu}S_\nu + H_2O, \tag{100}$$

which occurs industrially in the modified Claus process, is an excellent benchmark for testing the full capabilities of the coupled hydrodynamic and kinetic reaction model. The Liu II model (Birkholz et al., 1987) gives the intrinsic rate expression for Reaction 100 on the Kaiser 201 alumina catalyst:

$$\begin{aligned} -r'_{H_2S} &= 1.663 \times 10^{-4} \exp\left(\frac{-30780}{R_g T}\right) \\ &\times \frac{P_{H_2S}\sqrt{P_{SO_2}} - \dfrac{P_{H_2O}P_{S_8}^{0.1875}}{\sqrt{K}}}{\left(1 + 1.125 \times 10^{-5} \exp\left(\dfrac{-2510}{R_g T}\right) P_{H_2O}\right)^2} \end{aligned} \tag{101}$$

where

$$K = \frac{P_{H_2O}P_{S_8}^{0.1875}}{P_{H_2S}\sqrt{P_{SO_2}}} \tag{102}$$

evaluated at equilibrium.

The simulation to demonstrate the thermal predictive capabilities of the proposed model uses a riser reactor with the same geometry as the reactor Ouyang et al. (1995) use but has a feed composition similar to one found in a Claus plant, which Table 13 presents. The inlet pressure to the reactor is 120.0 kPa and the temperature is 400 K for both phases. For the simulation, the Kaiser-201 alumina catalyst ($D_p = 150\,\mu$m, $\rho_p = 1200\,\mathrm{kg\,m^{-3}}$) has a temperature dependent heat capacity of $754.78 + 0.2213T$, expressed in $\mathrm{J\,mol^{-1}\,K^{-1}}$.

The predicted axial temperature profile in Figure 67 (Page 169) corresponds to an inlet superficial gas velocity of $3.8\,\mathrm{m\,s^{-1}}$ and an inlet solids mass flux of $106\,\mathrm{kg\,m^{-2}s^{-1}}$. The temperature rise is remarkably small due to the heat carrying capacity of the

Table 13: Feed Composition For The Adiabatic LDCFB Riser Reactor Simulation

Component	Mole Fraction
H_2O	0.2969
H_2S	0.0658
N_2	0.5986
S_8	0.0003
SO_2	0.2704

solids. However, there is a relatively marked increase in the temperature near the exit of the riser due to the internal re-circulation of matter. This phenomenon is does not occur at the base of the reactor because of the intense mixing of a large amount of cold feed with the internally re-circulated matter. The moderate temperature gradient at the base of the reactor is a primarily a consequence of the high solids concentration and associated reaction rate.

Figure 67 also shows the axial temperature profile for a PFR that is equivalent to the core in the adiabatic LDCFB riser reactor, i.e. the PFR has identical axial voidage and pressure gradient profiles but no radial transfer occurs. In the middle of the riser, the temperature in the PFR is greater than the temperature in the LDCFB because of the internal re-circulation of solids, which provide a greater bulk heat capacity in the LDCFB thereby resulting in less of a temperature rise. Near the exit of the riser, where the reduced solids mass fluxes in both the LDCFB and PFR are close to one, the temperature in the LDCFB is greater than in the PFR because of the internal re-circulation of relatively hot matter.

Figure 68 (Page 171) compares the adiabatic and isothermal operation of the reactor in this Subsection by presenting the net, core plus (negative) annulus, mole flow of sulfur. Clearly, for the specified operating conditions, assuming isothermal operation of the reactor is totally reasonable. The conversion in the adiabatic reactor is 22.1%, which is 0.6% higher than the conversion in the isothermal reactor. The

Figure 67: Axial Temperature Profile For The Adiabatic LDCFB Riser Reactor Simulation ($u_{gin} = 3.8\,\mathrm{m\,s^{-1}}$, $G_{sin} = 106\,\mathrm{kg\,m^{-2}s^{-1}}$, $H = 10.85\,\mathrm{m}$, $D = 0.254\,\mathrm{m}$, $\rho_p = 1200\,\mathrm{kg\,m^{-3}}$, $D_p = 150\,\mu\mathrm{m}$)

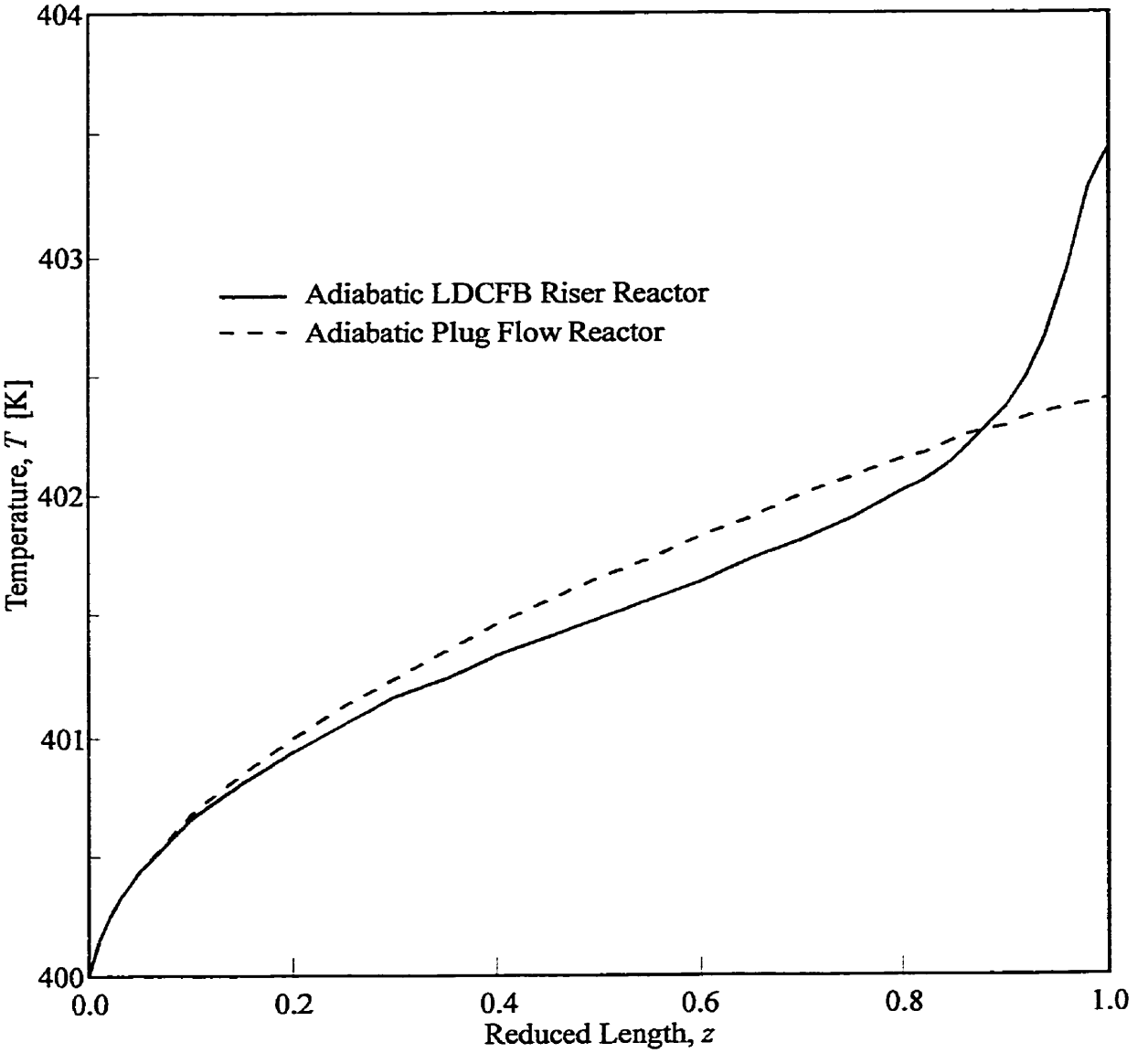

conversion is higher in the adiabatic case, even though the reaction is exothermic and reversible, because it is not limited by equilibrium at the conditions in the reactor. The reaction rate is higher in the adiabatic case due to the higher temperature.

Figure 68: Net Axial Sulfur Mole Flow Rate Profile For The LDCFB Riser Reactor Simulation ($u_{gin} = 3.8\,\mathrm{m\,s^{-1}}$, $G_{sin} = 106\,\mathrm{kg\,m^{-2}s^{-1}}$, $H = 10.85\,\mathrm{m}$, $D = 0.254\,\mathrm{m}$, $\rho_p = 1200\,\mathrm{kg\,m^{-3}}$, $D_p = 150\,\mu\mathrm{m}$)

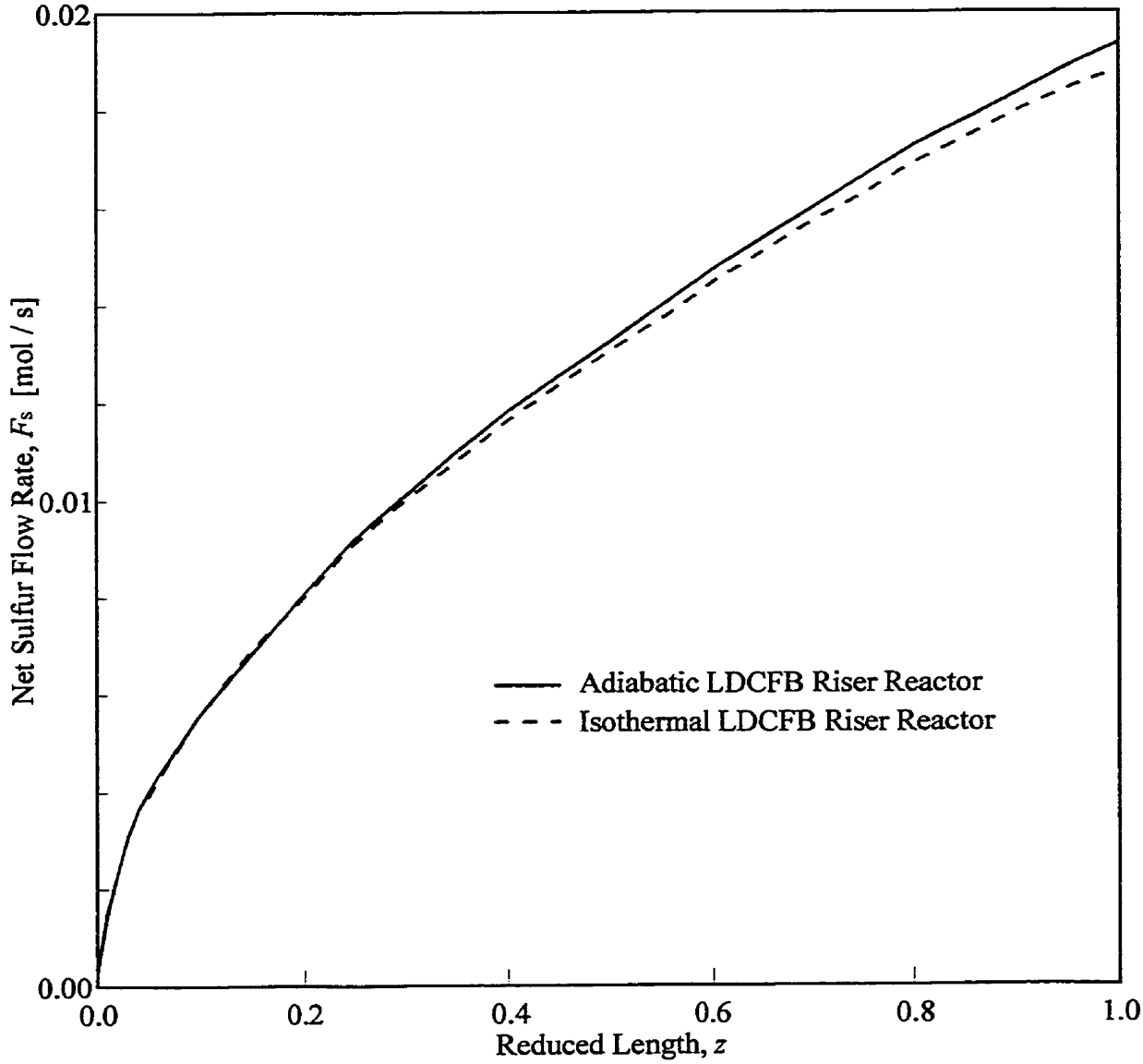

6 Discussion

As previously mentioned, all fluidized bed models have shortcomings and the model presented in this dissertation is no exception. This Section suggests alternative approaches or rationalizations to the shortcomings in the proposed model.

The most glaring shortcoming is in the assumed center-line solids velocity profile near $z = 0.5$, where the model prediction is much less than the measured velocity. The four bases for the center-line solids velocity profile are:

1. The profile is a first order response,
2. The velocity at the base of the riser is a function of the inlet solids mass flux, inlet voidage, and particle density,
3. The velocity at the LZUZI is equal to the inlet superficial gas velocity plus the (negative) terminal velocity of a single particle, and
4. The slip velocity at the exit of the riser is equal to the terminal velocity of a single particle.

Basis 3 is the most suspect for improvement judging from the experimental data that clearly show center-line solids velocities in excess of two times the inlet superficial gas velocity. The observation is undoubtedly due to massive internal re-circulation of matter. Therefore, a seemingly more appropriate prescribed value for the center-line solids velocity at the LZUZI would be $u_s(0, z_i) = 2u_{g\text{in}} + u_t$; however, prescribing such a value would necessitate modification of the assumption determining the solids velocity at the wall and LZUZI.

In the proposed model, a parabolic radial profile determines the solids velocity at the wall and LZUZI. Using Basis 3, the predicted values at the wall are good so increasing the center-line value to twice the inlet superficial gas velocity plus the terminal velocity of a particle would require prescribing a different radial profile to maintain a reasonable match at the wall. Increasing the order of the prescribed

profile would cause an increase in the magnitude of $u_s(1, z_i)$, which is undesirable, and decreasing the order of the profile has the limit of one and does not give a reasonable representation of experimental data. These two conflicting attributes suggest that the solids velocity at the wall and LZUZI should somehow be prescribed independently of the velocity at the center-line and LZUZI.

Also, it is clear that prescribing a monotonically increasing profile at the center-line, Basis 1, is incorrect. Given that the local solids velocity at any point in the riser cannot exceed the local gas velocity and that the center-line solids velocity exceeds the inlet superficial gas velocity in the middle of the riser, Bases 2 and 4 are sound and the center-line solids velocity must exhibit a maximum. Therefore, prescribing a second order response for the center-line solids velocity profile is justifiable. It is also blatantly apparent that the idea of a "fully developed zone" only applies to the upper most fraction of a very tall riser.

In the model presented in this dissertation, two unforeseen problems arise by prescribing the center-line and wall mass fluxes independently of the core radius correlation. A catastrophic loss of numerical precision, which is not a shortcoming in the model, virtually always masks the first problem that is quite fundamental but not always present: At the top of the riser, Equation 31 may not have a positive root because both the center-line mass flux and core radius are too small. Recall that the sum of the first moments of the reduced mass fluxes with respect to $\hat{r} = 0$ in the core and annular regions, respectively, is 1/2 (Equation 30) for all z. If the center-line mass flux and core radius are too small, the first moment of the reduced mass flux in the core is less than 1/2 even if $b = \infty$, i.e. closure of the local mass balance is impossible even if the core is in perfect plug flow, which is the limit. Hence, the center-line mass flux and core radius cannot be entirely independent of each other.

The second problem that arises manifests itself in the axial pressure gradient profile, which is the superposition of the static head of solids and rate of change of momentum. Figure 69 shows the overall pressure gradient and its contributors for

a 5 m tall, 0.083 m diameter riser fluidizing Lane Mount Silica Sand (D_p=208 μm, ρ_p=2580 kg m^{-3}) with air at 8.5 m s^{-1} and an inlet solids mass flux of 400 kg m^{-2}s^{-1}. The static head contribution exhibits the frequently cited "S" shape and inflection point while the rate of change of momentum contribution exhibits bizarre behavior in the domain $0.4 \leq z \leq 1$.

The rate of change of momentum, $\Delta\Lambda$, which is comprised of the rate of change of core area and average solids mass flux and velocity in the core and annular regions with respect to axial location, respectively, behaves expectedly in the domain $0 \leq z \leq 0.4$; it is relatively large at $z = 0$ and increases to a near constant value up to $z = 0.4$. Indeed, $\Delta\Lambda$ should increase to, but never exceed, zero at $z = 1$; however, Figure 69 shows that $\Delta\Lambda$ is greater than zero in $0.5 \leq z \leq 0.8$. Moreover, near the top of the riser, $\Delta\Lambda$ should diminish to zero, which the rate of change of momentum gradient does not do in Figure 69. The only explanation for these characteristics of the model presented in this dissertation is that the quantities constituting the rate of change of momentum are somehow coupled, which is not accounted for in the model development.

An interesting consequence of prescribing solids mass flux and velocity profiles at the wall with coincidental extrema is that the voidage at the wall is constant for all z. This trait of the model presented in this dissertation does not reflect observations, although accurate experimental readings of voidages at the wall are notoriously difficult to obtain. Intuitively, the voidage at the wall is most likely highest at the riser exit; speculation describing the voidage at other axial locations is virtually futile due to the chaotic internal re-circulation of matter in an LDCFB.

The steepness of the radial mass flux and solids velocity profiles near the core radius makes the profiles *extremely* strong functions of the core radius correlation. Consequently, accuracy in the prediction of the core radius profoundly affects the shape of the radial profiles, as attested to by Figure 26. Additionally, because the scheme for material interchange between the core and annulus is a function of the mass

Figure 69: Axial Pressure Gradient Profile Static Head And Rate Of Change Of Momentum Contributions (P_{in} = 115.0 kPa, T_{in} = 300 K, G_{sin} = 400 kg m^{-2}s^{-1}, H = 5 m, D = 0.083 m, ρ_p = 2580 kg m^{-3}, D_p = 208 μm)

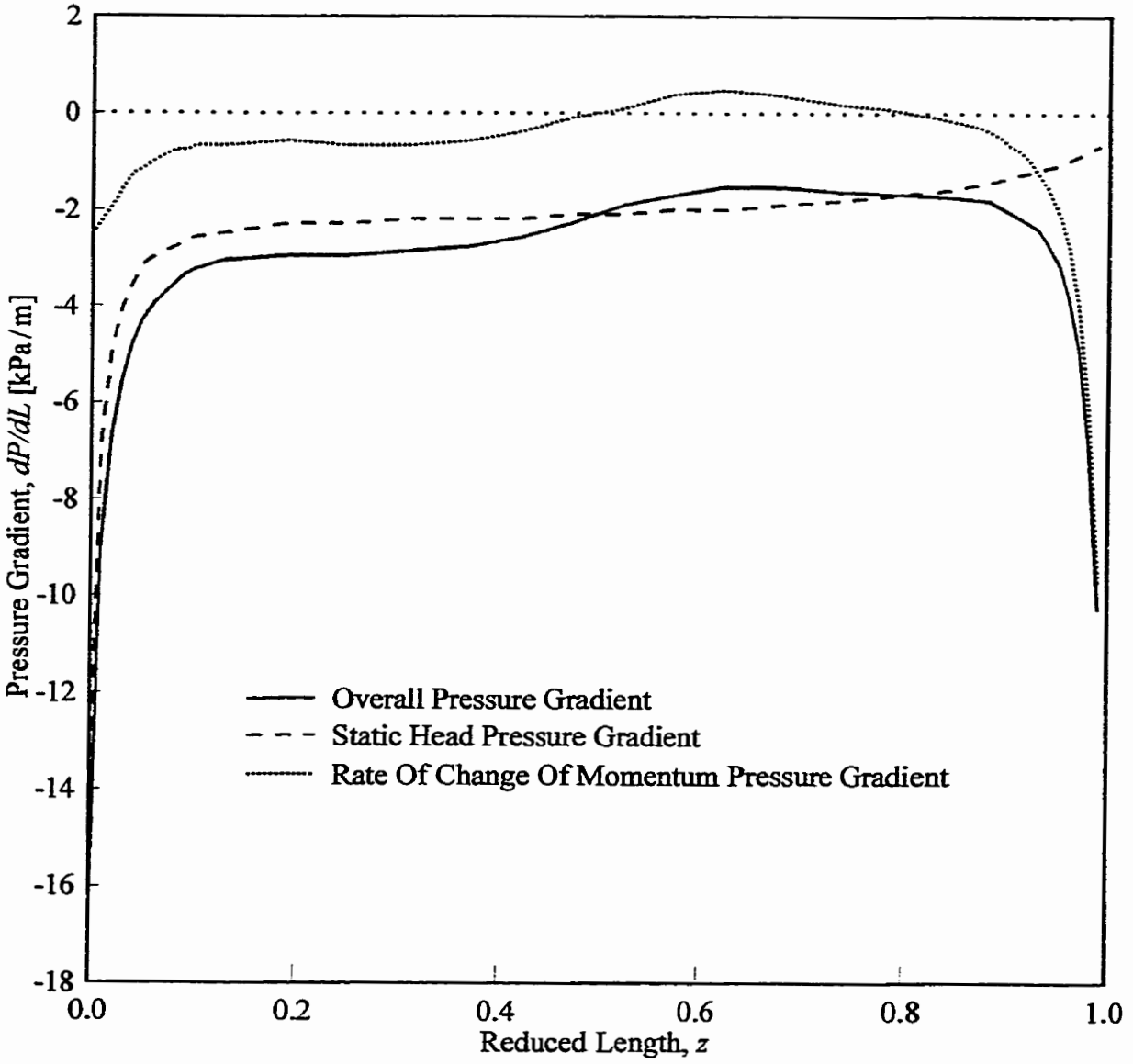

flux profiles and core radius, it too is hypersensitive to changes in $\hat{r}_c$. Equation 12 is the best available core radius correlation but, if a better correlation becomes available, is easily replaceable in the model proposed in this dissertation because of the modular design.

Descending material near the wall in an LDCFB profoundly affects the hydrodynamics in a riser as well as its performance as a reactor. For the riser reactor described in Section 5.8, in which the main Claus reaction occurs, the back-mixing reduces conversion by 4.6% when compared to an equivalent PFR. (Figure 70 shows the difference in sulfur production between the two types of reactors with identical operational parameters.) For an applications such as the modified Claus process or synthetic crude oil production, a difference in conversion of as little as tenths of a percent translates into millions of dollars. Thus, the importance of reactor selection and reactor model accuracy is evident.

Figure 70: Net Axial Sulfur Mole Flow Rate Comparison Between An LDCFB Riser Reactor And Plug Flow Reactor ($u_{gin} = 3.8\ \mathrm{m\,s^{-1}}$, $G_{sin} = 106\ \mathrm{kg\,m^{-2}s^{-1}}$, $H = 10.85$ m, $D = 0.254$ m, $\rho_p = 1200\ \mathrm{kg\,m^{-3}}$, $D_p = 150\ \mu$m)

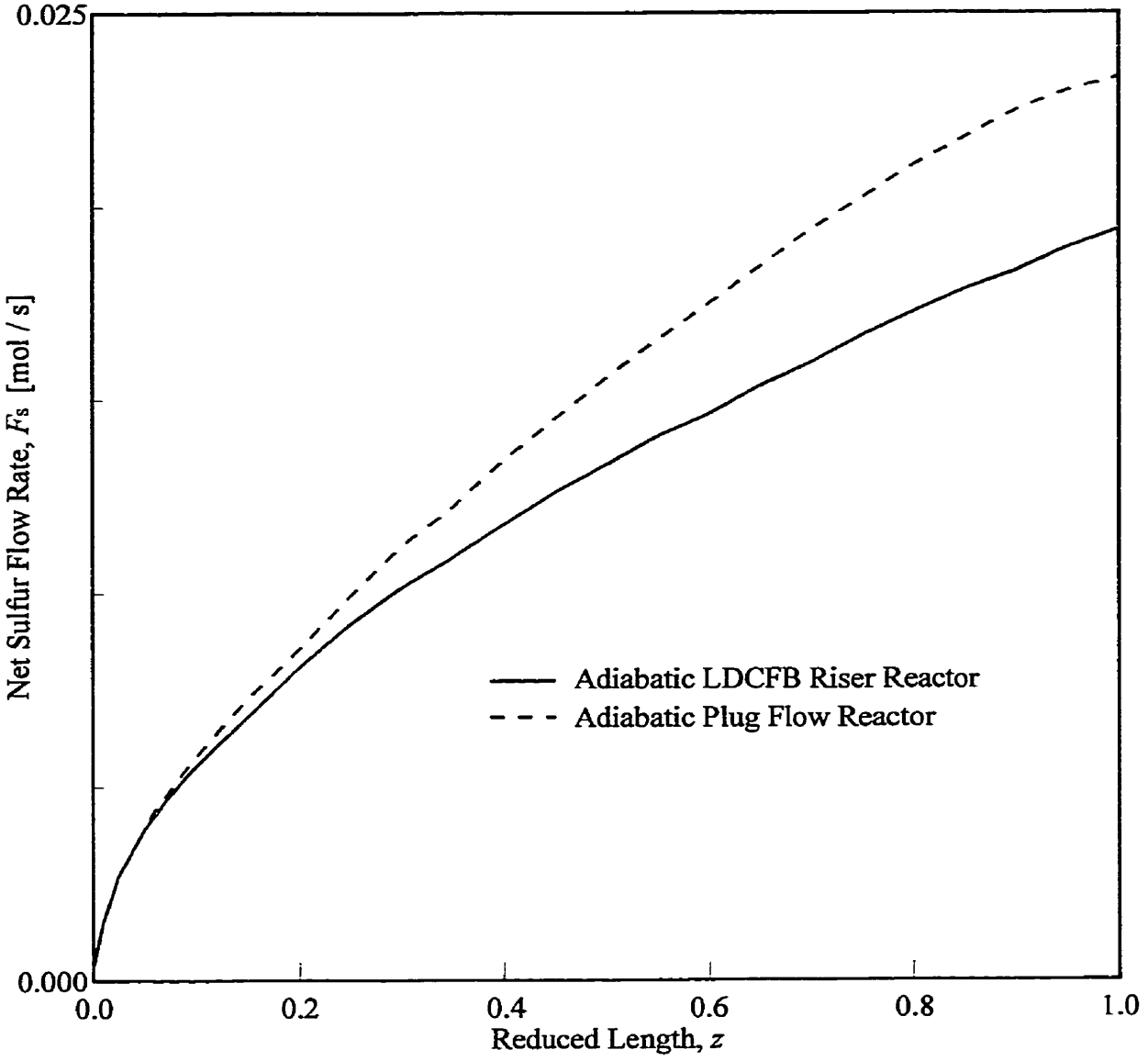

7 Conclusions

The predictive LDCFB riser reactor model presented in this dissertation accounts for the descending gas and solids near the wall of a riser, uses a core-annulus material interchange scheme based on constitutive equations, and includes the contribution of the acceleration of solids to the pressure drop throughout the entire riser length. Additionally, it has the capability to predict axial composition and temperature profiles in the core and annular regions of an adiabatic, kinetically limited LDCFB riser reactor that incurs a change in moles. The robust solution methodology has the capability to deal with multiple reactions with non-linear intrinsic kinetics.

Comprehensive comparisons between the predictions of the proposed model and experimental data validate the model for usage at least at the pilot-scale level. Augmentation of the re-circulation ratio correlation, a key component of the model, could extend the application of the model to industrial scale risers. Improving the basis for the assigned center-line solids velocity at the lower zone-upper zone interface would enhance the model. By design, the model is remarkably extensible and, as it stands, could incorporate axial and radial diffusion and/or dispersion.

Near isothermal operation of an adiabatic LDCFB riser reactor is possible even for highly exothermic reactions; however, conversion deviates from ideality due to the back-mixing caused by the internal re-circulation of gas and solids.

References

Berruti, F., J. Chaouki, L. Godfroy, T.S. Pugsley, and G.S. Patience, "Hydrodynamics Of Circulating Fluidized Bed Risers: A Review", *Can. J. Chem. Eng.*, **73**, 579–602 (1995).

Bi, H.T., private communication, (1997).

Bi, H.T., J.R. Grace, and J.X. Zhu, "Regime Transitions Affecting Gas–Solids Suspensions And Fluidized Beds", *Trans. Inst. Chem. Eng.*, **73**, 154–161 (1995).

Bi, H.T., J. Zhou, S.Z. Qin, and J.R. Grace, "Annular Wall Layer Thickness In Circulating Fluidized Bed Risers", *Can. J. Chem. Eng.*, **74**, 811–814 (1996).

Bi, H.T. and L.S. Fan, "Regime Transitions In Gas–Solid Circulating Fluidized Beds", paper 101e presented at the AIChE Annual Meeting, Los Angeles, CA (1991).

Birkholz, R.K.O., L.A. Behie, and I.G. Dalla Lana, "Kinetic Modelling Of A Fluidized Bed Claus Plant", *Can. J. Chem. Eng.*, **65**, 778–784 (1987).

Bolio, E.J., J.A. Yasuna, and J.L. Sinclair, "Dilute Turbulent Gas-Solid Flow In Risers With Particle-Particle Interactions", *AIChE J.*, **41**, 1375–1388 (1995).

Brereton, C.M.H. and J.R. Grace, "End Effects In Circulating Fluidized Bed Hydrodynamics", in "Circulating Fluidized Bed Technology IV", A.A. Avidan, Ed., AIChE, 137–144 (1994).

Brereton, C., J.R. Grace, C.J. Lim, and J. Zhu, "Engineering Aspects Of Recirculating Fluidised Bed Combustion", in "Chemical Reactor Technology For Environmentally Safe Reactors And Products", H.I. de Lasa, G. Dogu, and A. Ravella, Eds., 507–536 (1993).

Brereton, C.M.H., J.R. Grace, and J. Yu, "Axial Gas Mixing In A Circulating Fluidized Bed", in "Circulating Fluidized Bed Technology II", P. Basu and J.F. Large, Eds., Permagon Press, 307–314 (1988).

Contractor, R.M., G.S. Patience, D.I. Garnett, H.S. Horowitz, G.M. Sisler, and H.E. Bergna, "A New Process For *n*-Butane Oxidation To Maleic Anhydride Using A Circulating Fluidized Bed Reactor", in "Circulating Fluidized Bed Technology IV", A.A. Avidan, Ed., AIChE, 387–389 (1994).

Chehbouni, A., J. Chaouki, C. Guy, and D. Klvana, "Characterization Of The Flow Transition Between Bubbling And Turbulent Fluidization", *Ind. Eng. Chem. Res.*, **33**, 1889–1896 (1994).

Dankwerts, P.V., "Continuous Flow Systems Distribution Of Residence Times", *Chem. Eng. Sci.*, **2**, 1–13 (1952).

Ding, J., and D. Gidaspow, "A Bubbling Fluidization Model Using Kinetic Theory Of Granular Flow", *AIChE J.*, **36**, 523–538 (1990).

Ergun, S., "Fluid Flow Through Packed Columns", *Chem. Eng. Prog.*, **48**, 89–94 (1952).

Farrell, P.A., M.R. Hyre, and L.R. Glicksman, "Importance Of The Solids-To-Gas Density Ratio For Scaling Fluidized Bed Hydrodynamics", in "Fluidization IX", L.S. Fan, T.M. Knowlton, Eds., Durango, CO, 85–92 (1998).

Flemmer, R.L.C. and C.L. Banks, "On The Drag Coefficient Of A Sphere", *Powder Technol.*, **48**, 217–221 (1986).

Geldart, D., *Powder Technol.*, **1**, 725 (1973).

Gidaspow, D., and L. Huilin, "Collisional Viscosity Of FCC Particles In A CFB", *AIChE J.*, **42**, 2503–2510 (1996).

Glicksman, L.R., "Scaling Relationships For Fluidized Beds", *Chem. Eng. Sci.*, **39**, 1373–1379 (1984).

Grace, J.R., "Contacting Modes And Behaviour Classification Of Gas–Solids And Other Two–Phase Systems", *Can. J. Chem. Eng.*, **64**, 353–361 (1986).

Harris, B.J. and J.F. Davidson, "Modelling Options For Circulating Fluidized Beds: A Core/Annulus Depositions Model", in "Circulating Fluidized Bed Technology IV", A.A. Avidan, Ed., AIChE, 32–39 (1994).

Hartge, E.U., D. Rensner, and J. Werther, "Solids Concentration And Velocity Patterns In Circulating Fluidized Beds", in "Circulating Fluidized Bed Technology II", P. Basu and J.F. Large, Eds., Permagon Press, 165–180 (1988).

Hoomans, B.P.B., Fluidization IX presentation, Durango, CO (1998).

Issangya, A.S., D. Bai, J.R. Grace, K.S. Lim, and J. Zhu, "Flow Behavior In The Riser Of A High-Density Circulating Fluidized Bed", presented at the AIChE Annual Meeting, Chicago, IL (1996).

Kruse, M. and J. Werther, "2D Gas And Solids Flow Prediction In Circulating Fluidized Beds Based On Suction Probe And Pressure Measurements", *Chem. Eng. Proc.*, **34**, 185 (1995).

Kruse, M., H. Schoenfelder, and J. Werther, "A Two-Dimensional Model For Gas Mixing In The Upper Dilute Zone Of A Circulating Fluidized Bed Reactor", *Can. J. Chem. Eng.*, **73**, 620–634 (1995).

Kuipers, J.A.M., B.P.B. Hoomans, and W.P.M. van Swaaij, "Hydrodynamic Models Of Gas-Fluidized Beds And Their Role For Design And Operation Of Fluidized Bed Chemical Reactors", in "Fluidization IX", L.S. Fan, T.M. Knowlton, Eds., Durango, CO, 15–30 (1998).

Kunii, D. and O. Levenspiel, "Flow Modeling Of Fast Fluidized Beds", in "Circulating Fluidized Bed Technology III", P. Basu, M. Horio, and M. Hasatani, Eds., Permagon Press, 91–98 (1991).

Louge, M., E. Mastorakos, and J. Jenkins, "The Role Of Particle Collisions In Pneumatic Transport", *J. Fluid Mech.*, **231**, 345 (1991).

McCabe, W.L. and J.C. Smith, "Unit Operations Of Chemical Engineering", McGraw-Hill, New York, NY (1976).

McMillan, G., R. Kelahan, M. Gamel, and A. Garcia, "Model Based Horizon Predictive Control Of Reactor Swell", Hyprotech International Technology Conference, San Antonio, TX, October 13–16 (1996).

Miller, A. and D. Gidaspow, "Dense, Vertical Gas–Solid Flow In A Pipe", *AIChE J.*, **38**, 1801–1845 (1992).

Monceaux, L., M. Azzi, Y. Molodtsof, and J.F. Large "Overall And Local Characterisation Of Flow Regimes In A Circulating Fluidized Bed", in "Circulating Fluidized Bed Technology", P. Basu, Ed., Permagon Press, 185 (1986).

Motte, J., Y. Molodtsof, and A. Delebarre, "Flow Development And Re-Development Scales In A CFB", paper DB16 in "Circulating Fluidized Bed Technology V—Preprints", 1–6 (1996).

Namkung, W. and S.D. Kim, "Gas Mixing In The Upper Dilute Region Of A Circulating Fluidized Bed", paper DGS1 in "Circulating Fluidized Bed Technology V—Preprints", 1–6 (1996).

Nieuwland, J., J.A.M. Kuipers, and W.P.M. van Swaaij, "Theoretical And Experimental Study Of CFB Riser Hydrodynamics", paper MSS3 in "Circulating Fluidized Bed Technology V—Preprints", 1–7 (1996).

Nieuwland, J., M. van Sint Annaland, J.A.M. Kuipers, and W.P.M. van Swaaij, "Hydrodynamic Modeling Of Gas/Particle Flows In Riser Reactors", *AIChE J.*, **42**, 1569–1582 (1996).

Ouyang, S., X.G. Li, and O.E. Potter, "Investigation Of Ozone Decomposition In A Circulating Fluidized Bed On The Basis Of A Core–Annulus Model", in "Fluidization VIII Preprints", Tours, France, 457–466 (1995).

Ouyang, S., X.G. Li, and O.E. Potter, "Circulating Fluidized Bed As A Catalytic Reactor: Experimental Study", *AIChE J.*, **41**, 1534–1542 (1996).

Patience, G.S. and J. Chaouki, "Gas Phase Hydrodynamics In The Riser Of A Circulating Fluidized Bed", *Chem. Eng. Sci.*, **48**, 3195–3205 (1993).

Patience, G.S. and J. Chaouki, "Solids Hydrodynamics In The Fully Developed Region Of CFB Risers", in "Fluidization VIII Preprints", Tours, France, 33–40 (1995).

Patience, G.S., J. Chaouki., F. Berruti, and R. Wong, "Scaling Considerations For Circulating Fluidized Bed Risers", *Powder Technol.*, **72**, 31–37 (1992).

Pita, J. and S. Sundaresan, "Gas-Solid Flow In Vertical Tubes", *AIChE J.*, **37**, 1009 (1991).

Press, W.H., S.A. Teukolsky, W.T. Vetterling, and B.P. Flannery, "Numerical Recipes In C", Second Edition, Cambridge University Press (1992).

Puchyr, D.M.J., A.K. Mehrotra, N.E. Kalogerakis, and L.A. Behie, "Hydrodynamic And Kinetic Modelling Of Circulating Fluidized Bed Reactors Applied To A Modified Claus Plant", *Chem. Eng. Sci.*, **51**, 5251–5262 (1996).

Puchyr, D.M.J., A.K. Mehrotra, N.E. Kalogerakis, and L.A. Behie, "Modelling A Circulating Fluidized Bed Riser Reactor With Gas-Solids Downflow At The Wall", *Can. J. Chem. Eng.*, **75**, 317–326 (1997).

Pugsley, T.S., "The Hydrodynamics Of Circulating Fluidized Beds", PhD Dissertation, The University Of Calgary, Calgary, AB (1995).

Pugsley, T., D. Lapointe, B. Hirschberg, and J. Werther, "Exit Effects In Circulating Fluidized Bed Risers", *Can. J. Chem. Eng.*, **75**, 1001–1010 (1997).

Punwani, D.V., M.V. Modi, and P.B. Tarman, "A Generalized Correlation For Estimating Choking Velocity In Vertical Solids Transport", presented at the International Powder Bulk Solids Handling and Processing Conference, Chicago, IL (1976).

Rhodes, M.J., X.S. Wang, T. Hirama, and B.M. Gibbs, "Similar Profiles Of Solids Flux In Circulating Fluidized–Bed Risers", *Chem. Eng. Sci.*, **47**, 1635–1643 (1992).

Schoenfelder, H., M. Kruse, and J. Werther, "Spatial Reactant Distribution In A Pilot-Scale CFB Riser—Model Predictions And Measurements", paper MSS4 in "Circulating Fluidized Bed Technology V—Preprints", 1–6 (1996a).

Schoenfelder, H., M. Kruse, and J. Werther, "Two-Dimensional Model For Circulating Fluidized-Bed Reactors", *AIChE J.*, 1875–1887 (1996b).

Sinclair, J.L. and R. Jackson, "Gas-Particle Flow In A Vertical Pipe With Particle-Particle Interactions", *AIChE J.*, **35**, 1473–1486 (1989).

Soong, C.H., K. Tuzla, and J.C. Chen, "Experimental Determination Of Cluster Size And Velocity In Circulating Fluidized Bed", in "Fluidization VIII Preprints", Tours, France, 1–8 (1995).

Svensson, A., F. Johnsson, and B. Leckner, "Fluid-Dynamics Of The Bottom Bed Of Circulating Fluidized Bed Boilers", in "Proc. XII International Conference On Fluidized Bed Combustion", L. N. Rubow, Ed., San Diego, CA, 887–897 (1993).

Toomey, R.D. and H.F. Johnstone, "Gaseous Fluidization Of Solid Particles", *Chem. Eng. Prog.*, **48**, 220–226 (1952).

Tsuo, Y.P., and D. Gidaspow, "Computation Of Flow Patterns In Circulating Fluidized Beds", *AIChE J.*, **36**, 885–896 (1990).

Weinstein, H., J. Li, E. Bandlamudi, J.J. Feindt, and R.A. Graff, "Gas Backmixing Of Fluidized Beds In Different Regimes And Different Regions", in "Fluidization IV", J.R. Grace, L.W. Schemilt, and M. Bergougnou, Eds., Engineering Foundation, New York, 57–64 (1989).

Werther, J., "Fluid Mechanics Of Large–Scale Units", in "Circulating Fluidized Bed Technology IV", A.A. Avidan, Ed., AIChE, 1–14 (1994).

Werther, J. and J. Wein, "Expansion Behavior Of Gas Fluidized Beds In The Turbulent Regime", AIChE Symposium Series, **301**, 31–44 (1994).

Yang, W.C., "A Mechanistic Model For Estimating Annuluar Wall Layer Thickness In Circulating Fluidized Bed Risers", in "Fluidization IX", L.S. Fan, T.M. Knowlton, Eds., Durango, CO, 149–156 (1998).

Yang, W.C., "Criteria For Choking In Vertical Pneumatic Conveying Lines", *Powder Technol.*, **35**, 143 (1983).

Yang, W.C., "A Mathematical Definition Of Choking Phenomenon And A Mathematical Model For Predicting Choking Velocity And Choking Voidage", *AIChE J.*, **21**, 1013 (1975).

Zhang, W., Y. Tung, and F. Johnsson, "Radial Voidage Profiles In Fast Fluidized Beds Of Different Diameters", *Chem. Eng. Sci.*, **46**, 3045–3052 (1991).

Zhu, J.X. and H.T. Bi, "Distinctions Between Low Density And High Density Circulating Fluidized Beds", *Can. J. Chem. Eng.*, **73**, 644–649 (1995).

A Assumptions At The Lower Zone-Upper Zone Interface

At the lower zone-upper zone interface (LZUZI), which is the axial location of interest throughout this Appendix, Equation 11 (Page 26) specifies the form of the mass flux profile for all r. Examination of the characteristics of Equation 11 in the LDCFB context is necessary before delving into the determination of the actual location of the LZUZI.

The model presented in this dissertation postulates that the value of the center-line mass flux is available for all z, which yields:

$$a + c = \hat{G}(0, z_i). \tag{103}$$

Additionally, since the mass flux is zero at the core radius,

$$a = \frac{\hat{G}(0, z_i)}{\hat{r}_c^b}. \tag{104}$$

Using Equation 11, the local mass balance is:

$$\frac{1}{2} = \int_0^1 \hat{G}(\hat{r})\hat{r}d\hat{r} \tag{105}$$

$$= \int_0^1 (a + c)\,\hat{r} - a\hat{r}^{b+1}d\hat{r}. \tag{106}$$

Evaluating the integral in Equation 106, exploiting Equations 103 and 104, and manipulating the result algebraically gives:

$$\Omega = \hat{r}_c^b\,(b + 2) - \frac{2\hat{G}(0, z_i)}{\hat{G}(0, z_i) - 1} = 0. \tag{107}$$

Equation 107 is two-dimensional at the LZUZI because Equation 12 correlates the core radius with axial position and design variables alone. Figure 71 is the graphical representation of Equation 107 with the core radius set at 0.9. The three curves correspond to center-line mass fluxes of $\hat{G}(0, z_i) = [1.5, 1.866, 2]$ and generate the data for Table 14. The physical meaning of the data in Figure 71 and Table 14 is that

Figure 71: Dimensionless Mass Balance Versus Radial Mass Flux Profile Degree With $\hat{r}_c = 0.9$ And $\hat{G}(0, z_i) = [1.5, 1.866, 2]$

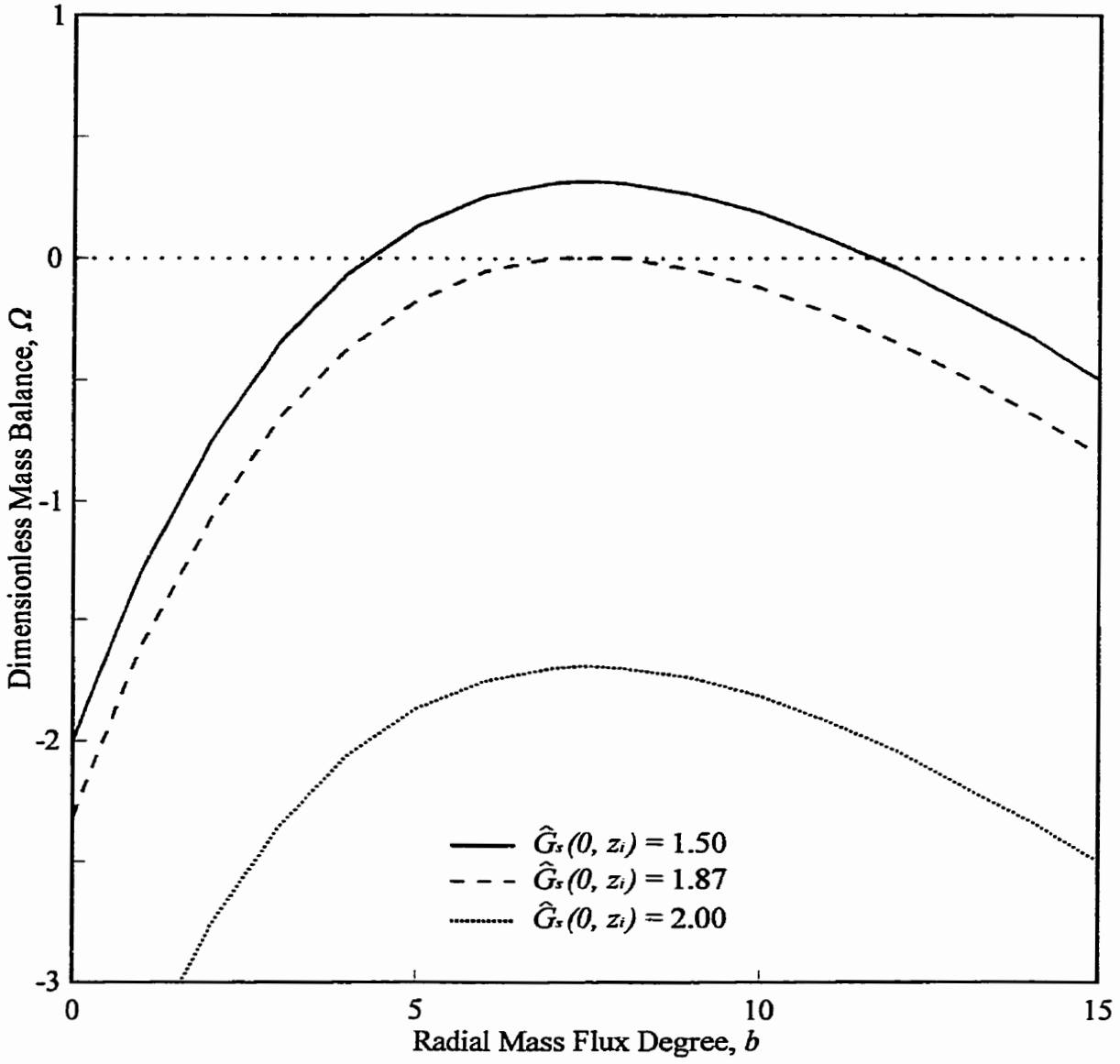

Table 14: Characteristics Of The Dimensionless Mass Balance With $\hat{r}_c = 0.9$ And $\hat{G}(0, z_i) = [1.5, 1.866, 2]$

$\hat{G}(0, zi)$	Roots Of Ω
1.500	None.
1.866	One at $b = 7.491$.
2.000	Two at $b = 4.278$ and 11.65.

there is a minimum center-line mass flux, $\hat{G}(0, z_i)_{\text{minimum}}$, that allows closure of the local mass balance. If $\hat{G}(0, z_i) < \hat{G}(0, z_i)_{\text{minimum}}$, there is no solution to Equation 106; contrarily, if $\hat{G}(0, z_i) > \hat{G}(0, z_i)_{\text{minimum}}$, there are two solutions. A major assumption of the model proposed in this dissertation is that the center-line mass flux at the LZUZI is the minimum mass flux that allows closure of the mass balance.

As Figure 71 clearly shows, $\hat{G}(0, z_i)_{\text{minimum}}$ corresponds with the maximum in Ω, which occurs when

$$b = \frac{-1}{\ln(\hat{r}_c)} - 2. \tag{108}$$

The value of the minimum center-line mass flux that closes the mass balance is:

$$\hat{G}(0, z_i)_{\text{minimum}} = 1 - \frac{2}{\hat{r}_c^b (b+2)}. \tag{109}$$

The core radius is the only variable in Equations 108 and 109 and Equation 12 correlates its value with axial location, so knowing z_i allows for the calculation of $\hat{G}(0, z_i)_{\text{minimum}}$.

In the model presented in this dissertation, the LZUZI is marked by the minimum core radius, maximum center-line mass flux, and minimum wall mass flux and solids velocity. To date, only Rhodes et al. (1998), Miller and Gidaspow (1992), and Hartge et al. (1988) present experimental data at both axial and radial locations with in a particular riser. Moreover, the picture of the axial characteristics is not clear because of the extremely limited number of sampling locations—five in the

case of Rhodes et al. (1998) and three in the case of Hartge et al. and Miller and Gidaspow (1992). Consequently, means other than direct measurement must determine the physical location of the LZUZI, which is required for the formulation of the re-circulation ratio correlation.

Since the center-line solids mass flux is at a maximum at the LZUZI, it is reasonable to infer that the most significant portion of the pressure drop marks its physical location. Therefore, for the purpose of generating the re-circulation ratio correlation, the LZUZI is the location where dP/dL becomes relatively constant. Some authors (Puchyr et al., 1996; Berruti et al., 1995; Pugsley, 1995; Patience and Chaouki, 1995) refer to this point as the end of the "acceleration zone" or the beginning of the "fully developed zone". Using pressure gradient data to determine the location of the LZUZI and assuming that the center-line solids mass flux is the minimum that will allow closure of the mass balance using Equation 11, generation of a correlation that provides the re-circulation ratio at the LZUZI is possible.

The model presented in this dissertation is abstract, to a certain extent, because of its modularity and extensible design. The design is the focus of the research and, academically, the implementation details are of less importance. Thus, a very limited data set determines the parameters in the re-circulation ratio correlation presented in this dissertation. Augmenting the data set would enhance the range of applicability of the model.

Equation 21 gives the form of the correlation; 19 data sets generated by five independent research groups form the foundation for determining the parameters α, β, γ and δ. Table 15 presents the researchers and the constant values used in their experiments. Table 16 shows the ranges of geometries and operating conditions for the risers, all of which experience downward flowing matter at the wall.

The correlation formulation procedure consists of 5 steps:

1. Obtain the location of the LZUZI from pressure gradient data, which is the axial location of interest throughout this procedure.

Table 15: Invariant Characteristics Of LDCFB Rigs In The Re-Circulation Ratio Correlation Data Set

Researchers	L [m]	D [m]	ρ_p [kg m^{-3}]	Inlet T^* [K]
Rhodes et al. (1992)	6.6	0.305	2456	300
Pugsley (1995)	5.0	0.050	2580	300
Patience et al. (1992)	5.0	0.083	2630	300
Ouyang et al. (1995)	10.5	0.250	1380	300
Motte et al. (1992)	10.0	0.144	5200	300

* Indicates an estimate of an unreported value.

Table 16: Operating Ranges Of LDCFB Rigs In The Re-Circulation Ratio Correlation Data Set

Property	Range
Length (L)	5 - 10.5 m
Diameter (D)	0.050 - 0.305 m
Inlet Solids Mass Flux (G_{sin})	34 - 400 kg m^{-2}s^{-1}
Inlet Superficial Gas Velocity (u_{gin})	3.8 - 8.5 m s^{-1}

2. Calculate the core radius using Equation 12.

3. Calculate the re-circulation using Equations 11, 108, and 109.

4. Repeat Steps 1 through 3 for all data sets.

5. Perform a linear least squares regression using Equation 21 and the calculated re-circulation ratios.

Table 17 shows operating conditions and intermediate results of the least squares regression.

None of the researchers report the inlet pressure to the riser, which is required for the calculation of the inlet gas mass flux. Consequently, the pressure values in Table 17 are estimates based on a discharge pressure of 105 kPa and a pressure drop based solely on the hydrostatic head of solids in the riser. Equation 6 is the basis for the calculation of the average voidage in the riser.

In Equation 21, the particle Reynolds number is at standard temperature and pressure.

The results of the regression are $[\alpha, \beta, \gamma, \delta] = [0.9825, 0.5644, 0.0366, -0.2225]$. Admittedly, the pool of data used to determine the parameters is limited; however, Figure 7 (Page 38) does show reasonable parity between the calculated and predicted values of the re-circulation ratio, which is promising.

Table 17: Re-Circulation Ratio Correlation Data Set

G_s [kg m^{-2}s^{-1}]	u_{gin} [m s^{-1}]	$P^{\star}$ [Pa]	z_i []	$\hat{r}_c$ []	b []	$\hat{G}(0, z_i)$ []	$\dot{m}_{sc}/\dot{m}_{sa}$ []
60.0$^{\oplus}$	4.0	108475	0.32	0.869	5.102	2.367	-4.529
40.0$^{\oplus}$	4.0	107334	0.27	0.862	4.734	2.499	-4.273
56.0$^{\ominus}$	5.5	106165	0.20	0.716	0.995	14.467	-1.682
140.0$^{\ominus}$	5.5	107872	0.40	0.771	1.840	6.289	-2.266
240.0$^{\ominus}$	5.5	109845	0.60	0.830	3.372	3.305	-3.327
61.4$^{\ominus}$	6.5	106031	0.20	0.726	1.127	12.058	-1.773
143.0$^{\ominus}$	6.5	107376	0.30	0.752	1.516	8.031	-2.041
230.0$^{\ominus}$	6.5	108778	0.60	0.836	3.580	3.133	-3.472
240.0$^{\ominus}$	8.5	107846	0.46	0.807	2.666	4.149	-2.838
400.0$^{\ominus}$	8.5	109673	0.67	0.865	4.887	2.442	-4.380
102.0$^{\otimes}$	6.0	107059	0.36	0.810	2.748	4.023	-2.894
198.0$^{\otimes}$	6.0	108938	0.48	0.837	3.636	3.091	-3.511
87.0$^{\otimes}$	8.0	106215	0.18	0.786	2.153	5.229	-2.482
34.0$^{\oslash}$	3.9	108021	0.15	0.815	2.898	3.815	-2.998
106.0$^{\oslash}$	3.8	114384	0.69	0.911	8.741	1.725	-7.059
68.5$^{\odot}$	6.0	107960	0.15	0.789	2.214	5.066	-2.525
99.9$^{\odot}$	6.0	109305	0.25	0.808	2.683	4.122	-2.850
116.4$^{\odot}$	6.0	110009	0.30	0.817	2.961	3.736	-3.042
165.1$^{\odot}$	6.0	112075	0.40	0.838	3.640	3.088	-3.514

* Indicates an estimate of an unreported value.

$^{\oplus}$ Rhodes et al. (1992)

$^{\ominus}$ Pugsley (1995)

$^{\otimes}$ Patience et al. (1992)

$^{\oslash}$ Ouyang et al. (1995)

$^{\odot}$ Motte et al. (1992)

B Simulator C++ Source Code

As mentioned in Section 5, implementation of the model presented in this dissertation is in the form of a simulator to expedite the extensive validation process. (Figure 72 is a screen shot of the simulator interface.) The C++ code for the simulator consists of over 30,000 lines, with engineering objects accounting for approximately 75% of the total. An electronic version of the code is available from:

Professor Leo Augustus Behie

Department Of Chemical And Petroleum Engineering

The University Of Calgary

2500 University Drive NW

Calgary, AB T2N 1N4

Figure 72: Screen Shot Of The Simulator Used To Implement The Proposed Model

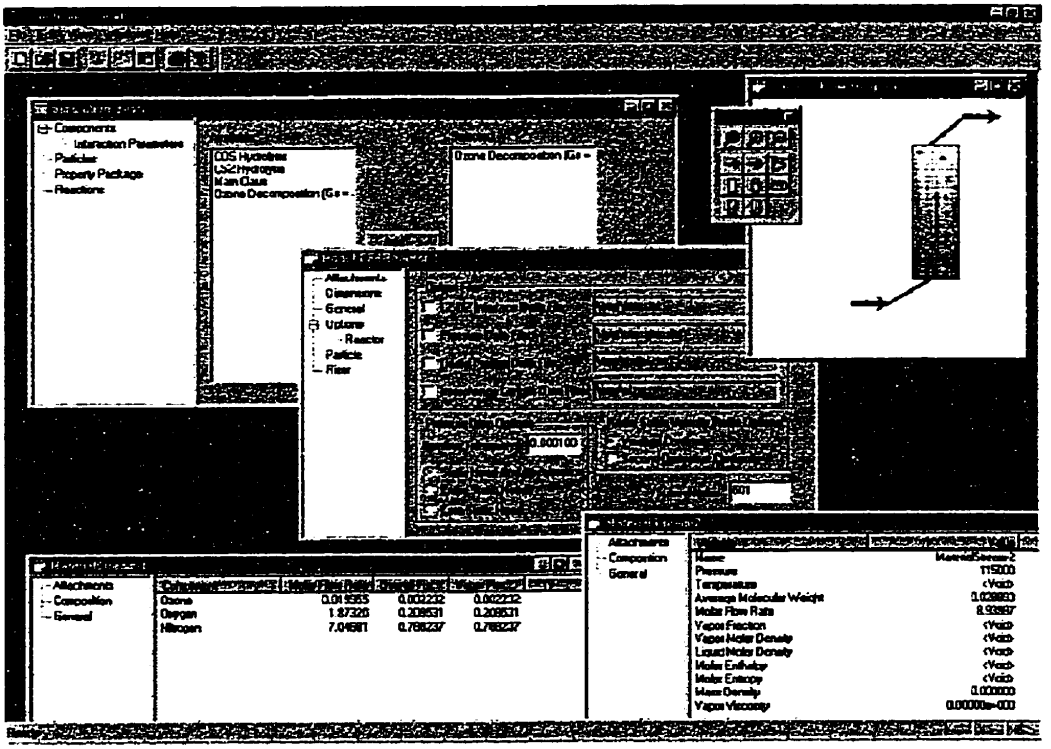

C Pugsley's Solecisms

The key to Pugsley's (1995) model, as with most core-annulus type models, is the determination of the core radius. His model uses a system of six equations to solve for r_c, three of which are (Pugsley, 1995):

$$\bar{u_{sc}} = \frac{G_c}{\rho_p(1-\bar{\epsilon}_c)\phi_s}, \tag{110}$$

$$\bar{u_{sa}} = \frac{G_a}{\rho_p(1-\bar{\epsilon}_a)(1-\phi_s)}, \tag{111}$$

and

$$|G_a| = G_c - G_{\text{in}}. \tag{112}$$

Equations 110, 111, and 112 are incorrect.

The problem with the first two equations is the inclusion of the ϕ_s terms since the average solids mass flux and average voidage in each of the core and annular regions, respectively, implicitly account for the area of the riser that is occupied by the core.

Equation 112, reputed as a mass balance by Pugsley (1995), is erroneous because mass *fluxes* are not conserved. The mass balance, in terms of solids mass fluxes and the fraction of the riser area that is occupied by the core, is:

$$\dot{m}_{\text{in}} = \dot{m}_{sc} + \dot{m}_{sa} \tag{113}$$

$$AG_{\text{in}} = A_cG_c + A_aG_a \tag{114}$$

$$AG_{\text{in}} = A\phi_sG_c + A(1-\phi_s)G_a \tag{115}$$

$$G_{\text{in}} = \phi_sG_c + (1-\phi_s)G_a \tag{116}$$

$$G_{\text{in}} = \hat{r}_c^{\,2}G_c + (1-\hat{r}_c^{\,2})G_a. \tag{117}$$

The combination of Equations 110, 111, and 112, along with algebraic manipulation, yields the correct mass balance equation; however, since Equations 110, 111, and 112 are used independently in Pugsley's (1995) model, it is incorrect. Correcting his model is not difficult but its validity is uncertain.